



Physical and statistical modeling of interstellar grains : Preparation for the JWST

Dangning Hu

► To cite this version:

Dangning Hu. Physical and statistical modeling of interstellar grains : Preparation for the JWST. Astrophysics [astro-ph]. Université Paris Cité, 2022. English. NNT : 2022UNIP7299 . tel-04486033

HAL Id: tel-04486033

<https://theses.hal.science/tel-04486033>

Submitted on 1 Mar 2024

HAL is a multi-disciplinary open access archive for the deposit and dissemination of scientific research documents, whether they are published or not. The documents may come from teaching and research institutions in France or abroad, or from public or private research centers.

L'archive ouverte pluridisciplinaire **HAL**, est destinée au dépôt et à la diffusion de documents scientifiques de niveau recherche, publiés ou non, émanant des établissements d'enseignement et de recherche français ou étrangers, des laboratoires publics ou privés.



Université
Paris Cité



Université Paris Cité

École Doctorale d'Astronomie et Astrophysique d'Île de France (ED 127 AAIF)

Département d'Astrophysique (DAP) // UMR AIM au CEA Paris-Saclay

Physical and statistical modeling of interstellar grains

- Preparation for the JWST

Par **Dangning HU**

Thèse de doctorat d'Astronomie et Astrophysique

Dirigée par Frédéric GALLIANO
Et par Suzanne MADDEN

Présentée et soutenue publiquement le 29 Septembre 2022
Saclay, France

Devant un jury composé de :

Jacques LE BOURLOT	Professor, Université Paris Cité / CNRS	Président
Christine JOBLIN	Professor, IRAP / CNRS	Rapporteuse
Els PEETERS	Professor, UWO / SETI	Rapporteuse
Alexander TIELENS	Professor, Universiteit Leiden / UMD	Examineur
Francisca KEMPER	Research Professor, ICE-CSIC	Examinatrice
Olivier BERNÉ	Chercheur, IRAP / CNRS	Examineur
Suzanne MADDEN	Chercheuse, CEA-Saclay	Directrice de thèse
Frédéric GALLIANO	Chercheur, CEA-Saclay / CNRS	Directeur de thèse



Except where otherwise noted, this is work licensed under
<https://creativecommons.org/licenses/by-nc-nd/3.0/fr/>

Titre :

Modélisation physique et statistique des grains interstellaires
- Préparation au JWST

Résumé : La compréhension des propriétés des grains de poussière interstellaire (abondance, composition chimique, distribution de taille, *etc.*) est cruciale pour comprendre de nombreux processus physiques en jeu dans les galaxies. Le domaine de l'infrarouge moyen (MIR) contient le plus grand nombre de bandes de résonance de ces solides, dont les bandes infrarouges non identifiées (UIB). Ces dernières proviennent d'un mélange statistique d'hydrocarbures aromatiques polycycliques (PAH) de tailles et de structures variées. Leurs propriétés sont une source précieuse d'information sur les conditions physiques (métallicité, intensité du champ de rayonnement, *etc.*) du milieu interstellaire (MIS).

Le satellite ISO (1995-1998) a été le premier observatoire à couvrir la gamme spectrale complète des UIB, de 3,3 à 17 microns. La résolution et la sensibilité des observations ont été largement améliorées avec le spectrographe IRS à bord du *Télescope Spatial Spitzer* (2003-2009; 5.2-38 microns), cependant les bandes aromatique et aliphatique à 3.3 et 3.4 microns n'étaient pas couvertes. Ces deux caractéristiques ont été observées avec le spectrographe IRC (2.5-5 microns) à bord du satellite AKARI (2005-2007). Ainsi, les deux derniers instruments nous permettent d'étudier ces UIB de manière complète.

Pour ce faire, j'ai combiné les cartes spectrales observées avec les deux instruments et étudié leur inter-calibration. J'ai ensuite effectué une décomposition spectrale pour extraire les bandes d'émission. Le nouveau code de décomposition spectrale que j'ai développé adopte l'approche bayésienne hiérarchique (HB). Cette approche permet de modéliser simultanément les paramètres physiques d'échantillons hétérogènes de

galaxies proches et régions Galactiques et la distribution statistique de ces paramètres. Cela nous permet de lever plusieurs dégénérescences et d'extraire le maximum d'information des données, en tenant compte des différentes sources d'incertitudes, sans sur-interpréter les observations. J'ai souligné les défis que j'ai rencontrés en combinant ces ensembles hétérogènes d'observations d'archives (données manquantes, biais d'inter-calibration, couverture spatiale incomplète, *etc.*).

Avec les spectres MIR décomposés de manière cohérente, j'ai extrait les nombreuses bandes d'émission dans cette gamme, non seulement les bandes principales à 3,3, 6,2, 7,7, 8,6, 11,2, 12,7 et 17 microns, mais aussi les bandes plus faibles. J'ai cherché des corrélations entre les intensités de ces bandes, les raies ioniques et les émissions du continuum. J'ai appliqué des modèles de chauffage stochastique pour relier les variations des propriétés des grains aux conditions physiques qu'ils subissent. J'ai effectué une analyse pour l'une des galaxies dans notre échantillon, M 82. Ce travail a servi de projet pilote pour une étude systématique des propriétés des petits grains de carbone avec un large échantillon de galaxies proches observées par les télescopes *Spitzer* et AKARI.

Ce projet de thèse se veut une préparation au *Télescope Spatial James Webb* (JWST; 2021-), qui observera un grand nombre de galaxies résolues avec une résolution angulaire et une sensibilité sans précédent. Nous appliquerons notre code pour analyser les propriétés des grains de poussière afin de contraindre l'évolution des galaxies dans l'univers lointain après le lancement du JWST.

Mots clefs : Milieu interstellaire : Poussière : PAH - Évolution des galaxies - Galaxies : Individuelles : M82 - Méthode : Statistique

Title :

Physical and statistical modeling of interstellar grains
- Preparation for the JWST

Abstract : The knowledge of interstellar dust grain properties (abundance, chemical composition, size distribution, *etc.*) is crucial to understand numerous physical processes at play in galaxies. The mid-infrared (MIR) domain contains most of the solid-state resonance features of interstellar grains, including the unidentified infrared bands (UIBs). The latter are considered to arise from a statistical mixing of polycyclic aromatic hydrocarbons (PAHs) of different sizes and structures. Their properties are a valuable source of information on the physical conditions (metallicity, radiation field intensity, *etc.*) of the interstellar medium (ISM).

The ISO satellite (1995-1998) was the first observatory to cover the full spectral range of the UIBs, from 3.3 up to 17 microns. The resolution and sensitivity of the observations were largely improved with the Infrared Spectrograph (IRS) onboard the *Spitzer Space Telescope* (2003-2009; 5.2-38 microns), however, the 3.3 aromatic and 3.4 micron aliphatic bands were not covered. These two features were observed with the Infrared Camera (IRC, 2.5-5 microns slit-spectrograph) onboard the AKARI satellite (2005-2007). Thus the two latest instruments allow us to simultaneously study all UIBs.

To that purpose, I combined the spectral maps observed with both instruments and assessed their inter-calibration. I then performed spectral fitting to extract emission band intensities. The new spectral decomposition code I developed adopts the hierarchical Bayesian (HB) approach. This approach allows us to simultaneously model the physical parameters of heterogeneous samples of nearby galaxies and Ga-

lactic regions and the statistical distribution of these parameters. It allows us to remove several degeneracies and extract the maximum information from the data, taking into account the various sources of uncertainties, without overinterpreting the observations. I emphasized the challenges I have encountered combining these heterogeneous sets of archival observations (missing data, inter-calibration biases, incomplete beam coverage, *etc.*) and how I addressed them.

With the consistently decomposed MIR spectra, I identified the rich emission features in this range including not only the major bands at 3.3, 6.2, 7.7, 8.6, 11.2, 12.7, and 17 microns, but also the weaker bands. I searched for correlations between the intensities of these bands, the ionic lines, and the continuum emissions. I applied stochastic heating models to link the variations of the grain properties with physical conditions they experience and discussed the band ratios as a diagnostic of galaxy properties. I performed the analysis for one of the galaxies in our sample, M 82. This work served as the pilot project of a systematic study of small carbon grain properties with a large sample of nearby galaxies observed by both *Spitzer* and AKARI.

This thesis project is meant as a preparation for the *James Webb Space Telescope* (JWST; 2021-), which will observe a large number of spatially resolved galaxies with unprecedented angular resolution and sensitivity. We will apply our code to analyze the dust grain properties in order to constrain the galaxy evolution in the distant Universe after the launch of the JWST.

Keywords : Interstellar medium : Dust : PAH - Galaxy evolution - Galaxies : Individuals : M82 - Method : Statistical

Table des matières

Résumé	i
Remerciements	v
Dédicace	vii
Foreword	ix
1 Éléments de la physique de la poussière interstellaire	1
1.1 Motivations : pourquoi étudier la poussière interstellaire ?	2
1.1.1 Phases caractéristiques du milieu interstellaire	2
1.1.2 Importance de la poussière pour la physique galactique	3
1.1.2.1 Processus macroscopiques	3
1.1.2.2 Microphysique	5
1.1.3 Pertinence des galaxies proches	6
1.1.3.1 Par rapport à la Voie lactée	6
1.1.3.2 Par rapport aux galaxies lointaines	7
1.2 Défis de l’astronomie infrarouge	7
1.2.1 Distribution d’énergie spectrale (SED) panchromatique d’une galaxie	7
1.2.2 Différents types d’observatoires infrarouges	9
1.2.2.1 Télescopes spatiaux	9
1.2.2.2 Observatoires aéroportés	11
1.2.2.3 Observatoires au sol	12
1.2.3 Bref historique de la spectroscopie infrarouge	12
1.3 Contraintes empiriques sur les propriétés de la poussière	15
1.3.1 Extinction de la poussière interstellaire	15
1.3.1.1 Extinction de la poussière dans l’UV-optique	16

1.3.1.2	Extinction de la poussière dans l'infrarouge moyen (MIR)	17
1.3.1.3	Extinction par des glaces	17
1.3.2	Observations de l'émission thermique	17
1.3.2.1	Continuum de poussière	18
1.3.2.2	Bandes infrarouges non identifiées (UIB)	18
1.3.3	Déplétion des éléments	21
1.3.3.1	Abondance totale des éléments lourds	21
1.3.3.2	Éléments lourds enfermés dans les grains	21
1.4	Propriétés physiques de la poussière interstellaire	23
1.4.1	Composition chimique des principales espèces de grains	23
1.4.1.1	Silicates	24
1.4.1.2	Hydrocarbures aromatiques polycycliques (PAH)	24
1.4.1.3	Autres grains carbonés	25
1.4.2	Propriétés optiques des grains	26
1.4.2.1	Fonctions diélectriques	26
1.4.2.2	Sections efficaces	28
1.4.3	Rayonnement thermique des grains	30
1.4.3.1	Chauffage à l'équilibre	30
1.4.3.2	Chauffage stochastique	31
1.5	Modélisation des mélanges de poussière interstellaire	33
1.5.1	Perspective historique	34
1.5.2	Processus d'évolution de poussière	36
1.5.2.1	Formation des grains	36
1.5.2.2	Transformation des grains	36
1.5.2.3	Destruction des grains	37
1.6	Mise en évidence des caractéristiques de l'infrarouge moyen (MIR)	37
1.6.1	Études expérimentales et théoriques	37
1.6.2	Impact des propriétés des PAH sur les spectres MIR	39
1.6.2.1	État de charge et ionisation	39
1.6.2.2	Distribution des tailles	40
1.6.2.3	Structure moléculaire et hydrogénation	40
1.6.3	Évolution de l'abondance des PAH en fonction des conditions physiques	41
1.6.3.1	D'une phase diffuse à une phase dense	42
1.6.3.2	Destruction par le champ de rayonnement dur	42

1.6.3.3	Variation entre galaxies de métallicité différente	44
2	Observations avec AKARI et <i>Spitzer</i>	45
2.1	AKARI	46
2.1.1	InfraRed Camera (IRC)	46
2.1.1.1	Instrumentation et observation	46
2.1.1.2	Exploitation des données	48
2.1.2	Traitement des données IRC	49
2.1.2.1	Propagation des incertitudes	49
2.1.2.2	Montage du cube spectral	51
2.1.2.3	Fonction d'étalement du point (PSF)	53
2.1.2.4	Astrométrie des fentes IRC	53
2.1.2.5	Artifacts dans les spectres IRC	55
2.2	<i>Spitzer</i>	55
2.2.1	InfraRed Spectrograph (IRS)	55
2.2.1.1	Instrumentation et observation	56
2.2.1.2	Base de données	57
2.2.1.3	Outils d'analyse des données	58
2.2.2	Traitement des données IRS	58
2.2.2.1	CUBISM	58
2.2.2.2	Sources d'incertitude	64
2.2.2.3	Dégradation de la PSF	66
2.2.3	Coaddition de cartes spectrales	69
2.2.3.1	Reprojection des images	69
2.2.3.2	Broderie des spectres	69
2.2.4	Cartes éparses	69
2.3	Inter-calibration	71
2.4	Étude de cas	73
2.4.1	M 82 (NGC 3034)	73
2.4.1.1	Mesures de distance	75
2.4.1.2	Observations précédentes	75
2.4.2	Les spectres combinés	76
2.4.2.1	Spectres AKARI/IRC	76
2.4.2.2	Spectres <i>Spitzer</i> /IRS	77

2.4.2.3	Inter-calibration	80
2.4.2.4	Spectres finaux	81
3	Modélisation des spectres en infrarouge moyen	85
3.1	Modèles physiques	86
3.1.1	Les enjeux techniques	86
3.1.2	Étalonnage des propriétés des UIB	89
3.1.3	Caractéristiques des UIB	91
3.1.4	Raies du gas	93
3.1.5	Continuum de poussière	93
3.1.6	Contamination stellaire	95
3.1.7	Extinction d'avant-plan	95
3.1.8	Modèle total	97
3.2	Méthodes de fit	99
3.2.1	Incertitudes d'observation	99
3.2.1.1	Bruit aléatoire	99
3.2.1.2	Facteur de calibration	100
3.2.2	Méthode des moindres carrés	100
3.2.3	Méthode bayésienne non hiérarchique (non-HB)	101
3.2.3.1	Loi de probabilité a posteriori	102
3.2.3.2	Loi de probabilité a priori	103
3.2.4	Méthode bayésienne hiérarchique (HB)	103
3.2.4.1	Loi a priori des hyperparamètres	104
3.2.5	Application numérique	105
3.2.5.1	Méthode de Monte-Carlo par chaînes de Markov (MCMC)	105
3.2.5.2	Échantillonnage de loi a posteriori	105
3.2.5.3	Traitement ultérieur	106
3.2.5.4	Optimisation de l'algorithme	107
3.3	Application numérique	109
3.3.1	Générer des spectres de galaxies	110
3.3.2	Ajustement des spectres synthétiques	113
3.3.2.1	Modèle ajusté et modèle médian	113
3.3.2.2	Distributions des paramètres ajustés	116
3.3.2.3	Autocorrélation des paramètres	117

3.3.3	Corrélations des UIB et des complexes d'UIB	118
4	Exploratrion des propriétés des petits grains de carbone	121
4.1	Résultats d'ajustement - M 82	122
4.2	Caractéristiques aromatiques dans les galaxies proches	124
4.2.1	Impact de l'extinction	124
4.2.2	Attributions des bandes d'émission	126
4.2.3	Corrélations des rapports de bande	129
4.3	Interprétation physique	129
4.3.1	Diagnostics par des rapports de bande	129
4.3.2	Découplage des effets de taille et de charge	130
4.3.3	Déshydrogénation et dureté d'ISRF	131
4.3.3.1	Déshydrogénation	132
4.3.3.2	Dureté de l'ISRF	132
4.4	Étude dans l'Univers proche	134
4.4.1	Sélection des échantillons	135
4.4.2	Stratégie de l'analyse	135
5	Conclusion et perspectives	137
5.1	Remarques finales	137
5.1.1	Étude des rapports de bande	137
5.2	Perspectives de l'ère JWST	138
5.2.1	Dans l'Univers local	138
5.2.1.1	Spectroscopie dans l'infrarouge moyen	138
5.2.1.2	Outil de diagnostic des conditions ISM	138
5.2.2	Vers des galaxies lointaines	139
A	Le transfert radiatif en quelques mots	141
A.1	Base élémentaire et terminologie	141
A.2	Équation du transfert radiatif	142
B	Recette pour les statistiques	144
B.1	Fonctions statistiques	144
B.1.1	Loi normale (gaussienne)	144
B.1.2	Loi de Student	145
B.1.3	Loi log-normal	145

B.2	Calcul de la matrice inverse	146
B.2.1	Décomposition LU	146
B.2.2	Factorisation de Cholesky	146
B.2.3	Approche de Sherman-Morrison modifiée	147
C	Recette pour l'univers à grand décalage vers le rouge	149
C.1	Paramètres cosmographiques	149
C.2	Décalage vers le rouge cosmologique	150
C.3	Mesures de distance en cosmologie	151
C.4	Tolman dimming	152
C.5	Correction K	152
D	Figures complémentaires	153
D.1	Tests de MILES	153
D.1.1	Ajustements des spectres synthétiques	153
D.1.2	Distributions des paramètres ajustés	155
D.1.3	Autocorrélation des paramètres	159
D.2	Résultats de M 82	161
D.2.1	Inter-calibration des sous-cartes IRS	161
D.2.2	Spectre combinés	162
D.2.3	Spectre ajustés (méthode HB)	168
D.3	Échantillon de galaxies proches	172
E	Résumé de ma vie scientifiques	182
E.1	Techniques d'observation et de modélisation	182
E.2	Publications et proposals	182
E.3	Communications scientifiques	183
	Bibliographie	187
	Indice	200
	Liste des acronymes	205
	Liste des figures	207
	Liste des tableaux	211

Contents

Résumé	i
Acknowledgements	v
Dedication	vii
Foreword	ix
1 Elements of interstellar dust physics	1
1.1 Motivations: why study interstellar dust?	2
1.1.1 Characteristic phases of the interstellar medium	2
1.1.2 Importance of dust for galactic physics	3
1.1.2.1 Macroscopic processes	3
1.1.2.2 Microphysics	5
1.1.3 Relevance of nearby galaxies	6
1.1.3.1 Compared to the Milky Way	6
1.1.3.2 Compared to distant galaxies	7
1.2 Challenges of infrared astronomy	7
1.2.1 Panchromatic spectral energy distribution (SED) of a galaxy	7
1.2.2 Different types of infrared observatories	9
1.2.2.1 Space-based telescopes	9
1.2.2.2 Airborne observatories	11
1.2.2.3 Ground-based observatories	12
1.2.3 Brief history of infrared spectroscopy	12
1.3 Empirical constraints on dust properties	15
1.3.1 Interstellar dust extinction	15
1.3.1.1 Dust extinction in the UV-optical	16

1.3.1.2	Dust extinction in the mid-infrared (MIR)	17
1.3.1.3	Extinction by ices	17
1.3.2	Observations of the thermal emission	17
1.3.2.1	Dust continuum	18
1.3.2.2	Unidentified infrared bands (UIBs)	18
1.3.3	Elemental depletions	21
1.3.3.1	Total abundance of heavy elements	21
1.3.3.2	Heavy elements locked in grains	21
1.4	Physical properties of interstellar dust	23
1.4.1	Chemical composition of the main grain species	23
1.4.1.1	Silicates	24
1.4.1.2	Polycyclic aromatic hydrocarbons (PAHs)	24
1.4.1.3	Other carbonaceous grains	25
1.4.2	Optical properties of grains	26
1.4.2.1	Dielectric functions	26
1.4.2.2	Cross-sections	28
1.4.3	Thermal grain radiation	30
1.4.3.1	Equilibrium heating	30
1.4.3.2	Stochastic heating	31
1.5	Modeling interstellar dust mixtures	33
1.5.1	Historical perspective	34
1.5.2	Dust evolution processes	36
1.5.2.1	Grain formation	36
1.5.2.2	Grain transformation	36
1.5.2.3	Grain destruction	37
1.6	Focusing on the mid-infrared (MIR) features	37
1.6.1	Experimental and theoretical studies	37
1.6.2	Impact of PAH properties on MIR spectra	39
1.6.2.1	Charge state and ionization	39
1.6.2.2	Size distribution	40
1.6.2.3	Molecular structure and hydrogenation	40
1.6.3	Evolution of PAH abundance as a function of physical conditions	41
1.6.3.1	Going from diffuse to dense regions	42
1.6.3.2	Destruction by the hard radiation field	42

1.6.3.3	Variation across galaxies with different metallicities	44
2	Observing with AKARI and <i>Spitzer</i>	45
2.1	AKARI	46
2.1.1	InfraRed Camera (IRC)	46
2.1.1.1	Instrumentation and observation	46
2.1.1.2	Data mining	48
2.1.2	IRC data processing	49
2.1.2.1	Propagation of the uncertainties	49
2.1.2.2	Spectral cube assembly	51
2.1.2.3	Point spread function (PSF)	53
2.1.2.4	Astrometry of the IRC slits	53
2.1.2.5	Artifacts in IRC spectra	55
2.2	<i>Spitzer</i>	55
2.2.1	The InfraRed Spectrograph (IRS)	55
2.2.1.1	Instrumentation and observation	56
2.2.1.2	Database	57
2.2.1.3	Data analysis tools	58
2.2.2	IRS data processing	58
2.2.2.1	CUBISM	58
2.2.2.2	Uncertainty sources	64
2.2.2.3	PSF degradation	66
2.2.3	Spectral map coaddition	69
2.2.3.1	Image reprojection	69
2.2.3.2	Spectrum stitching	69
2.2.4	Sparsely sampled maps	69
2.3	Inter-calibration	71
2.4	Case study	73
2.4.1	M 82 (NGC 3034)	73
2.4.1.1	Distance measurements	75
2.4.1.2	Previous observations	75
2.4.2	Combined spectra	76
2.4.2.1	AKARI/IRC spectra	76
2.4.2.2	<i>Spitzer</i> /IRS spectra	77

2.4.2.3	Inter-calibration	80
2.4.2.4	Final spectra	81
3	Modeling MIR emission	85
3.1	Physical model	86
3.1.1	The Technical Challenges	86
3.1.2	Calibrating the UIB properties	89
3.1.3	UIB features	91
3.1.4	Gas lines	93
3.1.5	Dust continuum	93
3.1.6	Stellar contamination	95
3.1.7	Foreground extinction	95
3.1.8	Total model	97
3.2	Fitting methods	99
3.2.1	Observation uncertainties	99
3.2.1.1	Random noise	99
3.2.1.2	Calibration factor	100
3.2.2	Least-squares method	100
3.2.3	Non-hierarchical Bayesian (non-HB) inference	101
3.2.3.1	Posterior probability distribution	102
3.2.3.2	Prior probability distribution	103
3.2.4	Hierarchical Bayesian (HB) formalism	103
3.2.4.1	Prior of the hyperparameters	104
3.2.5	Numerical implementation	105
3.2.5.1	Markov chain Monte Carlo (MCMC)	105
3.2.5.2	Sampling the posterior	105
3.2.5.3	Post-processing	106
3.2.5.4	Optimizing the algorithm	107
3.3	Model demonstration	109
3.3.1	Generating galaxy spectra	110
3.3.2	Fit of synthetic spectra	113
3.3.2.1	Fitted model and median model	113
3.3.2.2	Distributions of fitted parameters	116
3.3.2.3	Autocorrelation of parameters	117

3.3.3	Correlations of UIBs and UIB complexes	118
4	Exploring the properties of small carbon grains	121
4.1	Fitting results - M 82	122
4.2	Aromatic features in nearby galaxies	124
4.2.1	Impact of extinction	124
4.2.2	Emission band assignments	126
4.2.3	Band ratio correlations	129
4.3	Physical interpretation	129
4.3.1	Band ratios as diagnostic tools	129
4.3.2	Decoupling size and charge effects	130
4.3.3	Dehydrogenation and ISRF hardness	131
4.3.3.1	Dehydrogenation	132
4.3.3.2	ISRF hardness	132
4.4	Survey study in nearby Universe	134
4.4.1	Sample selection	135
4.4.2	Analysis guideline	135
5	Conclusion and perspectives	137
5.1	Concluding remarks	137
5.1.1	Small carbon grain property	137
5.2	Perspectives towards the JWST era	138
5.2.1	In the local Universe	138
5.2.1.1	Mid-IR spectroscopy	138
5.2.1.2	Diagnostics of the ISM conditions	138
5.2.2	Towards distant galaxies	139
A	Radiative transfer in a nutshell	141
A.1	Elemental basis and terminology	141
A.2	Equation of radiative transfer	142
B	Recipe for statistics	144
B.1	Statistical functions	144
B.1.1	Normal (Gaussian) distribution	144
B.1.2	Student's t-distribution	145
B.1.3	Log-normal distribution	145

B.2	Numerical matrix inversion	146
B.2.1	LU decomposition	146
B.2.2	Cholesky decomposition	146
B.2.3	Modified Sherman-Morrison approach	147
C	Recipe for high-redshift universe	149
C.1	Cosmographic parameters	149
C.2	Cosmological redshift	150
C.3	Distance measures in cosmology	151
C.4	Tolman dimming	152
C.5	K-correction	152
D	Complementary figures	153
D.1	MILES tests	153
D.1.1	Fits of synthetic spectra	153
D.1.2	Distributions of fitted parameters	155
D.1.3	Autocorrelation of parameters	159
D.2	M 82 results	161
D.2.1	Inter-calibration of IRS sub-maps	161
D.2.2	Combined spectra	162
D.2.3	Fitted spectra (HB method)	168
D.3	Nearby galaxy sample	172
E	Summary of my scientific life	182
E.1	Observational and modeling techniques	182
E.2	Publications and proposals	182
E.3	Scientific communications	183
	Bibliography	187
	Index	200
	List of Acronyms	205
	List of Figures	207
	List of Tables	211

Résumé

Une galaxie est constituée de matière baryonique et de matière noire. Les baryons représentent la masse visible des galaxies. Ils en constituent les étoiles et le *milieu interstellaire* (MIS), ce dernier étant la matière située entre les étoiles. À l'intérieur du MIS se trouvent des atomes en phases gazeuse et solide, à savoir le gaz et la poussière interstellaires. Le gaz interstellaire est pour l'essentiel constitué d'hydrogène ($\approx 73\%$) sous forme atomique et moléculaire et d'hélium ($\approx 25\%$), alors que la poussière est principalement constituée d'éléments plus lourds que l'hélium (*e.g.* carbone, oxygène, azote, fer, magnésium, *etc.* souvent assemblés en composés silicatés et carbonés) sous forme de particules solides que nous appelons grains interstellaires. Ces grains ont majoritairement une taille inférieure au micron. Le sujet de cette thèse est la composante la plus poétique des galaxies : la poussière interstellaire. En effet, le MIS est le berceau des étoiles où elles naissent par effondrement gravitationnel des nuages moléculaires, et en même temps la tombe où elles meurent en rejetant violemment leur matière.

Les grains de poussière interstellaire ont un rôle crucial dans la physique du MIS, bien que leur masse n'en représente qu'un pourcent. La compréhension des propriétés de ces grains (abondance, composition chimique, distribution de taille, *etc.*) est la clé pour comprendre de nombreux processus physiques en jeu dans les galaxies. Par exemple, la poussière absorbe la puissance rayonnée par les étoiles et la réémet dans l'infrarouge. En particulier, les régions de formation d'étoiles sont totalement opaques en lumière visible. Le rayonnement infrarouge, émis jusqu'à 99% par la poussière, est le moyen le plus robuste de les étudier. Les grains sont également à l'origine du chauffage du gaz, par effet photo-électrique, dans les *régions de photodissociation* (PDR). Enfin, les grains servent de catalyseurs à de nombreuses réactions chimiques, dont la formation du dihydrogène, molécule la plus abondante de l'univers.

L'émission infrarouge est très difficile à observer au sol à cause de l'absorption de l'atmosphère de la Terre. Ce n'est que depuis le lancement des premiers observatoires aéroportés et spatiaux que nous avons accès à cette fenêtre spectrale, dans son intégralité. En particulier, le domaine de l'*infrarouge moyen* (MIR) contient le plus grand nombre de bandes de résonance des solides, dont les *bandes infrarouges non identifiées* (UIB). Ces bandes proviennent d'un mélange d'*hydrocarbures aromatiques polycycliques* (PAH) de tailles et de structures différentes. Leurs propriétés sont une source précieuse d'information sur les conditions physiques (métallicité, intensité et dureté du champ de rayonnement, *etc.*) du MIS.

Le satellite ISO (1995-1998) a été le premier observatoire à spectrographier la gamme complète des UIB, de 3.3 à 17 μm . La résolution et la sensibilité des observations ont été largement améliorées avec le spectrographe IRS à bord du *Télescope*

Spatial Spitzer (2003-2009 ; 5.2-38 μm). Cependant, les bandes aromatique à 3.3 μm et aliphatique à 3.4 μm n'étaient pas couvertes. En revanche, ces deux bandes ont été observées par le spectrographe IRC (2.5-5 μm) à bord du satellite AKARI (2005-2007), avec une résolution spectrale et angulaire comparable. Ainsi, ces deux derniers instruments nous permettent d'étudier les **UIB** de manière complète. Pour ce faire, j'ai développé un outil permettant de combiner les cartes spectrales provenant de différentes observations, en réalisant une procédure d'homogénéisation des données. En outre, j'ai étudié l'inter-calibration de mes données, de manière systématique. Cette étape permet de corriger les biais entre les spectres des différents modules de *Spitzer*/IRS et d'AKARI/IRC, grâce à la comparaison entre la photométrie synthétique et la photométrie réelle de *Spitzer*/IRAC ou de *Spitzer*/MIPS. Finalement, la propagation d'incertitudes est prise en compte par une méthode de *bootstrapping* Monte-Carlo. J'ai souligné les défis que j'ai rencontrés en combinant ces ensembles hétérogènes d'observations d'archives (données manquantes, biais d'inter-calibration, couverture spatiale incomplète, *etc.*). Cela m'a incité à écrire un logiciel, **MIRAGE**¹, qui nous permet de construire des cubes spectraux dans le **MIR**, à partir d'observations hétérogènes.

Dans un deuxième temps, j'ai mis en œuvre la décomposition spectrale de ces données, afin d'en extraire les bandes d'émission. Le nouveau code de décomposition spectrale (**MILES**²), que j'ai développé, ajuste un ensemble de spectres **MIR** avec une combinaison d'**UIB**, de raies du gaz, de continuums de poussière, d'un continuum stellaire, et d'une extinction. Trois méthodes, celle des moindres carrés, la méthode bayésienne et la méthode *bayésienne hiérarchique* (**HB**), sont appliquées à l'ajustement. Les originalités de ce code sont les suivantes.

- Chaque **UIB** a un profil de Lorentz asymétrique dont les paramètres ont été étalonnés dans des régions Galactiques, en utilisant des spectres à haut rapport signal-sur-bruit d'ISO-SWS et de *Spitzer*/IRS.
- Notre code adopte l'approche **HB**, ce qui permet de modéliser simultanément les paramètres physiques d'échantillons hétérogènes de galaxies proches et de régions Galactiques et la distribution statistique de ces paramètres. Cela nous permet de lever plusieurs dégénérescences et d'extraire le maximum d'informations des données, en tenant compte des différentes sources d'incertitude, sans pour autant sur-interpréter les observations.

J'ai comparé les différentes méthodes d'ajustement en les appliquant à des spectres simulés, reproduisant les observations typiques de galaxies proches. En variant le rapport signal-sur-bruit et le niveau de continuum, j'ai prouvé que la méthode **HB** était plus efficace pour les corrélations entre rapports d'intensité de bandes que les autres méthodes. De plus, les méthodes bayésiennes permettent d'explorer la distribution de paramètres, calculée par une *chaîne de Markov Monte Carlo* (**MCMC**), et donc d'étudier des distributions qui sont parfois multimodales. Cela implique que les fortes dégénérescences entre paramètres peuvent être mieux inférées à l'aide de leurs hyperparamètres, dans le cas hiérarchique.

Cette étude s'est concentrée sur plusieurs galaxies proches (à une distance de quelques dizaines de millions d'années-lumière), dont la galaxie M 82, pour laquelle j'ai réalisé une analyse complète dans Hu et al. (2022a). Elle a servi de projet pilote pour une étude systématique des propriétés des petits grains de carbone dans un large échantillon de galaxies proches observées

1. **MIRAGE** : Mid-InfraRed spectra cube Assembly enGinE (<https://github.com/kxxdhdn/MISSILE/tree/main/MIRAGE>).

2. **MILES** : Mid-Infrared Line Extraction Software (<https://github.com/kxxdhdn/MISSILE/tree/main/MILES>).

par les télescopes *Spitzer* et AKARI. En effet, l'intérêt d'étudier les galaxies proches plutôt que le MIS de notre Galaxie se trouve dans la diversité des conditions physiques environnementales, parfois même extrêmes, auxquelles l'on peut accéder. Par exemple, dans les *noyaux actifs de galaxie* (AGN), les grains sont fortement transformés par le champ de rayonnement très dur produit par le disque d'accrétion. Similairement, la faible métallicité des galaxies naines a un impact radical sur la composition et l'abondance des grains.

M 82 (NGC 3034) est une galaxie irrégulière vue de profil, dans un groupe de galaxies dominé par M 81. C'est une Galaxie À Flambée de Formation d'Étoiles (GAFFE) avec un super-vent galactique. Elle est l'une des galaxies les plus étudiées en raison de sa proximité (à une distance de 3.63 ± 0.3 Mpc). M 82 a été observée à la fois par *Spitzer*/IRS et AKARI/IRC (Beirão et al., 2008, 2015; Yamagishi et al., 2012), et nous avons collecté 12 fentes d'IRC recouvrant la carte spectrale d'IRS. En intégrant spatialement les pixels à partir d'un critère basé sur leur brillance de surface, nous avons finalement produit 41 spectres MIR ayant une couverture spectrale de 2.5 à 20 μm . Ces spectres couvrent le disque central de M 82 jusqu'à l'extrémité de son vent. Après avoir ajusté ces spectres à l'aide des trois méthodes du logiciel MILES, j'ai identifié et extrait l'intensité de toutes les bandes d'émission dans ce régime, aussi bien les bandes principales à 3,3, 6,2, 7,7, 8,6, 11,2, 12,7, et 17 μm , que les bandes plus faibles.

J'ai étudié les corrélations entre les rapports d'intensité de ces bandes, des raies ioniques du gaz et de l'émission du continuum. La variation de la plupart de ces rapports peut être interprétée par l'effet de l'ionisation, parce que les bandes ont pour origine différents modes de vibration des liaisons C–C et de C–H, comme le montrent les expériences de laboratoire et les calculs théoriques. En suivant le travail de Galliano et al. (2008b), j'ai quantifié la charge des porteurs de bandes, les PAH, avec le rapport de bandes I(6.2)/I(11.3), en supposant un équilibre de charge entre le taux de photons ionisants et le taux de recombinaison avec les électrons. Ainsi, nous avons pu utiliser ces corrélations entre les rapports de bandes comme diagnostics des conditions physiques pour les sources lointaines. Par rapport à M 82, l'ionisation est plus importante au centre de la galaxie, tandis qu'elle décroît rapidement le long des super-vents galactiques.

L'autre origine possible de la variation des bandes est la taille des PAH, cette taille pouvant être affectée par des processus violents comme les chocs ou un champ de rayonnement intense. La variation de la distribution de taille se superpose à celle de l'ionisation, puisque la taille, comme la charge, affecte les rapports d'intensité des bandes. Afin de découpler ces deux effets, j'ai utilisé un modèle de chauffage stochastique pour prédire l'émission de PAH de différentes tailles (Draine & Li, 2007; Zubko et al., 2004), et ainsi estimer les rapports de bandes théoriques qui permettent de lever cette dégénérescence. En comparant les rapports de bandes observées, I(3.3)/I(11.3) et I(7.7)/I(11.3), à leurs valeurs théoriques, nous avons contraint la distribution de taille de grains représentée par le nombre moyen d'atomes de carbone et la fraction d'ionisation, pour des propriétés optiques et un *champ de rayonnement interstellaire* (ISRF) donnés.

La bande à 3.4 μm est caractéristique de groupes aliphatiques dans des PAH hydrogénés (HPAH). Leur déshydrogenation peut être étudiée à l'aide du rapport I(3.4)/I(3.3). Cette valeur diminue avec la distance du disque de M 82, jusqu'à deux ordres de grandeur à l'extrémité du vent galactique. Il a été proposé que cet effet pouvait être expliqué par la production de PAH par fragmentation de gros grains carbonés dans le halo de la galaxie. L'autre possibilité est que la déshydrogenation des PAH soit le

résultat d'un **ISRF** dur, qui peut être tracé par le rapport $[\text{Ne III}]/[\text{Ne II}]$. Ce dernier rapport varie d'un facteur ≈ 4 autour du plan galactique de M 82, et est anti-corrélé avec $I(3.4)/I(3.3)$, mais il ne varie quasiment pas dans le vent. De plus, si l'on regarde les raies de ro vibration de l'hydrogène moléculaire, il y a plus de H_2 chaud dans le vent, probablement chauffé par les chocs. J'en ai donc conclu que le champ de rayonnement dur domine la déshydrogenation des **HPAH** proche du plan galactique de M 82, alors que la fragmentation des grains est la source principale de la production des **PAH**, dans le vent. Notez que cette tendance ne se voit qu'avec la méthode **HB**, alors que les autres méthodes tendent à produire une fausse corrélation positive entre ces deux rapports.

La prochaine étape est d'appliquer notre méthode, développée et validée par le présent travail, à un grand échantillon de galaxies proches et spatialement résolues. Cet échantillon contient à peu près 500 pointages de spectroscopie à fente d'AKARI/IRC, observés également par *Spitzer*/IRS. Cela représente quelques milliers de spectres individuels. J'ai appliqué la méthode **HB** aux différents sous-échantillons, pour étudier (i) une source individuelle résolue (*e.g.* IC 10, NGC 1140), (ii) un certain type de régions (*e.g.* **PDR**, régions H II) dans différentes galaxies résolues, et (iii) un ensemble de sources intégrées à l'échelle galactique. Une étude systématique des propriétés des petits grains de carbone est en cours, et sera présentée dans [Hu et al. \(2022b\)](#).

Ce projet de thèse se veut une préparation à l'analyse des observations du *Télescope Spatial James Webb* (JWST ; 2021–), dont le lancement a eu lieu à la fin de cette thèse. JWST nous permettra d'accéder à une résolution angulaire inférieure à la seconde d'arc dans le régime **MIR** avec une sensibilité sans précédent. Notre modèle spectral pourra être appliqué à l'analyse des propriétés des grains de poussière dans différentes régions galactiques dans l'univers local, ou au niveau global des galaxies de l'univers plus lointain, afin de contraindre l'évolution des galaxies à différentes échelles.

Acknowledgements

I have been enjoying the somehow “*endless*” work, or rather the state of working as a doctoral student...in Paris! Then I realized that time’s up! “*Le moment est venu.*” There is never an endless thing. (You say the Universe?) However, there is always an end, even if I do not want it to end.

First of all, I would like to thank my supervisor Fred. He has been my major encouragement on research since the first day of my thesis³ through his generosity, his patience, his diligence, his efficiency, his double-precision, his nerdy numerical libraries, his jazz guitar skills and his bad jokes⁴.

I would like to thank my directrice de thèse Suzanne. Indeed, she is a real director guiding whoever is around her!

I am grateful to my referee, Christine and Els, whose careful reading and thoughtful comments led to considerable improvements in the manuscript.

I thank the Chinese Scholarship Council (CSC) and Le Commissariat à l’énergie atomique et aux énergies alternatives (CEA) of France for funding this thesis.

I thank Antigone, Corentin, Diane & Sacha, Fiorella, Frances, Lara, Lise, Maud, Marc-Antoine, Maryam & Sambit, Ronin, Vianney, ... all people of the NUAGES group I have met. I thank the colleagues at CEA for the discussions and chats of all kinds. They have made my laboratory life happy and meaningful.

Special thanks to Onaka-san for all the help he has provided for me and his ginkgo/sakura photos!

I thank those friends and classmates who accompanied me during these years in Paris. I thank my cat Mao’dou. Finally, I thank my parents, the only ones who I know will always be there.

I do want it to end. So I can keep all these precious memories before they deteriorate. And more importantly, I can move on.

3. Starting with a six-page TODO list, which I have never the courage to check since maybe mid-term...

4. e.g. “*I see I can own jokes I don’t even make, the same way the silence after Mozart is still from Mozart.*” You know who I quoted.

Dedication

Le savant n'étudie pas la nature parce que cela est utile ; il l'étudie parce qu'il y prend plaisir et il y prend plaisir parce qu'elle est belle.

Science et méthode (1908) de Henri Poincaré

Foreword

The subject of this thesis is the most poetic component of galaxies: interstellar dust.

A galaxy consists of baryonic and dark matters. The baryons residing in stars and the **InterStellar Medium (ISM)** make up the visible mass of galaxies. Inside the **ISM** are gas-phase and solid-state materials, namely interstellar gas and dust. The observed **Spectral Energy Distribution (SED)** of a galaxy encodes most information of its composition, dynamics, and evolutionary history. Stars shine in the ultraviolet and optical regimes, whereas the infrared glow mainly rises from interstellar dust.

This thesis focuses on the observed **Mid-InfraRed (MIR)** emission spectra of nearby galaxies. Most of the abundant spectral features in this regime are attributed to the smallest interstellar carbon grains⁵, the **Polycyclic Aromatic Hydrocarbons (PAHs)**.

For the first part of the work, we have homogenized the AKARI/IRC and *Spitzer*/IRS spectroscopic observations of sources in our nearby galaxy sample. By combining spectra from both instruments, we have been able to study all the emission features from 3.3 up to 17 μm in a consistent way.

As the second part of the work, we have developed a state-of-the-art **MIR** spectral decomposition code, MILES, to study the complex **MIR** spectral features and build diagnostics using correlations between the spectral properties and the physical conditions. Our software is dedicated to analyzing galaxies and galactic regions and can be easily adapted to **MIR** spectra obtained from different telescopes. In particular, the launch of the *James Webb Space Telescope* (JWST; 2021–) will allow us to access sub-arcsec resolution in the **MIR** regime. Our spectral model is pertinent to analyzing the JWST data, revealing the grain properties on smaller scales or in a more distant universe.

We have performed the entire work for the galaxy M 82 as a case study.

The current manuscript has included the author’s work between October 2018 and October 2021, under the supervision of Dr. Frédéric Galliano and Dr. Suzanne Madden, in collaboration with Dr. Vianney Lebouteiller, Dr. Sacha Honý, Prof. Takashi Onaka, Dr. Ronin Wu, and Prof. Itsuki Sakon.

The complete bibliography of this manuscript can also be found on the SAO/NASA Astrophysics Data System (ADS): <https://ui.adsabs.harvard.edu/public-libraries/laV7PiCbRiKKpYmh6yYQgA>.

The thesis project was jointly funded by the China Scholarship Council (CSC) and the French Commissariat à l’énergie atomique et aux énergies alternatives (CEA).

5. By saying a “*grain*”, we assume a particle with the size of several hundred nanometers down to the molecular domain (a few angstroms).

Chapter 1

Elements of interstellar dust physics

We are but dust and shadow.

Odes Book IV, ode vii, line 16 by Horace

This introductory chapter aims at providing a broad scope of our knowledge of interstellar dust, accompanied by some fundamental concepts in physics that are relevant to its study. This field has been tremendously blooming since the 1980s - the beginning of the space age in astrophysics - and has rapidly developed.

Our journey starts with the hosts of interstellar dust, galaxies. In [Sect. 1.1](#), we describe the motivations of this thesis in a general way. We present how dust makes up a galaxy, along with other components such as gas and stars, and emphasize the essential role that interstellar dust plays in various physical processes leading to galaxy evolution. We follow by discussing the challenges of observing the infrared wavelength regime, instrumental in constraining dust properties ([Sect. 1.2](#)). We then introduce the main observables ([Sect. 1.3](#)) used to constrain the physical properties of dust grains ([Sect. 1.4](#)). In [Sect. 1.5](#), we briefly discuss how to model dust properties and their evolution. Finally, we devote the last section ([Sect. 1.6](#)) to **Polycyclic Aromatic Hydrocarbons (PAHs)**, the small grains carrying the **Unidentified Infrared Bands (UIBs)**. These bands dominate the **Mid-InfraRed (MIR)** emission spectra and are ubiquitous in the Universe. Despite their complexity, we argue these observed features can be used to characterize the dust properties in different astrophysical environments.

1.1 Motivations: why study interstellar dust?

1.1.1 Characteristic phases of the interstellar medium

Interstellar dust lies within the **InterStellar Medium (ISM)**. As an essential component of a galaxy, the **ISM** consists of baryonic matter that fills the vast space between stars. The baryons in the **ISM** are found in a wide diversity of physical conditions, characterized, in particular, by their gas density, temperature, metallicity (mass fraction of elements heavier than He, [Sect. 1.3.3.1](#)) and radiative energy density. These differences have a radical and poorly-understood impact on the dust properties. The following distinct **ISM** phases can be characterized. We refer the reader to [Tielens \(2005\)](#) and [Draine \(2011\)](#) for a more complete discussion.

- The **Warm Neutral Medium (WNM)** consists of diffuse atomic gas (H I) with a density $n_{\text{gas}} \simeq 0.3 \text{ cm}^{-3}$ and a temperature $T_{\text{gas}} \simeq 10^4 \text{ K}$. It is heated by electrons ejected from dust grains consecutively to the absorption of photons with sufficiently high energy. This phenomenon is called the photoelectric effect ([Sect. 1.1.2.2](#)). The **WNM** cools mainly through optical line ($[\text{Ly}\alpha]_{121.6\text{nm}}$) and fine-structure line emission.
- The **Cool Neutral Medium (CNM)** constitutes denser, colder H I clouds with a density $n_{\text{gas}} \simeq 30 \text{ cm}^{-3}$ and a temperature $T_{\text{gas}} \simeq 100 \text{ K}$. It is also heated by the photoelectric effect. The predominant cooling mechanism of this phase is the emission of fine-structure lines ($[\text{C II}]_{158\mu\text{m}}$ and $[\text{O I}]_{63\mu\text{m}}$). The **WNM** and the **CNM** are two stable phases at pressure equilibrium.
- The **Hot Ionized Medium (HIM)** is a coronal gas with a density $n_{\text{gas}} \simeq 3 \times 10^{-3} \text{ cm}^{-3}$ and a temperature $T_{\text{gas}} \simeq 10^6 \text{ K}$. It is shock heated by **SuperNovae (SNe)**. The gas is highly ionized by collisions and can be observed through ultraviolet (UV) absorption lines, diffuse soft X-ray and synchrotron emission ([Sect. 1.2.1](#)). This gas cools mainly through X-ray and free-free emission ([Sect. 1.2.1](#)), as well as adiabatic expansion. The **HIM** is at rough pressure equilibrium with the **WNM** and the **CNM** ([McKee & Ostriker, 1977](#)). It fills up to half the volume of the Galaxy ([Draine, 2011](#)) and most of the volume of the Galactic halo.
- **H II regions** consists of gas ionized by **Far-UltraViolet (FUV)** photons from OB star associations. The photoionized gas (H II) is heated by photoelectrons from H and He. The H II gas cooling is dominated by optical line emission, free-free emission and fine-structure emission ($[\text{O III}]_{88\mu\text{m}}$). Well-known H II regions, such as the Orion Nebula (M 42) and its companion M 43, have dimensions of a few parsecs (pc), with a temperature of $T_{\text{gas}} \simeq 10^4 \text{ K}$ and a wide density range, $n_{\text{gas}} \simeq 1 - 10^5 \text{ cm}^{-3}$.
- The **Warm Ionized Medium (WIM)** consists of diffuse H II gas with a density $n_{\text{gas}} \simeq 0.1 \text{ cm}^{-3}$ and a temperature $T_{\text{gas}} \simeq 10^4 \text{ K}$. The gas is ionized and heated by photons escaping from H II regions. It cools mainly through optical emission lines ($[\text{H}\alpha]_{656.3\text{nm}}$).
- The *diffuse molecular gas* (H_2) mixed with H I clouds has a density large enough ($n_{\text{gas}} \simeq 100 \text{ cm}^{-3}$) for H_2 self-shielding

to prevent its photodissociation. It is heated by the photoelectric effect. It has a temperature $T_{\text{gas}} \simeq 50$ K and cools mainly through the emission of fine-structure lines ($[\text{C II}]_{158\mu\text{m}}$).

- The gravitationally bound *dense H_2 clouds* ($T_{\text{gas}} \simeq 10$ K, $n_{\text{gas}} \simeq 10^3 - 10^6 \text{ cm}^{-3}$) are the sites where stars form (Sect. 1.1.2). Their visual extinction exceeds $A_V \simeq 3$ mag. They cool mainly through the emission of CO rotational lines and C I fine-structure lines.

In addition, **PhotoDissociation Regions (PDR)** (Hollenbach & Tielens, 1997, for a review), which are the interface between an H II region and a molecular cloud are an important type of **ISM** environment. In **PDRs**, **FUV** lights from OB stars are significantly absorbed by dust and are reemitted in the infrared (IR). These regions are bright in thermal dust emission and atomic fine-structure lines. Moreover, molecules are dissociated and are ionized by **FUV** photons. Subsequently, these ions recombine, making **PDRs**, rich in chemical reactions.

1.1.2 Importance of dust for galactic physics

Accounting for only $\sim 1\%$ of the mass of the **ISM** (in the Milky Way; Draine, 2003a), dust plays a crucial role in star formation and galaxy evolution. In what follows, we discuss the importance of dust for several macroscopic and microscopic phenomena.

1.1.2.1 Macroscopic processes

Interstellar dust has been discovered by its visible light dimming effect, known as *extinction* (Sect. 1.3.1). The first evidence of interstellar dust can be dated back to Sir William Herschel’s work “*On the construction of the heavens*” (Herschel, 1785), where he reported “*in the body of the scorpion is an opening or hole*”. It was indeed a dust-obscured dark nebula. One of the most famous debates in astrophysics related to this issue was the *Olbers’ Paradox*, also known as the “*Dark night sky paradox; 1823*”¹. Heinrich Wilhelm Olbers, after whom the paradox was named, proposed that the stellar light could be absorbed by dust.

Interstellar dust has first been extensively studied through the extinction in the **Near-UltraViolet (NUV)** and the visible because those were the only regimes accessible from the ground (Sect. 1.2.2). At the beginning of the twentieth century, Edward Barnard patched Herschel’s starless holes with “*real, obscuring masses, most probably dark nebulae*” (Barnard, 1919), thanks to his photographs of dark lanes in Ophiuchus. Since the 1970s, the rapid development of infrared facilities (Sect. 1.2.2) has opened the window on dust emission in various astrophysical environments, allowing us to drastically progress in our understanding of its properties.

1. This paradox argues that if the Universe is static and infinite, populated with an infinite number of uniformly distributed stars, then every line-of-sight would be filled by starlight, which implies the sky should always be bright even at night. Nowadays, the commonly accepted resolution to Olbers’ Paradox is that the observed Universe is not infinitely old and light travels at a finite speed. Moreover, stars and galaxies are not infinitely long-lived. Therefore they will dim.

A background source seen through a foreground dust cloud appears redder than it intrinsically is because of selective extinction, that is, the fact that dust extinguishes more at shorter wavelengths. This is why it is often referred to as *interstellar reddening* (Sect. 1.3.1). For example, Fig. 1.1 shows the dark cloud, Barnard 68 (Bok & Reilly, 1947; Clemens & Barvainis, 1988), observed at different wavelengths from optical to infrared. Because of the presence of dust, the stars behind the globule are not visible in the optical (top panels in Fig. 1.1) but appear at longer wavelengths (bottom panels in Fig. 1.1).

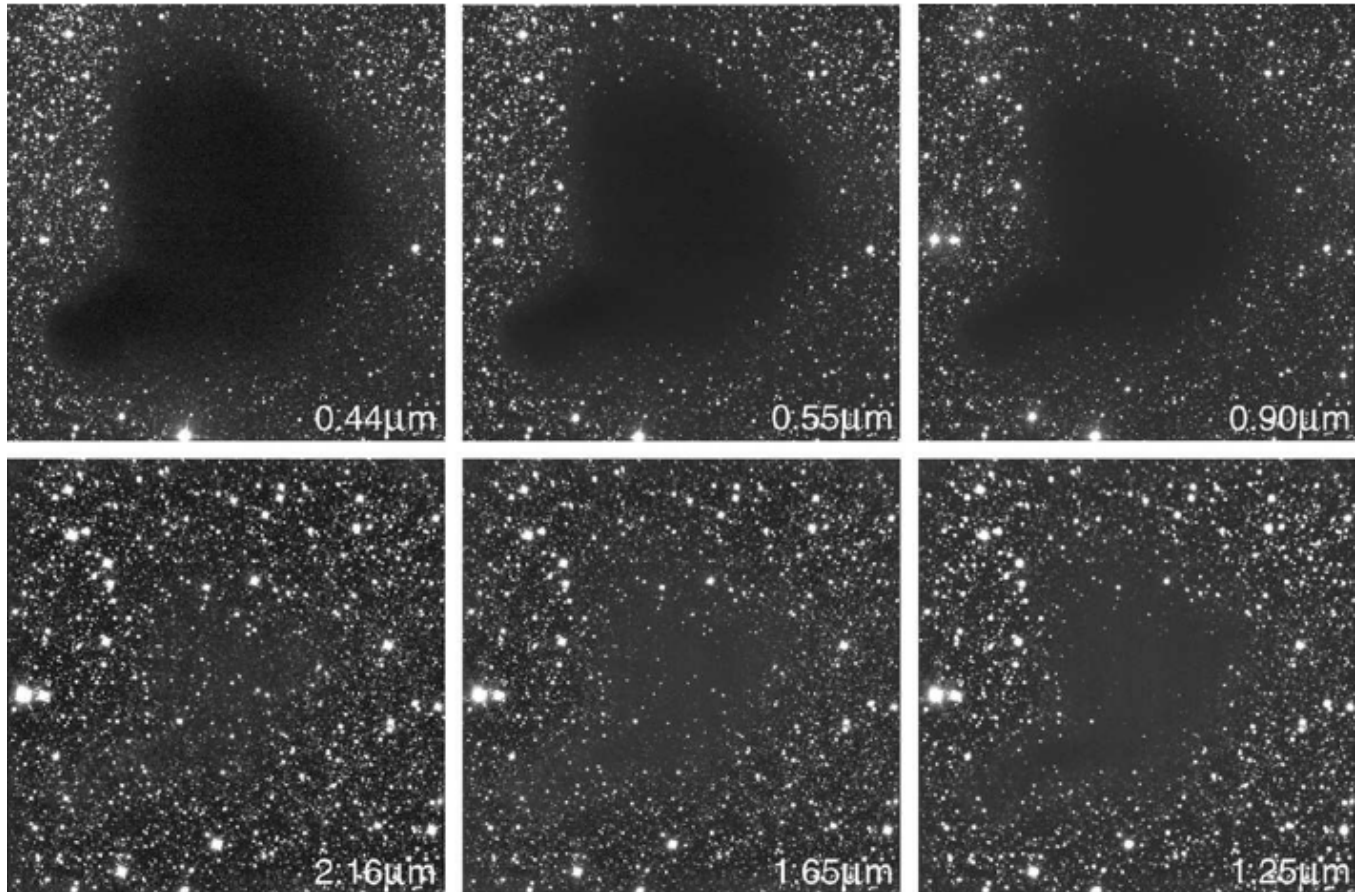


Figure 1.1 – Optical (BVI) and infrared (JHK) images of the globule Barnard 68 obtained with ESO’s VLT and NTT. These are a famous series of images demonstrating the effect of interstellar reddening. The globule is completely opaque in the optical bands B ($0.44 \mu\text{m}$) and V ($0.55 \mu\text{m}$), while entirely transparent in the K band ($2.16 \mu\text{m}$) because of interstellar dust. Figure taken from Alves et al. (2001).

The power absorbed by interstellar dust in the visible range is thermally reemitted in the infrared. Bernstein et al. (2002) estimated that roughly 30% of the light from stellar nucleosynthesis has been redistributed into the $\lambda \approx 10 - 1000 \mu\text{m}$ range through interstellar reddening. This is about the fraction emitted in the infrared by a typical disk galaxy, in the local Universe (e.g. Soifer & Neugebauer, 1991). This fraction can however go up to 99% for an UltraLuminous InfraRed Galaxy (ULIRG; e.g. Clements et al., 1996).

Dust observables can quantify the physical conditions of a given region. In particular, dust brings valuable information on

the process of star formation. Star formation is found to occur within molecular clouds (Kennicutt & Evans, 2012, for a review). Therefore, star-forming regions are usually opaque to visible light. The **Star Formation Rate (SFR)**, that is, the mass of stars formed per unit time, is the most widely-used tracer of this process.

SFR indicators are among the most sought-after astrophysical diagnostics over the whole electromagnetic range. They include the X-ray luminosity, the UV continuum, optical emission lines, the IR emission, the radio continuum, millimeter lines, *etc.* Dust reddening correction is essential when using UV or optical tracers. Because star formation is majoritarily a dust-obscured process, we can measure **SFR** directly in the infrared, using broadbands (*e.g.* the 24 μm band combined with $\text{H}\alpha$ luminosities; Calzetti et al., 2007), narrow bands (*e.g.* the 6.2 μm feature; Peeters et al., 2004a), or the **Total InfraRed (TIR)**; the bolometric luminosity over the wavelength range 3–1100 μm ; *e.g.* Galametz et al., 2013). We also refer to Sect. 1.6.3.2 for more discussions. Alternatively, the synchrotron emission (non-thermal radio continuum) and dense gas lines are dust-free measures of **SFR**.

1.1.2.2 Microphysics

Grain surfaces serve as chemical factories by catalyzing numerous chemical reactions, particularly the formation of the dihydrogen, H_2 . Molecular hydrogen is the most abundant molecule in the Universe. H_2 formation is inefficient in the gas phase because the formation process needs to release about 4.5 eV energy for the freshly-formed molecule to remain stable. However, H_2 does not have rotational transitions due to its symmetry (*e.g.* Bron et al., 2014). If the gas-phase H atom can find either a free *adsorption* site or an already adsorbed H on a grain surface, then the formation energy can be evacuated through the ejection the newly-formed H_2 (*desorption*; Fig. 1.2).

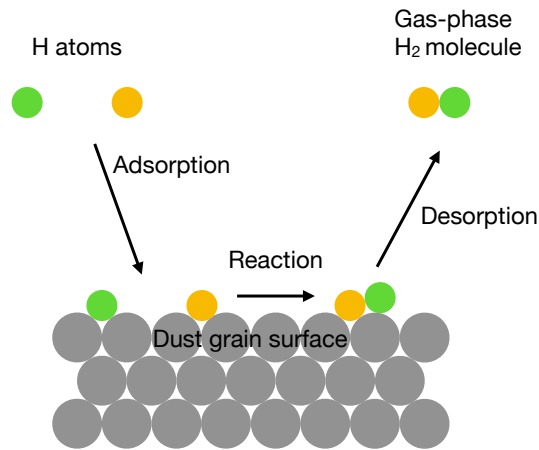


Figure 1.2 – Mechanism of H_2 formation on grain surfaces.

First, the gas-phase H atom finds either a free *adsorption* site or an already adsorbed H on grain surfaces. Then the reaction takes place between two adsorbed atoms (by either physisorption or chemisorption). The newly-formed H_2 is ejected through desorption.

Possible H_2 formation mechanisms include: (i) the *Langmuir-Hinshelwood* mechanism, where two physisorbed H atoms

encounter each other on the grain surface and form a molecule before leaving the surface by desorption; (ii) the *Eley-Rideal* mechanism, where a gas-phase H atom hits a chemisorbed H atom on the grain surface to produce a H₂ molecule. The efficiency of these mechanisms depends strongly on the grain temperature (Le Bourlot et al., 2012).

Moreover, grains are responsible for the gas heating by photoelectric effect (e.g. Draine, 1978) in the neutral ISM. As shown in Fig. 1.3, a FUV photon, absorbed by a Polycyclic Aromatic Hydrocarbon (PAH) (Sect. 1.4.1.2) or a grain, can lead to the ejection of a photoelectron, e^- :



The photoelectric efficiency of individual grains is represented in Fig. 1.3. Therefore, the total photoelectric heating rate depends on the abundance, properties and size distribution of these grains. Our main objects of study, PAHs, are instrumental in this effect, and their charge is a fundamental quantity.

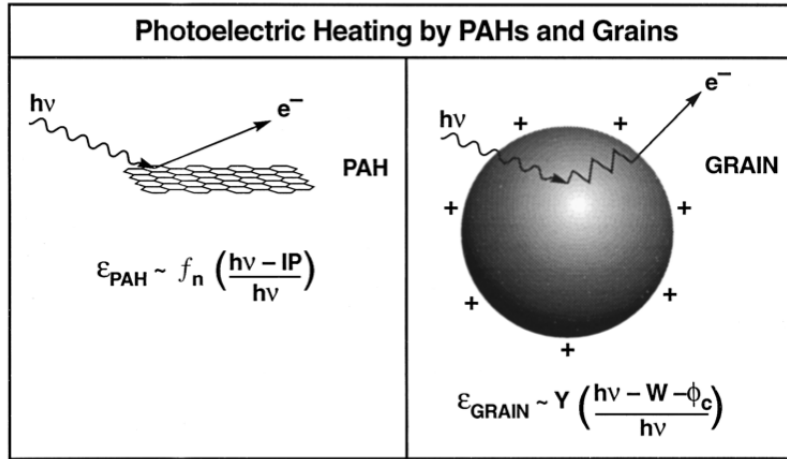


Figure 1.3 – Schematic of the photoelectric heating mechanism.

A Far-UltraViolet (FUV) photon absorbed by a Polycyclic Aromatic Hydrocarbon (PAH) or grain can lead to the ejection of an electron, via the photoelectric effect. On the left panel, ϵ_{PAH} is the heating efficiency as a function of the photon energy ($h\nu$) and Ionization Potential (IP). For a larger grain, diffusion must be taken into account. On the right panel, ϵ_{GRAIN} is the heating efficiency as a function of the photon energy ($h\nu$) and of the work function (W) and Coulomb potential (ϕ_c). Figure taken from Hollenbach & Tielens (1999).

1.1.3 Relevance of nearby galaxies

1.1.3.1 Compared to the Milky Way

Dust properties are known to vary across environments, from circumstellar regions (e.g. Beintema et al., 1996; Hony et al., 2001) to H II regions (e.g. Roelfsema et al., 1996; Verstraete et al., 1996) to PDRs (e.g. Allamandola et al., 1985; Pety et al., 2005) to the diffuse ISM (e.g. Chan et al., 2000) and to dense molecular clouds (e.g. Wakelam & Herbst, 2008). They have been studied in detail in the Milky Way, thanks to the proximity. Most dust models (Sect. 1.5.1) are constrained by

observations of the diffuse **ISM** of the Milky Way, including (i) extinction curves (Sect. 1.3.1), (ii) IR emission (Sect. 1.3.2), (iii) elemental abundances (Sect. 1.3.3) and (iv) polarization (e.g. Planck Collaboration et al., 2015). However, there are no consistently-constrained extragalactic dust models because these observational constraints are not all unambiguously available for the diffuse **ISM** of external galaxies. The main obstacles are the difficulty to isolate the IR emission of the diffuse **ISM** and the limited number of sightlines where the extinction and abundances can be measured (e.g. Sofia & Meyer, 2001). For example, our knowledge of the dust extinction law in other galaxies is mainly limited to the Large and Small Magellanic Clouds (**LMC** and **SMC**; e.g. Weingartner & Draine, 2001) and M 31 (e.g. Bianchi et al., 1996), where we can study the extinction towards individual stars².

By contrast, Milky Way studies are limited by the narrow range of environmental conditions. For instance, there is a weak metallicity gradient ($\sim 0.7 - 2$ Solar; Henry & Worthey, 1999) and there is no strong **Active Galactic Nucleus** (**AGN**) activity (e.g. NGC 1068; Le Floch et al., 2001) in the relatively calm Galaxy center (Mezger et al., 1996). Compared to the Milky Way, nearby galaxies can provide access to extreme metallicity and gas fraction, high **specific Star Formation Rate** (**sSFR**; $\text{sSFR} \equiv \text{SFR} / M_\star$) and a flat UV continuum. The compact size of external galaxies also gives us the possibility to study them as a whole and compare them to high-redshift³ sources. Milky Way studies are limited by the confusion with the rest of its disk along most sightlines, contrary to face-on galaxies observed at high Galactic latitude.

1.1.3.2 Compared to distant galaxies

An issue with external galaxies is the limited spatial resolution we can achieve using modern observatories. For example, with a typical angular resolution of $\sim 10''$ (e.g. Spitzer Space Telescope; Sect. 1.2.2), we can still resolve structures of a few hundreds of parsecs in a galaxy such as M 82, at ~ 3.6 Mpc (Sect. 2.4.1). We can thus study average properties across nearby galaxies. However, at higher redshifts, galaxies become unresolved. Several galaxies can even occupy the same telescope beam (an artifact called *confusion*). In addition, observations of distant objects require deeper integrations. Consequently, nearby galaxies present some clear advantages from an observational point of view.

1.2 Challenges of infrared astronomy

1.2.1 Panchromatic spectral energy distribution (SED) of a galaxy

When observing a galaxy or star-forming region, the different wavelength regimes, from the ultraviolet to the radio, trace the emission from various galactic components. For example, Fig. 1.4 shows the synthetic **Spectral Energy Distribution** (**SED**) of a typical **Late-Type Galaxy**⁴ (also in Sect. 1.3.2.2). We can see in this figure that the different stellar populations dominate

2. There are alternative methods to measure the extinction curve in galaxies where individual stars are not resolved, for example, by using a background galaxy (e.g. Berlind et al., 1997) or a **Quasi-Stellar Object** (**QSO**; e.g. Falco et al., 1999), but these are limited.

3. We provide a list of formulae relevant to high-redshift studies in Appendix C.

4. The *Hubble sequence* classifies galaxies into three major categories based on their morphology (Hubble, 1926): elliptical, spiral and barred spiral galaxies. A fourth, less populated category at the time was added: the irregulars. The terms “late-type” and “early-type” were referring at the time to what was thought to be their evolutionary sequence. We now know this sequence is reversed: **LTGs** are the youngest objects and **ETGs**, the oldest.

the UV-optical domain, whereas dust dominates the infrared. In addition, gas lines are distributed over the whole spectral range, but the free-free and synchrotron continua, also coming from the gas, dominate at radio wavelengths. The *free-free continuum*, also known as *Bremsstrahlung*, is emitted by the deceleration of free electrons scattering off ions in ionized regions (HIM, H II regions and WIM). In such regions, the free-free emission is essential in the cooling process of the gas. The *synchrotron continuum* is a type of non-thermal emission radiated by relativistic electrons gyrating in a strong magnetic field. Finally, we have highlighted the *Diffuse Interstellar Bands* (DIBs), which are ubiquitous absorption features in the $\lambda \simeq 0.4 - 2 \mu\text{m}$ range. Their origin is still unknown, but they are thought to be carried by large molecules or small grains (e.g. Fan et al., 2019).

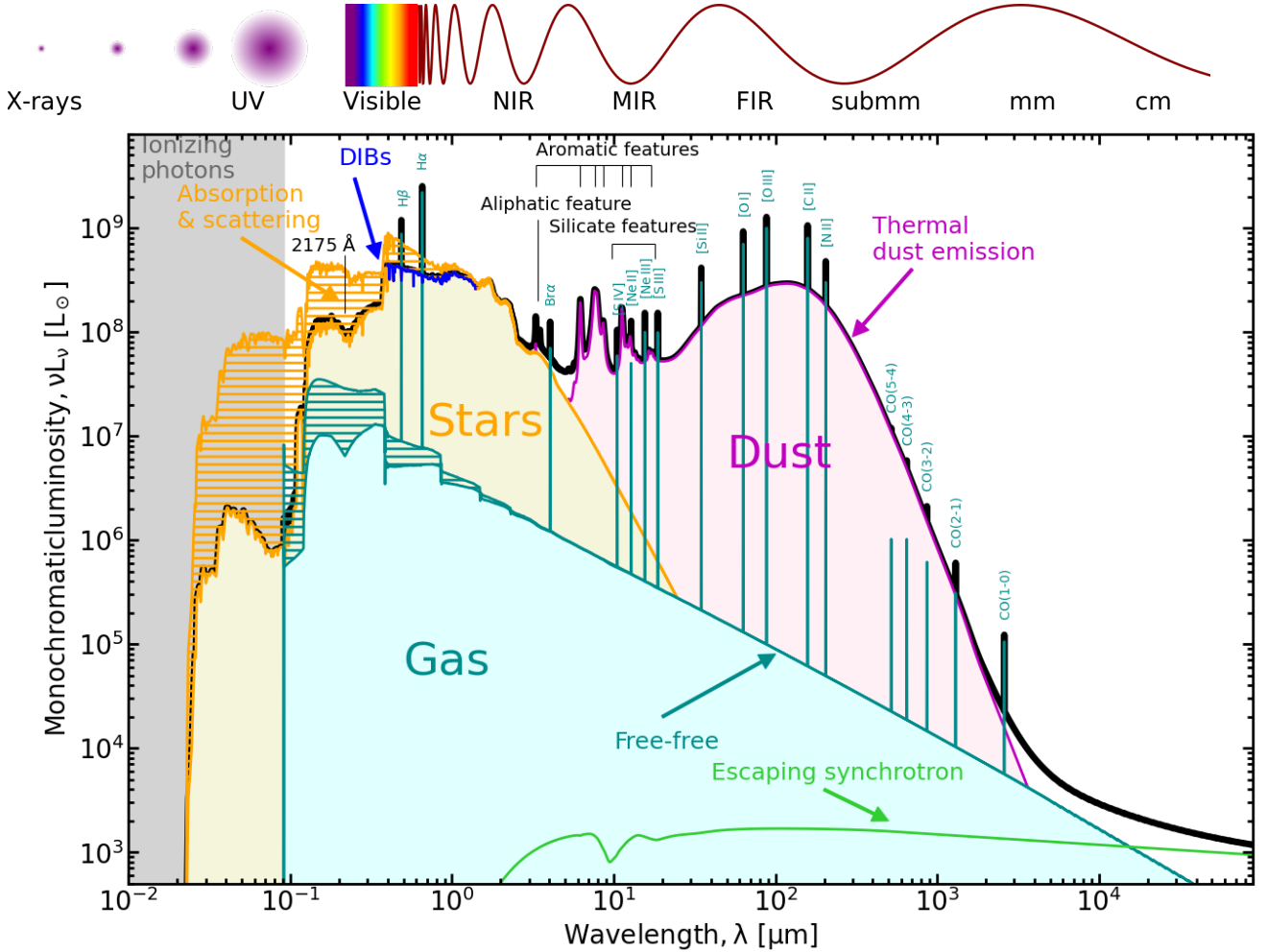


Figure 1.4 – Panchromatic spectral energy distribution (SED) of a synthetic typical late-type galaxy. On the top, we have schematically represented the different spectral regimes. On the main panel, the total simulated spectrum (black) is the sum of the escaping stellar emission (orange), the thermal dust continuum (magenta), the gas lines, the free-free continuum (dark cyan) and the synchrotron continuum (green). The hatched area shows the power absorbed by the dust. We have indicated the 2175 Å extinction bump, as well as the *Diffuse Interstellar Bands* (DIBs; blue; Herbig, 1995). We have also indicated the prominent emission and absorption features in the mid-infrared. The figure originates from Figure 1 of Galliano et al. (2018) and is modified with the author’s permission.

The infrared radiation was discovered when Sir William Herschel performed the first SED measurement of the Sun with thermometers to study the “heating powers of colored rays” (Herschel, 1800b,a). He detected an invisible heating source be-

yond the red part of the spectrum, which accounted for more than half of the total energy of the Sun (represented by temperature increments). This led him to extend the spectrum beyond the red visible - the infrared. Within a century, the rest of the electromagnetic spectrum was discovered (from short to long wavelengths): gamma rays (Villard, 1900), X-rays (Röntgen, 1895), ultraviolet (Ritter, 1801) and radio waves (Hertz, 1888). The nature of light was described as a propagating wave of electric and magnetic fields by Maxwell (1865).

Interstellar dust studies often focus on the infrared spectrum, where dust emission dominates. This domain can be formally divided into three regimes: the near-infrared (NIR; from $0.8 \mu\text{m}$ to $2.5 \mu\text{m}$), the mid-infrared (MIR; from $2.5 \mu\text{m}$ to $25 \mu\text{m}$) and the far-infrared (FIR; from $25 \mu\text{m}$ to $300 \mu\text{m}$). As can be seen in Fig. 1.4, the NIR is where the dust and stellar emission intersect. The MIR is characterized by prominent aromatic and aliphatic features (also referred to as UIBs; Sect. 1.3.2.2) and potentially strong silicate absorption at $\approx 9.7 \mu\text{m}$ and $\approx 18 \mu\text{m}$. The emission in the MIR is mainly carried by small grains ($0.35 \lesssim r \lesssim 20 \text{ nm}$), which fluctuate in temperature as they are out of equilibrium with the radiation field (Sect. 1.4.3.2). The shape of the FIR spectrum is roughly similar to a modified blackbody Sect. 1.4.3.1. It originates from the emission of large grains ($0.02 \leq r < 0.3 \mu\text{m}$) which are at equilibrium with the radiation field (Sect. 1.4.3.1).

In summary, the IR emission originates in radiative transitions of atoms, rotational-vibrational (or rovibrational) modes of molecules and thermal vibration of molecular bonds in solids. Extinction is usually limited to the range around the silicate features. The rest of the infrared spectrum is much less affected than the UV-optical range. It thus provides complementary diagnostics of galaxy properties that are not biased by extinction.

1.2.2 Different types of infrared observatories

Dinitrogen and dioxygen are the two main constituents of the Earth’s atmosphere. They are transparent to most of the electromagnetic spectrum. However, greenhouse gases, such as water vapor (H_2O), carbon dioxide (CO_2), methane (CH_4), nitrous oxide (N_2O) and ozone (O_3), contribute a lot to the absorption. They make it very difficult to study the infrared spectrum from the ground, as demonstrated in Fig. 1.5. Consequently, space satellites and airborne observatories are the only recourse in this domain.

1.2.2.1 Space-based telescopes

The interest in sending telescopes in space was first promoted by Spitzer (1946) in Appendix V of the Douglas Aircraft Company’s Project RAND. The dream of Lyman Spitzer Jr. led to the first astronomical satellite in orbit around the Earth in 1968⁵ did “*revolutionize astronomical techniques and open up completely new vistas of astronomical research*”. Among NASA’s four space-borne Great Observatories (operating in gamma rays, X-rays, visible and infrared wavelengths), the last one operating in the infrared has been named after Spitzer.

5. Known as the *Orbiting Astronomical Observatory* (OAO; Code et al., 1970), it operated in the UV.

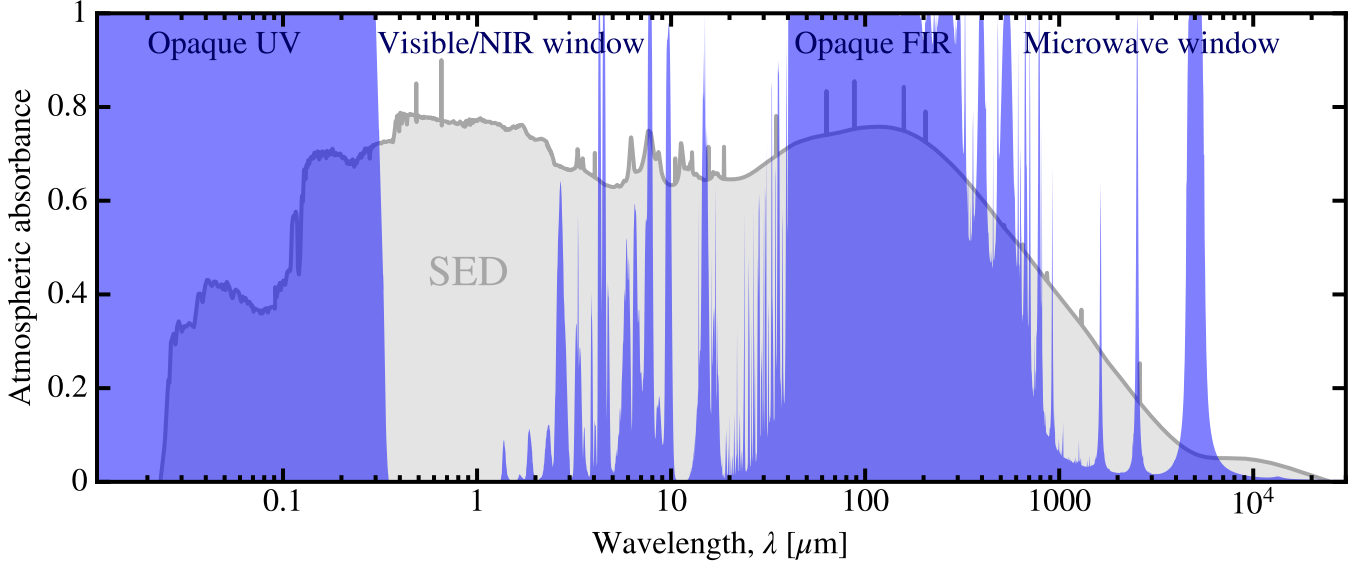


Figure 1.5 – Atmosphere absorbance and multi-wavelength astronomy.

The figure shows the absorbance of Earth’s atmosphere as a function of wavelength (blue), overlaid over the galaxy SED (gray) of Fig. 1.4. We can see that the visible and radio windows are roughly transparent. The translucent NIR and MIR regimes suffer from several absorption bands, whereas the ultraviolet and FIR are completely opaque from the ground. Figure taken from Galliano (2022), hereafter G22.

The very first infrared space observatory, the *InfraRed Astronomical Satellite* (IRAS; $\varnothing = 0.57$ m; Neugebauer et al., 1984) was launched on 25 January 1983. It has opened the infrared window allowing us to see the entire infrared sky at 12, 25, 60 and 100 μm . It allowed us to discover the new categories of Luminous InfraRed Galaxy (LIRG) and ULIRG (Soifer et al., 1987) and to put new constraints on dust models (Desert et al., 1990), among many other results.

The following *Infrared Space Observatory* (ISO; 1995-1998; $\varnothing = 0.6$ m; Kessler et al., 1996) has reinforced the study of infrared light at wavelengths of 2.5 – 240 μm with a unique spectroscopic capability over the whole infrared range. In particular, ISO has given access to interstellar dust physics at all scales, from our Galaxy to the distant Universe (Genzel & Cesarsky, 2000; van Dishoeck, 2004, for reviews).

In 2003, the launch of the *Spitzer Space Telescope* (cryogenic phase: 2003-2009; warm phase: 2009-2020; $\varnothing = 0.85$ m; Werner et al., 2004) has brought us unprecedented resolution and sensitivity in this field. *Spitzer* retired on 30 January 2020, right in the middle of my thesis.

The *Wide-field Infrared Survey Explorer* (WISE; 2009-2011; $\varnothing = 0.4$ m; Wright et al., 2010) was a mid-infrared all sky surveyor. It mapped the sky through four broad photometric bands centered at 3.4, 4.6, 12 and 22 μm .

The *AKARI satellite* (phase 1&2: 2006-2007; phase 3: 2008-2011; $\varnothing = 0.69$ m; Murakami et al., 2007) has performed all-sky surveys in its NIR, MIR and FIR bands during the same period as the *Spitzer* and WISE missions.

In memory of Herschel’s discovery of the infrared radiation and the contribution of his sister Caroline Herschel to astronomy, one of the two infrared-submm space observatories launched by ESA in 2009 has been named after them. The *Herschel Space Telescope* (2009-2013; $\varnothing = 3.5$ m; Pilbratt et al., 2010) was operating in the FIR-submm. With two of its instruments, PACS

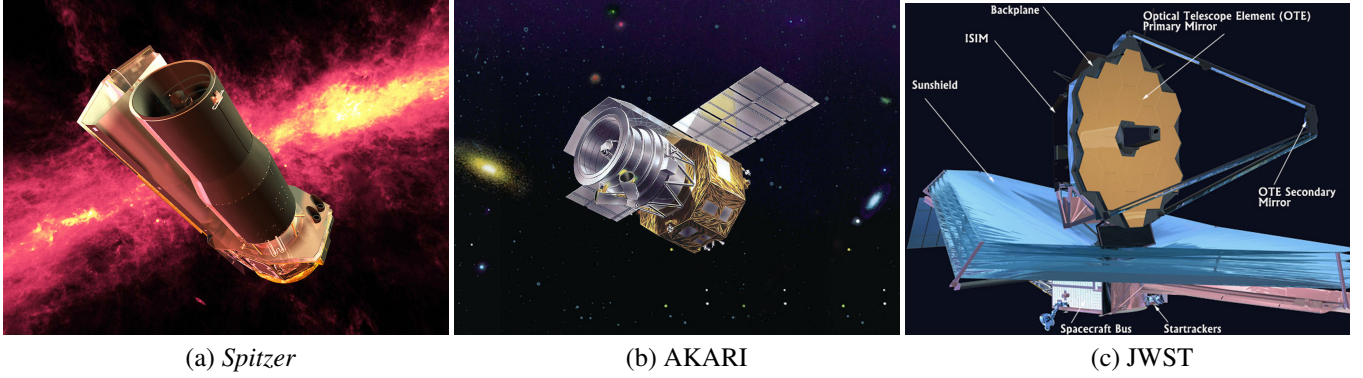


Figure 1.6 – Infrared space telescopes.

Panel (a) shows the *Spitzer Space Telescope* with the multiple instrument chamber, the cryostat (a tank of liquid helium) and the outer shell made of aluminum;

Credit: NASA/JPL-Caltech/R. Hurt (SSC)

Panel (b) shows the AKARI satellite with the cryostat, the solar paddle and the bus module;

Credit: ISAS/JAXA

Panel (c) shows the front view of JWST with the integrated science instrument module (ISIM), the optical telescope element (OTE) and the spacecraft element (spacecraft bus and sunshield).

Credit: NASA

and SPIRE, it has unprecedentedly observed the wavelengths attributed to large dust grain emission, thus allowing the first reliable estimates of the dust content in a wide diversity of environments.

The *Planck space observatory* (2009-2013; $\varnothing = 1.5$ m; Tauber et al., 2010) was launched with *Herschel* and did observe the FIR-mm range but at a lower angular resolution. One of its advantages was that it could also measure the linear polarization in all its bands, allowing studies of the Galactic magnetic field (Planck Collaboration et al., 2016a). It provided important constraints on the dust emission in the Milky Way that are used by recent dust models (Compiègne et al., 2011, e.g.), updating those provided by the *COsmic Background Explorer* (COBE; 1989-1993; $\varnothing = 0.2$ m; Boggess et al., 1992; Dwek et al., 1997).

The *James Webb Space Telescope* (JWST; 2021–; $\varnothing = 6.5$ m; Gardner et al., 2006) was launched on 25 December 2021. This much-awaited observatory is expected to bring new details, in the NIR-to-MIR range, on the ISM and the properties of galaxies close to the reionization era. JWST data, combined with the abundant archives of the past infrared observatories, will provide a mine of information for the next decade.

1.2.2.2 Airborne observatories

An airborne observatory consists of a sub-orbital astronomical telescope and its payload lift, operating above the lower dense layers of the Earth’s atmosphere. The first balloon-borne astronomical telescope was *Stratoscope I* (1957-1959; $\varnothing = 0.3$ m; Danielson, 1961). Balloon-borne telescopes are limited by the maximum altitude (50 km), short flight time (a few days) and risky landing.

The other type of airborne observatories concerns those embarked on an airplane. The first one was the Solar eclipse hunter, *Galileo I*, onboard the NASA 711 (CV-990) Aircraft (1965-1973; $\varnothing = 0.3$ m; Bader & Wagoner, 1970); NASA’s

Stratospheric Observatory for Infrared Astronomy (SOFIA; 2010-; $\varnothing = 2.5$ m; [Young et al., 2012](#)), successor of the *Kuiper Airborne Observatory* (KAO; 1974-1995; $\varnothing = 0.9$ m; [Erickson & Meyer, 2013](#)), is currently operating. It is the only observatory covering the **FIR** window at the moment.

Compared to space telescopes, airborne observatories are relatively cheaper. And it is possible for frequent maintenance and hardware upgrades as well.

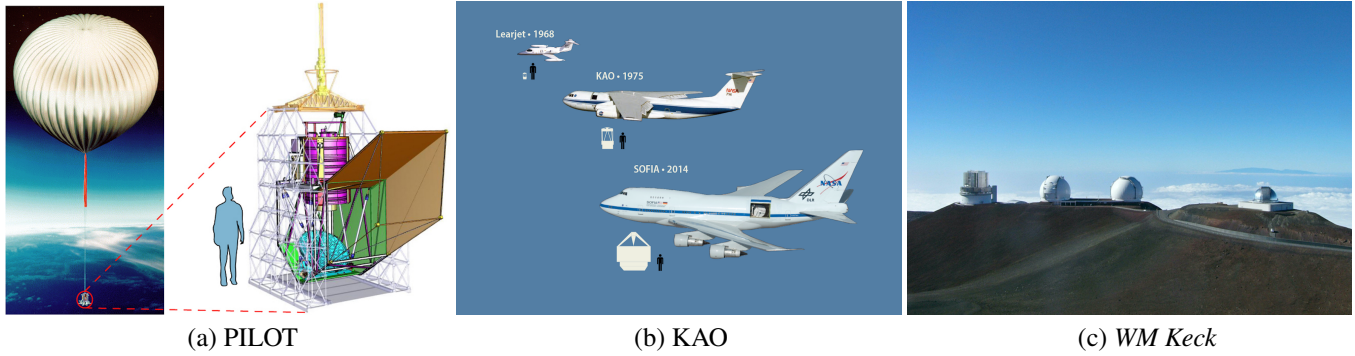


Figure 1.7 – Airborne and ground-based infrared observatories.

Panel (a) shows the balloon-borne astronomy experiment PILOT (2015-2017; $\varnothing = 0.73$ m;) focusing on the dust polarization in the diffuse **ISM**;

Credit: IRAP

Panel (b) shows NASA’s three aircraft-borne observatories - the *Learjet Observatory*, KAO and SOFIA;

Credit: NASA/SOFIA/L. Proudfit

Panel (c) shows Subaru Telescope alongside the twin *W. M. Keck Observatory* telescopes and IRTF.

Credit: Sasquatch

1.2.2.3 Ground-based observatories

Although the infrared window is almost entirely opaque from the Earth’s surface, a part of the **NIR-to-MIR** range is less affected by atmospheric absorption ([Fig. 1.5](#)). A few ground-based observatories are dedicated to infrared observations. They are preferentially located at high altitudes with low humidity conditions. For example, the *United Kingdom Infra-Red Telescope* (UKIRT; 1978; $\varnothing = 3.8$ m), NASA’s *Infrared Telescope Facility* (IRTF; 1979; $\varnothing = 3$ m) and NAOJ’s *Subaru Telescope* (1999; $\varnothing = 8.2$ m; [Kobayashi et al., 2000](#)) are all located at the summit of Mauna Kea on Hawai’i. Chilean mountains are another ideal place for infrared observations. The *Very Large Telescope* (VLT; $\varnothing = 8.2$ m; e.g. [Lopez et al., 2008](#); [Gillessen et al., 2010](#); [Petrov et al., 2007](#); [Leinert et al., 2003](#)) and the most powerful **NIR** survey telescope, VISTA ($\varnothing = 8.2$ m; [Sutherland et al., 2015](#)), are both located on Cerro Paranal.

1.2.3 Brief history of infrared spectroscopy

The technique used in Herschel’s experiment leading to the discovery of infrared radiation ([Sect. 1.2.1](#)) is called *spectroscopy*. A large fraction of our knowledge about stars and the **ISM** has been built on spectroscopic studies, as it gives access

to the atomic and molecular properties of matter. It is generally admitted that the generalization of the use of spectroscopy, at the beginning of the XXth century, is what transformed *astronomy* into *astrophysics*.

From a terminological point of view, the term *spectroscopy* encompasses several concepts: (i) *spectrography*, which consists in recording a spectrum on physical support; and (ii) *spectrometry*, which consists in measuring a spectrum, that is, applying some quantification to it. The three terms above are rather close and are used indifferently in practice. The *spectrometers* we will discuss in this manuscript are scientific instruments used to measure the properties of an electromagnetic spectrum as a function of wavelength. A spectrometer usually measures a monochromatic flux density (Table A.1). A brief history of the development of astronomical spectroscopy is summarized below.

In 1666, Sir Isaac Newton first used the term *spectrum* to describe the optical experiment (using *prisms*) he had designed to decompose the Solar light. In 1800, Sir William Herschel performed the first visible-to-NIR SED of the Sun in history using thermometers (Herschel, 1800b). In 1802, William Hyde Wollaston built a spectrometer including a lens to focus the spectrum on a screen (Wollaston, 1802). In 1815, Joseph von Fraunhofer invented the *diffraction grating*, a device that has a greater dispersion power than prisms. Later in 1817, he observed the first spectra of stars other than the Sun (Fraunhofer, 1817). In 1842, Edmond Becquerel was the first to record the Solar spectrum using the invention of Louis Daguerre, the *daguerreotype* (Becquerel, 1842). Followed many improvements, until, in 1969, the first CCD was invented at Bell laboratories (Boyle & Smith, 1970; Amelio et al., 1970).

Infrared spectroscopy provides physical information on the following galactic components.

Interstellar dust. As mentioned earlier, interstellar dust thermally emits in the NIR-to-millimeter regime. Its spectrum peaks in the FIR and presents a complex MIR spectrum of emission features, as shown in Fig. 1.4. Dust grains are ubiquitous in the Universe and are even seen in extreme environments (*e.g.* the silicate absorption features in SBS 0335-052, a galaxy with $\simeq 1/41$ Solar metallicity; Thuan et al., 1999; Houck et al., 2004b).

Interstellar gas. Numerous fine-structure lines of ionized and neutral atoms are found in the infrared. Some of these lines are the primary coolants of the ISM (Sect. 1.1.1). They are also good tracers of the physical conditions in each phase they originate from. For example, in the MIR, the $[\text{Ne III}]_{15.56\mu\text{m}}/[\text{Ne II}]_{12.81\mu\text{m}}$ ratio is an indicator of the hardness of the radiation field (Thornley et al., 2000; Wu et al., 2006; Madden et al., 2006). The $[\text{C II}]_{158\mu\text{m}}$ line can be used to trace the potentially important reservoir of H_2 not traced by CO, the *dark gas*, in low-metallicity⁶ systems (Madden et al., 2020). The atomic line, $[\text{O I}]_{63\mu\text{m}}$, can be as bright as $[\text{C II}]_{158\mu\text{m}}$ and trace denser PDRs. There are also transition lines from molecules such as H_2 , O_2 , H_2O , *etc.*

Accretion disks. Infrared observations provide essential constraints on the accretion process, either around stars or galactic nuclei. Young Stellar Objects (YSOs) pass through three distinct classes during their evolution. These classes show a drastic evolution of their infrared SED, as the dust cocoon and the subsequent accretion disk clear out (left panel of Fig. 1.8; Lada & Wilking, 1984; Lada, 1987). The infrared slope, $\alpha_{\text{IR}} = d \log(\lambda F_\lambda) / d \log(\lambda)$, taken between $2.2 \mu\text{m}$ and

6. We define the following metallicity (Z) ranges according to dust evolution regimes of nearby galaxies: (i) very low Z : $Z \lesssim 0.2 \times Z_\odot$; (ii) low Z : $0.2 \times Z_\odot \lesssim Z \lesssim 0.45 \times Z_\odot$; (iii) normal Z : $Z \gtrsim 0.45 \times Z_\odot$.

$10 - 25 \mu\text{m}$, is used to classify these objects. At the scale of a galaxy, infrared observations are instrumental in identifying **Active Galactic Nuclei (AGNs)**, since the majority of them are dust-obscured. The right panel of Fig. 1.8 demonstrates the power of **MIR** observations to determine the type of a **QSO** (Hickox et al., 2017).

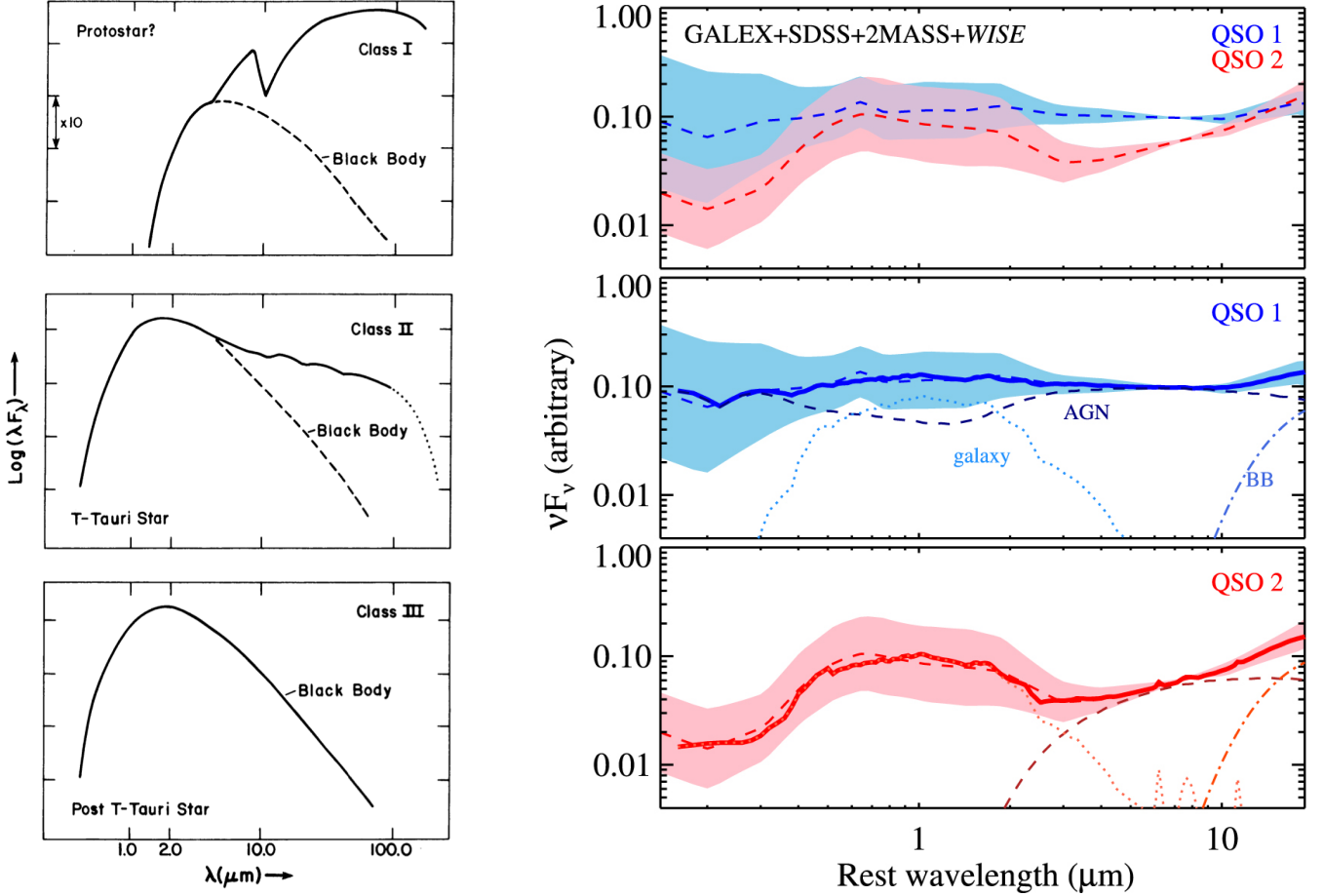


Figure 1.8 – Infrared **SEDs** of accretion disks, on stellar and galaxy scales.

The left panel illustrates the classification of **YSOs**, from their **SED** (Lada, 1987). The right panel presents the normalized composite **SED** templates of type 1 and type 2 quasars (**QSOs**) selected from the SDSS, using data from the SDSS, UKIDSS and WISE (Hickox et al., 2017). These **SEDs** are modeled with a reddened **AGN** (dashed), the stellar populations of the host galaxy (dotted) and a cold **ISM** dust component assumed isothermal (dot-dashed). The main difference between the two types of **QSOs** is the reddening of the central engine continuum for type 2. The **MIR** profile can thus determine the type of a **QSO**.

Old stars. Stars with different initial masses have drastically different **SEDs**. Massive stars, such as O and B types, emit mainly in the UV-optical (left panel of Fig. 1.9) and have a short lifetime (a few million years). On the contrary, low-mass stars are colder, emitting essentially in the **NIR**, but they can live up to several billion years. At the scale of a galaxy, when we measure the integrated emission of a stellar population, low-mass stars are the most numerous. In addition, because they are long-lived, they rapidly dominate the **NIR SED** of a galaxy (Fig. 1.9 right panel). This is why the **NIR** is generally used to estimate the stellar mass of galaxies.

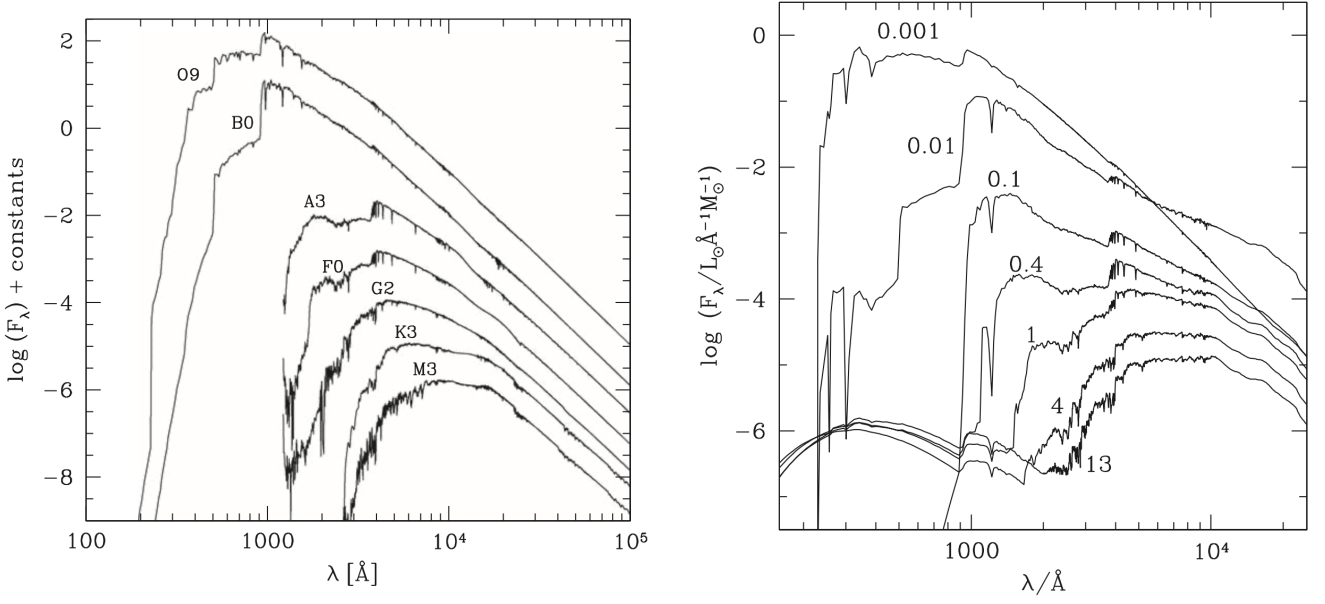


Figure 1.9 – Synthetic stellar spectra.

The left panel shows the spectra of stars of different types, using the Morgan–Keenan (MK) classification system. These spectra are scaled with an arbitrary factor to avoid overlap. The right panel shows the evolution as a function of time of a stellar population, from 0.001 to 13 Gyr, assuming a Solar initial metallicity and the Salpeter **Initial Mass Function** (IMF; an empirical function describing the initial distribution of stellar masses for a population of stars; [Salpeter, 1955](#)). Figure taken from [Mo et al. \(2010\)](#).

1.3 Empirical constraints on dust properties

Direct observational studies of interstellar dust all rely on our understanding of the interaction of grains with electromagnetic waves. This interaction is threefold. It can be separated into absorption, scattering and emission. This section details the observational constraints we can obtain on these three processes. We finish by discussing indirect constraints on the elemental abundances locked in grains.

1.3.1 Interstellar dust extinction

Extinction is the combined effect of absorption and scattering. Interstellar dust extinction can be studied in the UV-to-IR range, as shown by the hatched area of the **SED** in [Fig. 1.4](#). By convention, several extinction properties are based on the magnitude system⁷. The *magnitude* (m) of an object, usually a star, with an observed flux $F_\nu^{\text{obs}}(\lambda_0)$, at wavelength λ_0 , is:

$$m(\lambda_0) \equiv -2.5 \log_{10} \left[\frac{F_\nu^{\text{obs}}(\lambda_0)}{F_\nu^{\text{ref}}(\lambda_0)} \right], \quad (1.2)$$

7. The use of the magnitude system can be dated back to ancient Greek. The modern definition was proposed by [Pogson \(1856\)](#), using a logarithmic scale of $\sqrt[5]{100} \approx 2.512$.

where $F_v^{\text{ref}}(\lambda_0)$ is a reference flux. The *extinction in magnitude* at λ_0 , $A(\lambda_0)$, is then defined as:

$$A(\lambda_0) \equiv m_{\text{obs}}(\lambda_0) - m_{\text{int}}(\lambda_0) = 2.5 \log_{10} \left[\frac{F_v^{\text{int}}(\lambda_0)}{F_v^{\text{obs}}(\lambda_0)} \right], \quad (1.3)$$

where $m_{\text{int}}(\lambda_0)$ and $F_v^{\text{int}}(\lambda_0)$ are the intrinsic (*i.e.* unextincted) magnitude and flux of the object.

A more physical quantity, the *optical depth*, τ , can be used to express the extinction magnitude (Eq. A.8). The radiative transfer equation, quantifying the way the intensity of a light beam varies through a medium (Appendix A), can be expressed, in the case of the extinction by a star, as:

$$\frac{dI_v(\lambda)}{d\tau} = -I_v(\lambda), \quad (1.4)$$

where I_v is the specific intensity, defined in Appendix A. The solution is $I_v(\lambda) = I_v^*(\lambda) \exp[-\tau(\lambda)]$, where I_v^* is the intrinsic specific intensity of the star. If we integrate this solution in an arbitrary solid angle, representing the resolution of our telescope, we obtain:

$$F_v^{\text{obs}}(\lambda) = F_v^{\text{int}}(\lambda) \times \exp[-\tau(\lambda)]. \quad (1.5)$$

Therefore, Eq. (1.3) becomes

$$A(\lambda) = 1.086 \times \tau(\lambda). \quad (1.6)$$

1.3.1.1 Dust extinction in the UV-optical

The visible range is the domain where extinction studies were historically started. In the Milky Way, the spectral shape of the extinction curve varies from one line-of-sight to another. Cardelli et al. (1989) however showed that it could be parametrized by a single parameter $R(V)$, the *visual-to-selective extinction ratio*:

$$R(V) \equiv \frac{A(V)}{A(B) - A(V)}. \quad (1.7)$$

This variation is likely the result of a change in grain properties as a function of the environment. In the Milky Way, $R(V)$ indeed correlates primarily with the H column density, $N(\text{H})$, varying from ~ 2 to 5, with on average, $R(V) \sim 3.1$ (*e.g.* Draine, 2003a). In Fig. 1.10. a, we show four extinction curves, with different values of $R(V)$. We have highlighted the main spectral features, common to each extinction curve: (i) the FUV rise, (ii) the 2175 Å bump and (iii) the optical knee.

Finally, extinction can also be observed with polarimeters. If the light from a background source passes through a cloud of elongated grains aligned with the interstellar magnetic field, the extinction will be partially *polarized*. This polarization is due to *dichroic extinction* (Davis & Greenstein, 1951). It can thus be used to study the orientation of the magnetic field.

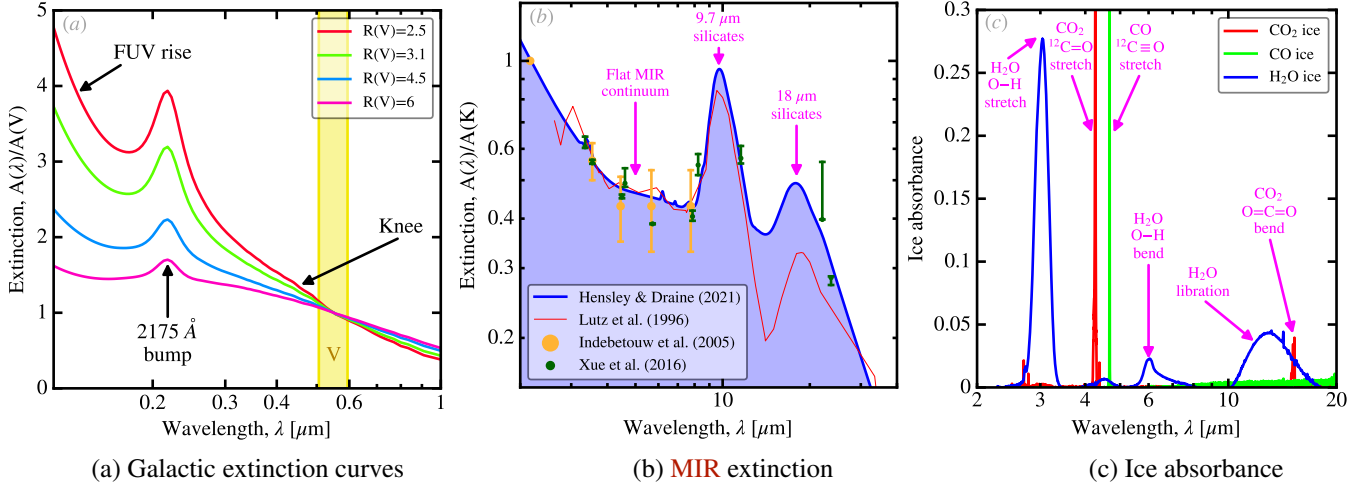


Figure 1.10 – Extinction by dust and ices.

Panel (a) shows average extinction curves for different $R(V)$ (Fitzpatrick et al., 2019). Panel (b) shows the synthetic MIR extinction curve of Hensley & Draine (2021) overlaid with observations from Lutz et al. (1996), Indebetouw et al. (2005) and Xue et al. (2016). Panel (c) shows the absorbance of the most abundant ices, taken from the *Leiden Database for Ice*. Figure taken from G22.

1.3.1.2 Dust extinction in the mid-infrared (MIR)

The extinction in the MIR range is more difficult to constrain compared to its UV-to-NIR counterpart because it is much more difficult to find a background source with known intrinsic SED. Stars are indeed impractical in this range as dust emission mixes with their spectra (Fig. 1.4). Instead, a bright MIR source, such as a star-forming region or an AGN, can be used. The MIR extinction curve is characterized by the 9.7 μm and 18 μm silicate features, as well as the flat MIR continuum (Fig. 1.10. b). The 9.7 μm and 18 μm features are attributed to the Si-O stretching and O-Si-O bending modes of silicates, respectively. The profile of these features varies significantly between sightlines (e.g. Lutz et al., 1996; Indebetouw et al., 2005; Xue et al., 2016). We have represented the synthetic extinction curve of Hensley & Draine (2021) in Fig. 1.10. b (blue curve).

1.3.1.3 Extinction by ices

In dense regions, molecules such as H_2O , CO and CO_2 can condense on grain surfaces and form icy mantles (Boogert et al., 2015, for a review). Interstellar ices are thus responsible for several MIR absorption bands, as shown in Fig. 1.10. c. For instance, notice that there is a dip around 3.0 μm absorption on the ISO Galactic center extinction curve (Lutz et al., 1996, the red curve in Fig. 1.10. b). This feature may be attributed to an O-H stretching mode, carried by frozen water. In the diffuse ISM, however, these features are not detected (e.g. Gibb et al., 2004) since ices can not survive the harsh radiation field.

1.3.2 Observations of the thermal emission

As we have already mentioned, the UV-optical power absorbed by a dust mixture is thermally reradiated in the infrared. This infrared emission can be decomposed into two components: (i) continuum emission that appears featureless and (ii) emission

features arising from specific molecular modes (stretching and bending modes) in the grain (we refer to the Chap. 2 of [Tielens, 2005](#), for a review).

1.3.2.1 Dust continuum

The dust continuum dominates the IR-to-mm emission of a galaxy, as we have seen in [Fig. 1.4](#). Typical interstellar grains, having sizes of several angstroms to a few hundred nanometers, are large enough so that their density of states is practically continuous. They thus radiate a continuum, not only specific resonance bands. As we will see in detail in [Sect. 1.4.3.2](#), the **NIR-to-MIR** range in the diffuse **ISM** is dominated by the emission of small grains ($\lesssim 10$ nm) that are out of equilibrium with the radiation field. The temperature of these grains fluctuates between the absorption of two successive photons, reaching a few 100 K for a brief time. The **FIR-to-mm** emission of the diffuse **ISM** is dominated by the emission of larger grains that are at thermal equilibrium with the radiation field ($T \simeq 15 - 20$ K; [Sect. 1.4.3.1](#)).

This is important because all dust models until now have been calibrated on observations of the diffuse Galactic **ISM** ([Sect. 1.5.1](#)). This medium can reasonably be assumed to be homogeneous in composition and uniformly illuminated. Even above the atmosphere, there are several contamination contributions rendering observations of the diffuse infrared emission challenging: the zodiacal foreground emission, the **Cosmic Infrared Background** (**CIB**; *e.g.* [Dole et al., 2006](#)) and the **Cosmic Microwave Background** (**CMB**; [Mather et al., 1994](#); [Planck Collaboration et al., 2016b](#)). To consistently constrain the dust continuum emission at these wavelengths, it is thus crucial to subtract these contaminations and homogenize the data coming from different instruments (*e.g.* [Hensley & Draine, 2021](#), for more detailed discussions).

The IR emission can also be polarized if the grains are elongated and aligned (*e.g.* [Guillet et al., 2018](#)). Even when the dielectric function ([Sect. 1.4.2.1](#)) is isotropic, a submicron grain radiates more effectively, at submillimeter wavelengths, with the electric field parallel to its long axis. The rotation axis of the grain tends to align with the magnetic field. The study of **FIR**-submm polarization thus provides important constraints on the Galactic magnetic field. The whole sky polarized emission has been mapped in several submillimeter bands by the *Planck* satellite ([Planck Collaboration et al., 2016a](#)).

1.3.2.2 Unidentified infrared bands (UIBs)

Unidentified Infrared Band (**UIB**), which are the main focus of this thesis, are the brightest emission features in most environments. They dominate the emission at galactic scales in most types of objects, as demonstrated in [Fig. 1.11](#).

- **Late-Type Galaxies** (**LTGs**), such as NGC 1097, are gas-rich disk galaxies with moderate to intense star-formation activity. They are essentially spiral galaxies. Because of their gas fractions and UV photons, **UIBs** are bright in these objects.
- **Early-Type Galaxies** (**ETGs**), such as Centaurus A, are gas-poor, elliptical galaxies. Their **ISM** is tenuous and concentrated in a few lanes. Their stellar populations are mainly old and red. For these reasons, **UIBs** tend to be relatively less intense in **ETGs** than in **LTGs**.

— *Blue compact dwarf* galaxies, such as NGC 1569, are gas-rich, low-metallicity systems with intense star-formation activity. The hard radiation field, permeating their **ISM**, tends to destroy the carriers of the **UIBs**. **UIBs** are consequently weak in these objects, as we will discuss in more detail, in **Sect. 1.6.3**.

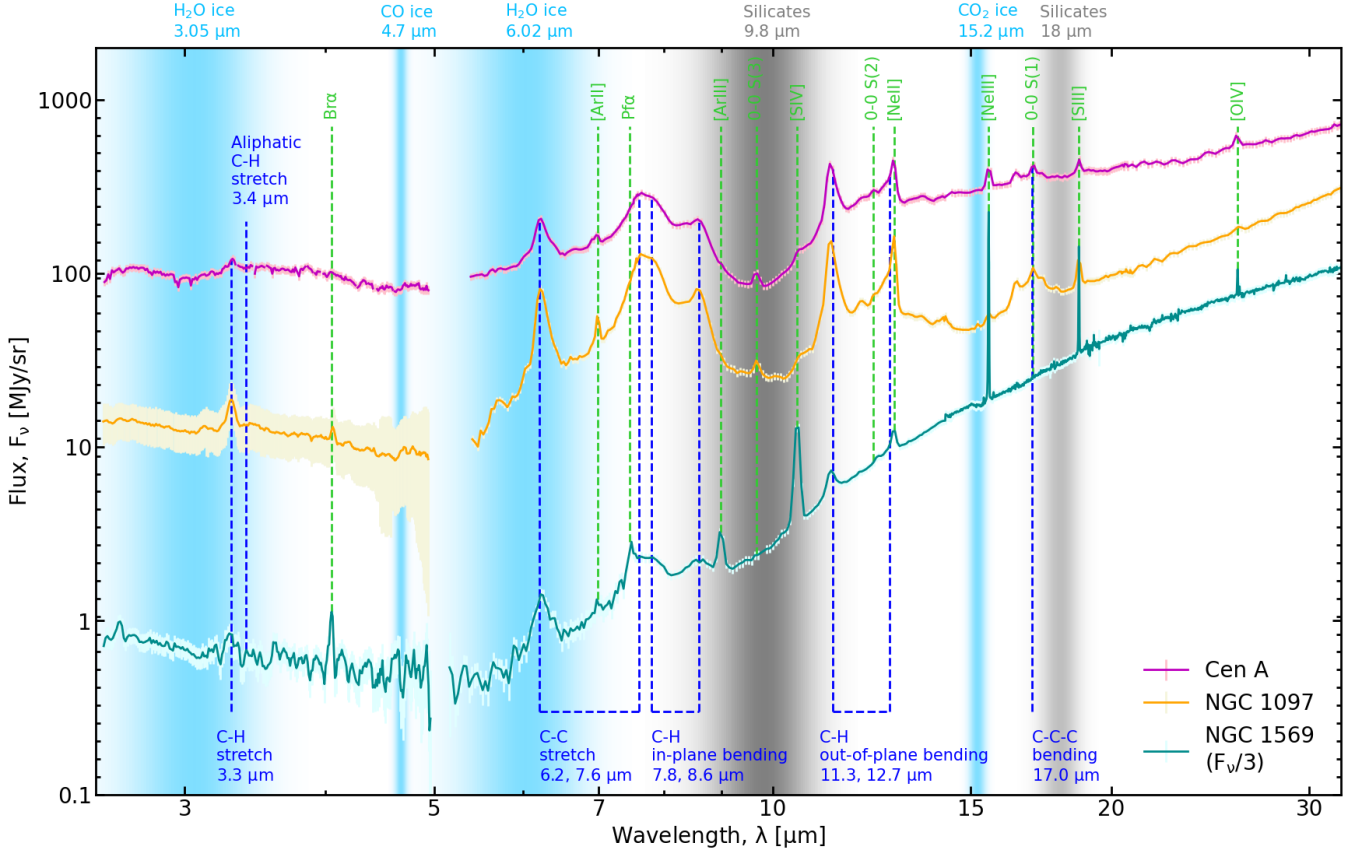


Figure 1.11 – Galaxy spectra observed in the mid-infrared.

Here is the combination of AKARI/IRC and *Spitzer*/IRS spectra extracted from the central region of different galaxies. Centaurus A (magenta) is an **ETG** with a powerful **AGN**. NGC 1097 (orange) is a **LTG** with a low-luminosity **AGN**. NGC 1569 (dark cyan) is a blue compact dwarf (scaled down by a factor of 3, for clarity). The predominant **MIR** emission (dashed lines) and extinction features (shaded areas) are indicated. The spectrum of NGC 1097 is from Wu et al. (2018). The spectra of Centaurus A and NGC 1569 have been produced by T. Roland & R. Wu (private communication). The H₂O ice absorption features are taken from Öberg et al. (2007). The CO ice absorption data are from Bouwman et al. (2007). The CO₂ ice absorption data are from Bisschop et al. (2007). The silicate extinction features are from Weingartner & Draine (2001).

UIBs were first detected by Gillett et al. (1973) in the planetary nebula, NGC 7027 (Fig. 1.12. a). The high feature-to-continuum ratio indicated a molecular rather than a solid-state origin. Allamandola et al. (1985) first matched the observed **UIB** features with a laboratory-measured spectrum of gas-phase soot containing **PAHs** (Fig. 1.12. b). Aromatic rings, which are hexagonal rings made of six sp² hybridized C atoms, are the building blocks of **PAHs**. Their peculiarity is that the p electrons of the six C atoms share a single ring-shaped π bond⁸.

8. In quantum mechanics, the letters s, p, d, f are used to designate orbitals with azimuthal quantum numbers $l = 0, 1, 2, 3$, respectively. Covalent chemical bonds result from the overlap of the outer electrons of two atoms with vacant valence orbitals. These valence orbitals can, in some cases, be combined, forming *hybrid orbitals*. For instance, sp² hybrids are orbitals made of 1/3 s and 2/3 p. This is important for C atoms, as the electronic configuration of the $n = 2$ shell in an aromatic cycle becomes sp²-sp²-sp²-p. A π bond is formed if the lobes of two parallel p orbitals of two atoms overlap.

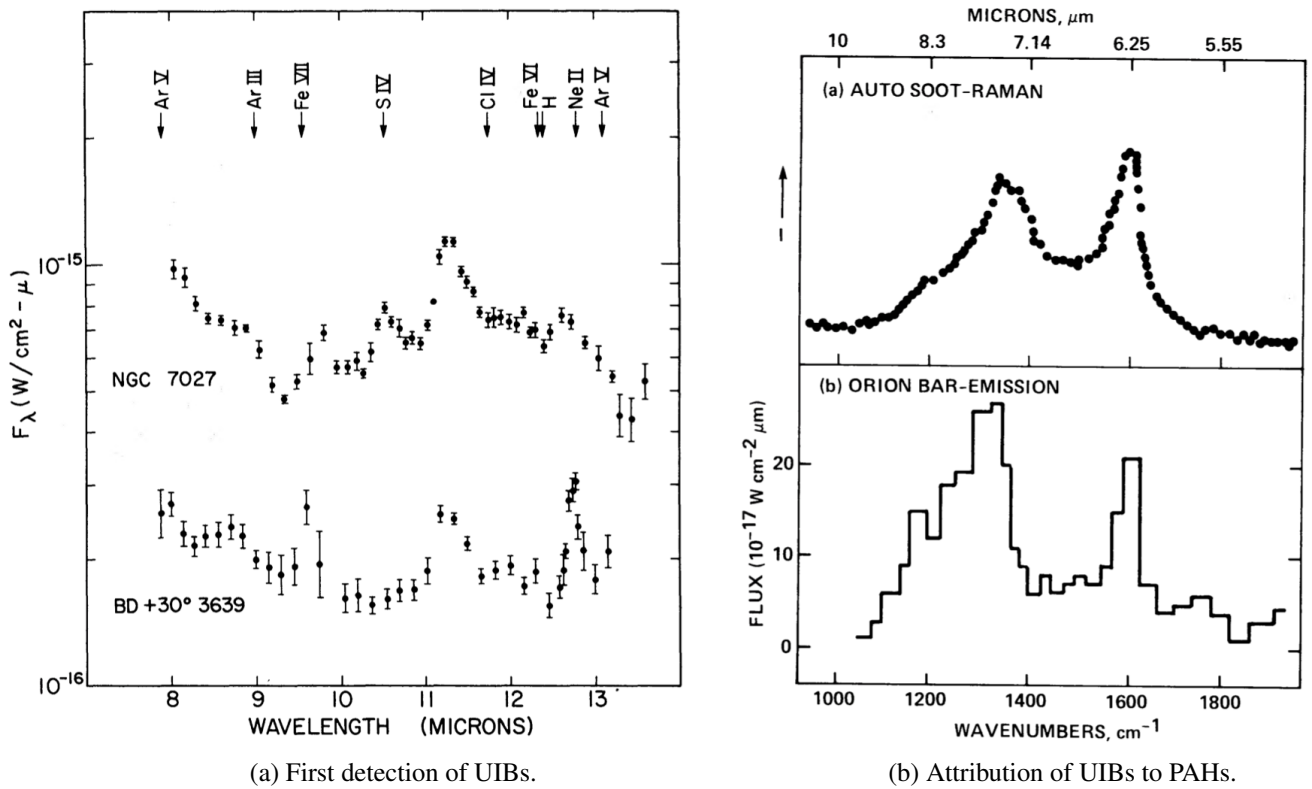


Figure 1.12 – Spectral identification of UIBs.

Panel (a), extracted from [Gillett et al. \(1973\)](#), shows the first detection of **UIB** features, at 8.6 and 11.3 μm in the planetary nebulae, NGC 7072 and BD +30°3639. Panel (b), extracted from [Allamandola et al. \(1985\)](#), shows the comparison between a laboratory-measured soot spectrum and the **UIBs** observed in the Orion Bar.

The most prominent **UIBs** and their associated molecular vibrational modes are the following.

- The 3.3 μm band is attributed to the peripheral C-H stretching mode.
- The 3.4 μm band is an aliphatic feature, carried by an alkyl (-CH₃) side group on the **PAH** ([Duley & Williams, 1981](#); [Joblin et al., 1996](#)).
- At around 6.2 μm and 7.7 μm, there are a few C-C stretching modes.
- Aromatic features within the wavelength range 7 – 13 μm are mainly attributed to C-H in-plane and out-of-plane bending modes, notably the 8.6 μm band and the 11.3 μm and the 12.7 μm complexes. Their activation is sensitive to the charge fraction of the molecule.
- The 17 μm complex originates in C-C-C bending modes.

These vibrational modes are illustrated in [Fig. 1.15. a](#).

1.3.3 Elemental depletions

1.3.3.1 Total abundance of heavy elements

In astronomy, the term “*metals*” refers to all chemical elements with a mass heavier than helium (He). We define the mass fraction of metals, also known as the *metallicity*, Z , as:

$$Z \equiv \frac{M_{\text{metal}}}{M_{\text{ISM}}}. \quad (1.8)$$

Present-day Solar photospheric measurements indicate that the Solar metallicity is $Z_{\odot} = 0.0134$.

The *abundance* relative to hydrogen, $(X/H)_{\text{gas}}$, of an element X , can be directly measured through atomic absorption lines. This measure is actually the ratio of the estimated column densities of the two elements:

$$(X/H)_{\text{gas}} \equiv \frac{N(X)}{N(H)}, \quad (1.9)$$

where $N(X)$ refers to the column density (atoms cm^{-2}) of species X , and $N(H)$ is the column density of hydrogen in both atomic and molecular forms. Since the abundances of most elements and their isotopes are accurately measured in the Solar System (*e.g.* [Asplund et al., 2009](#), for a review), they are used as a reference in the **ISM**, after correcting for the evolution of the Milky Way since the Sun’s formation. Assuming these Solar, corrected abundances, $(X/H)_{\odot}$, truly reflect the total abundances (gas and dust) in the **ISM**, the difference between the observed gas-phase and these total abundances provides an indirect estimate of the fraction of elements locked in dust grains. These differences are the *interstellar depletions* (or underabundances).

1.3.3.2 Heavy elements locked in grains

As we have just seen, the amount of an element X locked in dust grains can be inferred through its gas-phase abundance. The *logarithmic depletion factor* of this element X , $\delta(X)$, is defined as:

$$\delta(X) = [X_{\text{gas}}/H] \equiv \log_{10}(X/H)_{\text{gas}} - \log_{10}(X/H)_{\odot}. \quad (1.10)$$

In other words, this is the gas-phase abundance normalized by the reference abundance (*i.e.* the Solar abundance, $(X/H)_{\odot}$).

The relevance of the depletions to measure the elemental abundances locked in grains can be assessed by comparing them to the condensation temperature, at which 50% of an element has been removed from the gas phase. This is demonstrated in [Fig. 1.13](#) ([Savage & Sembach, 1996](#)). It shows the depletions in cool diffuse clouds towards ζ Oph sightlines, as a function of the condensation temperature for a large collection of heavy elements. If this is true, the higher the condensation temperature, the more difficult it should be to remove an atom from a grain. We should thus find that elements with the highest condensation temperature, indicated as *refractory*, are also the most depleted. This is indeed what the observed trend indicates. Elements with a low condensation temperature are described as *volatile*.

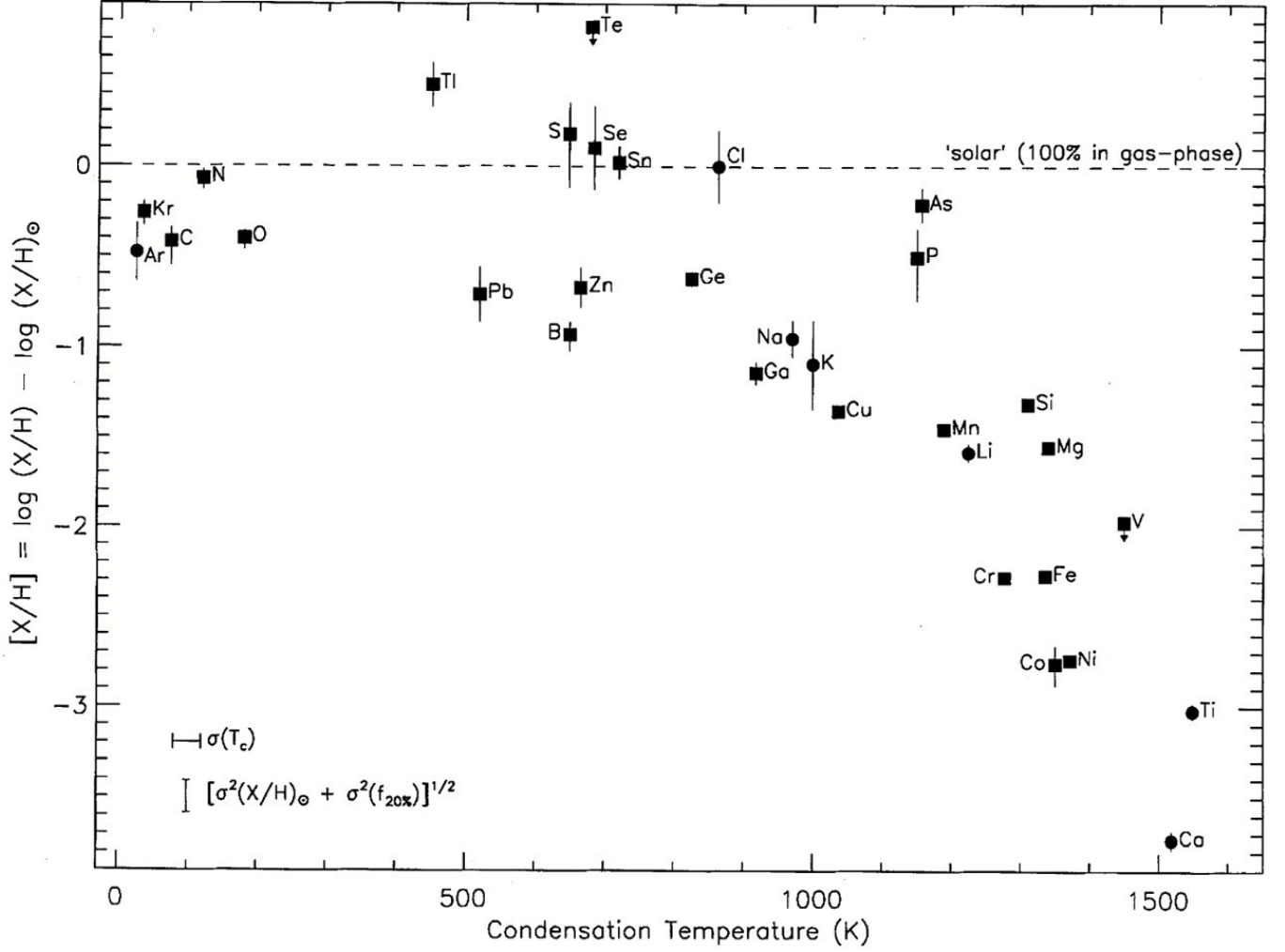


Figure 1.13 – Depletions in cool diffuse clouds towards ζ Oph.

This figure shows the elemental depletion (Eq. 1.10) along the line of sight towards Zeta Ophiuchi (ζ Oph) as a function of the condensation temperature. The condensation temperature is the temperature at which 50% of an element has been removed from the gas phase. Figure taken from [Savage & Sembach \(1996\)](#).

To account for the fact that the depletions of different elements are well correlated in the [ISM](#), [Jenkins \(2009\)](#) introduced the line-of-sight *depletion strength factor*, $0 \leq F_\star \leq 1$, defined as follows:

$$\delta(X) \simeq A_X \times F_\star + B_X, \quad (1.11)$$

where A_X and B_X are two factors empirically determined for each element X . B_X is the minimum depletion of X , occurring when $F_\star = 0$. The logarithmic depletion amplitude, A_X , quantifies the variation of the depletion of element X through the [ISM](#). The larger A_X is, the stronger the tendency of an element is to be depleted into dust grains. For instance, Fe is refractory and has a large A_X , whereas N is volatile and has a roughly constant $\delta(X)$.

The depletion strength factor is a single parameter that can be used to quantify the extent of the depletion of all elements in a given region. It indeed appears that the amount of depletion is well correlated with the average density of the [ISM](#) (e.g. [Savage](#)

& Bohlin, 1979; Harris et al., 1984). Therefore, the denser the medium is, the more gas phase atoms are locked in the grains. This evidence thus supports the scenario that grain growth in the **ISM**, by accretion of gas-phase atoms, is an important dust build-up mechanism.

1.4 Physical properties of interstellar dust

The Galactic observables presented in Sect. 1.3 are instrumental in constraining the physical properties of the grains. In particular, the chemical composition of interstellar dust is the first essential knowledge we need either to acquire or assume to model these properties.

1.4.1 Chemical composition of the main grain species

Our knowledge of the dust composition is primarily based on observations of particular spectral features that can be compared to laboratory data in order to identify the most abundant species (Sect. 1.6.1). The most plausible interstellar dust carriers are silicates, **PAHs** and other carbon-based grains, including graphite and amorphous carbon, *etc.* (Fig. 1.14).

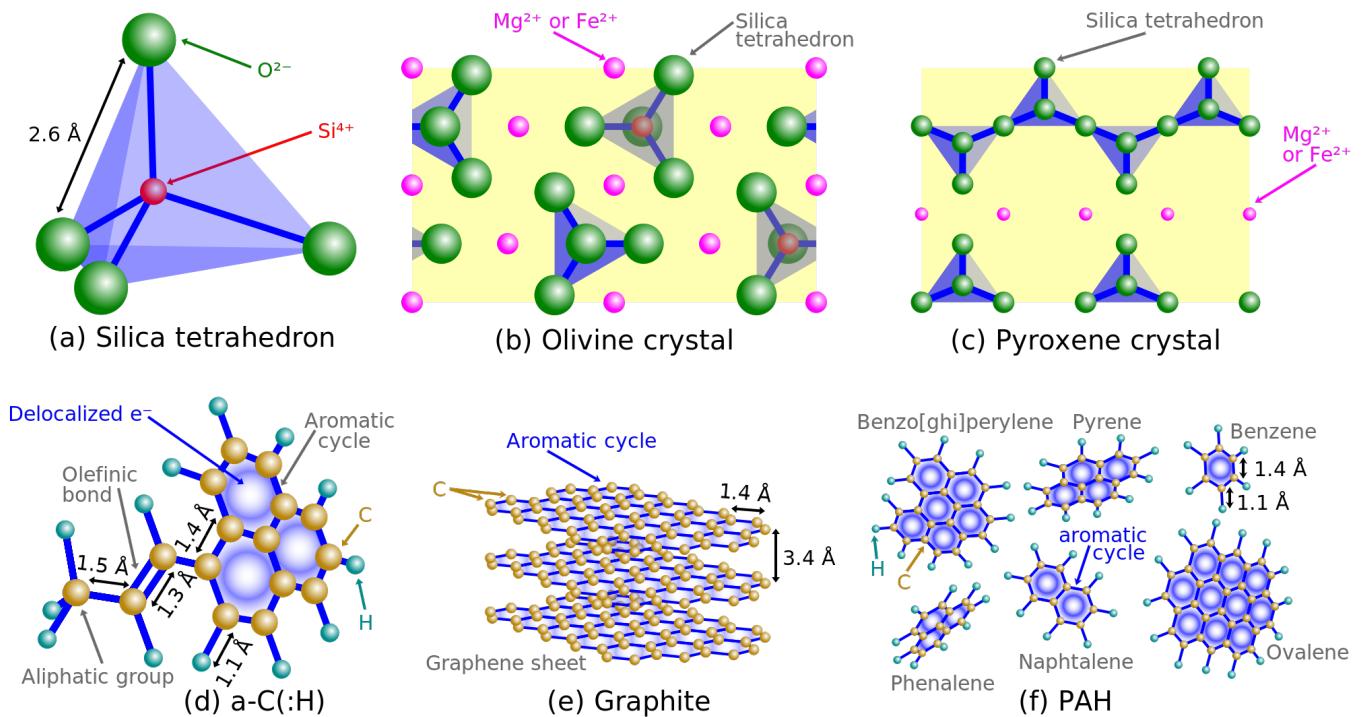


Figure 1.14 – Solid-state structure of interstellar dust candidates.

Panel (a) shows the building block of silicates, the silica tetrahedron. Panel (b) shows the structure of crystalline olivine. Panel (c) shows the structure of crystalline pyroxene. Panel (d) gives an example of the different groups encountered in an amorphous carbon, noted a-C(:H): aliphatic, aromatic and olefinic. Panel (e) shows the stack of graphene sheets tied by van der Waals forces, known as graphite. Panel (f) shows a few **PAHs**. Figure taken from G22.

1.4.1.1 Silicates

Silicates are a family of oxygen-rich solids. Their elementary building blocks are silica tetrahedra, SiO_4^{4-} (Fig. 1.14. a; Henning, 2010, for a review). These tetrahedra are tied to cations (mainly Mg^{2+} or Fe^{2+}) in different configurations. There are two main series:

- Olivine (Fig. 1.14. b), the magnesium-rich and iron-rich ends of this serie are Forsterite (Mg_2SiO_4) and Fayalite (Fe_2SiO_4), respectively;
- Pyroxene (Fig. 1.14. c), with the magnesium-rich end (Enstatite; MgSiO_3) and the iron-rich end (Ferrosilite; FeSiO_3).

Interstellar silicates are essentially amorphous (Kemper et al., 2004). These structures are thus likely to represent only small, heterogeneous domains in an actual grain. There are two strong MIR features (Fig. 1.10. b) attributed to silicates: (i) the $9.7\ \mu\text{m}$ band due to Si-O stretching and (ii) the $18\ \mu\text{m}$ band due to O-Si-O bending (e.g. Gillett et al., 1975b; Russell et al., 1975).

1.4.1.2 Polycyclic aromatic hydrocarbons (PAHs)

Carbonaceous compounds constitute the other main class of interstellar dust. Within this class, PAHs are a critical species, and they are the center of this thesis. They are molecules made of aromatic cycles with peripheral H atoms (Fig. 1.14. f). PAHs are carriers of most UIB features (e.g. Tielens, 2008). They could be the leading carriers of the $\pi \rightarrow \pi^*$ feature at $2175\ \text{\AA}$ (Joblin et al., 1992). PAHs are known to be highly flammable and carcinogenic in our daily lives. However, they are of great interest as a component of the ISM.

Fig. 1.15. a shows the main vibrational modes of PAHs. They can be divided into in-plane and out-of-plane modes or C-H, C-C, C=C and C-C-C bonds. These modes give rise to the predominant emission features in the MIR spectra of galaxies. Observations of their spectral features can be used to infer the average properties of PAHs: their molecular structure (Fig. 1.15. b), dehydrogenation (Sect. 1.6.2.3), etc.

UIBs likely originate from a mixture of a wide variety of PAHs with different molecular structures. Some species can even contain impurities, such as N (Mattioda et al., 2008). However, it remains challenging to identify specific molecules. Moreover, a neutral PAH can be photoionized by UV photons ($h\nu \gtrsim 10\ \text{eV}$) from stars, forming a PAH^+ cation, or combined with a free electron in a dense region to create a PAH^- anion. The fundamental vibrational modes, mentioned in Sect. 1.3.2.2, of PAHs with different charge states, all have similar resonant frequencies (e.g. Sidhu, 2021).

Although the abundance of C incorporated in interstellar PAHs is uncertain, it can be estimated from observations of the UIBs (detailed discussion in Sect. 1.6.3). It requires some assumptions to synthesize the optical properties of a mixture of astrophysical PAHs, such as those implemented in dust models (Sect. 1.5). Recent dust models need about 4 to 8% of the dust mass to be in the form of PAHs, in the diffuse ISM of the Milky Way (e.g. Zubko et al., 2004; Draine & Li, 2007; Compiègne et al., 2011). This represents roughly 15% to 30% of the interstellar C abundance (Draine, 2003a).

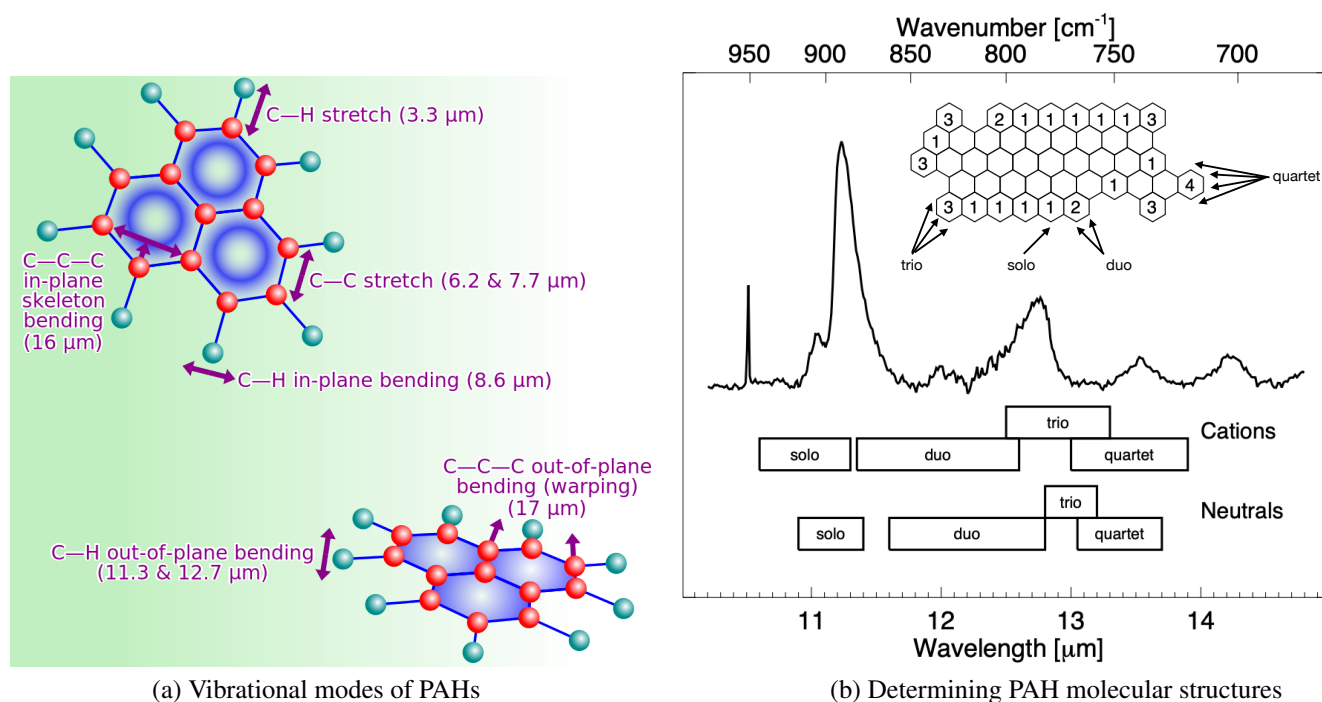


Figure 1.15 – Vibrational modes and structures of PAHs.

Panel (a), taken from G22, illustrates the major in-plane and out-of-plane vibrational motions of PAHs. C atoms are represented by red spheres and H atoms by cyan spheres. Panel (b), taken from Hony et al. (2001), shows the features attributed to out-of-plane bending modes, depending on the position of the H atom, on a laboratory spectrum (Hudgins & Allamandola, 1999b). The overlaid PAH molecule gives examples of solo, duo, trio and quartet H sites.

1.4.1.3 Other carbonaceous grains

There are several other carbonaceous solids relevant to interstellar dust. The most well-studied is graphite. It is made of stacks of graphene sheets bonded by van der Waals interactions. It thus has an anisotropic structure (Fig. 1.14. e). Graphene sheets are planar compounds exclusively constituted of aromatic cycles. As PAHs, graphite is also a candidate carrier of the extinction bump near 2175 Å, as it has the $\pi \rightarrow \pi^*$ transition associated with sp^2 -bonded carbons. Moreover, graphite has a broadband feature at 30 μm corresponding to the oscillation frequency of the delocalized electrons parallel to the sheets (Venghaus, 1977; Draine & Li, 2007). It is the main carbonaceous component of numerous dust models (e.g. Mathis et al., 1977; Draine & Li, 2001).

Alternatively, carbonaceous solids are often disordered, with a mix of sp^2 - and sp^3 -bonds (e.g. Robertson, 2003). (Hydrogenated) amorphous carbon is a broad species of carbon compounds, noted as a-C(:H), where the parentheses denote partial hydrogenation, from H-poor a-C to H-rich a-C:H (Jones, 2012). In a-C(:H), the following chemical substructures can be found (Fig. 1.14. d): (i) aromatic cycles; (ii) aliphatic groups, centered around a sp^3 hybridized C atom (CH_3); and (iii) olefinic bonds, which are alkene-type double bonds between two sp^2 hybridized C atoms ($C=C$). These grains have been proposed to explain the 3.4 μm interstellar absorption band (Dartois et al., 2004a,b).

Finally, nano-diamonds with a median radius of 1.3 – 1.5 nm are the most abundant pre-solar grains (e.g. Daulton et al.,

1996). They were the first candidates measured in the laboratory to explain the UV features in the extinction curve (Saslaw & Gaustad, 1969). Later, nano-diamonds were clearly detected in circumstellar proto-planetary discs (e.g. Guillois et al., 1999; Habart et al., 2004) via their characteristic emission features at $3.43 \mu\text{m}$ (CH_2 group) and $3.53 \mu\text{m}$ (CH group). Through the relative abundance ratio of these two C-H stretching mode bands, we can model the particle size and shape of nano-diamonds (e.g. Jones, 2022). Based on the fact that nano-diamonds have also been extracted from primitive meteorites and the premise that they can not form in the Solar system, they must have been traveling here and thus exist (but hide) in the diffuse ISM (e.g. Jones & Ysard, 2022).

1.4.2 Optical properties of grains

An electromagnetic wave interacting with a dust grain is either scattered (*i.e.* changing direction and polarization) or absorbed (*i.e.* its energy is transformed into heat). The energy absorbed by the grain is later emitted in the infrared. These different processes can be characterized by a set of wavelength-dependent optical properties: the extinction cross-section (Sect. 1.4.2.2), the albedo and the average scattering angle. These optical properties, which are specific to the composition, size and shape of the grain, can be derived from the dielectric function, which is directly related to the microscopic electronic structure of the solid (e.g. Wooten, 1972, for a review).

1.4.2.1 Dielectric functions

Hendrik Antoon Lorentz was the first to model the motion of an electron in an atom with a harmonic oscillator (or *Lorentz oscillator*; e.g. Krügel, 2003). Such an oscillator, in the one-dimensional case, is defined by only three quantities: (i) the electron charge-to-mass ratio, e/m_e ; (ii) the damping constant, $\gamma \equiv b/m_e$, where b is a dissipation constant; and (iii) the natural (*i.e.* undamped) frequency, $\omega_0 \equiv \sqrt{k_e/m_e}$, with k_e the strength of the restoring force. The resonant frequency equals the natural frequency when there is no damping. This model can describe the oscillation of electrons in a solid.

In a conducting medium such as a plasma or an ohmic conductor (e.g. a metal), a fraction of the valence electrons are delocalized. These free electrons, with number density n_e , oscillate around heavy cations. Ignoring their thermal motion, their oscillation frequency is called the *plasma frequency*, ω_p , as:

$$\omega_p \equiv \sqrt{\frac{n_e e^2}{m_e \epsilon_0}}, \quad (1.12)$$

where ϵ_0 is the vacuum permittivity. This frequency is specific to the physical nature of conductors. It, however, also appears mathematically in the dielectric function of insulators.

In an idealized medium consisting of only one type of harmonic oscillators, the dispersion relation of propagating electromagnetic waves is called the *dielectric function*, ϵ_r . It happens to also be the relative electric permittivity of the medium, the absolute electric permittivity being $\epsilon = \epsilon_r \epsilon_0$. Assuming each bond in the dielectric behaves as a dipole and simplifying using

the plasma frequency (Eq. 1.12), the dielectric function takes the following form (e.g. Krügel, 2003):

$$\epsilon_r(\omega) = \epsilon_1(\omega) + i\epsilon_2(\omega) = 1 + \frac{\omega_p^2(\omega_0^2 - \omega^2)}{(\omega_0^2 - \omega^2)^2 + \gamma^2\omega^2} + i \frac{\omega_p^2\gamma\omega}{(\omega_0^2 - \omega^2)^2 + \gamma^2\omega^2} . \quad (1.13)$$

It describes the response of the medium (specifically, chemical bonds for a dielectric) to the applied electric field of the incident photon.

Fig. 1.16. a shows the optical constants of an idealized dielectric (Eq. 1.13). The real part, ϵ_1 , describes the ability of a medium to respond to an electric field by storing and reemitting energy. ϵ_1 induces a phase lag between frequencies of the external field and the medium response⁹. At a resonance $\epsilon_1 = 1$. The imaginary part ϵ_2 is symmetric and peaks around the resonant frequency ω_0 , where the absorption dominates. ϵ_2 goes to zero when the external field frequency is far from the resonant frequency. Because the dielectric function is a linear physical response, we can apply the *Kramers-Kronig relations* (causality relations) to connect the real response term ϵ_1 and the dissipative term ϵ_2 . Often, only the imaginary part of the dielectric function is measured, and the real part is derived using the Kramers-Kronig relations (e.g. Draine & Lee, 1984).

Similar modeling can be applied to idealized conductors. This time, the oscillators are free electrons instead of chemical bonds. The relation will differ from Eq. (1.13) because of the conductivity of the medium (cf. e.g. Krügel, 2003, for the relation in this case).

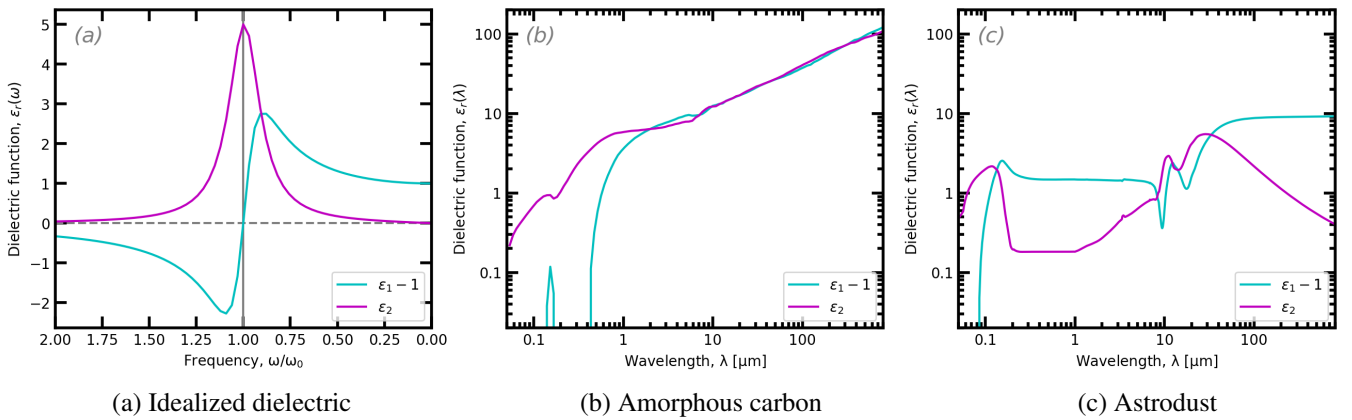


Figure 1.16 – Dielectric functions of different materials.

Panel (a) shows the idealized dielectric function of Eq. (1.13), with $\omega_p = \omega_0$ and $\gamma/\omega_0 = 0.2$. Panel (b) shows the BE type of amorphous carbon (burning of benzene in air under normal conditions; Zubko et al., 1996). Panel (c) shows spheroidal astrodust particles (Draine & Hensley, 2021). In this last case, we took a grain porosity (vacuum fraction), $\mathcal{P}=0.2$, a fraction of the Fe in metallic form, $f_{\text{Fe}} = 0$, and an axial ratio $b/a=0.5$ (prolate shape; a and b being respectively the long and short axes of the spheroids.).

Realistic dielectric functions are the linear combination of several oscillators that are not necessarily harmonic. For a given chemical composition, they are usually derived with the help of three complementary sources of information: astronomical observations (e.g. the profile of the *astronomical silicate* feature by Draine & Lee, 1984; Draine, 1985), laboratory data

⁹. From a macroscopic perspective, the optical constant is related to the refractive index, $m(\omega) = n(\omega) + ik(\omega)$, through $\epsilon_r = m^2$, so that $\epsilon_1 = n^2 - k^2$ and $\epsilon_2 = 2nk$.

(e.g. amorphous carbon in Fig. 1.16. b; Zubko et al., 1996) and theoretical calculations (e.g. using the Kramers-Kronig relations to derive ϵ_2 from ϵ_1). Recently, Draine & Hensley (2021) modeled interstellar dust with a mash-up of amorphous silicates, carbonaceous grains and other materials (e.g. metal oxides, metallic iron, etc.). Fig. 1.16. c gives an example of the effective dielectric function of this so-called “Astrodust”.

1.4.2.2 Cross-sections

For now, let us assume that we have a homogeneous, spherical grain of radius a . Its *extinction cross-section*, C_{ext} , will depend both on a and on the wavelength of the incident photon, λ . It can be decomposed as

$$C_{\text{ext}}(\lambda, a) = \pi a^2 Q_{\text{ext}}(\lambda, a), \quad (1.14)$$

which is simply the product of the geometrical cross-section of the grain, πa^2 and its *extinction efficiency*, Q_{ext} . *Idem* for scattering (C_{sca}) and absorption (C_{abs}):

$$C_{\text{sca}}(\lambda, a) = \pi a^2 Q_{\text{sca}}(\lambda, a), \quad (1.15)$$

$$C_{\text{abs}}(\lambda, a) = \pi a^2 Q_{\text{abs}}(\lambda, a). \quad (1.16)$$

These three quantities are related by $C_{\text{ext}} \equiv C_{\text{sca}} + C_{\text{abs}}$. The *albedo* ($\tilde{\omega}$), which is the fraction of scattered light, can be written as:

$$\tilde{\omega}(\lambda, a) \equiv \frac{C_{\text{sca}}(\lambda, a)}{C_{\text{ext}}(\lambda, a)} = \frac{Q_{\text{sca}}(\lambda, a)}{Q_{\text{ext}}(\lambda, a)}. \quad (1.17)$$

The scattering direction is also an important quantity. It is required when solving the radiative transfer equation through a dusty medium. If we denote θ the angle between the incident and scattered directions, its probability distribution is called the *scattering phase function*, Φ , as:

$$\Phi(\cos \theta, \lambda, a) \equiv \frac{1}{C_{\text{sca}}(\lambda, a)} \frac{dC_{\text{sca}}(\cos \theta, \lambda, a)}{d\Omega}, \quad (1.18)$$

where we have introduced the *differential scattering cross-section*, $dC_{\text{sca}}/d\Omega$, as:

$$\frac{dC_{\text{sca}}(\cos \theta, \lambda, a)}{d\Omega} = \frac{dC_{\text{sca}}(\cos \theta, \lambda, a)}{d \cos \theta d\phi}, \quad (1.19)$$

that is normalized over all directions. For isotropic scattering, $\Phi(\cos \theta, \lambda, a) = 1/(4\pi)$. The first moment of the scattering angle distribution is called the *asymmetry parameter*, g , as:

$$g(\lambda, a) = \langle \cos \theta \rangle = 2\pi \int_{-1}^1 \Phi(\cos \theta, \lambda, a) \cos \theta d \cos \theta. \quad (1.20)$$

Forward and backward scattering correspond to $g \simeq 1$ and $g \simeq -1$, respectively, whereas isotropic scatterers have $g \simeq 0$. The choice of the phase function is a debated topic. A widely-used analytical approximation was proposed by Henyey & Greenstein

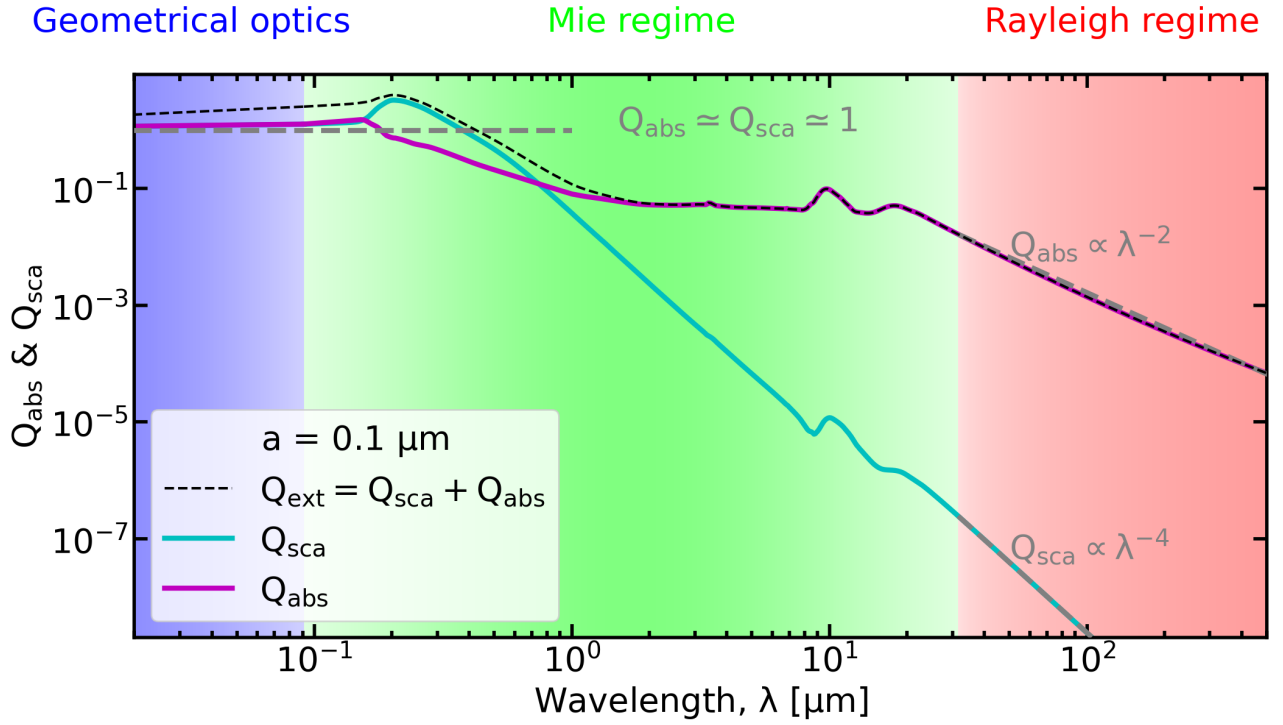


Figure 1.17 – Absorption, scattering and extinction efficiencies of an astrodust grain.

The absorption (magenta), scattering (cyan) and extinction (black dashed) efficiency factors are calculated using optical constants of the same astrodust grain in Fig. 1.16. c ($\mathcal{P}=0.2$, $b/a=0.5$, $f_{\text{Fe}} = 0$), for an effective radius of $0.1 \mu\text{m}$ (Draine & Hensley, 2021). The geometric optics (blue), Mie (green) and Rayleigh (red) regimes are highlighted, with approximate functions of Q_{sca} and Q_{abs} in two extremes (gray dashed). These regimes depend on the value of the size parameter (Eq. 1.21).

(1941). Alternative expressions have been derived to provide a better fit to the actual phase function (e.g. Draine, 2003b).

C_{ext} , C_{sca} and g can be computed from the dielectric function using Mie scattering theory (e.g. Bohren & Huffman, 1998). Mie theory (Mie, 1908; Debye, 1909) is a numerical method solving the Maxwell equations through a homogeneous, spherical grain. The results of the Mie theory depend on a single parameter, called the *size parameter*, x , as:

$$x = \frac{2\pi a}{\lambda} . \quad (1.21)$$

Two limiting regimes on each sides of the non-trivial regime can be delimited as a function of x (Fig. 1.17).

Geometrical optics. When $x \gg 1$, grain sizes are much larger than wavelengths. We have $Q_{\text{sca}} \simeq Q_{\text{abs}} \simeq 1$.

The Mie regime. When $x \simeq 1$, grain sizes are comparable to wavelengths. The optical properties in this regime are nontrivial, and Mie theory is necessary to estimate them.

The Rayleigh regime. When $x \ll 1$, grain sizes are significantly smaller than wavelengths. For interstellar dust sizes, it concerns the NIR to longer wavelengths.

1.4.3 Thermal grain radiation

We have already mentioned the fact that grains absorb mainly UV-visible photons and reemit their absorbed power in the infrared. Let us now go into more details about this emission process. We first need to define the following general quantities.

- The *opacity* of a spherical grain, $\kappa_{\text{abs}}(\lambda, a)$, is its absorption cross-section per unit mass:

$$\kappa_{\text{abs}}(\lambda, a) = \frac{C_{\text{abs}}(\lambda, a)}{\frac{4\pi}{3} a^3 \rho} = \frac{3}{4\rho} \frac{Q_{\text{abs}}(\lambda, a)}{a}, \quad (1.22)$$

where we have applied Eq. (1.16).

- The mean intensity of the **InterStellar Radiation Field (ISRF)**, J_ν , heating the grain is the average over a solid angle of its specific intensity (at frequency ν):

$$J_\nu(\lambda) = \frac{1}{4\pi} \iint_{\text{sphere}} I_\nu^{\text{ISRF}}(\lambda, \Omega) d\Omega, \quad (1.23)$$

- The power absorbed by a grain heated by this **ISRF**, P_{abs} , is:

$$P_{\text{abs}}(a) = \int_0^\infty 4\pi J_\nu(\nu) \times \pi a^2 Q_{\text{abs}}(\nu, a) d\nu. \quad (1.24)$$

The heating regime depends on the grain size and the **ISRF** intensity. This is demonstrated by the Monte-Carlo simulation presented in Fig. 1.18 (Draine, 2011). These panels show the variation of the grain temperature, T , as a function of time, t . We see that the largest grains have a roughly flat temperature history. It is even enhanced if the **ISRF** intensity is higher (right panels). We say in this instance that grains are at thermal equilibrium with the **ISRF**. Indeed, they do not have time to cool down significantly before two successive photon absorptions. On the contrary, smaller grains can exhibit temperature fluctuations as exhibited in the lower panels of Fig. 1.18. This is because they have time to cool down significantly between two-photon absorptions. We now enter into more details about these two regimes.

1.4.3.1 Equilibrium heating

A grain is at thermal equilibrium if its temperature evolution can be considered steady state: $T(t) = T_{\text{eq}}$. A body at thermal equilibrium with a radiation source, perfectly absorbing all the incident light, is a *blackbody*. *Planck's law*, B_ν , gives the specific intensity, I_ν , radiated by such a blackbody, at wavelength λ (or frequency ν , hereafter):

$$I_\nu = B_\nu(T, \lambda) \equiv \frac{2hc}{\lambda^3} \frac{1}{\exp\left(\frac{hc}{\lambda k_B T}\right) - 1}, \quad (1.25)$$

where k_B is the *Boltzmann constant*, h is the *Planck constant*, and c is the speed of light. It is a function of the grain temperature T . A grain is an imperfect absorber. Its absorption efficiency is lower than one, outside of the geometrical optics regime

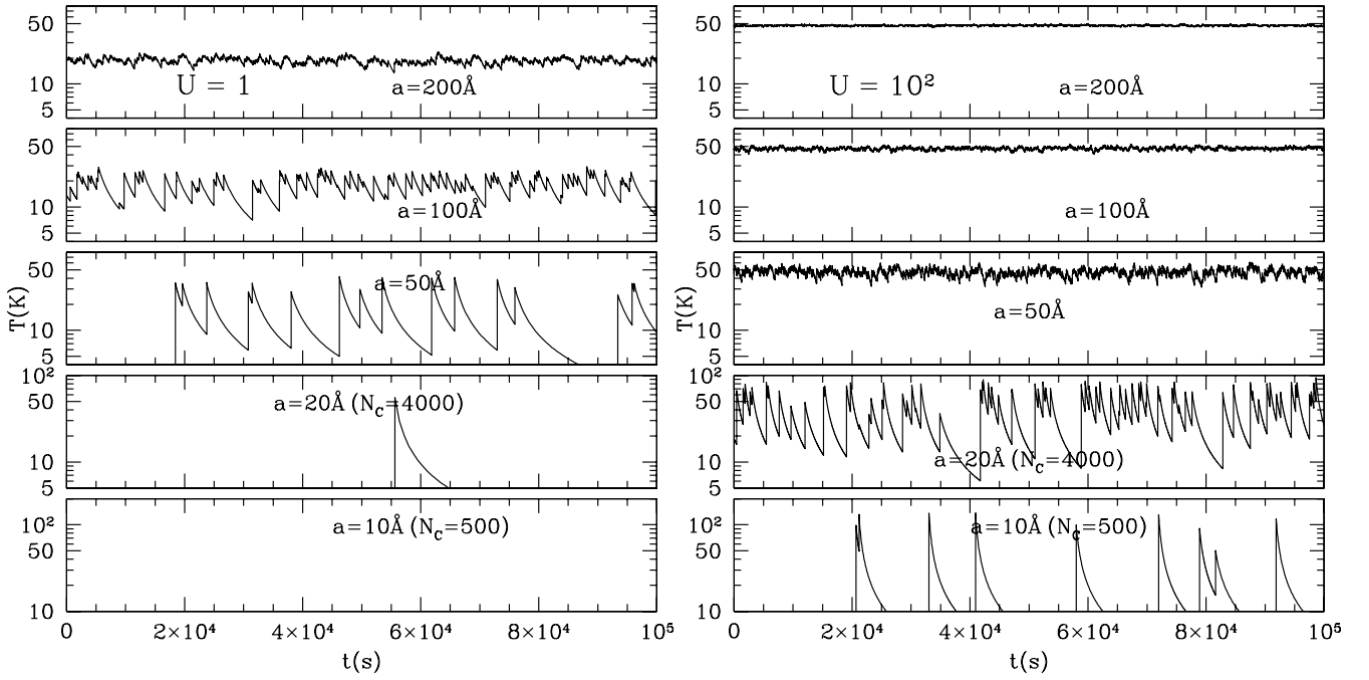


Figure 1.18 – A day in the life of five carbonaceous grains heated by the local **ISRF**.

This figure shows the time-dependent temperature variation of different grains (with sizes $a = 200, 100, 50, 20, 10 \text{ \AA}$). These grains are heated by the local **ISRF** (Mathis et al., 1983) with intensities $U = 1$ (left panel) and $U = 10^2$ (right panel). Figure taken from Draine (2011).

(Sect. 1.4.2.2). Its *emissivity*, ϵ_ν (Eq. A.4), is actually the Planck function, modified by its opacity:

$$\epsilon_\nu(\lambda) = 4\pi\kappa_{\text{abs}}(\lambda, a) \times B_\nu(T, \lambda) . \quad (1.26)$$

The absorbed power, P_{em} , is thus simply the integral of Eq. (1.26) over frequencies:

$$P_{\text{em}}(a, T) = \int_0^\infty 4\pi B_\nu(T, \nu) \times \pi a^2 Q_{\text{abs}}(\nu, a) d\nu . \quad (1.27)$$

The equilibrium temperature can then be calculated by solving:

$$P_{\text{em}}(a, T_{\text{eq}}) = P_{\text{abs}}(a), \quad (1.28)$$

that is by imposing that the absorbed and emitted powers are equal.

1.4.3.2 Stochastic heating

If the temperature of a grain fluctuates significantly with time, this grain is considered out-of-equilibrium with the radiation field. We also say that this grain is stochastically heated. We can determine if the grain is at thermal equilibrium or stochastically

heated by comparing the mean stellar photon energy, $\langle h\nu \rangle$, to the vibrational energy content (or *enthalpy*) of the grain, $H(T_{\text{eq}})$. Note that the enthalpy is evaluated at T_{eq} , from Eq. (1.28), even if the grain is not at thermal equilibrium. The mean photon energy, $\langle h\nu \rangle$, is simply:

$$\langle h\nu \rangle \equiv \frac{\int_0^\infty J_\nu(\nu) d\nu}{\int_0^\infty \frac{J_\nu(\nu)}{h\nu} d\nu}. \quad (1.29)$$

Grains of small sizes ranging down to large molecules are often stochastically heated, because they can store less energy in their phonon modes¹⁰. This can be understood by estimating the *photon absorption rate* of a grain, $1/\tau_{\text{abs}}$, as:

$$\frac{1}{\tau_{\text{abs}}(a)} = \int_0^\infty \frac{4\pi J_\nu(\nu)}{h\nu} \times \pi a^2 Q_{\text{abs}}(\nu, a) d\nu. \quad (1.30)$$

The smaller the grain is, the larger τ_{abs} is. The mean time between two successive photon absorptions strongly increases when the grain radius diminishes. On the other hand, the *radiative cooling rate* of the grain, $1/\tau_{\text{cool}}$, is simply:

$$\frac{1}{\tau_{\text{cool}}(a, T)} = \frac{P_{\text{em}}(a, T)}{H(T)}. \quad (1.31)$$

Both $P_{\text{em}}(a, T)$ and $H(T)$ are proportional to the grain volume. The cooling time is thus independent of grain size. We thus see that, for small grains, the cooling is going to become shorter than the absorption time ($\tau_{\text{cool}} \lesssim \tau_{\text{abs}}$), thus explaining their temperature fluctuations. The approximate transition radius where a grain becomes stochastically heated depends on its composition and size, as well as on the radiation field intensity and on its spectral shape.

Since their temperature changes with time, the key to calculating the emission from small, stochastically-heated grains is to estimate their temperature probability distribution, $dP(T, a)/dT$, where $P(T, a)$ is the probability that the grain will have a temperature less than or equal to T . Several numerical methods to compute this temperature distribution have been proposed (e.g. Draine & Anderson, 1985; Desert et al., 1986; Guhathakurta & Draine, 1989). Then, the total grain emission, ϵ_ν , is simply the integration of Eq. (1.26) over the temperature distribution:

$$\epsilon_\nu(a, \nu) = \frac{3\pi}{\rho} \frac{Q_{\text{abs}}(a, \nu)}{a} \int_0^\infty B_\nu(T, \nu) \frac{dP(T, a)}{dT} dT. \quad (1.32)$$

The two heating regimes have consequences on the emission spectrum. This is demonstrated in Fig. 1.19. We see that the spectral shape of the small grain emission is virtually independent of the radiation field intensity, U (Fig. 1.19. a). This is because small grains are sensitive only to single photon events. On the contrary, large grains are sensitive to the total absorbed power. Their equilibrium temperature, therefore, increases with U . This is why their emission shifts to shorter wavelengths when U increases.

10. In quantum mechanics, a *phonon* is a collective vibrational mode of a lattice of atoms or molecules oscillating uniformly at a single frequency.

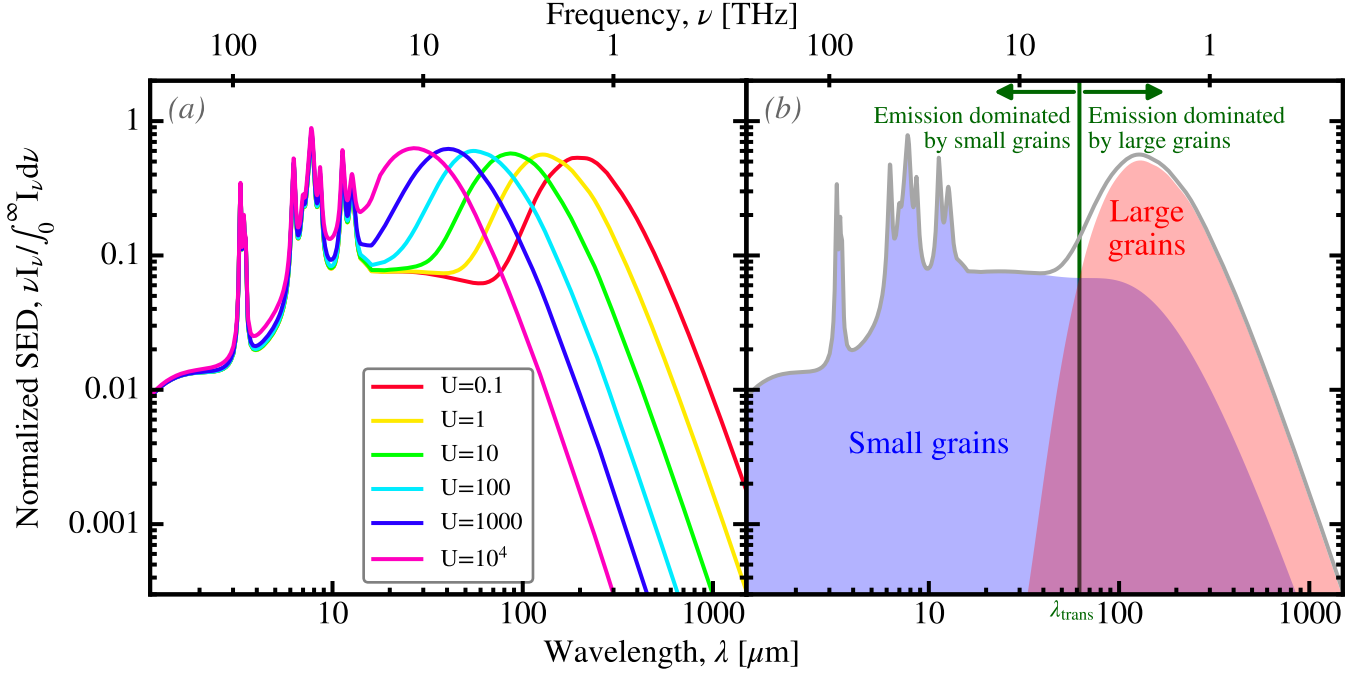


Figure 1.19 – Effect of the ISRF intensity U on the infrared spectrum.

Panel (a) shows the SED of the THEMIS model (Sect. 1.5.1) illuminated by different U (each normalized by the total power). Panel (b) shows the contribution of small size grains (amorphous carbon) and large grains (amorphous silicates and amorphous carbon) to the total emission in the $U = 1$ case. Figure taken from G22.

1.5 Modeling interstellar dust mixtures

Interstellar dust models are the conceptual tools that allow us to synthesize all the information we have about dust properties, coming from the laboratory, from observations and from our theoretical knowledge. They constitute frameworks that can be used to interpret observations, in a physical way. More precisely, interstellar dust models determine a set of grain properties (chemical composition and structure, size distribution, abundances, *etc.*) that can account for the observations of the diffuse Galactic ISM: extinction curve, infrared emission, elemental depletions, interstellar polarization, *etc.* These models can then be applied to denser interstellar phases or to external galaxies, by varying some of their parameters.

The differences between the dust properties of the diffuse Galactic ISM and those of other systems can be estimated with cosmic dust evolution models. These models account for the evolution of a galaxy, following the evolution of its different stellar populations, the successive ejection of heavy elements and the grain formation and destruction processes within the ISM. Consequently, they provide a way to relate the dust properties to global galaxy parameters, such as the SFR or the gas and stellar masses. These models start to be incorporated into numerical simulations (*e.g.* Aoyama et al., 2017). Combined with radiative transfer models they open the door to accurate synthetic images of galaxies (*e.g.* Trčka et al., 2020).

1.5.1 Historical perspective

In 1930, Robert J. Trumpler’s seminal work on *color excess* or *selective absorption* with increasing distance (Trumpler, 1930) provided the first unambiguous evidence of interstellar dust. Similar results were independently presented by Schalén (1929) at the same time. Following this discovery, the first dust models of the 1930s assumed interstellar grains were made of small metallic particles (*e.g.* Schoenberg & Jung, 1937; Greenstein, 1938) or dirty ices (*e.g.* Oort & van de Hulst, 1946). These speculations were mainly based on analogy with the composition of meteorites. It was hypothesized that dust forms by condensation in the interstellar medium (Lindblad, 1935), due to the very low temperature in space (Eddington, 1926).

After these initial findings, several breakthroughs followed. We list here the most noteworthy.

- In 1949, Hiltner (1949a,b) and Hall & Mikesell (1949) discovered the polarization of starlight by dust grains. Cayrel & Schatzman (1954) suggested that graphite could be a dust constituent in order to explain the interstellar polarization. Graphite was indeed a very efficient polarizer compared to ice grains. In addition, graphite was supported by the discovery of the 2175 Å bump (Stecher, 1965).
- In 1969, silicates were first detected in emission in M stars (Woolf & Ney, 1969).
- The first dust radiative transfer numerical computations were performed using iterative methods (Mathis, 1970) and Monte Carlo methods (Mattila, 1970).
- In 1973, Gillett & Forrest (1973) first detected H₂O ice through its 3.1-μm absorption feature. Gillett et al. (1973) first detected UIBs in planetary nebulae. Later in the 1980s, UIBs were attributed to the bending and stretching modes of PAHs (Fig. 1.12; Duley & Williams, 1981; Leger & Puget, 1984; Allamandola et al., 1985).
- The Mathis, Rumpl, & Nordsieck (1977, hereafter MRN) interstellar grain model successfully reproduced observations of the extinction and polarization of the diffuse ISM. The MRN model was the first to fit the average extinction curve of the Milky Way over the wavelength range $0.11 \mu\text{m} < \lambda < 1 \mu\text{m}$ with a mixture of bare graphite and silicate grains. These authors derived a power-law size distribution¹¹, $f(a)$, as:

$$f(a) \equiv \frac{dn}{da} \propto a^{-3.5} \text{ for } a_- < a < a_+, \quad (1.33)$$

where the grain size ranges are $[a_-, a_+] = [0.005, 1] \mu\text{m}$ for graphite and $[a_-, a_+] = [0.025, 0.25] \mu\text{m}$ for silicates (Fig. 1.20). Combined with the first UV-to-mm optical properties of astronomical silicate and graphite presented by Draine & Lee (1984, hereafter DL84), MRN-type models became the new standard.

- In 1983, the launch of the first infrared space telescope, IRAS (Sect. 1.2.2), opened the FIR window and revolutionized our understanding of interstellar dust. In particular, it allowed fitting the thermal emission from grains, with four broadbands at 12, 25, 60 and 100 μm, providing the first reliable SEDs of Galactic regions and external galaxies.

11. It was later shown that grain-grain collisions would lead to a power-law dust size distribution with an index ~ -3.5 (Biermann & Harwit, 1980).

- The **DBP90** model (Desert et al., 1990) was the first model to fit both the interstellar extinction and the infrared emission of the Galactic diffuse **ISM**. It consisted not only of big grains (mantled silicates), but also **Very Small Grains** (VSGs; carbonaceous; 3D) and **PAHs** (2D). Therefore, **DBP90** and later dust models have extended the MRN grain size distribution down into the molecular domain (e.g. Dwek et al., 1997).
- Li & Draine (2001, hereafter **LD01**) revised the work of **DL84** and proposed a model quite similar to **DBP90**. Their originality was to synthesize the optical properties of a mixture of astronomical **PAHs**. It was updated by Draine & Li (2007, hereafter **DL07**), accounting for the observations of **PAH** spectra by Spitzer.

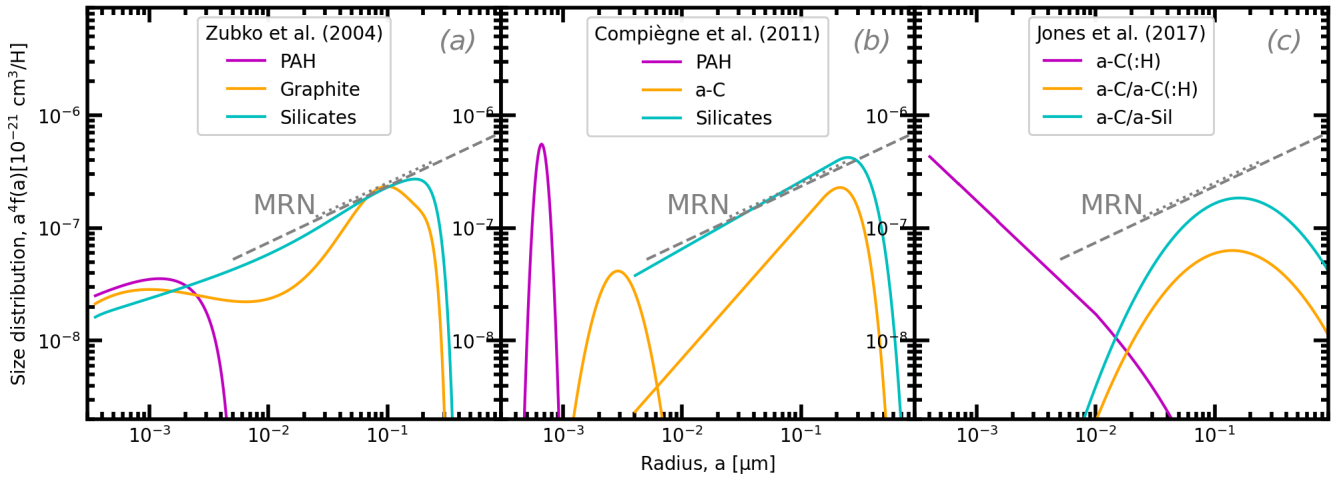


Figure 1.20 – Grain size distributions of different dust models.

Panel (a) shows the **ZDA04** (BARE-GR-S) model (Zubko et al., 2004). Panel (b) shows the **DHGL** model (Compiègne et al., 2011). Panel (c) shows the **THEMIS** model (Jones et al., 2017). In each panel, the two gray lines are the MRN size distributions for silicates (dotted) and graphite (dashed). Note that these distributions are mass-weighted, as we have multiplied $af(a)$ by a^3 .

- The Zubko et al. (2004, hereafter **ZDA04**) model was the first to add the constraints provided by elemental depletions to those provided by extinction and emission. This study also demonstrated the uncertainty in the actual composition of the grains by fitting the same set of constraints with different grain mixtures, including composite particles. The grain size distribution of their bare-grain/Solar-abundance model, **ZDA04** (BARE-GR-S), is displayed in Fig. 1.20. a.
- The Compiègne et al. (2011) model was the first one to use *Planck* and *Herschel* observations of the Diffuse ISM at High-Galactic Latitude (**DHGL**). A power-law size distribution with an exponential cut-off was used for large grains, whereas they adopted separate log-normal size distributions for **PAHs** and small a-C (Fig. 1.20. b)¹².
- The *Heterogeneous Evolution Model for Interstellar Solids* (**THEMIS**; Jones et al., 2013, 2017) is the first model conceived to account for dust evolution. It is extensively based on laboratory data, and several of its parameters are meant to describe the evolution of the dust mixture through different conditions in the **ISM**. It consists of a population of small a-C(:H) and a population of large grains with metallic inclusions and carbonaceous mantles. The variation of the thickness of this mantle can account for matter accretion in the dense **ISM**. Note that there are no **PAHs** in this model, but small a-C(:H)

12. Mattsson (2020) has shown that turbulent grain growth leads to a log-normal size distribution.

accounting for **UIB** emission. The functional form of the size distribution is reversed compared to [Compiègne et al. \(2011\)](#), that is, THEMIS adopts log-normals for large grains and a power-law with an exponential cut-off for small $a-C(:H)$ ([Fig. 1.20. c](#)). [Guillet et al. \(2018\)](#) adapted the THEMIS model to elongated grains in order to account for polarization constraints in extinction and in emission (data from the *Planck* satellite).

We refer to [Li \(2005\)](#) and [Galliano \(2022\)](#), hereafter **G22**, for more detailed historical reviews.

1.5.2 Dust evolution processes

Dust evolution is the modification of the dust properties with time. Since the timescales at play are long (several Myr), we usually study dust evolution by comparing regions with different physical conditions. This spatial comparison is thus a proxy for the temporal evolution. If instead of comparing regions within a galaxy, we compare galaxies as a whole, there are still differences in average dust properties that can be linked to the star formation history of each object. In this instance, we rather talk about *cosmic* dust evolution (*e.g.* [Dwek & Scalo, 1980](#); [Galliano et al., 2021](#)).

1.5.2.1 Grain formation

Grain formation is the incorporation of gas-phase heavy elements into interstellar solids. We can list two main sources:

Stardust: condensation of grain seeds in the ejecta of **Core-Collapse SuperNovae (CCSNe; type II)** and in **Asymptotic Giant Branch (AGB)** stars;

Grain growth: accretion of gas-phase atoms onto pre-existing grains, in the **ISM**, mainly in the **CNM** and molecular clouds (*e.g.* [Hirashita, 2012](#)).

A fraction of interstellar dust is potentially “*stardust*” (*e.g.* see the discussion in [Nittler & Ciesla, 2016](#)). However, this fraction might be small, because: (i) the stellar yields of **CCSN** and **AGB** stars are potentially low and very uncertain ([Matsuura et al., 2015](#)) and (ii) the dust destruction in the **ISM** is faster than the stellar injection ([Draine, 2009](#)). The main argument against stardust as the origin of interstellar dust is the variations of the gas depletions with density ([Jenkins, 2009](#)). Only rapid destruction and re-formation in the **ISM** can explain these variations. According to [Draine \(2009\)](#), in the Milky Way, stardust has been estimated to have produced less than 10% of the interstellar dust in mass.

1.5.2.2 Grain transformation

The chemical structure and size distribution of interstellar grains can be altered by different processes. We call “*grain transformation*” those that do not change the total dust content. We can list: (i) grain-grain coagulation in cold regions, (ii) structural modifications by high energy photons or cosmic ray impacts and (iii) shattering by low-velocity shocks.

1.5.2.3 Grain destruction

Grain destruction is the return of a part or the entirety of the heavy elements in a grain to the gas phase. It can be attributed to: (i) astration, (ii) photodestruction and (iii) thermal or kinetic erosion and evaporation. Astration is simply the fraction of dust consumed by star formation. Small grains, including PAHs, are the most likely to undergo photodestruction near massive stars, because of their thermal spikes (Sect. 1.4.3.2). Larger grains can also sublime in the vicinity of hard radiation sources. Finally, erosion and evaporation happen either in coronal plasmas or in SN II blast waves. In both cases, ions are rapid enough to either remove atoms from the grain or pulverize it. The overall dust destruction efficiency by SN is still debated. The timescales are likely a few hundred million years (e.g. Draine, 2009; Slavin et al., 2015).

1.6 Focusing on the mid-infrared (MIR) features

Let us now focus on PAHs, as they are the prime object of this thesis. PAHs account for around 20% of the carbon in the Milky Way¹³. We have already discussed the molecular structure of PAHs in Fig. 1.14. f. PAH studies constitute an interdisciplinary research field from astronomical observations (Fig. 1.11) to laboratory experiments (Sect. 1.6.1) and theoretical computations (e.g. Fig. 1.23. b). We now discuss their emission spectra in more details.

1.6.1 Experimental and theoretical studies

With the development of experimental and theoretical quantum chemical techniques, the emission spectrum of numerous PAHs has been precisely characterized (e.g. Tielens, 2008, for a review). Extensive laboratory studies have shown in detail the rich collection of vibrational modes that these molecules can have in the MIR (e.g. Hudgins & Allamandola, 1999b; Mattioda et al., 2020). The knowledge of the physical origin of these modes is essential to constrain the molecular structure of their carriers (Fig. 1.15. b). Meanwhile, our understanding of the emission features and of the chemical evolution of PAHs have benefited from computational IR tools such as Density Functional Theory (DFT; e.g. Bauschlicher et al., 2008; Mackie et al., 2015; Mulas et al., 2018; Buragohain et al., 2020), molecular dynamics (e.g. Mao et al., 2017; Hanine et al., 2020) and Monte Carlo methods (e.g. Rapacioli et al., 2005b).

Different groups in the world have invested some efforts into laboratory studies of PAHs. Fig. 1.21 shows one of the state-of-the-art experimental devices to analyze the chemical composition and structure of the aromatic nano-grain analogs, AROMA (Sabbah et al., 2017). The PAH properties in the infrared can be measured by another instrument, PIRENEA/PIRENEA 2¹⁴ (Joblin et al., 2002; Bonnamy et al., 2018). Experimental data can be complemented by theoretical calculations, such as the PAH IR Spectroscopic Database (PAHdb)¹⁵ generated by the NASA Ames Research Center through laboratory experiments

13. The fraction of carbon incorporated in PAHs is model-dependent. For example, this value is 32% with the DHGL model (Compiègne et al., 2011), whereas it is only 13% using ZDA04 (BARE-GR-S). We will discuss more this value in Sect. 1.6.3.

14. AROMA is the acronym of “Astrochemistry Research of Organics using Molecular Analyzer”; PIRENEA is the acronym of “Piège à Ions pour la Recherche et l’Etude de Nouvelles Espèces Astrochimiques; Ion Trap for the Research and Study of New Astrochemical Species”. Both instruments are at IRAP (France).

15. <https://www.astrochemistry.org/pahdb/>

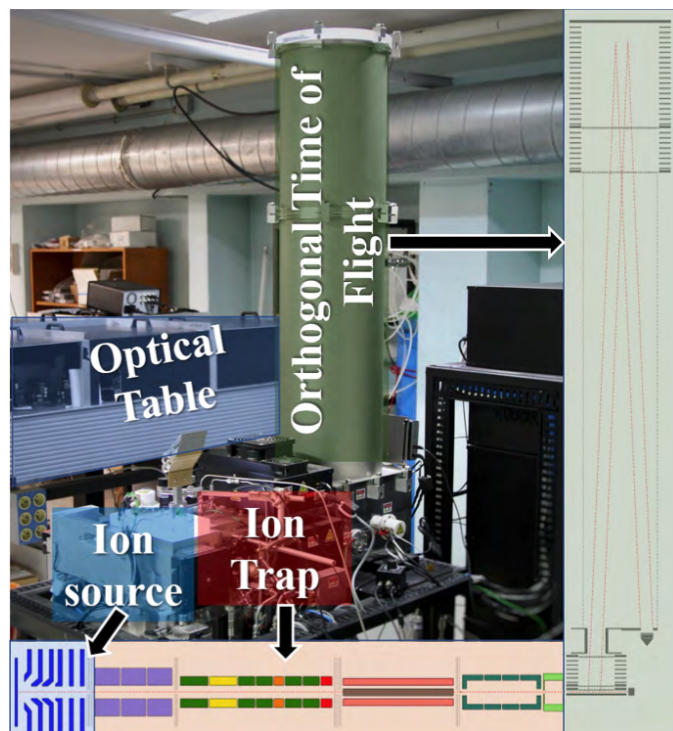


Figure 1.21 – Annotated AROMA experimental setup (IRAP, France).

The ion source is generated from the sample with laser beams from the optical table. Then ions are stored in the ion trap for collision or photodissociation. Finally, the processed ions are sent to an orthogonal time-of-flight mass spectrometer. Figure taken from [Carlos \(2020\)](#).

([Mattioda et al., 2020](#)) and computational modeling ([Bauschlicher et al., 2010, 2018](#)). For now, PAHdb is the largest collection of infrared properties of **PAHs** and related molecules (*e.g.* nitrogen-substituted PANHs; [Hudgins et al., 2005](#)). The PAHdb library currently contains computed spectra of more than 4000 species and laboratory-measured spectra of 84 species (Version 3.20).

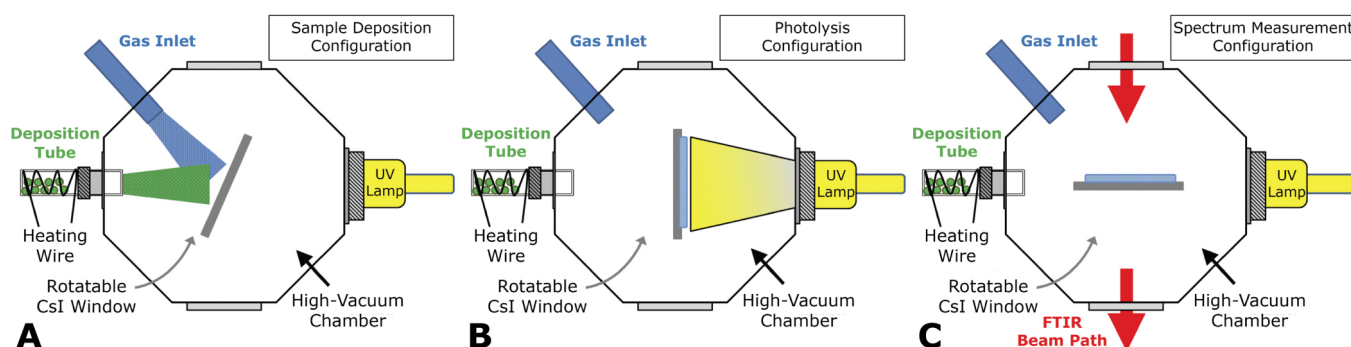


Figure 1.22 – Representation of the NASA Ames PAH experiment.

A typical setup for a matrix-isolation experiment: (A) sample deposition configuration, (B) UV photolysis configuration and (C) configuration for collecting the infrared spectrum. Figure taken from [Mattioda et al. \(2020\)](#).

1.6.2 Impact of PAH properties on MIR spectra

The relation between the strength of the different **UIBs** can be related to the chemical structure and to the physical conditions of their carriers. **MIR** spectra can thus be used as reliable diagnostics of the physical conditions and of the evolutionary stage of a galaxy or a region (*e.g.* Hony et al., 2001; Berné et al., 2007; Smith et al., 2007a; Galliano et al., 2008b; Mori et al., 2012; Croiset et al., 2016; Boersma et al., 2016). In what follows, we detail the different physical processes and their impact on **UIBs**.

1.6.2.1 Charge state and ionization

We have seen, in Sect. 1.3.2.2, that the bands associated with C-C modes (6.2 and 7.7 μm) are significantly brighter for ionized **PAHs**, whereas C-H modes (3.3, 8.6 and 11.3 μm) are dominated by neutral **PAH** emission. Laboratory data (Fig. 1.23. a) indeed show that the strength of the 6 – 9 μm C-C features increases when the **PAHs** are ionized. It is the opposite for C-H features, around 3 μm and in the 11 – 15 μm region, which are brighter when the **PAHs** are neutral. The intensity ratio of C-C to C-H features can thus provide a measure of the ionization fraction, as demonstrated by the modeled spectra in Fig. 1.11. b. Significant variations of the C-C/C-H strength ratios have been observed throughout the nearby Universe (*e.g.* Hony et al., 2001; Galliano et al., 2008b). These variations are primarily attributed to variations of the average **PAH** charge throughout different environments (Galliano et al., 2008b).

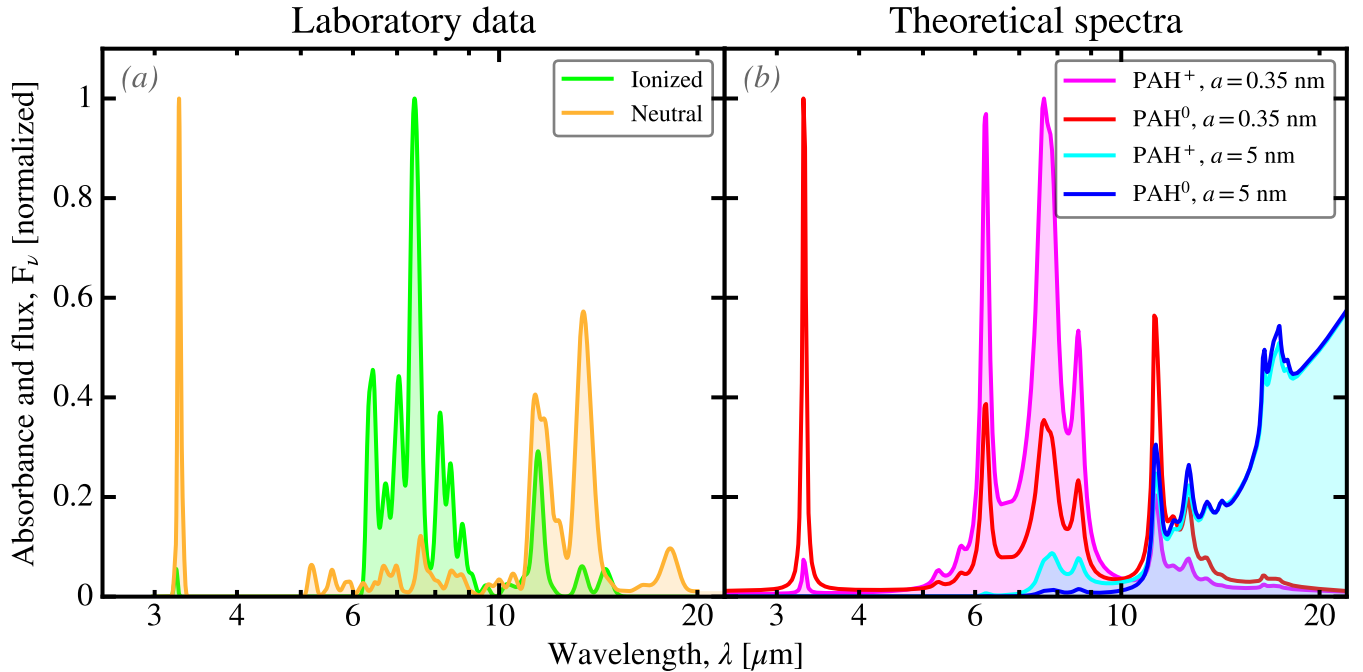


Figure 1.23 – Laboratory and modeled PAH spectra.

Panel (a) shows the laboratory measured absorption spectra for neutral (yellow) and ionized (green) **PAHs** of the same species (Allamandola et al., 1999). Panel (b) is a modeled spectrum of individual **PAH** anions (red & blue) and cations (magenta & cyan), with radii a . We have assumed the DL07 optical properties, stochastically heated by the Solar neighborhood **ISRF** ($U = 1$). Figure taken from G22.

The PAH charge state is quantified by the ionization fraction, f_+ , of the molecule distribution:

$$f_+ = \frac{PAH^+}{PAH^+ + PAH^0} . \quad (1.34)$$

The value of this parameter depends on the balance between ionization and recombination. This balance can be parametrized by the ionization parameter, $G_0 T^{0.5}/n_e$, where G_0 is the integral intensity of the ambient FUV radiation field (Hollenbach & Tielens, 1997), in units of the Habing field ($1.2 \times 10^{-4} \text{ erg cm}^{-2} \text{ s}^{-1} \text{ sr}^{-1}$), T is the gas temperature, and n_e is the electron density (Bakes & Tielens, 1994). Empirical and theoretical calibrations relating this ionization parameter to PAH band ratios have been proposed by Galliano et al. (2008b), Boersma et al. (2016) and Sidhu (2021), among others.

1.6.2.2 Size distribution

In addition to the charge, variations of the PAH size distribution can have drastic effects on the emitted spectrum, for two reasons. First, smaller PAHs will fluctuate up to higher temperatures than larger ones. These small PAHs will thus have more prominent emission in the short-wavelength features. Changing the size distribution will therefore affect the emission spectrum, even if we assume the same optical properties across sizes. This is demonstrated in Fig. 1.23. b. Second, the intrinsic spectra of small and large PAHs can be quite different. The PAH size can be expressed by the number of C atoms, N_C , hereafter. Small ($N_C < 50$) PAHs have rather diverse spectra (Hudgins & Allamandola, 1999a), whereas larger ones appear more uniform (e.g. Tielens, 2008, although this has been established mostly for symmetric and compact PAHs). The PAH size is thus another driver of aromatic feature variations, and it is always entangled with the ionization effects (Fig. 1.23. b). Fortunately, multiple ratios can be used to break the degeneracy (e.g. Draine & Li, 2007; Galliano et al., 2008b).

1.6.2.3 Molecular structure and hydrogenation

We have shown, in Fig. 1.14. f, several molecules from the PAH family. The fact is that, even for a given number of carbon atoms, there is a large diversity of PAH molecules. Astronomical observations do not allow us to identify the exact molecular structure of the PAHs¹⁶ because we see a mixture of them. The relative intensity of different features can however be used to characterize the structural properties of the PAHs, such as their compactness. The PAH compactness can be quantified by the number of peripheral H atoms per aromatic cycle (Fig. 1.15. b). This quantity can be traced by the solo-to-trio H intensity ratio, $I(11.3)/I(12.7)$. Studies of this ratio have suggested that large ($N_C \simeq 100 - 150$) compact PAHs are formed in winds of evolved stars and degraded into smaller, irregular molecules in the ISM (Hony et al., 2001). Knowledge of this property has primarily benefited from experimental and computational studies (e.g. Hudgins & Allamandola, 1999b; Bauschlicher et al., 2008).

At first order, dehydrogenation has a similar effect to ionization on the emission spectrum. In addition to $I(11.3)/I(12.7)$, other ratios between C-C and C-H mode bands, such as $I(6.2)/I(11.3)$, can also reflect the dehydrogenation of PAHs. However, for larger ($N_C \gtrsim 35$) PAHs, (re)hydrogenation through reactions with abundant atomic H is more important than H loss through

16. A few individual PAHs, with well-characterized features, have been detected. The most spectacular example is likely the fullerene (a football-shaped C_{60} ; Cami et al., 2010; Sellgren et al., 2010).

unimolecular dissociation. This argument was proven both theoretically (Le Page et al., 2003) and observationally (Hony et al., 2001). The hydrogenation balance depends on environmental conditions. For example, the aliphatic component at $3.4\ \mu\text{m}$, which is carried by super-hydrogenated PAHs, disappears rapidly towards PDR surfaces, where the radiation field becomes strong enough to dissociate C-H bonds (e.g. in the Orion Bar; Geballe et al., 1989; Joblin et al., 1996).

1.6.3 Evolution of PAH abundance as a function of physical conditions

PAHs can be observed through their absorption bands (e.g. Hensley & Draine, 2020), MIR emission bands (e.g. Galliano et al., 2021) or their rotational lines (e.g. McGuire et al., 2021). The abundance of interstellar C they contain, f_{C} , can be observationally measured by assuming an energy balance between the absorbed UV flux and their infrared thermal emission (Allamandola et al., 1989). Table 1.1 gives typical values of the abundance of different groups of PAHs in bright Galactic PDRs. From these values, we can estimate that $\sim 30\%$ of the interstellar C is locked up in PAHs containing fewer than 1000 C atoms.

Table 1.1 – Abundances of the carriers of infrared (IR) emission components. Typical values for the abundance of PAHs in bright PDRs. Table taken from Tielens (2008).

Carrier	IR emission component	N_{C} ^a	a (Å) ^b	f_{C} ^c (ppm) ^d
PAHs	IR emission features	20-100	4-10 ^e	14
PAH clusters	Plateaus	100-1000	10-20	8
Very small grains	25- μm cirrus	$10^3 - 10^4$	20-30	7
Small grains	60- μm cirrus	$\sim 10^5$	50	16
Classical grains	$\lambda > 100\ \mu\text{m}$		>100	35 ^{f?}
C chains ^g	IR emission	>3		< 0.3
C ₆₀ ^h	Far-red absorption bands			2

a. Number of C atoms.

b. Radius of the carrier in angstrom.

c. Abundance of C locked up in these species relative to H nuclei.

d. Parts per million.

e. Size corresponds to disk rather than sphere.

f. The abundance of C locked up in dust grains is uncertain.

g. Abundance of carbon chains estimated from upper limits on their IR emission. For comparison, the measured fraction of C locked up in carbon chains in dense clouds is 800 ppm.

h. Two far-red absorption bands have been attributed to C₆₀. Upper limits on IR emission bands due to this molecule are consistent with this estimate.

Another way to measure the total PAH abundance, that is often employed in SED modeling, is to estimate the PAH-to-total-dust mass fraction, q_{PAH} . This parameter was introduced by DL07 to study PAH evolution across environments. It requires the use of a dust model, such as that of DL07. At first order, q_{PAH} is proportional to the PAH luminosity over the total IR luminosity. The PAH mass can then be estimated using the dust mass, M_{dust} , derived from the SED fit: $M_{\text{PAH}} = q_{\text{PAH}} \times M_{\text{dust}}$ (e.g. Rémy-Ruyer et al., 2014; Galliano, 2018). The value of q_{PAH} in the diffuse ISM of the Milky Way varies between models. It is $\sim 4.6\%$ for the ZDA04 and DL07 models and $\sim 7.7\%$ for the DHGL model. This value strongly evolves across environments (e.g. Galliano et al., 2021). In what follows, we discuss the main parameters that impact it.

1.6.3.1 Going from diffuse to dense regions

The multiphase ISM harbors a wide range of gas densities and temperatures (Sect. 1.1.1), which impacts the PAH evolution in different ways, either destroying or forming new PAHs. For example, PAH species could form in dense molecular clouds and be photoprocessed in the diffuse ISM (Greenberg et al., 2000). In high gas density regions, PAHs are well shielded from UV photoprocessing but can become (super)hydrogenated (Le Page et al., 2003; Andrews et al., 2016). In interstellar shock waves, grain-grain collisions are believed to destroy PAHs (Jones et al., 1996). However, low-velocity shock waves could lead to the formation of PAHs (via shattering of large carbonaceous grains; Bocchio et al., 2014).

At the scale of interstellar clouds, PDRs are unique sites to study PAH evolution, as they are at the interface between H II regions and molecular clouds. They thus span a wide range of physical conditions. As shown in Fig. 1.24, the distance from the stars and the shielding of their radiation in molecular clouds determines the chemical structure of the PAHs. From the dense molecular cloud (right side) to the diffuse H II region (or cavity; left side), we see the PAH family evolves from VSGs and PAH clusters down to a mixture of neutral and positively charged PAHs (*cf.* the rise of the G7.8 and G8.2 components passing through the PDR front). Only the most stable, compact, highly symmetric and large ($N_C > 70$) PAH cations and fullerenes (C_{60} , C_{70}) survive in the region close to the star (*cf.* G7.6 and G8.6 components and the $11.0 \mu\text{m}$ band).

This trend has been well studied for a few PDRs (*e.g.* Berné et al., 2007; Andrews et al., 2015; Peeters et al., 2017) and will be scrutinized in more detail with the JWST (*e.g.* ERS program: “PDRs4All”; PI Team: Berné, Habart and Peeters; Berné et al., 2022).

1.6.3.2 Destruction by the hard radiation field

A hard radiation field is known to photodissociate and sublimate PAHs. This can be seen at the scale of H II regions, where OB star associations carve out the UIB emission (*e.g.* Cesarsky et al., 1996; Povich et al., 2007; Gordon et al., 2008; Galametz et al., 2016). This can also be witnessed at the scale of whole galaxies, such as dwarf galaxies (*e.g.* Madden, 2000; Madden et al., 2006; Rémy-Ruyer et al., 2015). Compared to normal galaxies, dwarf galaxies, are younger objects, they thus possess a larger number of O stars. In addition, low-metallicity O stars tend to produce a harder radiation, because of line-blanketing effects (Martins et al., 2002). Finally, the dust screening in these galaxies is lower, because of the overall dust paucity. Hard photons therefore travel on larger distances, destroying PAHs far away from OB associations. We will discuss this point more extensively in Sect. 1.6.3.3.

AGNs are another source of harsh and intense radiation fields. Pioneering ground-based observations (Roche et al., 1991) and subsequent ISO (Verma et al., 2005) and *Spitzer* data (Weedman et al., 2005) have demonstrated that the strength of the UIBs was significantly lower in the vicinity of an AGN, along with the high $[\text{Ne III}]/[\text{Ne II}]$ ratio, tracing the photon hardness (*cf.* Ionization Potential: $\text{IP}_{\text{Ne III}} = 41.0 \text{ eV}$, $\text{IP}_{\text{Ne II}} = 21.6 \text{ eV}$).

UIBs are ubiquitously associated with massive star-forming regions, because this is where UV heating is most efficient (*e.g.* Genzel et al., 1998). So, it is natural to trace the star formation activity with PAHs. For example, the $8 \mu\text{m}$ and $24 \mu\text{m}$

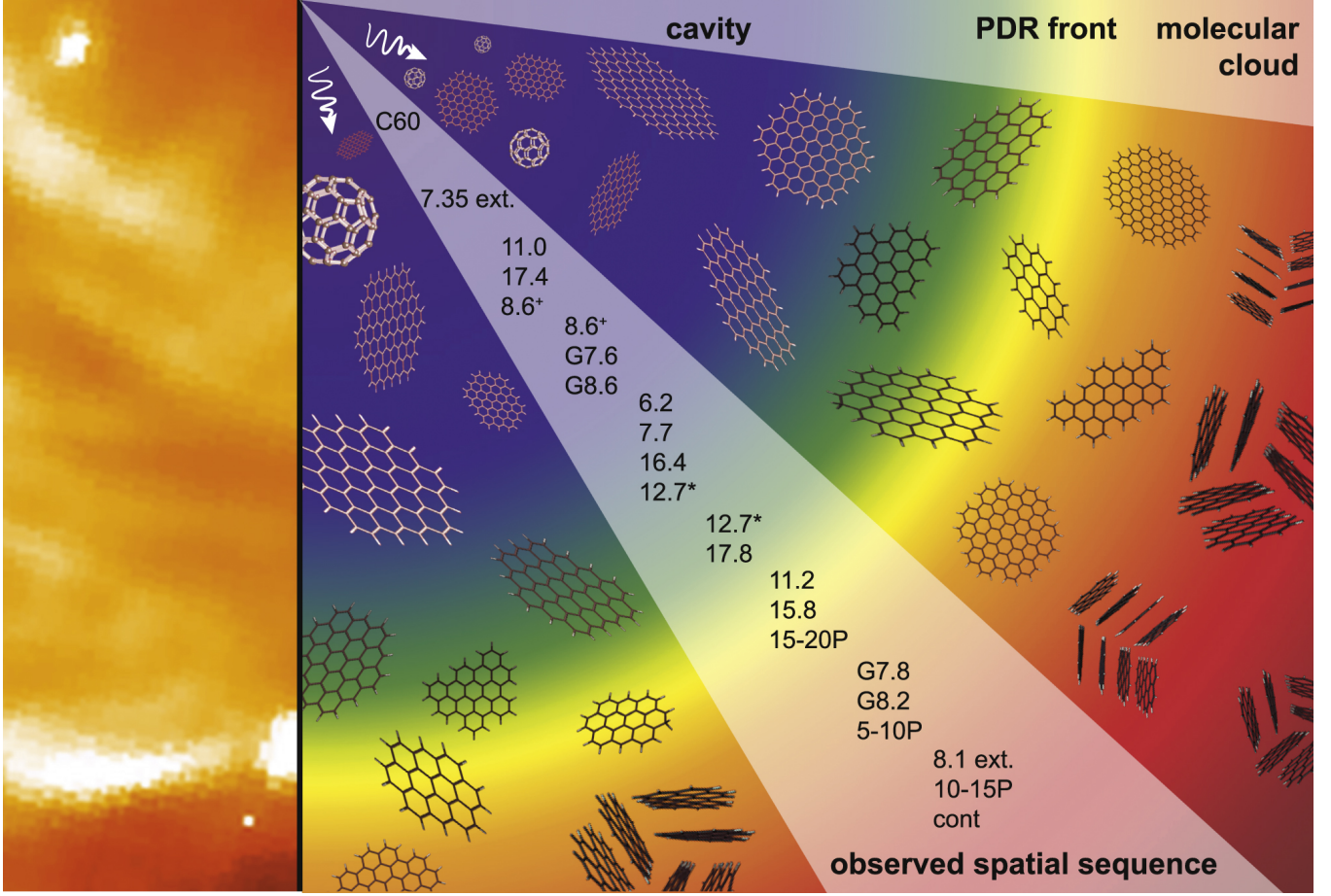


Figure 1.24 – Schematic representation of the evolution of interstellar PAH populations across a PDR. This figure represents the changes in the **PAH** population as we move away from the stars (left side), along the evaporative flows associated with the **PDR** until entering the molecular cloud (right side), in NGC 2023. The spatial sequence of the observed **MIR** feature intensities and continuum emission is overlaid. Annotations: (i) G corresponds to features fitted with a Gaussian; (ii) P indicates the plateau emission; (iii) ext. denotes the two extremes of the 7 – 9 μm region; (iv) cont refers to the continuum component, mainly attributed to **VSGs**; (v) * indicates that *Spitzer* low and high resolution spectroscopic data indicate slightly different morphologies; (vi) + indicates that the group depends on the way the continuum is modeled. Figure taken from [Peeters et al. \(2017\)](#).

broadbands have been calibrated with the $\text{Pa}\alpha$ (1.8756 μm) **SFR** indicator by [Calzetti et al. \(2007\)](#). For the same purpose, [Peeters et al. \(2004a\)](#) showed that the 6.2 μm band intensity correlates well with **SFR**, making it a reliable estimator. They also claimed this correlation has the same origin as the **TIR-SFR** correlation ([Galametz et al., 2013](#)) since the **UIB** strength is correlated with **TIR**, at first order.

However, the destruction of **PAHs** by the hard **ISRF** has challenged the role of the aromatic features as **SFR** indicators. For example, [Förster Schreiber et al. \(2004\)](#) calibrated the luminosity of the **PAH**-dominated 5 – 8.5 μm broadband as a **SFR** proxy using ISO-CAM photometric and spectroscopic data of their spiral and starburst galaxy sample. They confirmed the relationship between the aromatic emission and the **SFR** up to a level approaching that of M 82. They also studied the **VSGs**, probing the 15 μm monochromatic continuum (using a width $\Delta\lambda=0.4 \mu\text{m}$), because it traces the **SFR** in even more active regions

where PAH bands are generally weak or absent due to their suppression by high radiation field intensities. The limitation of the MIR SFR estimators induced by the ISRF hardness effect is crucial to understand luminous galaxies observed at higher redshift.

1.6.3.3 Variation across galaxies with different metallicities

Low-metallicity galaxies have weak (*e.g.* NGC 1569; Fig. 1.11) or undetected (*e.g.* I Zw 18 with $Z \approx 1/50 Z_{\odot}$; Izotov et al., 1999) aromatic features, even when integrating their spectrum over the whole galaxy. The striking non-linear drop of q_{PAH} in metal-poor environments was first demonstrated in the trend between Z and the PAH strength, with broadband photometry (Engelbracht et al., 2005) and spectroscopic observations (Madden et al., 2006). Possible explanations of this PAH paucity at low-metallicity are (i) the enhanced PAH destruction and (ii) reduced PAH formation at low Z . The first scenario suggests that the PAH destruction efficiency is enhanced by the increased hard photon flux from young stars (Galliano et al., 2003, 2005) and the lower dust opacity (Madden et al., 2020) in low-metallicity environments. Additional PAH destruction mechanisms such as SN shocks (O’Halloran et al., 2006) are debated. In the second scenario, a deficit of PAH production could occur at low-metallicity. Assuming the carbon ejected by AGB stars makes up most PAH mass, the delayed injection of this element by these long-lived stars provides a natural explanation to the trend (Galliano et al., 2008a). Alternatively, assuming PAHs form in dense molecular clouds, the reduced filling factor of molecular clouds at low-metallicity would impact their production (Sandstrom et al., 2010). Lastly, the shattering of carbonaceous dust grains has been proposed as a PAH formation mechanism, and it is enhanced at low-metallicity (Seok et al., 2014; Rau et al., 2019). Neither suppressed formation nor enhanced destruction alone succeed in reproducing the global PAH abundance trend (*e.g.* Wu et al., 2006; Galliano et al., 2021).

Finally, the interpretation of the $q_{\text{PAH}}-Z$ trend might be hampered by several observational biases, including: (i) sample selection effect and (ii) discrepancies between different size scales. Most galaxies that can be observed at infrared wavelengths are indeed Solar metallicity objects or actively star-forming low-metallicity objects (starbursts or post-starbursts). For that reason, there is a degeneracy between the effects of star formation activity and metallicity (*e.g.* Galliano et al., 2018). The only way to solve this degeneracy would be to observe quiescent low-metallicity galaxies, but these are currently beyond the sensitivity reach of infrared observatories. In terms of spatial scales, we have seen that, globally, PAHs are very weak in low-metallicity systems, but can be found to be prominent in particular regions of these objects. At Solar metallicities, MIR features are also dominated by the continuum of H II regions (*e.g.* Peeters et al., 2002a; Martín-Hernández et al., 2002), but not on global scales. The metallicity trend obviously breaks down at small scales, as there are important variations within galaxies, at a relatively constant metallicity, such as in the LMC ($Z \approx 1/2 Z_{\odot}$; Paradis et al., 2009; Meixner et al., 2010) and SMC ($Z \approx 1/6 Z_{\odot}$; Sandstrom et al., 2010, 2012), where different physical conditions can be resolved.

Chapter 2

Observing with AKARI and *Spitzer*

The craftsman who wants to do his work well must first sharpen his tools.

Analects 15.10

My thesis project relies on the precise analysis of **MIR** spectral maps of nearby galaxies. The quality of this analysis directly depends on the data quality and the assessment of data uncertainties and biases. I have consequently spent a large part of my time reducing and fine-tuning the AKARI/IRC and *Spitzer*/IRS spectroscopic observations of my nearby galaxy sample (**Sect. 2.1.1**). These data jointly provide comparable spectral information at the wavelengths ranging from 2.5-40 μm , and they are of the best resolution, sensitivity, and coverage before the dawn of the JWST era.

To learn the complexity of AKARI/IRC data reduction, I have collaborated with Dr. Takashi ONAKA, from the University of Tokyo, whom I visited for three weeks in December 2019. Concerning *Spitzer*/IRS data, I worked with our local expert, Dr. Vianney LEBOUTELLER. I have produced all the results presented in this chapter. I have written my own Python library that calls some of the routines of the instrument's pipeline and performs additional processing. In this chapter, I present, in particular, several tests assessing the various sources of uncertainties to deliver consistently combined **MIR** spectra. The case study of the nearby galaxy M 82 is detailed, and its outputs are shown at the end of this chapter.

2.1 AKARI

AKARI¹ was an infrared astronomical mission dedicated to an all-sky survey at infrared wavelengths. The AKARI satellite was launched on February 22, 2006, and terminated on November 24, 2011, including a cryogenic period of more than 400 days (phases-1 & 2). The satellite orbited around the Earth on a Sun-synchronous polar. The *Far-Infrared Surveyor* (FIS; [Kawada et al., 2007](#)) and the *InfraRed Camera* (IRC; [Onaka et al., 2007](#)) were the two focal plane instruments onboard AKARI.

2.1.1 InfraRed Camera (IRC)

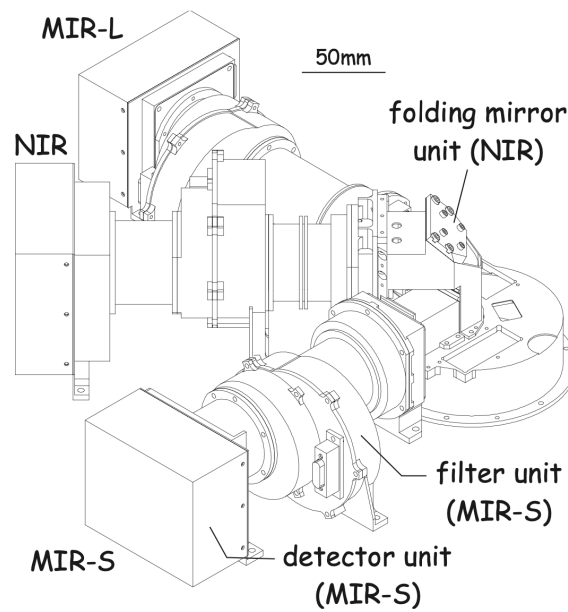


Figure 2.1 – Bird's-eye view of the IRC.

The detector unit, filter unit and folding mirror unit are indicated (see text). Figure taken from [Onaka et al. \(2007\)](#).

2.1.1.1 Instrumentation and observation

With a field coverage of $10' \times 10'$, the IRC was initially designed to make wide-field deep imaging and low-resolution spectroscopic observations in the *pointing mode*.

The IRC consists of three independent camera systems (or *channels*; [Fig. 2.1](#)):

- The Near-InfraRed (NIR) channel operates in the $2\text{--}5\ \mu\text{m}$ range;
- The Mid-InfraRed short (MIR-S) channel covers the $5\text{--}12\ \mu\text{m}$ range;
- The Mid-InfraRed long (MIR-L) channel works in the $12\text{--}26\ \mu\text{m}$ range.

1. Previously known as InfraRed Imaging Surveyor (IRIS) or ASTRO-F.

The NIR and MIR-S share the same field-of-view from the beam splitter, whereas the MIR-L's field-of-view is about 25' away from the NIR/MIR-S sky (Fig. 2.2).

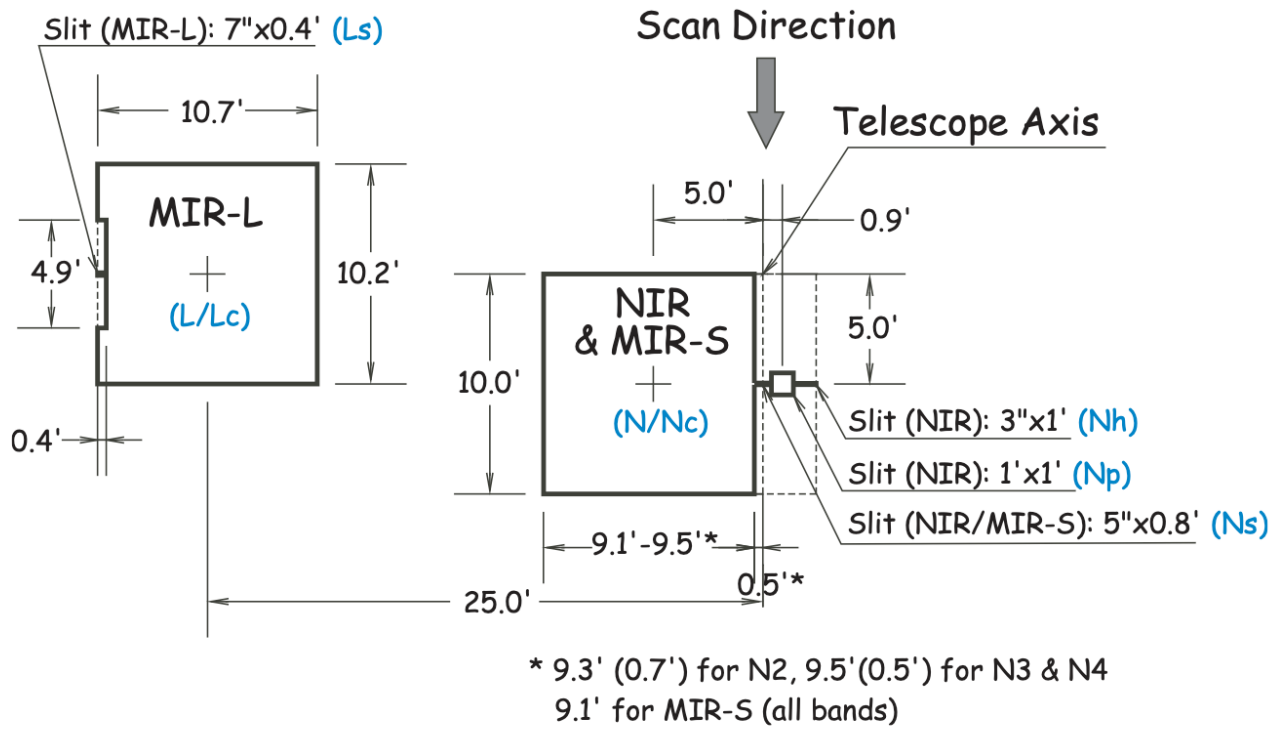


Figure 2.2 – Relative field-of-view location and size of the three channels of AKARI/IRC. The vertical arrow indicates the scan direction in the survey mode. The NIR and MIR-S channels share the same field-of-view with the help of a beam splitter. The notations of imaging and slit areas (explained in Sect. 2.1.1.2) are highlighted in blue. Figure taken from the IRC Data User Manual.

In this thesis, we have mainly used the NIR channel because it complements *Spitzer*/IRS's spectral coverage (Sect. 2.2.1.1). We list the characteristics of its available bands in Table 2.1.

Table 2.1 – IRC module characteristics.

Table extracted from the Table 1 of Onaka et al. (2007).

Mode	Disperser Element	Plate Scale ("pixel ⁻¹)	Wavelength Range (μm)	λ_{ref}^a (μm)	$\Delta\lambda^b$ (μm)	Dispersion Power (μm pixel ⁻¹)
N2	filter	1.46 ^c	1.9-2.8	2.4	0.71	-
N3	filter	1.46	2.7-3.8	3.2	0.87	-
N4	filter	1.46	3.6-5.3	4.1	1.53	-
NP	prism	1.46	1.8-5.5	-	-	0.06 (at 3.5 μm) ^d
NG	grism	1.46	2.5-5.0	-	-	0.097

a. Reference wavelength.

b. Effective bandwidth.

c. The scan direction as depicted in Fig. 2.2 is slightly narrower, that is 1.446×1.458 according to the Version 2.2 (July 6, 2016) of "IRC Data User Manual".

d. The dispersion power of NP depends on the wavelength because the dispersion equation for the prism spectra is highly non-linear at shorter wavelength end.

2.1.1.2 Data mining

The AKARI mission lifetime has been divided into two *performance verification* (PV) phases and three *observation phases*. The PV1-phase data is taken before the beginning of the phase-1 observations. The phase-1 observations are dedicated to the Large-Area-Survey Programs, and most of the Open Time observations are carried out during phase-2 of the mission. Between the end of the cold mission and the beginning of the warm mission, several PV2-phase observations are performed. Observations carried out during the post-helium phase of the mission are recorded as phase-3 observations. The PV1-phase and PV2-phase data are not publicly available since they concern instrumental calibration. It is only accessible through private communication with the AKARI team.

The *observing modes* used by the IRC have been standardized in several **Astronomical Observation Templates (AOTs)**². During the phase-2 observation, these **AOTs** include a one-filter mode (the originally planned IRC00 and the in-orbit used IRC05), a two-filter mode (IRC02), a three-filter mode (IRC03), a spectroscopic mode (IRC04), and a slow-scan mode (IRC11 and IRC51; only used for the MIR imaging mode).

We have used three IRC **AOTs** for general-purpose spectroscopic observations available in the NIR channel. The IRC04 was exclusively operated during the cold phase mission (phase-2) without dithering. This **AOT** includes one imaging observation sandwiched by two four-frames spectroscopic observations. The designation of IRC spectroscopic **AOT** was modified during PV2-phase and phase-3 by adding five dark frames before and after the former observation sequence³. The IRC04 **AOT** was thus renamed as IRC64 and IRCZ4, respectively. Both IRC04 and IRCZ4 data are publicly available on AKARI data archive, whereas IRC64 data are provided by Dr. Takashi ONAKA.

As shown in Fig. 2.2, the NIR frame is divided into two parts corresponding to slit and slitless spectroscopies. The NIR focal plane arrays are shared by three band filters, two dispersive elements, and a blank window acting as a shutter on the filter wheel. Spectroscopic mode **AOT** parameters are noted as “x;Yz”, where “Y” is “N” for the NIR and MIR-S channels, and “L” for the MIR-L channel. The letters “x” and “z” can be:

- “x”=[a-c] records the disperser used during the observation, with a for prism (NP), b for grism (grating-prism compound; NG), and c for both grism and prism dispersers.
- “z”=[s/h/p/c] records which slit is on target. For slit observations, it can be (i) Ns, for wider slits, (ii) Nh, for narrower slits, or (iii) Np, for 1' × 1' short slit area (spectroscopy of point sources). Nc indicates slitless observations, where “c” means the center of the detector array.

For example, a slit-spectroscopic observation carried out in the Nh slit with the grism disperser is logged as “b;Nh”.

2. For an IRC pointed observation, an **AOT** is defined as a specific pattern of the configuration of the filter wheel rotation operations and frame dithering operations.

3. There might be a fifth frame at the end taken during the satellite maneuver. This maneuver corresponds to an extra observation time which is not guaranteed. This last exposure should be discarded.

In this thesis, we have used N_s and N_p slits, with both NP and NG dispersers that have different spectral resolutions but similar wavelength coverages. In particular, the grism used in the NG mode is a versatile dispersion element with vast space astronomical applications. Its advantages include: (i) a smaller size of the optical system than a reflection grating, allowing other optical elements to be placed close to the grism; (ii) the flexibility to switch between imaging/spectroscopic modes (filter/grism); and (iii) a higher dispersion capability than a prism (e.g. Ebizuka et al., 2004).

The reference image taken with the $N3$ filter is used to correct the pointing information of slit spectroscopy⁴. Note that the IRC slit-spectroscopy with N_h and N_s slits is primarily designed for extended sources. The absolute pointing accuracy of AKARI is comparable to the width of the narrow slit (Sect. 2.1.2.4), except for the N_p slit, which has a much larger aperture.

The IRC spectroscopy is only available for individual pointings and not for the *survey mode*⁵. *A priori*, there is no spectral map available. However, it is possible to sample extended sources with multiple pointings.

2.1.2 IRC data processing

IRC slit spectroscopy can be performed only for pointed observations. Consequently, the observations of extended sources consist of a few separate narrow slits. We have extracted the raw 2D spectral records, using the *IRC Spectroscopy Toolkits (Version 20181203)* for phase-1 and 2 data, and the *IRC Spectroscopy Toolkit for Phase 3 data (Version 20181203)* for phase-3 data (Baba et al., 2019, hereafter the IRC pipeline). The official IRC pipeline performs dark subtraction, linearity correction, saturation masking, flat-fielding, background subtraction, second-order contamination correction, image registration, image stacking, wavelength calibration, and 2D spectrum extraction (IRC Data User Manual).

2.1.2.1 Propagation of the uncertainties

Before entering the heart of the data-processing sections, we present how we treat our uncertainties. We have implemented a *boot-strapping* method. This process is performed at almost every step of the data processing for both AKARI/IRC and Spitzer/IRS.

Any measure is tainted with uncertainties. In practice, a measured quantity, y_{meas} , will always differ from its true value, y_{true} , by a quantity, $\epsilon = y_{\text{true}} - y_{\text{meas}}$, the error. It is important to differentiate errors and uncertainties. *Errors* are the random deviations from the true value. *Uncertainties* are the statistical distribution of these errors. When the errors can be assumed to follow a *normal-law* (Sect. B.1.1), which we will see is not always the case, and we can simply represent the uncertainties by their standard deviation. We can separate the errors into different types.

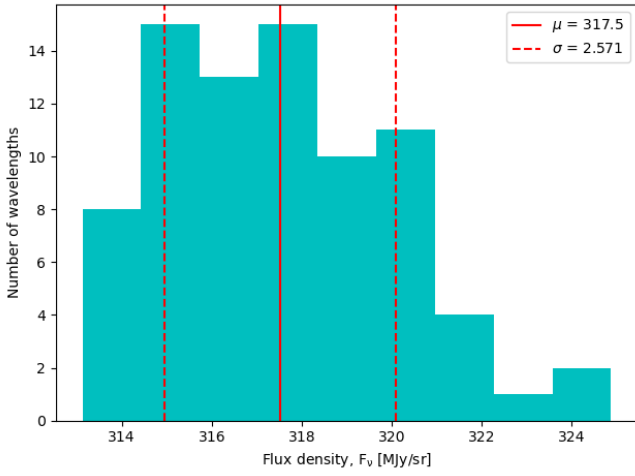
- *Statistical errors* are errors that can be assumed independent or only partially correlated. Consequently, when repeating the same measure several times, these random errors will average out, and the resulting uncertainty will be smaller.

4. The filters $N2$, $N3$, $N4$ correspond to the standard K, L, and M photometric bands, respectively. $N3$ images taken in spectroscopic AOTs are also used to determine the wavelength zero reference point for slitless spectroscopy. As for slit-spectroscopy, a wavelength zero reference point is pre-defined by the slit position.

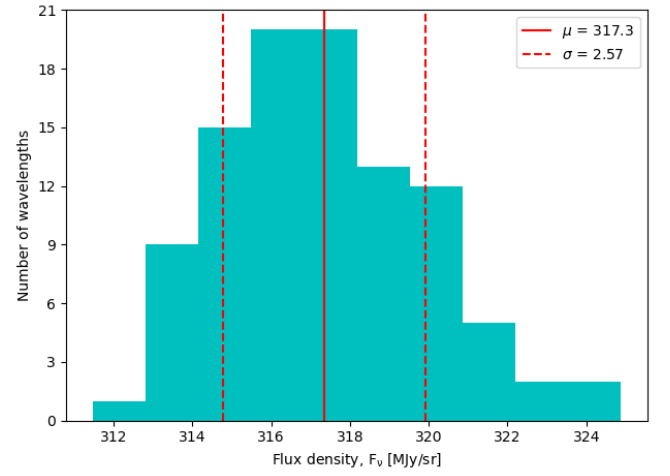
5. AKARI/IRC is also equipped with the capability for the mid-infrared all-sky survey, i.e. the survey mode.

- *Systematic* errors are correlated, during the whole experiment or observation campaign. Consequently, these errors are the same for all measurements, and their uncertainty does not diminish if we repeat several times the same experiment. The treatment of systematic errors is not trivial. We will discuss specific cases such as *calibration* error (Sect. 2.2.2.2) and telescope *pointing* error (Sect. 2.1.2.4).

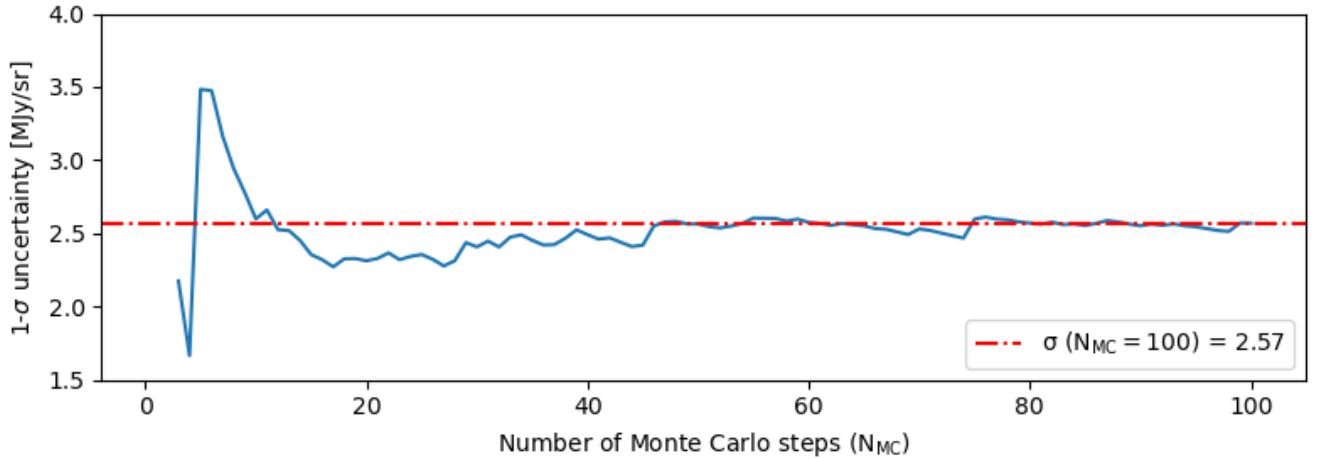
A given measure is often tainted by several sources of uncertainty. These uncertainties can be combined to provide an estimate of the total uncertainty. Fully independent uncertainties must be summed quadratically, whereas fully correlated uncertainties have to be summed linearly.



(a) $N_{MC} = 80$.



(b) $N_{MC} = 100$.



(c) Effect of sample size

Figure 2.3 – Demonstration of the *bootstrapping* method to propagate the uncertainties. Panels (a) & (b) show the flux density distribution of a *Spitzer*/IRS pixel within the M 82 spectral map at $\lambda = 7.29 \mu\text{m}$, with the number of Monte Carlo steps $N_{MC} = 80$ and $N_{MC} = 100$, respectively. Panel (c) shows the standard deviation of the above distribution as a function of N_{MC} , where the $1-\sigma$ uncertainty for $N_{MC} = 100$ is marked with a red dash-dotted line.

It is key to understand how the original uncertainties propagate through the different steps of the data processing we perform. In particular, convolution and astrometric reprojection create correlations between pixels. Yet, it is highly complicated to account for this propagation analytically. Fortunately, it can be evaluated numerically with a Monte Carlo *bootstrapping* method. This method consists in perturbing our data with a series of random variables distributed according to their uncertainties. For instance, if we have the flux density, $F_\nu(x, y)$, in different pixels, (x, y) , of an image, with uncertainties, $\sigma_\nu(x, y)$, we generate N_{MC} images with flux $F_\nu^{MC}(x, y, i) = F_\nu(x, y) + \delta(x, y, i) \times \sigma_\nu(x, y)$, for $i = 1, \dots, N_{MC}$, where $\delta(x, y, i)$ are normal random variables with mean 0 and standard deviation 1. We then perform data processing on these N_{MC} images. In the end, we obtain N_{MC} processed images. The distribution of the flux density of each pixel is an approximation of the uncertainty of this pixel. We can thus take its standard deviation, but also compute correlation coefficients, quantify its skewness, *etc.*

We have compared different numbers of Monte Carlo iterations. This is shown in Fig. 2.3. Panel (c) shows that beyond $N_{MC} = 80$ the estimated uncertainty does not fluctuate significantly. Using a value of $N_{MC} = 100$ seems thus sufficient. We emphasize that this *bootstrapping* procedure does not affect the central value of the flux density; it is just a means to estimate the uncertainties.

2.1.2.2 Spectral cube assembly

We have projected the 2D spectra extracted from the IRC pipeline (Fig. 2.4) on the celestial grid with the proper *right ascension* (R.A.) and *declination* (Dec.)⁶, and resulted in 3D spectral cubes with two spatial dimensions and one spectral dimension. The different steps performed by the IRC pipeline result in an asymmetric statistical uncertainty on the spectrum. We have thus propagated these errors, using our *bootstrapping* method described in Sect. 2.1.2.1, assuming a split-normal distribution (Sect. B.1.1).

In terms of building IRC spectral cubes, we have made the following choices, within the IRC pipeline, and the MIRAGE software⁷ developed during this thesis (Hu et al., 2022a, hereafter Paper I).

Dispersion direction. In the *dispersion direction* (*i.e.* the telescope scan direction), we have applied a boxcar kernel of equivalent width $\sim 0.0291 \mu\text{m}$ to smooth the spectral sampling to the actual resolution of the instrument. Indeed, the **Full Width at Half-Maximum** (FWHM) of this kernel applied to focal plane array pixels is $2.9 \times 1.46''$. This size corresponds to the in-orbit **Point Spread Function** (PSF; Sect. 2.1.2.3 and Sect. 2.2.2.3) of the *N3* frame since IRC slits share the same focal plane detector array. Given the dispersion power of the *NG* mode ($0.0097 \mu\text{m pixel}^{-1}$; Table 2.1), we obtain the spectral FWHM of $0.0291 \mu\text{m}$ by spatially smoothing the focal plane pixels by a factor of 3. This value is controlled by the parameter “*smooth*” in the IRC pipeline (*cf.* Fig. 2.4. a & b). Smoothing results in a spectral resolution loss, down to $R \equiv \lambda/\Delta\lambda \simeq 3.5/0.0291 = 120$ (at $3.5 \mu\text{m}$) for the *NG* mode. There might be a slight shift/offset in spectral sampling between the IRC pipeline outputs for *Ns* and *Nh*, depending on the wavelength calibration/zero-point. In this case, we interpolate the *Ns* spectra on the *Nh* wavelength grid. Otherwise, both slits share the same spectral grids. In our specific

6. We have adopted the *equatorial coordinate system*, the same as the astronomical coordinate system used by both *Spitzer* and AKARI observations.

7. MIRAGE: Mid-InfraRed spectra cube Assembly enGinE (open access on <https://github.com/kxxdhdn/MISSILE/tree/main/MIRAGE>). The workflow of MIRAGE is illustrated in Fig. 2.17.

study, we have truncated IRC spectra from above $4.25\ \mu\text{m}$ since longer wavelengths are usually noisy and do not contain any feature we are interested in.

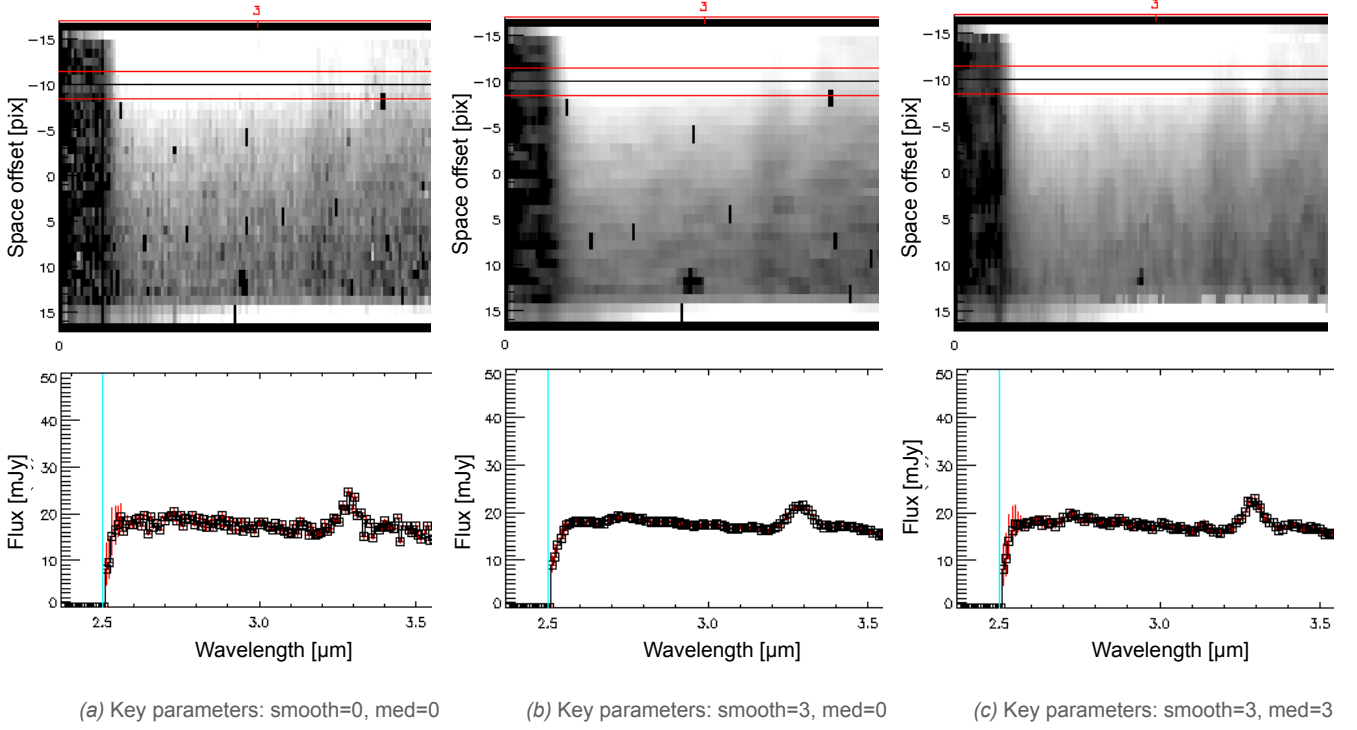


Figure 2.4 – Demonstration of the functions of the IRC pipeline parameters on IRC spectra.

At the top of each panel is the spectrum extracted directly from IRC focal plane arrays (Ns slit area). At the bottom of each panel is the corresponding line spectrum integrated between the red lines (controlled by the parameters “*nsum*” and “*space_shi*” in the IRC pipeline; in this example, *nsum*=3, *space_shi*=-10). Panel (a) is the free result, with *smooth*=0 and *med*=0. Panel (b) applies a boxcar kernel of 3-pixel width to smooth the dispersion (*smooth*=3). Panel (c) further applies a simple median averaging to neighboring 3 pixels in the cross-dispersion direction (*med*=3). Figure extracted from the IRC pipeline during data processing.

Cross-dispersion direction In the *cross-dispersion direction*, we have first median averaged the aperture with the in-orbit **PSF FWHM** of the N3 frame (3 pixels, using the parameter “*med*” in the IRC pipeline). We have extracted the spectra between the red lines shown in Fig. 2.4. c at the top. Within the IRC pipeline, the aperture width applied for spectrum extraction is adjusted by the parameter “*nsum*”, and their position is determined by the parameter “*space_shi*”.

Then, we have projected the IRC slits on their footprints on the focal plane arrays. The slit center coordinates are given by the IRC pipeline. However, we have adopted a pixel scale of $1''$ instead of keeping the detector array pixel size ($1.45''$; Table 2.1) to fit best the actual slit widths: $5''$ for Ns and $3''$ for Nh. In the end, we obtain 5-pixel wide Ns slits and 3-pixel wide Nh slits, making our spectral cubes. The aperture lengths of Ns and Nh slits have been cropped to 24 or 28 detector array pixels ($36''$ and $42''$, respectively) relative to the slit centers.

2.1.2.3 Point spread function (PSF)

As its name implies, a **Point Spread Function (PSF)** describes the response of an imaging system to a point source. The [IRC Data User Manual](#) gives a **PSF** of 4.2'' **FWHM** for all the IRC NIR filters (2.9 pixels of size 1.46'' on detector arrays; [Table 2.1](#)), whereas the NIR **PSF** for spectroscopic modes is poorly studied. We only know that (i) the N_s slit width (5'') is chosen to match typical imaging **PSF** sizes for the NIR channel in order to minimize flux loss outside the slit and maximize the spectral resolution ([Ohyama et al., 2007](#)); (ii) the **FWHM** of AKARI's **PSF**, in spectroscopic modes, is worse by one to three seconds of arc than that of the imaging mode ([IRC Data User Manual](#)); and (iii) the AKARI **PSF** is not spherical for the MIR **PSF** ([Arimatsu et al., 2011](#)), or even more elongated for the NIR channel (*e.g.* [Egusa et al., 2016](#)).

Consequently, we have adopted a reference **PSF** with a Gaussian profile and 6'' **FWHM** ([Table 2.4](#)). In addition, we have assumed a spectrally constant NIR **PSF** because the NIR broadband **PSF** does not vary significantly as a function of wavelength (*e.g.* [Egusa et al., 2016](#)).

2.1.2.4 Astrometry of the IRC slits

The determination of the astrometric position and orientation of the NIR narrow slits (N_s ; N_h) is performed using nearby point sources. This function is turned off by default in the IRC pipeline because it requires external software to access reference catalogs ([IRC Data User Manual](#)). In this work, we have used the 2MASS catalog within SAOImageDS9⁸. More precisely, we follow [Ohyama et al. \(2007\)](#) to determine the slit coordinates by using the **World Coordinate System (WCS)** of the reference images (N_3 frames for NIR channel) matched with the 2MASS all-sky catalog of point sources. This step is done using the “*IRC Imaging Toolkit*” ([Egusa & AKARI/IRC Team, 2017](#)).

The reference point of the wavelength scale also needs to be estimated. For that purpose, we use the IRC pipeline to perform a *cross-correlation image matching technique*. Once we have determined the exact slit position (zero-point) on the focal plane array, we can attribute wavelengths relative to this point as well as the N_3 image coordinates at this exact point.

Despite carefully performing the procedures described previously, the spectroscopic observations are still affected by angular drifts between the acquisitions of reference image frames due to the satellite altitude instability. The absolute pointing accuracy of the telescope is $\sim 3''$ ([Onaka et al., 2007](#)), as large as the slit width. Consequently, we have propagated this uncertainty throughout the remaining data-processing steps ([Sect. 2.1.2.1](#)). We have randomly drifted the slit assuming the pointing error was a $1-\sigma$ estimate⁹ and have recalculated the surface brightness within the assumed position of the slit. In this way, we have converted astrometric uncertainties to flux density uncertainties (an example is given in [Fig. 2.12. a](#)). The pointing uncertainties are thus a contribution to the total statistical uncertainties. They are not a systematic effect.

8. There are alternative infrared catalogs (*e.g.* WISE) embedded in other software (*e.g.* Aladin).

9. For diffuse sources in narrow slits, such as our observations of M 82, the IRC pipeline does not take into account the satellite attitude instability. However, in our case, it has a substantial effect when coadding AKARI slits with other spectral maps.

Note that coadding all the slits, having different orientations, projected on a common image grid will modify their projected shape because a given pixel will be projected across several pixels of the final grid. Moreover, as for slits with multiple pointings, there is a misalignment due to their astrometry discrepancies. Therefore, we have separately treated each IRC slit during data processing and analysis. We only have coadded them to show the spatial variation of the extracted spectral properties.

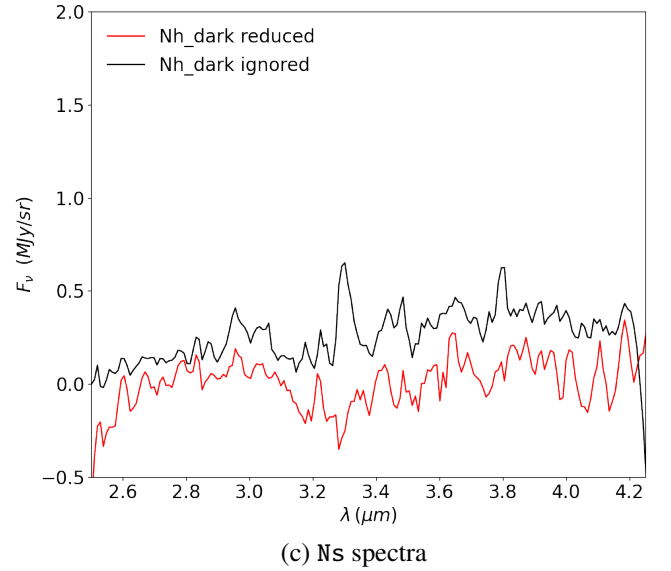
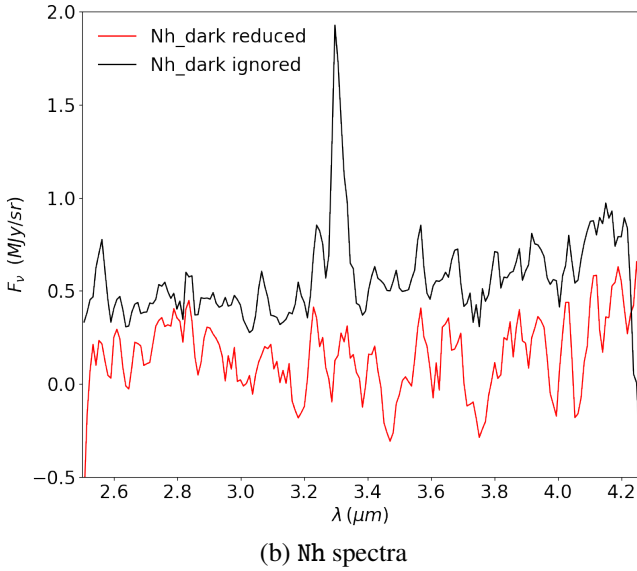
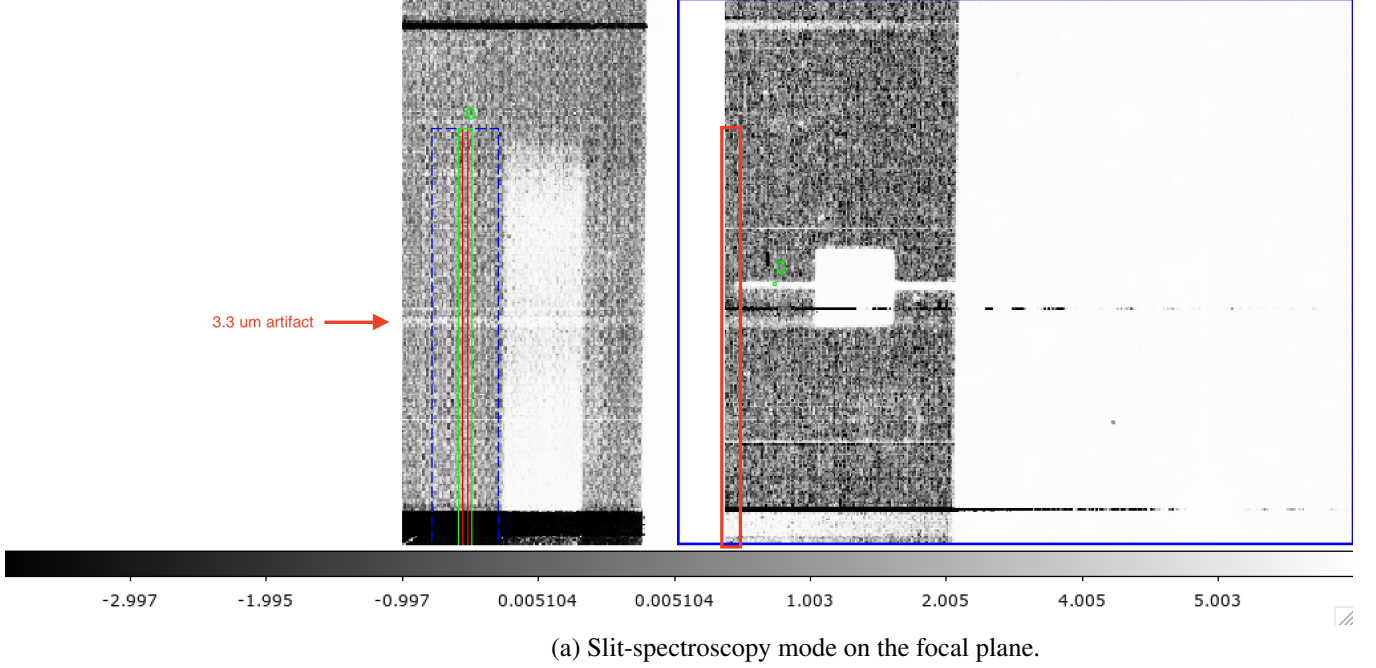


Figure 2.5 – Artifacts around $3.3 \mu\text{m}$ in the IRC spectra.

Panel (a) shows the locations of a bright stripe at $\approx 3.3 \mu\text{m}$ (horizontal) and the “*Nh dark*” zone (vertical red rectangle) on the focal plane. Panel (b) shows the corresponding artifact in the Nh spectra if the “*Nh dark*” is not corrected. Panel (c) shows the Ns counterpart.

2.1.2.5 Artifacts in IRC spectra

We have noticed several artifacts in some spectra. For example, a sharp feature around $3.3\ \mu\text{m}$, sharper than the aromatic band at $3.3\text{-}\mu\text{m}$ is seen in both Nh and Ns slits (Fig. 2.5). It corresponds to a bright stripe across the slit area on the focal plane array. To remove this artifact, we extract a 2D spectrum made of the median values in the 10-pixel wide masked area at the very edge of the Nh slit (red rectangle in Fig. 2.5), namely the “Nh dark”¹⁰ (a technique recommended by Dr. Takashi ONAKA; private communication). We have found that subtracting this median value efficiently corrects the artifact caused by the remaining dark current after the standard IRC pipeline. Indeed, if the signal-to-noise ratio (hereafter S/N ratio) of “Nh dark” is lower than the superdark treated in the IRC pipeline, “Nh dark” can improve the spectra since it also corrects hot pixels. This is especially the case for the NIR channel.

2.2 Spitzer

The *Spitzer Space Telescope*¹¹ was an infrared observatory in the Earth-trailing Solar orbit. It was the successor to the IRAS and ISO missions. The *InfraRed Spectrograph* (IRS; Houck et al., 2004a) was one of the three focal plane instruments onboard. It provided sensitive low- ($R \sim 60 - 130$) and moderate-resolution ($R \sim 600$) spectroscopy in the MIR ($5.2 - 38\ \mu\text{m}$). The other two instruments are the *InfraRed Array Camera* (IRAC; Fazio et al., 2004) and the *Multiband Imaging Photometer for Spitzer* (MIPS; Rieke et al., 2004).

2.2.1 The InfraRed Spectrograph (IRS)

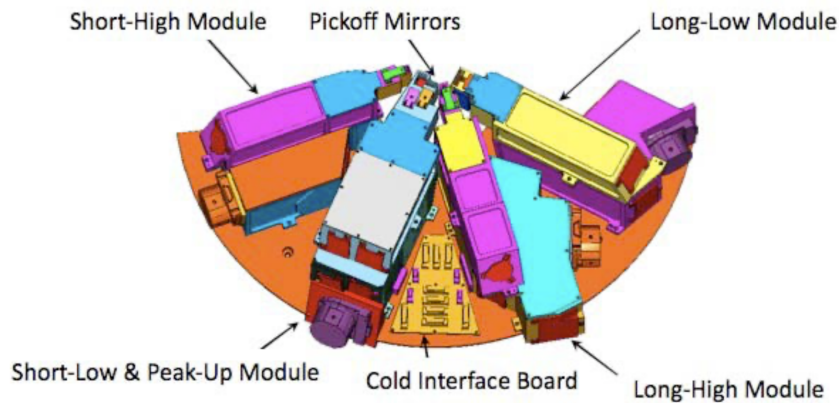


Figure 2.6 – The IRS cold assembly.

The relative location of the four IRS modules is depicted, including the Short-High (SH), Short-Low (SL), Long-High (LH), and Long-Low (LL). The SL module also includes two Peak-Up (PU) filters. Figure taken from the [IRS Instrument Handbook](#).

10. The “Nh dark” is distinct from the superdark corrected for by the standard IRC pipeline. The superdark, which is the usual dark current, has been determined from pre-dark measurement of [Large Magellanic Cloud \(LMC\)](#) observations, which have extensively been done at the beginning of Phase 1.

11. Launch date: August 25, 2003; cryogenic mission: December 1, 2003 - May 15, 2009; final voyage: January 30, 2020.

2.2.1.1 Instrumentation and observation

The IRS had four separated *modules*, corresponding to four *slits* (SH¹², SL, LH, LL) as well as two Peak-Up (PU) arrays for pointing and imaging.

As shown in Table 2.2, the four *channels* correspond to four IRS detectors (ch0-SL/PU, ch1-SH, ch2-LL, ch3-LH), which cannot observe at the same time. The low-resolution modules employ “*long-slit designs*” with two *sub-slits* (also called spectral orders: SL1 & SL2 or LL1 & LL2) sharing a long spectroscopic aperture¹³. Each high-resolution module has a single slit with a short aperture but ten spectral orders dispersed in parallel (“*cross-dispersed echelle design*”). These orders acquire data simultaneously. Fig. 2.7 shows detector arrays of different modules.

There are three possible *observing modes*, known as the IRS **Astronomical Observation Templates (AOTs)**: Staring Mode, Mapping Mode, and Peak-Up Imaging (PUI).

- The staring mode was the basic “*point and shoot*” operating mode of the IRS. Science targets were placed on one IRS slit for a specified integration time in this mode.
- The spectral mapping **AOT** allowed an observer to configure a grid of map positions around a central region and obtain spectra at each place. The telescope scans in the direction perpendicular to the slit (denoted as spectral axis v in Fig. 2.7. a; counterpart of the AKARI/IRC dispersion direction) for enough steps to cover the grid before moving along the slit aperture (denoted as spatial axis w ; counterpart of the AKARI/IRC cross-dispersion direction).
- IRS PU arrays provided science-quality imaging capability in the wavelength range between that covered by IRAC and MIPS, and as such were of interest for imaging alone¹⁴.

Table 2.2 – IRS module characteristics.

Table extracted from [IRS Instrument Team & Science User Support Team \(2011\)](#).

Module	Channel	Wavelength Range (μm)	Resolving Power R	Plate Scale ($''\text{pixel}^{-1}$)	Slit Width ($''$)	Slit Length ($''$)
SL2	0	5.13-7.60	60-127	1.8	3.6	57
SL3		7.33-8.66	60-127		3.6	57
SL1		7.46-14.29	61-120		3.7	57
PU-blue		13.3-18.7	~ 3		80	56
PU-red		18.5-26.0	~ 3		82	54
LL2	2	13.90-21.27	57-126	5.1	10.5	168
LL3		19.23-21.61	57-126		10.5	168
LL1		19.91-39.90	58-112		10.7	168
SH	1	9.89-19.51	600	2.3	4.7	11.3
LH	3	18.83-37.14	600	4.5	11.1	22.3

12. The first letter means Short/Long wavelength; the latter means Low/High spectral resolution.

13. Indeed there is a third “*bonus*” *segment* (SL3, LL3) because the first- and second-order segments of the spectrum are not of the same length. It was intended to aid the user in cross-calibrating the other two spectrum segments.

14. The AKARI/IRC Np slit can be recognized as the counterpart of the *Spitzer*/IRS PU slit.

2.2.1.2 Database

Each *Spitzer* observation was identified by an **Astronomical Observation Request (AOR)** with a unique AORKEY. An **AOR** was composed of **Data Collection Events (DCEs)** with one or several exposures. There were different level *Spitzer* data, including the unprocessed Raw Data (Level 0), the **Basic Calibrated Data (BCD)** (Level 1; *i.e.* the individual data frames that emerged calibrated from the *Spitzer* pipeline), and Post-BCD (**PBCD**; Level 2; *i.e.* the products that came from combining **BCDs** such as mosaics of individual pointings).

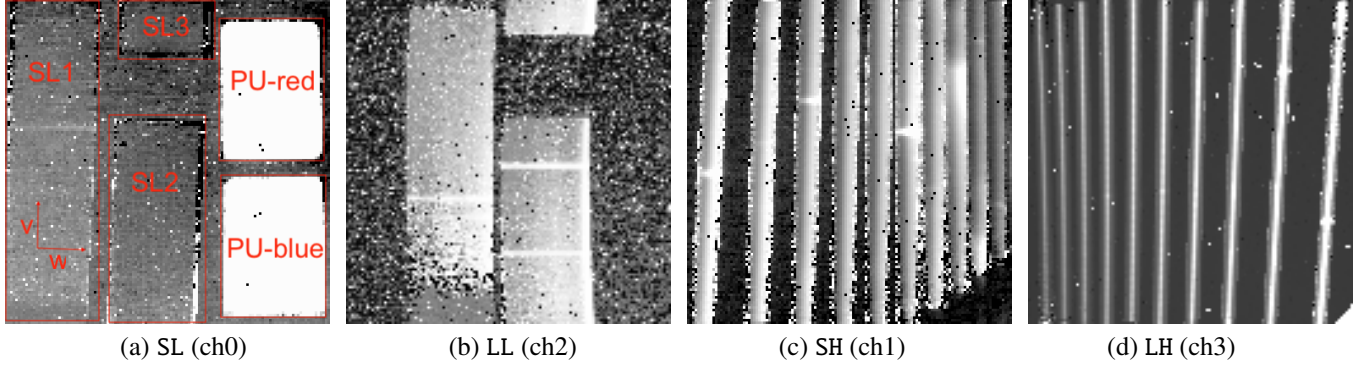


Figure 2.7 – IRS basic calibrated data (BCDs).

Panel (a) marks the location of SL/PU slits on the detector arrays. The axis v indicates the dispersion direction, which is also the telescope scanning direction. The axis w represents the slit aperture. Panel (b), (c), (d) are from LL, SH and LH. Bright areas are the light dispersed through IRS orders. Figure extracted from CUBISM during data processing.

Although various **PBCDs** from different science projects are available, they have not necessarily been reduced with the same pipeline. For instance, the background subtraction for an observation dedicated to studying **AGNs** can differ from that for a spectral map of a diffuse medium in the same galaxy. Our purpose is to study the **UIB** features in diverse environments. It is essential to perform such processes consistently for all the sources in our sample. On the other hand, we intend to make use of as many observations as possible, for which we would have to coadd spectral maps or pointing slits observed in different periods. **PBCDs** do not provide these.

Therefore, we have started with the level 1 **BCDs** processed by version S18.18 of the **Spitzer Science Center (SSC)** pipeline, retrieved from the Spitzer Heritage Archive (SHA)¹⁵. This processing includes flat-fielding, dark subtraction, linearity correction, wavelength calibration, orientation flipping, and unit conversion. They are accompanied by the following auxiliary calibration files from a given exposure:

- *bcd.fits*
- *bmask.fits*
- *func.fits*
- *spect.tbl*

15. <https://sha.ipac.caltech.edu/applications/Spitzer/SHA>

The nomenclature of **BCD** files downloaded from the SHA follows the convention below:

SPITZER_S+module_aorkey_expid_dcenum_version_type.suffix

- *S+module* = observation mode
- *aorkey* = **AOR** ID number
- *expid* = exposure ID number
- *dcenum* = **DCE** number (at a given spatial position)
- *version* = number of times data being processed
- *type* = type of pipeline product (*e.g.* *bcd*, *coa2d*.)
- *suffix* = file format *fits*, *tbl*.

2.2.1.3 Data analysis tools

The [Spitzer Data Analysis Cookbook](#) presents a software suitable for use with the **BCDs** obtained from *Spitzer*. We put forth the following ones dedicated to IRS data.

- The *CUBE Builder for IRS Spectral Mapping* (CUBISM; [Smith et al., 2007b](#)) is a tool for extracting 1D spectra and building 3D spectral cubes dedicated to the IRS mapping mode.
- The *Spectroscopic Modeling Analysis and Reduction Tool* (SMART; [Higdon et al., 2004](#); [Lebouteiller et al., 2010](#)) is a tool for real-time processing and analysis of IRS data. It can embed external data analysis tools such as PAHfit ([Smith et al., 2007a](#); [Lai et al., 2020](#)).
- IRSCLEAN¹⁶ allows users to remove remaining rogue pixels in IRS **BCDs** after background subtraction. This can be beneficial for faint objects. Here “*clean*” means replacing the offending pixels with interpolated values from neighboring pixels or with the “*Not a Number*” (NaN) value. The same algorithm is applied to uncertainty cubes.

All these software are written in IDL, and distributed and supported by the **SSC**. It is possible to use them one with another at the same time.

2.2.2 IRS data processing

2.2.2.1 CUBISM

With the “*raw*” **BCD** records, we have built 3D spectral cubes (with two spatial and one spectral dimension) using the **SSC** software CUBISM, developed by the SINGS team ([Smith et al., 2007b](#)). It is generally dedicated to projecting record-level pixels onto the sky with a custom flux-conserving algorithm. For our study, we have optimized the configuration within CUBISM, from the raw **BCD** data to the background treatment and bad pixel cleaning. These steps can be fine-tuned depending on the users’

16. <https://irsa.ipac.caltech.edu/data/SPITZER/docs/dataanalysis/tools/tools/irsclean>

interests. A demonstration of our pipeline, described here, can be found in [Sect. 2.4](#).

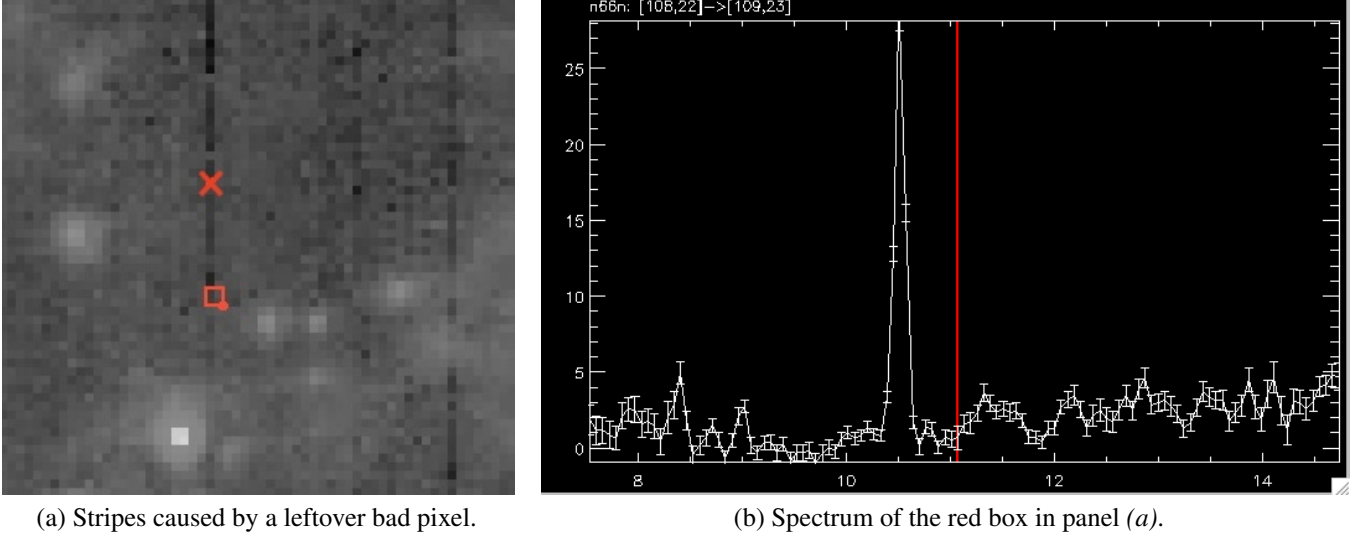
First, we have collected IRS mapping and staring mode **BCDs** from the SHA database. Since each CUBISM *project* pertains to a single IRS module, we have regrouped data according to each IRS module. The observing time and duration are also critical parameters. We should, in principle, not mix observations taken beyond a 24-hour interval for better reduction quality. Indeed, the telescope calibration mask (accounting for the time-varying zodiacal background) and the bad pixel mask (flagging cosmic rays, detector artifacts, *etc.*) would change between two observations too far apart. Observations taken more than 24 hours apart will be coadded ulteriorly. We can then consistently combine all CUBISM-processed IRS cubes and AKARI cubes taking into account all the sources of uncertainties ([Sect. 2.2.3](#)).

Background subtraction Most IRS mapping mode observations are associated with a dedicated sky observation before or after the exposures of the target. For a source observed with different IRS modules, sky observations with these modules might have been taken together before or after the series of exposures. We have imported the sky **AORs**, along with the target **AORs**, in a single CUBISM project and have subtracted them from the **BCD** records before the cube construction. The cube construction with CUBISM is performed for each order separately. Background subtraction and bad pixel cleaning are performed every time we change the **BCD** records.

Bad pixels. A rogue pixel is a pixel with abnormally high dark current or photon responsivity (a “*hot*” pixel) that manifests as a pattern artifact in an IRS **BCD** image. For example, it might emerge if the IRS array is hit by a Solar or cosmic particle. Such pixels vary on timescales of hours to months. In consequence, the effectiveness of a rogue mask for cleaning data is usually limited to data from the same **AOR** used to derive the mask. Though rogue pixels dominate the noise properties of spectral cubes, maps, and extracted spectra, it is not always trivial to define them. The two types of bad pixels that can be identified in CUBISM are the *Global-level* and the *Record-Level* bad pixels. A global bad pixel stays bright throughout the exposure of the spectral map, leaving spatially-periodic stripes on certain wavelength planes. A record-level bad pixel is intermittent. It affects only a single or a small cluster of cube pixels. If there are artifacts in the vertical direction (axis *v*) of the telescope scan, manually flagging record-level bad pixels will contribute to the data reduction quality.

Auto-gen. An automatic bad pixel tool (hereafter Auto-gen) embedded in CUBISM allows automatic selection and masking of bad pixels in an assembled cube. It uses two parameters to identify them: (i) “*Sigma-Trim*” sets the minimum number of standard deviations a pixel must lie away from the median value to be considered bad; (ii) “*MinBad-Frac*” lists the minimum fraction of occurrence of a given **BCD** pixel presumed bad according to “*Sigma-Trim*”. For example, if “*Sigma-Trim*” is 5 and “*Minbad-Frac*” is 0.5, then a given **BCD** pixel is considered bad if at least 50% of the time it appears in the cube, it is $5\text{-}\sigma$ away from the median pixel value. Note that the final flux density assembled in a cube’s pixel also depends on the fractional

contribution of each **BCD** pixel¹⁷. However, this fraction is used by Auto-gen. Consequently, if a bad **BCD** pixel accounts for a large fraction of a final, projected cube pixel, this cube pixel will be biased (*cf.* Fig. 2.9). Moreover, the uncertainties are not considered by Auto-gen, either. We can manually find the remaining bad pixels with the pixel backtracking tool described hereafter.



BackTracking: n66n

Cube: n66n Pix: [108,36] 11.073 μm

BCD	Pix	Frac	Val	Back	(Val-Back)	Flag
S0_18262784_0396_0000	(26, 68)	0.694	73.1±5.26	79.2±0.927	-6.06±5.34	
	(27, 68)	0.0435	13.0±2.96	11.2±0.533	1.86±3.01	
	(26, 67)	0.239	12.5±2.87	8.42±0.488	4.06±2.92	
S0_18262784_0397_0000	(27, 67)	0.000209	17.2±3.14	12.7±0.559	4.51±3.19	
	(26, 67)	0.00473	13.0±2.95	8.42±0.488	4.55±2.99	
S0_18262784_0396_0000	(27, 67)	0.0119	18.2±3.24	12.7±0.559	5.57±3.29	

(c) Bad pixel backtracking for the pixel (108,36) at 11.073 μm.

Figure 2.8 – Backtracking bad pixels surviving the Auto-gen tool within CUBISM.

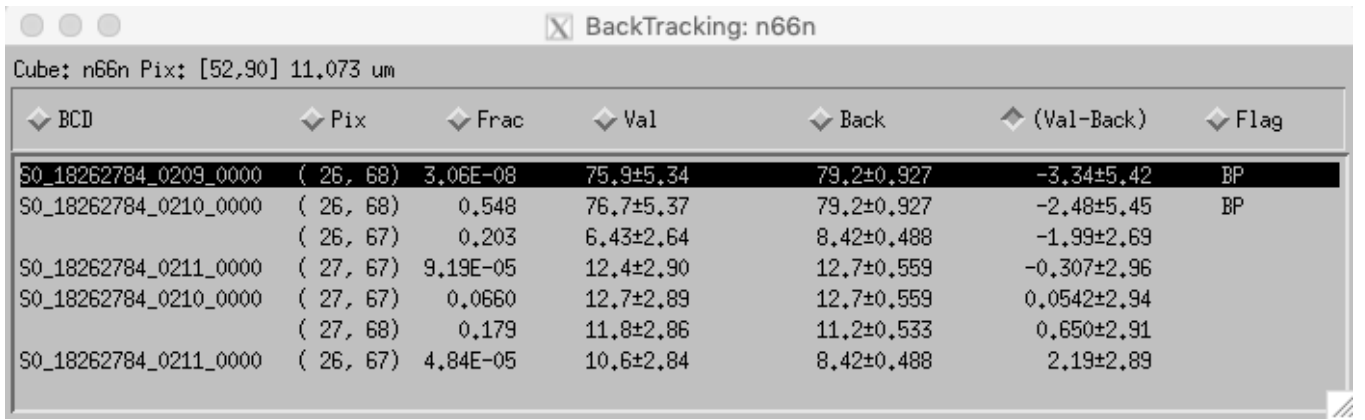
Panel (a) shows a IRS spectral cube of the north wind region of N66 in the **Small Magellanic Cloud** (SMC). The spectrum of the pixel indicated in the red box in panel (a) is presented in panel (b), where the red line indicates the wavelength of the image in panel (a). The contribution of record-level (**BCD**) pixels at the red point of panel (a) is listed in panel (c), extracted from CUBISM’s Backtracking tool.

Backtracking. Fig. 2.8. a shows a slice of the spectral cube after applying Auto-gen at the wavelength indicated by the red line in Fig. 2.8. b. In Fig. 2.8. b, we can also visualize the spectrum of the red box indicated in Fig. 2.8. a. The spectrum quality appears good, even if there are still periodic stripes in the image. Fig. 2.8. c lists the flux contribution of **BCD** pixels to the

17. This fraction indicates the percentage of cube pixel contributed by a clip-on **BCD** pixel (*i.e.* the “Frac” parameter displayed in Fig. 2.8. c). This fraction is different from the fractional occurrence mentioned before.

cube pixel indicated by the red dot in Fig. 2.8. a. These artifacts appear on the **BCD** pixels passing through a bright source. Hence they might be due to the saturation or the cosmic ray transient effects. Meanwhile, if the bias amplitude is smaller than the uncertainties, it will have a limited effect on the analysis.

Auto-gen may miss global bad pixels. Let’s look at the example in Fig. 2.9. The **BCD** pixel (26,68), which is bad, has a value within $5\text{-}\sigma$ deviating from the median value, “(Val-Back)” = -0.307, with a contribution greater than 50% (“Frac” = 0.548). It has thus not been identified by Auto-gen. Indeed, this pixel has a negative flux density with a small S/N ratio after background subtraction: “(Val-Back)” = -2.48 ± 5.45 . Note that Auto-gen always looks at the value after background subtraction, “(Val-Back)”. This pixel has a non-negligible impact: the periodic stripes in source-free regions. This effect appears in low-signal-to-noise ratio cases, where we avoid very low “Sigma-Trim” or “Minbad-Frac” in order not to flag real data.



BCD	Pix	Frac	Val	Back	(Val-Back)	Flag
SO_18262784_0209_0000	(26, 68)	3.06E-08	75.9±5.34	79.2±0.927	-3.34±5.42	BP
SO_18262784_0210_0000	(26, 68)	0.548	76.7±5.37	79.2±0.927	-2.48±5.45	BP
	(26, 67)	0.203	6.43±2.64	8.42±0.488	-1.99±2.69	
SO_18262784_0211_0000	(27, 67)	9.19E-05	12.4±2.90	12.7±0.559	-0.307±2.96	
SO_18262784_0210_0000	(27, 67)	0.0660	12.7±2.89	12.7±0.559	0.0542±2.94	
	(27, 68)	0.179	11.8±2.86	11.2±0.533	0.650±2.91	
SO_18262784_0211_0000	(26, 67)	4.84E-05	10.6±2.84	8.42±0.488	2.19±2.89	

Figure 2.9 – Possible causes for overlooking bad pixels.

This panel, extracted from CUBISM’s Backtracking tool, presents the backtracking result for a pixel (52,90) of the projected cube at $11.073\text{ }\mu\text{m}$. The “(Val-Back)” value of bad pixels is not conspicuous enough, considering the adopted Auto-gen parameters. In the low-signal-to-noise ratio case, manual backtracking of bad pixels is therefore highly recommended.

Aware of the limitations discussed above, we have performed manual backtracking after Auto-gen, for each reduction. Moreover, we have not flagged record-level bad pixels by hand unless they impacted the critical spectral features. This task would otherwise be tedious and extremely time-consuming for a negligible return. There are indeed few record-level bad pixels, so flagging global bad pixels is often sufficient for this step. For observations with a short integration time, the timescale of cosmic radiation hits is comparable to the whole exposure. Those cosmic rays causing bad pixels are presumed to be global bad pixels.

Uncertainty cube. An associated uncertainty cube is available with each product. The pipeline uncertainties consist only in statistical ramp uncertainties ([IRS Instrument Handbook](#)), which can under-estimate the total uncertainty for bright sources (above S/N ratio ~ 10), where systematic uncertainties dominate. We have verified the linearity of the uncertainties given by the CUBISM pipeline. To that purpose, we have amplified the **SSC** pipeline uncertainties (*func.fits*) by a factor of ten and performed the same CUBISM procedure for data with initial and amplified uncertainties, respectively. The new uncertainty cube given

by CUBISM shows precisely ten times the former value (Fig. 2.10). Therefore we have kept the pipeline uncertainty, whereas calibration errors will be treated during spectral fitting.

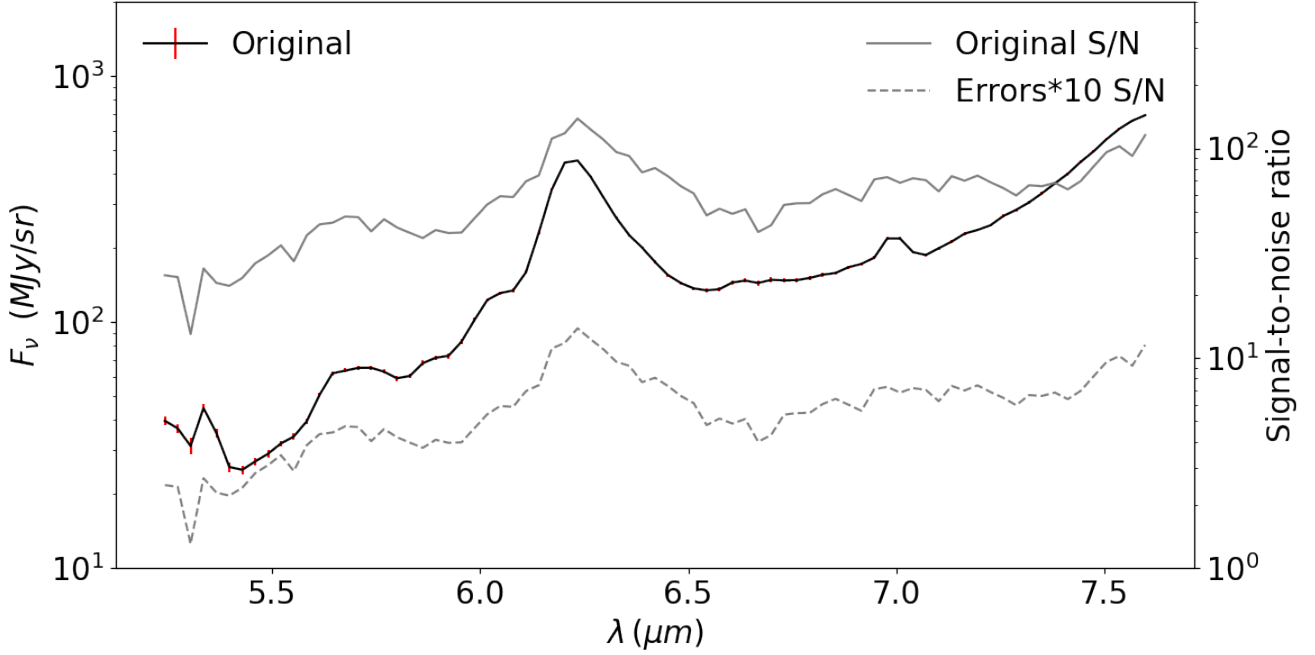


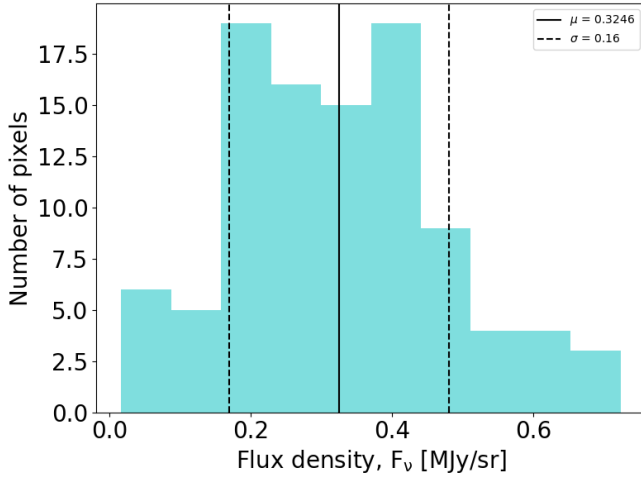
Figure 2.10 – Linearity assessment of the CUBISM-processed uncertainty.

The solid black line with red error bars is the original spectrum given by CUBISM. It is overlaid with the S/N ratio of the initial spectrum (solid gray line) and the one with amplified record uncertainty (by a factor of ten; dashed gray line), both processed by CUBISM. The resulting uncertainties of the latter are precisely ten times of the former, implying CUBISM generates linear uncertainties.

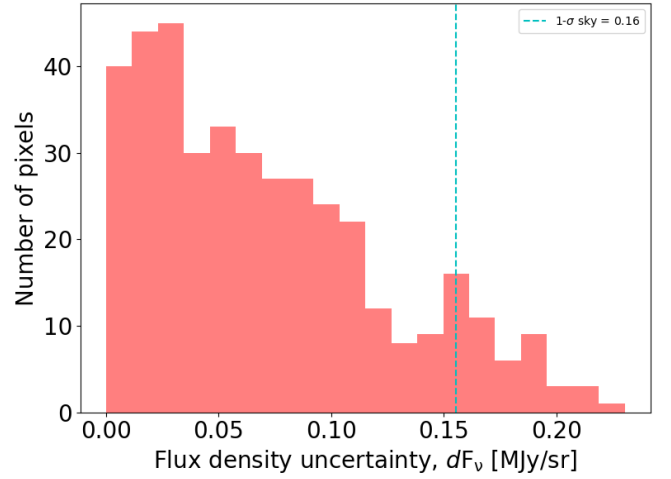
We have also compared the pixel distribution of the uncertainty given by CUBISM to the sky background residuals. Fig. 2.11 shows that the standard deviation of sky flux density is compatible with the CUBISM uncertainties for an observed extended region of M 82. Therefore, uncertainties estimated with sky residuals can be a, usually conservative, alternative when the uncertainties provided by CUBISM appear abnormally low.

CUBISM workflow. Here, we summarize the different steps we apply to our data. They are optimized for our study.

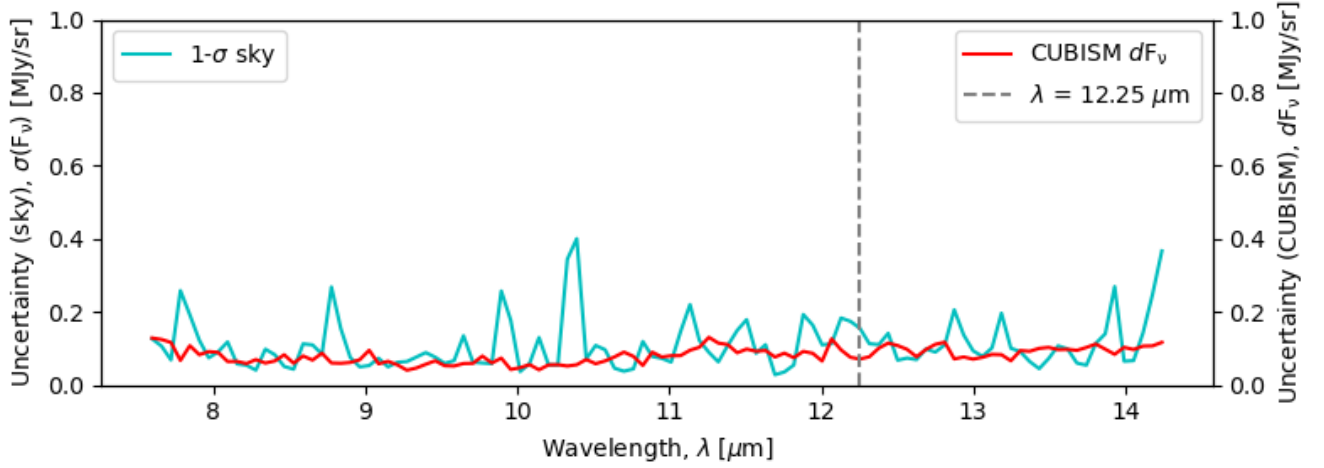
1. **Create project.** Each project pertains to a single IRS module.
2. **Import Data.** The **BCD** dataset could come from one or several **AORs** with the same IRS array. However, we only mix **AORs** taken within 24 hours of the target. Otherwise, it might introduce artifacts because of changes in observations (darks and onset of rogue pixels, *etc.*). To have a broader mosaic of extended sources, we reduce different observations with CUBISM separately, then combine them with appropriate calibrations.
3. **Set cube build order.**
4. **Trim each side by 3%.** In “CubeView” (custom viewer used to visualize **BCD** records, frames, or spectral cubes), there



(a) Sky observations.



(b) CUBISM uncertainties.



(c) CUBISM uncertainties overlaid with the standard deviation of sky observations.

Figure 2.11 – Comparison of the uncertainties derived from the sky and from CUBISM.

Panel (a) shows the flux density distribution of an observed part of the sky, near M 82, at $12.25 \mu\text{m}$. Panel (b) shows the CUBISM uncertainty distribution for an extended region in M 82 at $12.25 \mu\text{m}$. Panel (c) shows both values viewed over the SL1 range, where we indicate the wavelength corresponding to panels (a) & (b) with a gray dashed line.

is a “WAVSAMP Pane” below the image block when displaying a **BCD** record. The “Edit” button allows us to adjust spectral orders on the array. Here, we do not trim the wavelength range since we will do this later when combining spectra. However, we shrink the aperture to exclude spurious data at the edges. There should be enough redundancy at slit ends for the IRS mapping mode. Otherwise, there will be vertical ditches in the final cube. We trim each side of the slit aperture by 3% for low-resolution modules.

5. Set background (hereafter BG).

- [Optional] Import BG records. We only use the archived sky measurements taken less than one day before or after the source **BCDs**.
- [Optional] Check BG records to ensure they are free of unexpected source flux. To do that, you can either use

“AOR Visualization Tool” with IRAC/MIPS images or deactivate the dataset and then build the BG cube to see if it contains source emissions.

- Choose & set BG by choosing “Average + Min/Max Trim”
- [Optional] Check BG spectra with “Line Slicing (I)” in “CubeView”. Note that the BG here is subtracted at **BCD** level, a single record for the whole map.
- Save & deactivate BG records

6. **Build Data cube.** Since CUBISM uses the **BCD** pixel contributions to the cube in order to discover bad pixels, we must first build the cube before being able to identify them. Later there will be “QuickBuild” option.

7. **Flag bad pixel (hereafter BP).**

- Set auto-badpix parameters¹⁸.
- Auto-gen BP (global & record).
- Manual BP by backtracking.
- Rebuild cube and save BP¹⁹.

8. **Cube output.** There are two FITS files written for every order, including the uncertainty cube.

9. **Change order and repeat from step 6.** The bonus order is recommended for low-res modules for the sake of further calibration.

10. **Save everything.**

2.2.2.2 Uncertainty sources

The spectral mapping mode of IRS was implemented after launch, together with its corresponding pointing calibrations. The pointing suffered from random positional offsets for every commanded movement of the telescope, similar to AKARI’s drift. Peak-Up target Acquisitions (PUA), used to correct the offsets, were carried out only once at the beginning of each mapping cycle. A pointing error of $\sim 0.4''$ in the cross-dispersion direction (axis w) resulted from this uncertainty (Sloan et al., 2015). This value is relatively small compared to our final pixel size of several arcseconds that we use to extract spectra. However, when we perform the same error propagation as done for AKARI/IRC (Sect. 2.1.2.4; an example in Fig. 2.12. a), we find it can increase the IRS statistical uncertainty (given by CUBISM; Figs. 2.10 – 2.11) by an order of magnitude (Fig. 2.12. b). IRS pointing inaccuracy is thus one of the predominant sources of statistical uncertainty in high-signal-to-noise ratio observations. Note that our statistically-treated pointing uncertainties include the uncertainty in the PSF (Pereira-Santaella et al., 2010). Flux

18. In general, we find the following configuration finds reasonable BP for most observations.

BP	Sigma-Trim	MinBad-Frac
Global	5.00	0.25
Record	5.00	0.50

19. By default, the BP list is completed by subsequent Auto-gen processes or manual backtracking. It does not reset when changing the order. So we can update directly the former “.bpl” file every time we save BP to have a BP list for the whole CUBISM project. By contrast, make sure the BP list is empty by clearing them all before creating a new one.

calibration uncertainties (Table 2.3) also include the effects of pointing uncertainty, as pointing errors also apply to calibrators. The difference is that flux calibration uncertainties have a systematic effect on the spectra, whereas pointing uncertainties are random and can affect differently each slit.

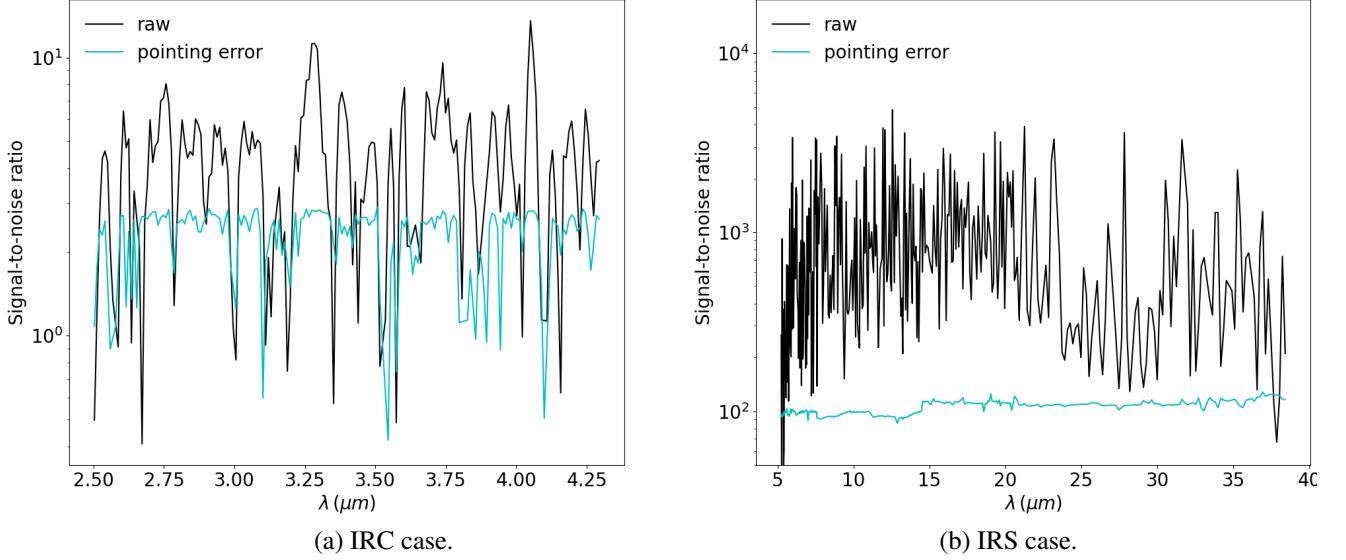


Figure 2.12 – Effect of pointing uncertainty on S/N ratio.

Panel (a) shows the S/N ratio of IRC spectrum with (cyan) and without (black) adding a pointing error of $3''$. Panel (b) shows the case of IRS with a pointing error of $0.4''$.

The total uncertainty is estimated with the boot-strapping method presented in Sect. 2.1.2.1, as follows:

$$\begin{aligned}
 F_{\nu}(x, y, \lambda) &= F_{\nu, 0}(x, y, \lambda) + \epsilon_0(x, y, \lambda) + \epsilon^{\text{pt}}(x, y, \lambda) + \epsilon^{\text{cal}}(x, y, \lambda) \\
 &= F_{\nu, 0}(x, y, \lambda) + \sigma_0(x, y, \lambda) \times \delta_0(x, y, \lambda) \\
 &\quad + \sum_i^n F_{\nu, 0}(x + dx, y + dy, \lambda) \times f_i(x, y) - F_{\nu, 0}(x, y, \lambda) \\
 &\quad + F_{\nu, 0}(x, y, \lambda) \times \Sigma^{\text{cal}}(\text{module}) \times \delta^{\text{cal}}(\text{module}),
 \end{aligned} \tag{2.1}$$

with $dx \sim \mathcal{N}(0, \sigma^{\text{pt}})$ and $dy \sim \mathcal{N}(0, \sigma^{\text{pt}})$ the same for all (x, y) on the spectral map.

The total flux density F_{ν} in pixel (x, y) at wavelength λ (or frequency ν) is the sum of (i) the actual flux density, $F_{\nu, 0}$, (ii) statistical errors, ϵ_0 , given by the pipeline uncertainties, σ_0 , (iii) pointing errors, ϵ^{pt} , derived from the pointing uncertainties, $\sigma^{\text{pt}} \simeq 0.4''$ (for IRS), and (iv) calibration errors, ϵ^{cal} , from the instrumental calibration uncertainties, $\Sigma^{\text{cal}}(\text{SL}) \simeq 5\%$ and $\Sigma^{\text{cal}}(\text{LL}) \simeq 5\%$ (Table 2.3). Since we jiggle the map around its position to evaluate the pointing error term, $f_i(x, y)$, $i=1, \dots, n$, is the fraction of n shifted pixels that contribute to the pixel (x, y) . The random variables are: (i) $\delta_0(x, y, \lambda) \sim \mathcal{N}(0, 1)$; (ii) $\delta^{\text{cal}}(\text{module}) \sim \mathcal{N}(0, 1)$; (iii) IRS pointing uncertainties are also normal, with $dx \sim \mathcal{N}(0, \sigma^{\text{pt}})$ and $dy \sim \mathcal{N}(0, \sigma^{\text{pt}})$, to produce a flux density error, ϵ^{pt} , for each pixel.

Table 2.3 – Uncertainty sources.

Different uncertainty sources are taken into account during the uncertainty propagation, for each instrument. The photometric observations are already reduced and calibrated data are taken directly from various databases (see the text in Sect. 2.3), so we do not consider their pointing errors.

Module	Statistical uncertainty		Systematic uncertainty
	Pipeline (σ_0)	Pointing (σ^{pt})	Calibration (Σ^{cal})
IRC	IRC pipeline	3'' ^a	10% - 20% ^b
IRS-SL1	CUBISM	0.4'' ^c	5% ^d
IRS-SL2	CUBISM	0.4'' ^c	5% ^d
IRS-LL1	CUBISM	0.4'' ^c	5% ^d
IRS-LL2	CUBISM	0.4'' ^c	5% ^d
IRS-SH	CUBISM	0.4'' ^c	5% ^d
IRS-LH	CUBISM	0.4'' ^c	5% ^d
IRAC _{3.6μm}	auxiliary ^e	-	3% ^d
IRAC _{4.5μm}	auxiliary	-	3% ^d
IRAC _{5.8μm}	auxiliary	-	3% ^d
IRAC _{8μm}	auxiliary	-	3% ^d
MIPS _{24μm}	auxiliary	-	4% ^d

a. Onaka et al. (2007)

b. Ohyama et al. (2007)

c. We refer to Sloan et al. (2015) for the typical IRS pointing uncertainty of $\sim 0.4''$. This value is consistent with the blind pointing uncertainty of *Spitzer* estimated to be $< 0.5''$ (*Spitzer Observer's Manual*). In our case, most observations are spectral mapping of extended sources, which generally do not require high pointing accuracy. We remind the reader that *Spitzer* pointing suffers random positional offsets of the order of $0.2''$, for every commanded movement of the telescope (*IRS Instrument Handbook*). In conclusion, we favor the $0.4''$ pointing uncertainty for the IRS spectral cubes.

d. Carey (2010)

e. We simply use the uncertainty map provided with the photometric data via database.

2.2.2.3 PSF degradation

The image provided by an instrument is the true flux distribution convolved by its **PSF**. Since the width of the **PSF** is different at each wavelength, we need to account for this effect when estimating the spectrum of a pixel. A solution is to degrade the images to a common resolution. In practice, given the **PSF**, $\Psi_A(x, y)$, of a camera²⁰, A, and a source, $\mathcal{S}(x, y)$, the observed image, $I_A(x, y)$ is the convolution of the source \mathcal{S} with the **PSF**, Ψ_A :

$$I_A(x, y) = \iint \mathcal{S}(x', y') \Psi_A(x - x', y - y') dx' dy' = (\mathcal{S} \star \Psi_A)(x, y), \quad (2.2)$$

where we have assumed that the **PSF** is normalized at any position (x', y') across the field-of-view of camera A:

$$\iint \Psi_A(x - x', y - y') dx dy = 1 ; \forall (x', y'). \quad (2.3)$$

Obviously, given two cameras, A and B, having different **PSF**, Ψ_A and Ψ_B , the images I_A and I_B of the same object will be different, even if the spectral response of the cameras were identical. The convolution method consists in transforming the higher resolution image of A to match the resolution image of B using a convolution kernel $\mathcal{K}\{A \Rightarrow B\}$ which satisfies:

$$\Psi_B = \Psi_A \star \mathcal{K}\{A \Rightarrow B\}. \quad (2.4)$$

20. Here “camera” encompasses the telescope optics and the detector.

It thus results in:

$$I_B(x, y) = \iint I_A(x', y') \mathcal{K}\{A \Rightarrow B\}(x - x', y - y') dx' dy' = (I_A \star \mathcal{K}\{A \Rightarrow B\})(x, y). \quad (2.5)$$

The **PSF** of *Spitzer*/IRS has been less studied than other instruments onboard *Spitzer*. In terms of IRS staring mode observations, [Lebouteiller et al. \(2010\)](#) developed an *optimal extraction* algorithm which provides an empirical super-sampled **PSF** for both IRS low-resolution ([Lebouteiller et al., 2011](#)) and medium-resolution ([Lebouteiller et al., 2015](#)) data. As for IRS mapping mode observations, for instance, [Sandstrom et al. \(2009\)](#) adopted the theoretical **PSF** created for the STinyTim program ([Krist, 2006](#), hereafter the STinyTim **PSF**). However, they found that the **PSF** of spectral cubes built by CUBISM can be somewhat elongated in a way that varies with wavelength. In practice, the extracted spectra convolved with a **PSF** that monotonically increases with wavelength are in good agreement with the optimal extraction (*e.g.* [Zhang et al., 2021](#)).

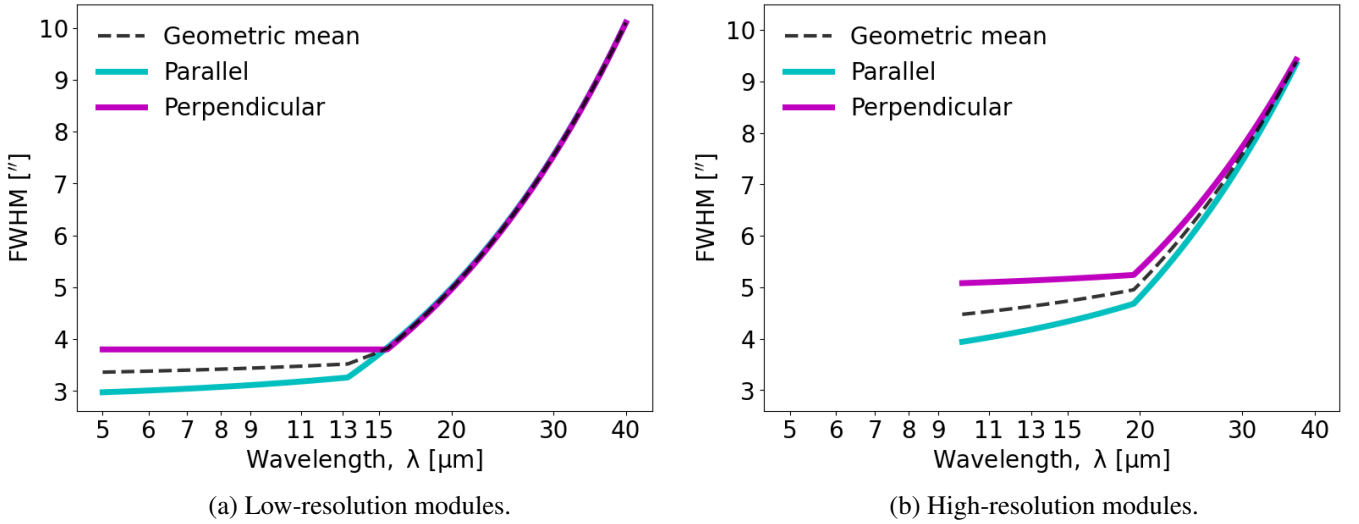


Figure 2.13 – IRS PSF size variation as a function of wavelength.

We have applied a simple interpolation of the averaged **FWHM** in [Table 2.4](#) to determine the wavelength-dependent **PSF** of IRS modules. The **PSF** of all IRS modules was calibrated by [Pereira-Santaella et al. \(2010\)](#) using archived IRS cubes of calibration stars. They fitted each frame of the IRS cube at sampled wavelengths with a two-dimensional Gaussian profile, accounting for the asymmetry. “*Perpendicular*” and “*parallel*” refer to the axis *v* and *w*, respectively.

With MIRAGE, we have applied the wavelength-dependent IRS **PSF** calibrated by [Pereira-Santaella et al. \(2010](#), hereafter the CUBISM **PSF**) using archived IRS mapping-mode data of calibration stars. This calibration of **PSF** profile is dedicated to IRS spectral cubes processed by CUBISM, which accounts for additional effects (*e.g.* the cube assembly and wavelength calibration uncertainties) compared to the simulated STinyTim **PSF**. The CUBISM **PSF** is globally wider than the STinyTim **PSF** in the wavelength range of IRS. In principle, it is more conservative to assume a broader instrumental **PSF**. Nevertheless, [Pereira-Santaella et al. \(2010\)](#) only measured the IRS short-wavelength modules (SL2, SL1 and SH) because other modules are heavily affected by the fringing patterns (*cf.* [Lebouteiller et al., 2015](#), which allows to identify and remove fringes), and a Gaussian does not well reproduce their **PSF**. Since there is a lack of knowledge, we simply assume that the **FWHM** of the **PSF** is proportional

to the wavelength, λ , which gives $\text{FWHM} ['] = 4 \times \lambda [\mu\text{m}]$ for IRS long-wavelength modules (LL2, LL1 and LH)²¹. We capture a schematic prescription of the IRS PSF described above, for low-resolution modules (Fig. 2.13. a) and medium-resolution modules (Fig. 2.13. b), respectively.

Table 2.4 – Full Width at Half-Maximum (FWHM) of spectral mapping PSF.

PSF size measured by FWHM ['] for images from AKARI/IRC and *Spitzer*/IRS spectral cubes and *Spitzer*/IRAC and *Spitzer*/MIPS photometric data.

Module	FWHM perpendicular (axis v; '')	FWHM parallel (axis w; '')	FWHM circular (2-D Gaussian; '')
IRC	3.3 ^a	6.0 ^a	6.0
IRS-SL1	3.76±0.07 ^b	3.27±0.21 ^b	3.51 ^c
IRS-SL2	3.88±0.04 ^b	3.02±0.17 ^b	3.42 ^c
IRS-LL1	-	-	10 (at 40 μm) ^d
IRS-LL2	-	-	4.98 (at 20 μm) ^d
IRS-SH	5.16±0.08 ^b	4.31±0.37 ^b	4.72 ^c
IRS-LH	-	-	4.81 (at 20 μm) ^e
IRAC _{3.6μm}	-	-	1.90 ^f
IRAC _{4.5μm}	-	-	1.81 ^f
IRAC _{5.8μm}	-	-	2.11 ^f
IRAC _{8μm}	-	-	2.82 ^f
MIPS _{24μm}	-	-	6.43 ^f

a. We refer to the PSF size of images taken by the N3 filter in IRC03 mode (Egusa et al., 2016).

b. The averaged value of the FWHM [']. The error bar in this table is derived from the (FWHM and centroid) variation of the PSF exhibiting an undulating pattern as a function of wavelength (Pereira-Santaella et al., 2010).

c. Geometric mean of the two mutually perpendicular directions.

d. Interpolated between 14.29 μm (the SL end) and 40 μm with a value of 10'' at the long-wavelength end.

e. Interpolated between 19.51 μm (the SH end) and 40 μm with a value of 10'' at the long-wavelength end.

f. Aniano et al. (2011)

Table 2.4 summarizes the average value of the PSF FWHM of each module used in our observations, including the AKARI/IRC ones described in Sect. 2.1.2.3. Note that the FWHM uncertainties in the IRS case reflect an undulating pattern of PSF variation observed during the calibration (Pereira-Santaella et al., 2010). In particular, the 1- σ deviations in the parallel direction (axis w) is relatively larger than the perpendicular axis (v). They are generally small when compared to the slit pixel size though (e.g. 0.21''/1.8'' = 11.7%, for SL1; Table 2.2). This PSF variation can be attributed to diverse origins, including the discrepancy of diffraction loss correction or other artifacts throughout the telescope optical system related to the source position within the slit.

To jointly analyze the spectroscopic data from AKARI/IRC and *Spitzer*/IRS (Sect. 2.2.3), as well as the auxiliary photometric data used to perform inter-calibration (Sect. 2.3), we choose a reference PSF with a Gaussian profile and a FWHM of 6'', for all modules in Table 2.4 (except IRS-LL1²²). This thus allows us to perform a consistent analysis on the same physical scales. We have degraded each IRS frame to the resolution of the reference PSF, before reprojecting and stitching (Sect. 2.2.3) the different orders of the SL and LL channels. The corresponding kernel was generated by Aniano et al. (2011).

21. The IRS spectrograph modules were designed to sample the PSF at the long end of each module's wavelength range (Smith et al., 2007b). Hence, we simply set a 10'' FWHM for the IRS PSF at 40 μm and interpolate between the short- and long-wavelength ends.

22. LL1 module is excluded primarily because there are not many features of interest for this study. Besides, introducing the LL1 spectrum requires a convolved PSF with a larger width, which will result in more degraded images.

Unlike *Spitzer*/IRS, we have not performed any kernel convolution for AKARI/IRC spectral cubes since the IRC PSF is approximately the same as the reference PSF. Another reason is that IRC slit widths are too narrow, making the interpolation within the image convolution process uncertain. PSF broader than the IRC slit widths causes flux loss by diffraction. The correction of this flux loss will be taken into account by performing inter-calibration (Sect. 2.3).

2.2.3 Spectral map coaddition

To obtain the complete spectra covering the MIR range ($3 - 20 \mu\text{m}$), we have coadded the individual spectral maps coming from different modules and different campaigns. It required two distinct tasks: (i) reprojecting images to sample them on a common grid and (ii) spectrally stitching the spectra from different modules.

2.2.3.1 Image reprojection

In our sample, *Spitzer*/IRS spectral maps generally have better spatial coverage than that of AKARI/IRC because only individual pointings are available for the latter. We have decided to reproject all IRS individual maps on the grids used to construct IRC cubes. IRC footprints are indeed very patchy because they are the coaddition of individual slits. To resample them on the IRS grid, the holes would add another layer of uncertainty, as we would have to make assumptions about the true flux distribution between the slits. Therefore, it is better to keep IRC slits on their initial grids.

2.2.3.2 Spectrum stitching

Using MIRAGE, we have applied a two-step spectral stitching procedure to combine spectra from different observing modules.

1. We have first normalized SL and LL spectra using their *bonus orders*, (SL3 and LL3). More precisely for each pixel, we have averaged the spectra at the usable segments (Table 2.2) where the regular and bonus orders overlap. Then, we have scaled each spectrum from the regular order to the bonus order, like what Sloan et al. (2015) did. The IRS data were quite consistent since the correction factors we derived were $\sim 0.8 - 1.2$ for both SL and LL modules of M 82.
2. The second step is stitching the spectra inter-calibrated spectra with photometric observations. This inter-calibration process will be discussed in Sect. 2.3.

2.2.4 Sparsely sampled maps

The IRS mapping mode allows spatially under-sampled observations (*Spitzer Observer's Manual*), for both low-resolution (*e.g.* IC 10) and high-resolution observations (*e.g.* NGC 253, NGC 1333). The resulting spectral maps are not continuous in the telescope scanning direction (axis ν). They are called *sparsely sampled maps* (Fig. 2.14). It is possible to reconstruct a continuous map from the sparse map of extended sources if the step size is smaller than the width of the PSF.

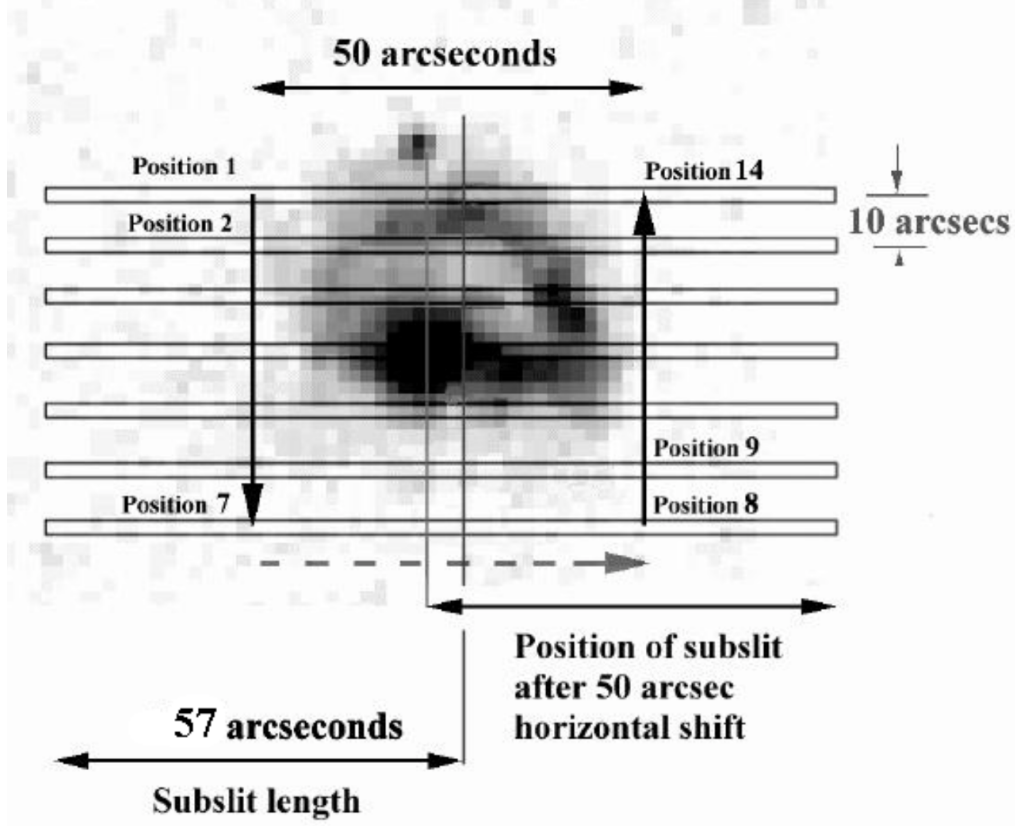


Figure 2.14 – Example of a sparse 7×2 spectral map with *Spitzer/IRS*.

Figure extracted from the [Spitzer Observer's Manual](#). An odd number of slits in the perpendicular direction ensures that a slit covers the center of the map.

Although CUBISM is optimized for fully sampled maps of extended sources, we can use it to build sparsely sampled maps. These maps will appear discontinuous. Taking IC 10 as an example, we notice that CUBISM has performed a partial interpolation of some slit edges, on its grid (Fig. 2.15 left panel). But the gap between slits remains. We thus need to perform an additional interpolation in order to obtain a continuous map. For that purpose, we have used a *B-spline* (or *basis spline*; Riesenfeld, 1973) interpolation along the axis v . Given a spline, $S_{k,\vec{t}}$, of degree, k , and knots, $\vec{t} = t_0, t_1, t_2, \dots, t_n$, it can be expressed as:

$$S_{k,\vec{t}}(x) = \sum_{i=0}^{n-1} c_i B_{i,k}(x) \quad (2.6)$$

with the spline coefficients c_i and the B-spline basis functions $B_{i,k}$ defined as follows:

$$B_{i,0}(x) = \begin{cases} 1, & \text{if } t_i \leq x < t_{i+k} \\ 0, & \text{otherwise} \end{cases} \quad (2.7)$$

$$B_{i,k}(x) = \frac{x - t_i}{t_{i+k} - t_i} B_{i,k-1}(x) + \frac{t_{i+k+1} - x}{t_{i+k+1} - t_{i+1}} B_{i+1,k-1}(x) .$$

The result is shown in Fig. 2.15 right panel. Given the FWHM of the degraded PSF ($6''$) compared to the scanning step size (slightly larger than SL slit width $3.6''$), the spatial information has been recovered without overinterpretation. Similar work about sparse map reconstruction can be found in the literature (e.g. Devost et al., 2004; Maret et al., 2009; Pilleri et al., 2012).

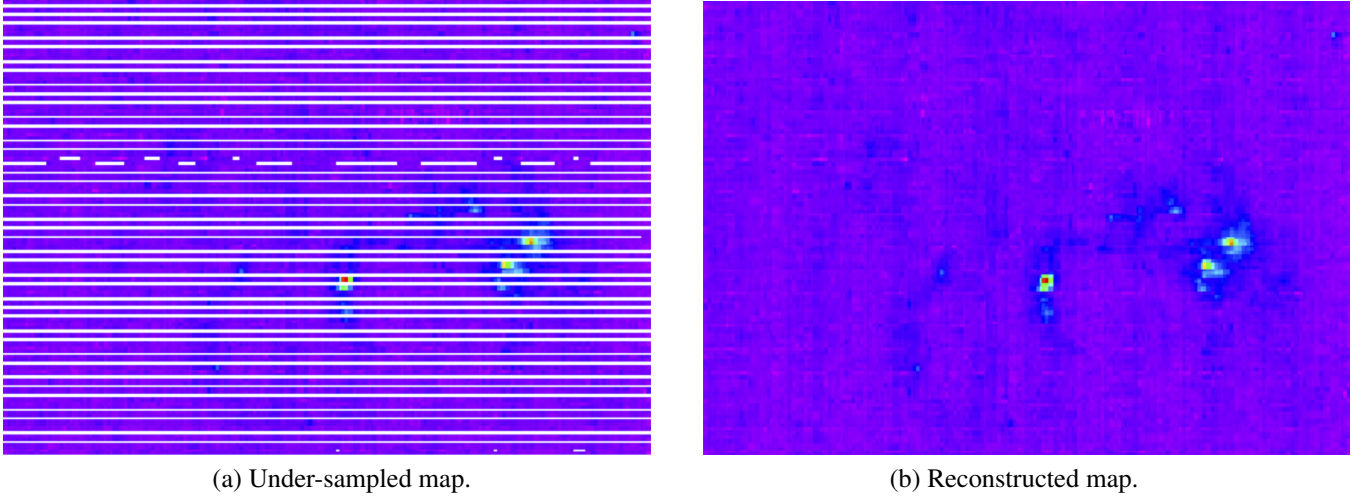


Figure 2.15 – Reconstruction of a sparsely sampled map.

Panel (a) shows the IRS mapping mode observation of IC 10 built by CUBISM (one frame from the SL1 channel). The sparse map results from spatially under-sampled observations. Panel (b) shows the reconstructed map using b-spline interpolation.

2.3 Inter-calibration

Due to their complexity, spectroscopic observations are less precise than photometry. We can, however, use the information provided by photometric maps of our source to improve the absolute calibration of their spectra. It is called *inter-calibration*. It consists in scaling our spectra to match the more accurate broadband fluxes that can be found in the IRC and IRS spectral ranges (Table 2.5).

Table 2.5 – MIR spectroscopy and broadband photometry wavelength ranges (μm).

The IRC spectrum covers the entire IRAC $_{3.6\mu\text{m}}$ broadband, so we are able to perform the inter-calibration between synthetic photometry of the IRC spectrum and the IRAC $_{3.6\mu\text{m}}$. Likewise for the IRAC $_{8\mu\text{m}}$ and the MIPS $_{24\mu\text{m}}$ which are covered by the SL and LL spectral ranges respectively.

Modules	Start ^a (μm)	End (μm)	Photometry	Start ^b (μm)	End (μm)
IRC (NG)	2.35	5.15	IRAC $_{3.6\mu\text{m}}$	3.08	4.01
			IRAC $_{4.5\mu\text{m}}$	3.72	5.22
			IRAC $_{5.8\mu\text{m}}$	4.74	6.62
IRS-SL2	5.21	7.56	IRAC $_{8\mu\text{m}}$	6.15	10.50
IRS-SL3	7.39	8.42			
IRS-SL1	7.57	14.28			
IRS-LL2	14.29	20.66	MIPS $_{24\mu\text{m}}$	18.01	32.21
IRS-LL3	19.28	21.23			
IRS-LL1	20.67	38.00			

a. Wavelengths outside these ranges have been trimmed to produce the composite spectra.

b. The wavelength ends of the broadband filters.

The photometric data we have used for this inter-calibration are taken from large surveys including the *Spitzer Infrared Nearby Galaxies Survey* (SINGS; [Kennicutt et al., 2003](#)), *DustPedia* ([Davies et al., 2017](#)), *Local Volume Legacy Survey* (LVL; [Dale et al., 2009](#)), SAGE-LMC ([Meixner et al., 2006](#)), SAGE-SMC ([Gordon et al., 2011](#)), *etc.* We perform the following steps:

1. First, we have calculated the synthetic photometry of each spectrum by integrating them within the corresponding broadband filter with its flux convention. To ensure accuracy, the integration of the spectrum has been performed on an adaptive wavelength grid.
2. Then, the observed photometric images were degraded to the angular resolution of the spectral images.
3. We have derived scaling factors for the whole map/slit and each pixel by comparing the actual photometry to the synthetic values. For the whole map, we have derived a scaling factor with a simple affine fit. The offset derived from the fit might stem from discrepancies between the background subtraction of the spectrum and that of the photometry. We have also applied the same process to each pixel independently. This will be illustrated in [Sect. 2.4.2.3](#).

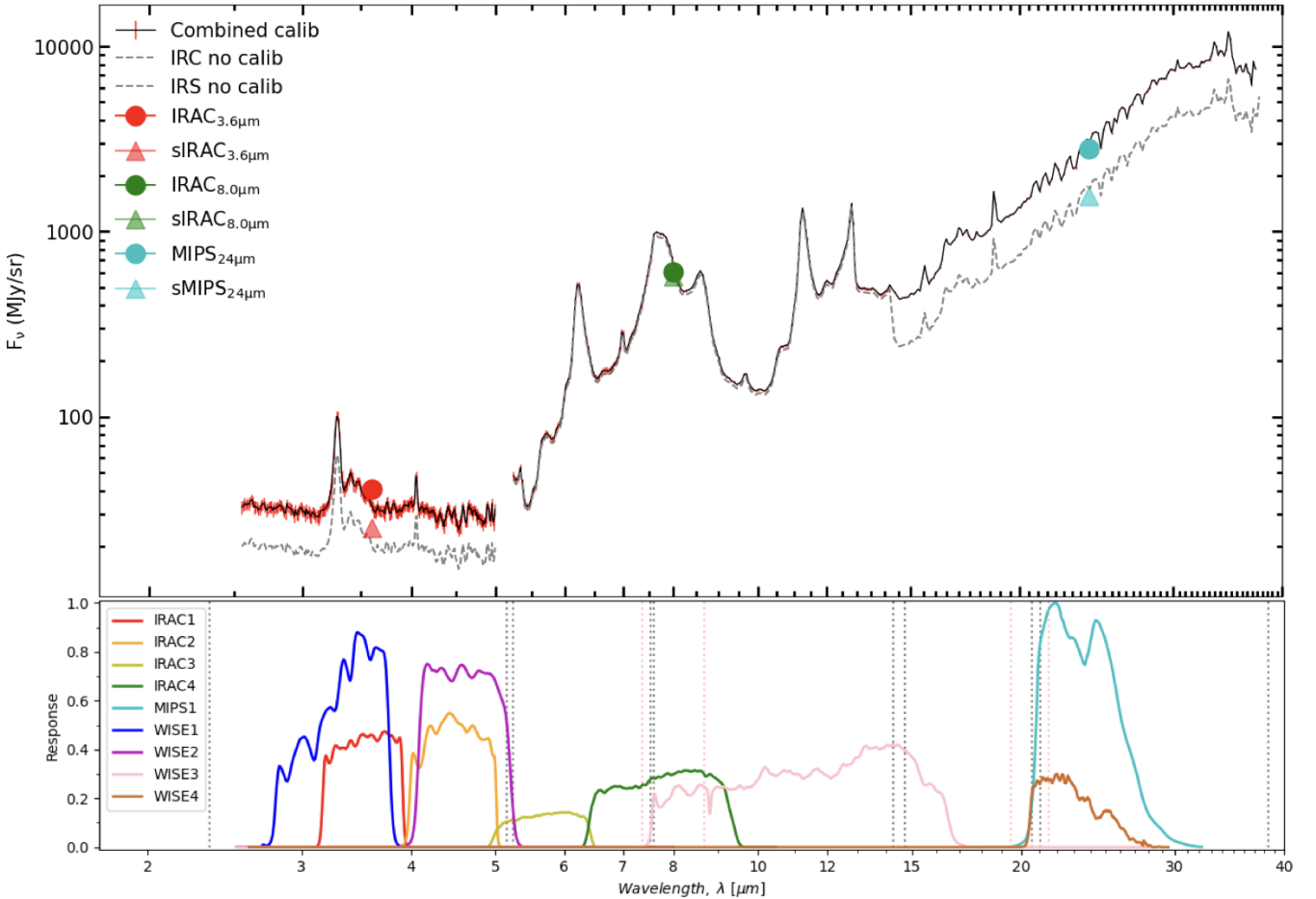


Figure 2.16 – Example of inter-calibration.

The upper part of the panel shows the original spectrum of a pixel in the M 82 disk in a gray dashed line and the inter-calibrated spectrum in a black solid line with uncertainties in red. The spectrum is overlaid with its synthetic photometry (triangles) and real photometry (circle) in the *Spitzer*/IRAC_{3.6μm}, *Spitzer*/IRAC_{8μm}, and *Spitzer*/MIPS_{24μm} broadbands. The lower part of the panel shows the broadband filters available in this wavelength range with their spectral response normalized to 1.

We show an example of this inter-calibration in Fig. 2.16. The inter-calibration procedure partially corrects the following effects:

- the difference between instrument calibrations;
- improper or inexistent background subtraction;
- diffractive flux losses out of the slit;
- the position misalignment or missing flux due to image resampling (*i.e.* rebinning and reprojection);
- the under-sampling of an irregular PSF;
- telescope pointing uncertainties.

We have checked if there were artifacts or saturation in the spectrum and in the photometry, which could lead to significant bias in the inter-calibration process (*e.g.* Fig. 2.21. d; detailed discussion in Sect. 2.4).

2.4 Case study

The entire data processing described in Sects. 2.1 – 2.2 can be summarised in Fig. 2.17. Following this workflow, we have performed a case study of M 82, which had been extensively observed by both IRS and IRC during their operating periods. M 82 is the *first light* target and the *calibrator* of many observational instruments. We have also chosen it as the “*first light*” of our software, and we have used it to demonstrate our model described in Chap. 3.

Table 2.6 – Observational parameter values for the galaxy M 82.

For parameters without a bibliographic reference, we refer to the NASA/IPAC Extragalactic Database (NED), which is funded by the National Aeronautics and Space Administration and operated by the California Institute of Technology. In addition, we quote the orientation of the IRC slits presented in Sect. 2.4.2.1.

Parameter	Value	Parameter	Value
Cross-identifications	M 82, NGC 3034, UGC 5322 Arp 337, CGCG 333-008	Equatorial coordinates ^a (J2000)	R.A.: 09h 55m 51.591s Dec.: +69d 40m 46.981s
Galaxy type	G	Disk inclination ^a (°)	81.5
Morphology	I0 edge-on	Position angle ^a (°)	65
Total mass ^a (M_{\odot})	2.7×10^{10}	IRC slit aperture angle ^b (°)	-55
Optical diameter (″)	780	Distance ^c (Mpc)	3.63 ± 0.3
(kpc) ^c	13.7	Redshift ^c z (Helio)	0.000848
Radial velocity ^a v (km s ⁻¹)	~ 300	Outflow velocity ^a v_{outflow} (km s ⁻¹)	up to 1000

^a. These parameters are from Lynds & Sandage (1963). The center of the IRC sub-slit A5 defined in Sect. 2.4.2.1 is close to the center of M 82. The inclined disk plane centered on this disk has a position angle of 65°. Velocities are measured with the H α line.

^b. This is the angle between the north celestial pole and the long axis of the IRC slits presented in Fig. 2.19. Note that M1-2 and N1-2 are rotated by 180°.

^c. Cepheid distance via Freedman et al. (1994, 2001).

2.4.1 M 82 (NGC 3034)

M 82 (NGC 3034) is an edge-on (with a favorable inclination angle of $\sim 81.5^\circ$; Lynds & Sandage, 1963), irregular, starburst galaxy. It belongs to the nearest interacting group of galaxies, dominated by M 81 (Fig. 2.18). M 82 exhibits a galactic

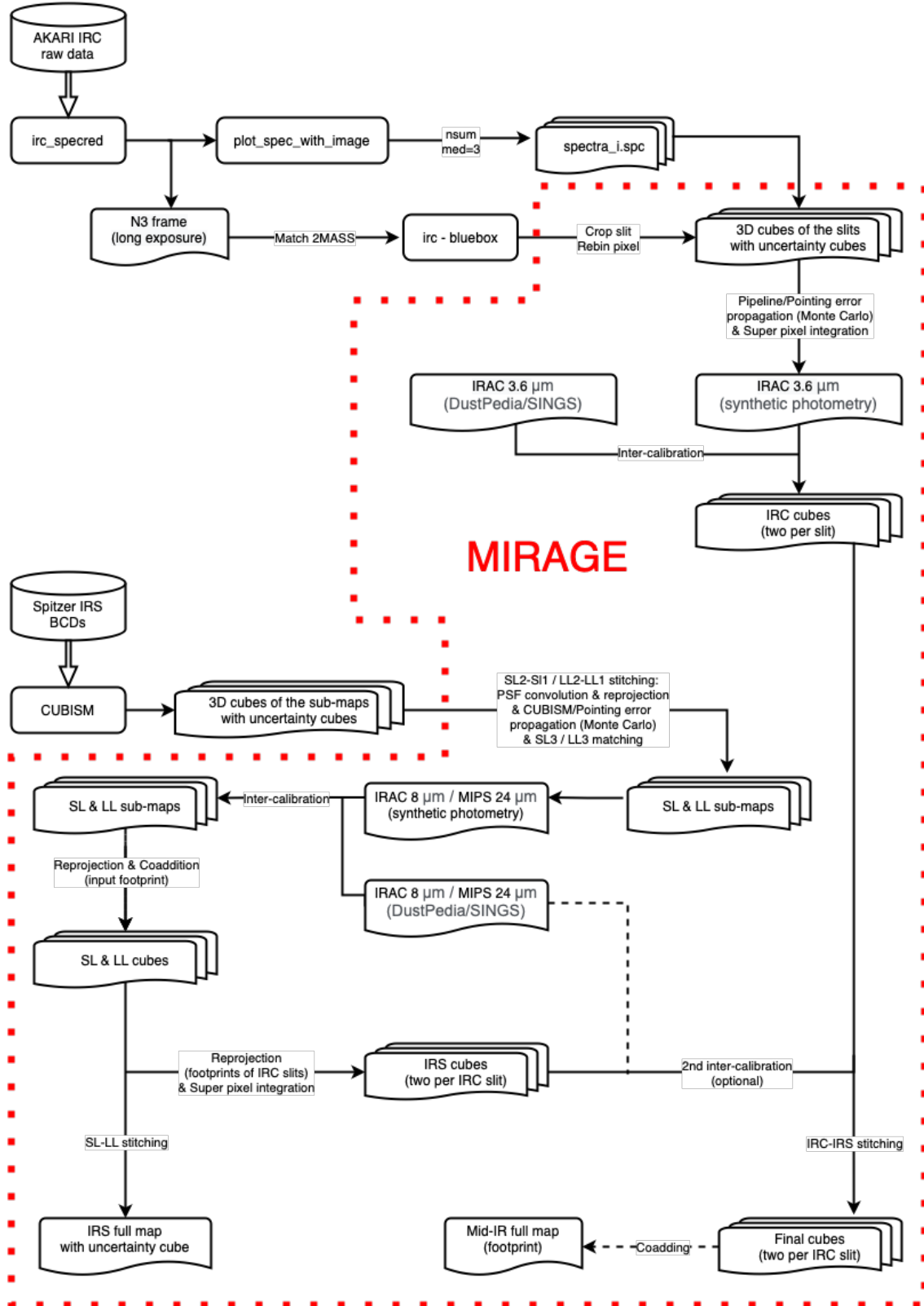


Figure 2.17 – An overview of data-processing workflow.

This schematic summarizes the entire process that we perform to construct **MIR** spectral cubes, including the extraction, calibration and coaddition of spectroscopic data from AKARI/IRC and *Spitzer*/IRS, as well as the uncertainty propagation with a *bootstrapping* method. The red dotted zone highlights the data-processing architecture of MIRAGE.

superwind triggered by its nuclear starburst. We summarize the useful observational parameters of M 82 in [Table 2.6](#).

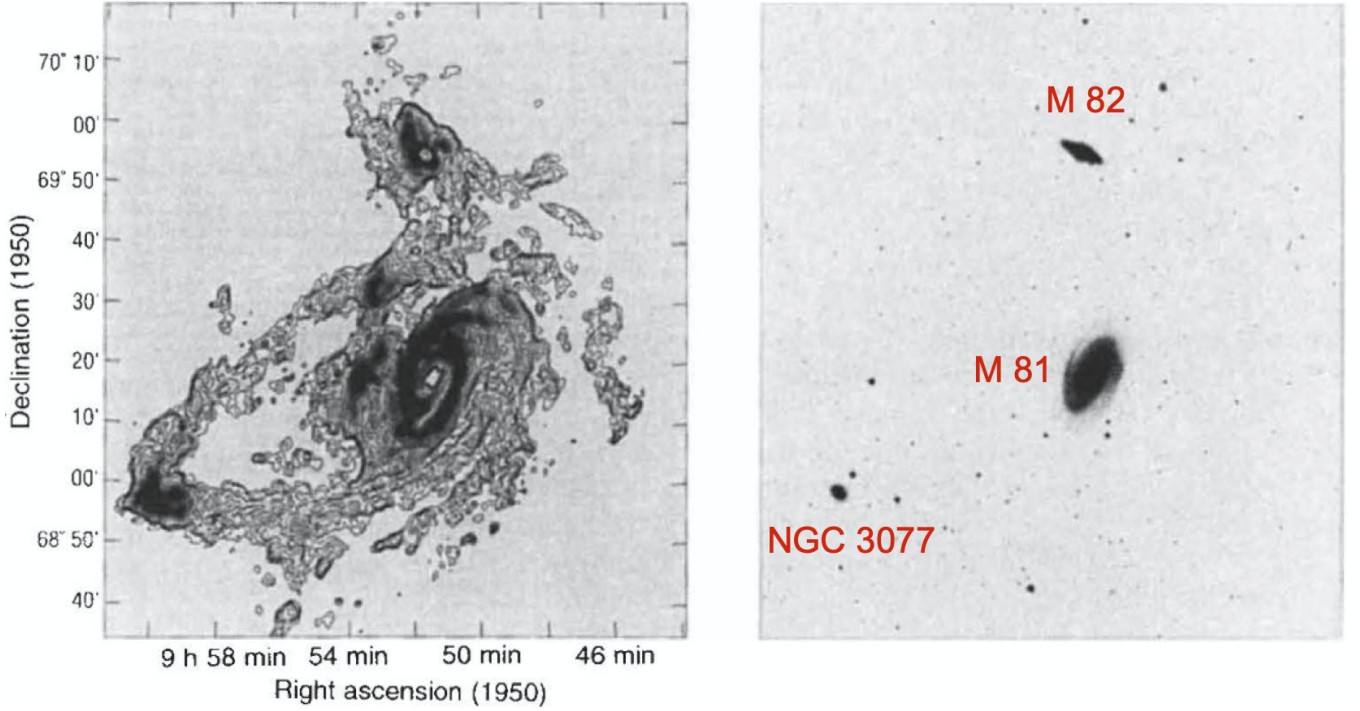


Figure 2.18 – M 82 in the M 81 group.

The left panel shows the integrated H I map from the D-array VLA mosaic observations, where we can see the north and south tidal bridges between three major galaxies. The right panel with the same field-of-view shows the Palomar sky survey image (in the red band). The three galaxies from top (north) to bottom (south) are M 82, M 81 and NGC 3077. Figure taken from [Yun et al. \(1994\)](#).

2.4.1.1 Distance measurements

M 82 is one of the most studied galaxies, thanks to its proximity and brightness. We have adopted a distance of 3.63 ± 0.3 Mpc. Indeed, it is the distance of its neighboring galaxy M 81 measured using Cepheids ([Freedman et al., 1994, 2001](#)). At this distance, an arcminute corresponds roughly to a kiloparsec²³.

H I observations imply a physical link between M 82 and M 81 (*e.g.* [Yun et al., 1994](#)). As shown in [Fig. 2.18](#), the projected separation between two galaxies is only a few tens of kiloparsecs, which is an order of magnitude smaller than the uncertainty of the distance. Moreover, this value is consistent with the distance measured with a SN Ia in M 82 (*e.g.* [Foley et al., 2014](#)).

2.4.1.2 Previous observations

Before the *space age* (1983–; the first space IR satellite), M 82 had been observed in the NIR-to-MIR by several ground-based infrared observatories (*e.g.* [Gillett et al., 1975a](#), studied the $8 - 13 \mu\text{m}$ features of M 82 with the data from the Kitt Peak National Observatory 2.1-m telescope). M 82 was one of the first identified starburst galaxies ([Rieke et al., 1980](#), using the

23. We have adopted $1.055 \text{ kpc}''$ or $17.6 \text{ pc}''$ for the unit conversions in this manuscript.

data from the Steward Observatory 2.3-m telescope). Its total IR luminosity is about $L_{\text{TIR}} \simeq 3.5 \times 10^{10} L_{\odot}$, corresponding to a TIR-estimated SFR of $\simeq 8 M_{\odot} \text{ yr}^{-1}$ (Heckman et al., 1990). According to the starburst model of Rieke et al. (1980), the burst of star formation in M 82 was triggered by its interaction with M 81. The central starburst activity has driven an asymmetric superwind (e.g. Heckman et al., 1990; Shopbell & Bland-Hawthorn, 1998). The gas content of the galactic outflow is the most evident in X-ray and H α (e.g. Strickland et al., 2004), whereas molecular lines were also detected (e.g. Taylor et al., 2001; Walter et al., 2002). Moreover, the superwind is quite dusty (e.g. Alton et al., 1999; Heckman et al., 2000), with carriers of the aromatic features surviving even in close proximity to the wind (Engelbracht et al., 2006). NIR integral field spectroscopy and ISO-SWS MIR spectroscopy (Förster Schreiber et al., 2001) allowed a detailed modeling of the starburst activity in the center of M 82 (Förster Schreiber et al., 2003b). ISO-CAM circular variable filters (CVFs; $\lambda = 5.0 - 16.5 \mu\text{m}$), despite of their low spectral resolution ($R \sim 35 - 45$), covered a wide spatial region of M 82 allowing spatially-resolved studies of the aromatic features (Förster Schreiber et al., 2003a; Galliano et al., 2008b). Follow-ups with IRC (Yamagishi et al., 2012) and IRS (Beirão et al., 2008, 2015) were conducted. Here, we have combined both IRC and IRS observations to provide a complete view of all UIB features and their variations in M 82.

2.4.2 Combined spectra

Fig. 2.19 summarizes all the IRC and IRS archived observations we have collected. We have listed the AKARI/IRC slits in Table 2.7 and the *Spitzer*/IRS maps in Table 2.8.

2.4.2.1 AKARI/IRC spectra

Following Yamagishi et al. (2011, 2012), we have defined “*sub-slits*”, which are part of the original slit that we have rebinned to improve the S/N ratio. We have determined the angular size of these sub-slits as a function of the surface brightness of $\text{IRAC}_{8\mu\text{m}}$ (Figs. 2.22 – 2.24) with the following criteria.

- Slits covering the galaxy center (inside the contour of 3% of the flux density peak) are divided into 7 sub-slits (A1-7, B1-7, C1-7).
- Slits on two edges of the galaxy disk (above 0.3% peak contour) are divided into 4 sub-slits (D1-4, E1-4).
- Slits in the southern and northern galactic winds (below 0.3% peak contour) are divided into 2 sub-slits (F1-2, G1-2, H1-2, I1-2, J1-2, K1-2, L1-2).
- We have also included slits near the northern wind cap (M1-2, N1-2). We integrate the flux in these faint slits.

All the 14 slits of M 82 that we have processed (Table 2.7) are from the IRC-NG mode²⁴. Among these slits, the M 82 northern wind cap regions (M1-2 & N1-2) were observed during phase 1&2 which prevented them from suffering from the $\sim 70\%$ reduction of sensitivity for slits observed during the post-Helium phase. This partially compensates for the low S/N ratio along

24. The IRC-NP data of M 82 are excluded because they suffer from an astrometric matching issue within the “IRC Imaging Toolkit” (Sect. 2.1.2.4).

with flux density binning. The D1-4, E1-4, F1-2, J1-2, K1-2 and L1-2 slits are taken during the instrument calibration time between phases 1&2 and phase 3. Other slits belong to phase 3 data.

Table 2.7 – AKARI/IRC AORs of M 82.

Obs. date	Obs. ID	AOT ^a	AOTP ^b	Sub-slit	Aperture size ["]	Projected size [kpc]	Location	IRS covered
18/04/2007	5124077.1	IRC04	b;Nh	N1-2	3 × 18	0.05 × 0.32	north wind cap	No
			b;Ns	M1-2	5 × 18	0.09 × 0.32	north wind cap	Yes
22/10/2007	5125403.1	IRC64	b;Nh	L1-2	3 × 18	0.05 × 0.32	north outer wind	Yes
			b;Ns	K1-2	5 × 18	0.09 × 0.32	north wind	Yes
22/10/2007	5125405.1	IRC64	b;Nh	D1-4	3 × 9	0.05 × 0.16	disk edge	Yes
			b;Ns	F1-2	5 × 18	0.09 × 0.32	south wind	Yes
23/10/2007	5125401.1	IRC64	b;Nh	J1-2	3 × 18	0.05 × 0.32	north wind	Yes
			b;Ns	E1-4	5 × 9	0.09 × 0.16	disk edge	No
22/10/2008	3390001.2	IRCZ4	b;Nh	A1-7	3 × 6	0.05 × 0.11	center disk	Yes
			b;Ns	H1-2	5 × 18	0.09 × 0.32	south wind	Yes
22/10/2008	3390003.1	IRCZ4	b;Nh	B1-7	3 × 6	0.05 × 0.11	center disk	Yes
			b;Ns	G1-2	5 × 18	0.09 × 0.32	south wind	Yes
23/10/2008	3390002.1	IRCZ4	b;Nh	C1-7	3 × 6	0.05 × 0.11	center disk	Yes
			b;Ns	I1-2	5 × 18	0.09 × 0.32	south wind	Yes

a. The IRC04 observations were taken during phase 1&2; the IRCZ4 observations were taken during phase 3. Both are publicly available on <http://darts.isas.jaxa.jp/astro/query/basic.php>. The IRC64 observations were taken during the instrumental calibration time, provided by the AKARI team. The IRC64 data can be reduced using the official pipeline tools for phase 3.

b. AOT parameters: [a-c];N[s/h]. The first letter marks the filter element; a for NP, b for NG, and c for both. The last letter indicates the target position; s for wider slit, h for narrower slit.

2.4.2.2 Spitzer/IRS spectra

IRS low-resolution observations of M 82 were all carried out during the cryogenic phase. We have listed all 14 maps of IRS (7 for SL; 7 for LL) in Table 2.8 with their observation time. We have put AORs that were carried out within 24 hours and with the same exposure time into one single CUBISM project to build a spectral cube. Hence, they share the same background (if available) and global-level bad pixels. Inter-calibration is performed after image convolution and reprojection for each IRS map. An important role of inter-calibration is to correct improper or inexistent background subtraction, such as in the case of 04-SL, which has no dedicated sky observations (*cf.* Sect. D.2.1). Finally, we have coadded and reprojected the SL and LL maps on the image grid of each IRC slit.

Table 2.8 – *Spitzer*/IRS AORs of M 82.

Target name ^a	AORKEY	Channels	Observation start time	Observation duration	Sub-map ^b
M82	7829760	LL	2003-11-16 11:17:06	00:30:23	03-LL
M82 lores	3840768	SL	2004-10-20 12:20:26	01:57:36	04-SL
		LL			04-LL
NGC 3034	9501184	LL	2005-03-11 06:59:15	00:55:49	05-LL
M82 sky LL	18376448	LL	2006-11-10 17:37:49	00:06:53	06-LL (BG)
M82 wind-N	18375936	LL	2006-11-10 17:45:37	01:17:16	06-LL
M82 sky LL	18376960	LL	2006-11-10 19:03:46	00:06:52	06-LL (BG)
M82 wind-N	18376192	LL	2006-11-10 19:11:31	01:17:16	06-LL
M82 sky SL	18377216	SL	2006-11-11 01:39:41	00:12:07	06S-SL (BG)
M82 wind-S	18375424	SL	2006-11-11 01:52:51	05:59:21	06S-SL
M82 sky SL	18377472	SL	2006-11-11 09:06:06	00:12:07	06S-SL (BG)
M82 wind-S	18375680	SL	2006-11-11 09:19:21	05:59:21	06S-SL
M82 sky SL	18375168	SL	2006-11-13 03:23:00	00:12:07	06N-SL (BG)
M82 wind-N	18374656	SL	2006-11-13 03:36:13	05:59:21	06N-SL
M82 sky SL	18376704	SL	2006-11-14 03:32:13	00:12:06	06N-SL (BG)
M82 wind-N	18374912	SL	2006-11-14 03:45:25	05:59:20	06N-SL
M82 outer wind	26468096	SL	2008-05-22 06:56:17	05:41:03	08-SL
M82 wind-cap	26467840	LL	2008-05-22 12:37:20	05:18:57	08-LL
M82 sky1a	27183872	LL	2008-05-22 17:56:13	00:07:06	-
M82 sky1	27183616	LL	2008-05-22 18:03:19	00:07:54	08-LL (BG)
M82 sky2	27183360	LL	2008-05-22 18:11:13	00:07:52	08-LL (BG)
M82 sky2a	27183104	LL	2008-05-22 18:19:05	00:07:13	-
M82 sky3	27182848	LL	2008-05-22 18:26:18	00:24:35	08-LL (BG)
M82 sky1a	27182592	SL	2008-05-22 18:50:59	00:26:47	-
M82 sky1	27182336	SL	2008-05-22 19:16:47	00:13:19	08-SL (BG)
M82 sky2	27182080	SL	2008-05-22 19:30:07	00:13:18	08-SL (BG)
M82 sky2a	27181568	SL	2008-05-22 19:43:25	00:26:53	08-SL
M82 outer wind	26465792	LL	2008-05-22 20:17:59	01:55:40	08-LL
M82 outer wind	26467328	SL	2008-05-22 22:13:40	05:40:27	08-SL
M82 wind-cap	26467584	SL	2008-05-23 10:56:30	06:48:42	08c-SL
M82 sky3	27181824	SL	2008-05-23 17:53:11	00:35:28	08c-SL (BG)
M82 wind-cap	26468352	SL	2008-05-23 18:28:39	06:43:54	08c-SL
M82 sky6	33396480	LL	2009-05-09 17:46:56	00:16:59	09N3-LL (BG)
M82 wind-N3	33397760	LL	2009-05-09 18:03:55	01:01:05	09N3-LL
M82 wind-N3	33395456	SL	2009-05-09 19:05:01	06:00:26	09N3-SL
M82 wind-N3	33395200	SL	2009-05-10 01:05:32	06:00:21	09N3-SL
M82 sky6	33397248	SL	2009-05-10 07:08:21	00:13:19	09N3-SL (BG)
M82 sky5	33397504	SL	2009-05-11 19:34:41	00:17:44	09N2-SL (BG)
M82 wind-N2	33394944	SL	2009-05-11 19:51:27	06:00:33	09N2-SL
M82 wind-N2	33394688	SL	2009-05-12 08:36:38	06:02:58	09N2-SL
M82 wind-N5	33394432	LL	2009-05-12 17:58:34	01:59:38	09N5-LL
M82 sky8	33395712	LL	2009-05-12 20:04:25	00:08:14	09N5-LL (BG)
M82 wind-N2	33394176	LL	2009-05-13 21:58:29	01:02:54	09N2-LL
M82 sky5	33396736	LL	2009-05-13 23:01:23	00:07:54	09N2-LL (BG)

^a. For each AOR, we adopt the same target name as that in the SHA database.

^b. The LL module is shaded grey. Dedicated background observations are marked with “(BG)”. Note that we have not used “M82 sky1a” and “M82 sky2a” because they are within the M 82 galactic wind regions.

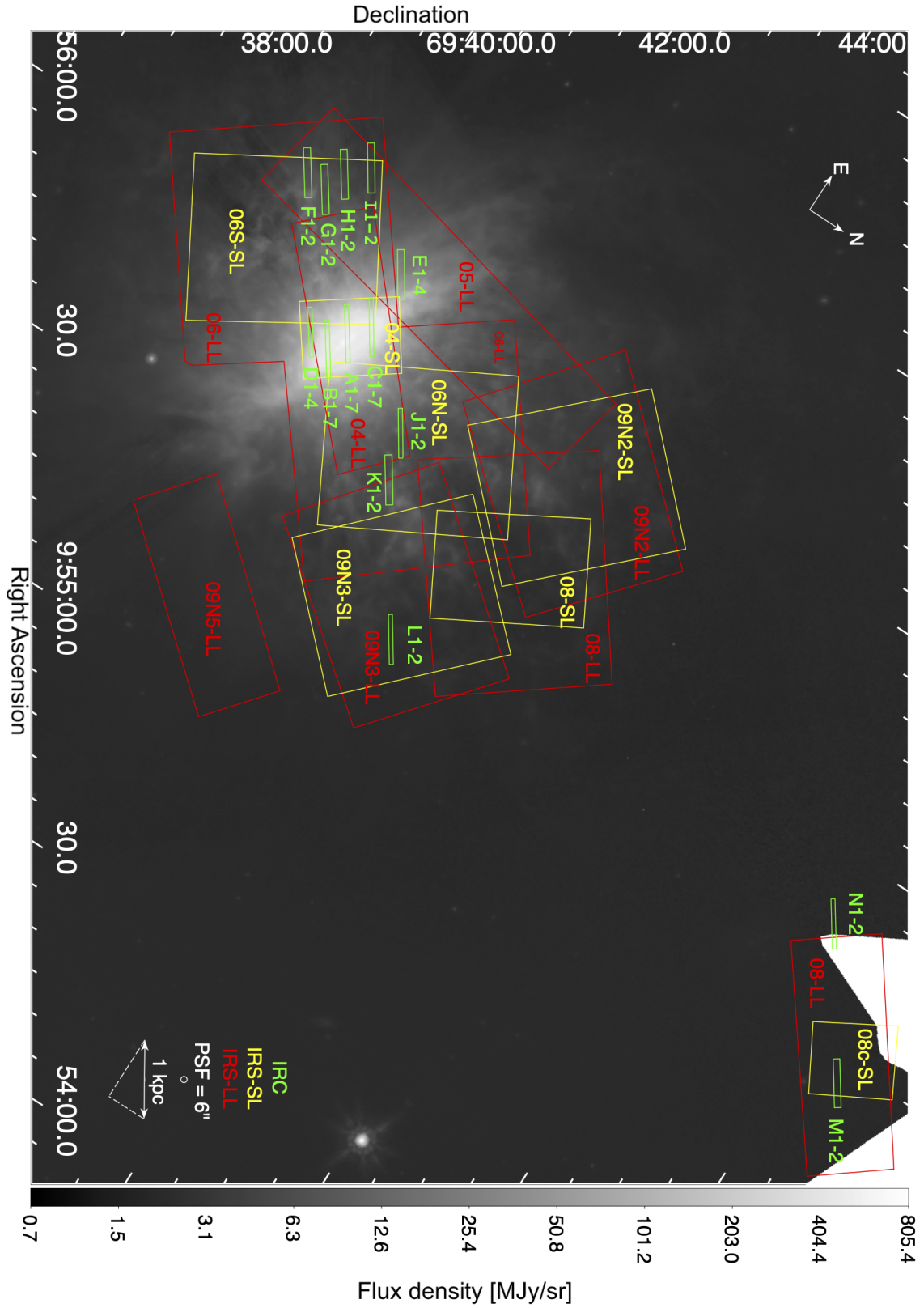


Figure 2.19 – Illustration of M 82 observations.

This schematic (IRC slit orientation; Table 2.6) shows the position of AKARI/IRC slits (green; indicated with the slit names defined in Table 2.7) and *Spitzer*/IRS SL/LL maps (yellow/red) overlaid on the IRAC_{8μm} image (source: DustPedia).

2.4.2.3 Inter-calibration

First, we have checked if there were artifacts or saturation in the spectral cubes or photometric images, which could lead to significant biases. There is a fringe pattern beyond $20\ \mu\text{m}$ in some spectra (e.g. Fig. 2.20. a) and the corresponding pixels fall into the saturation hole in the M 82 central nucleus of the MIPS $_{24\mu\text{m}}$ image (source: SINGS; Fig. 2.20. b). *A priori*, this artifact will not be a problem for our spectral decomposition since there are no UIBs in this spectral range, and we truncate our spectra above $20\ \mu\text{m}$ before fitting them.

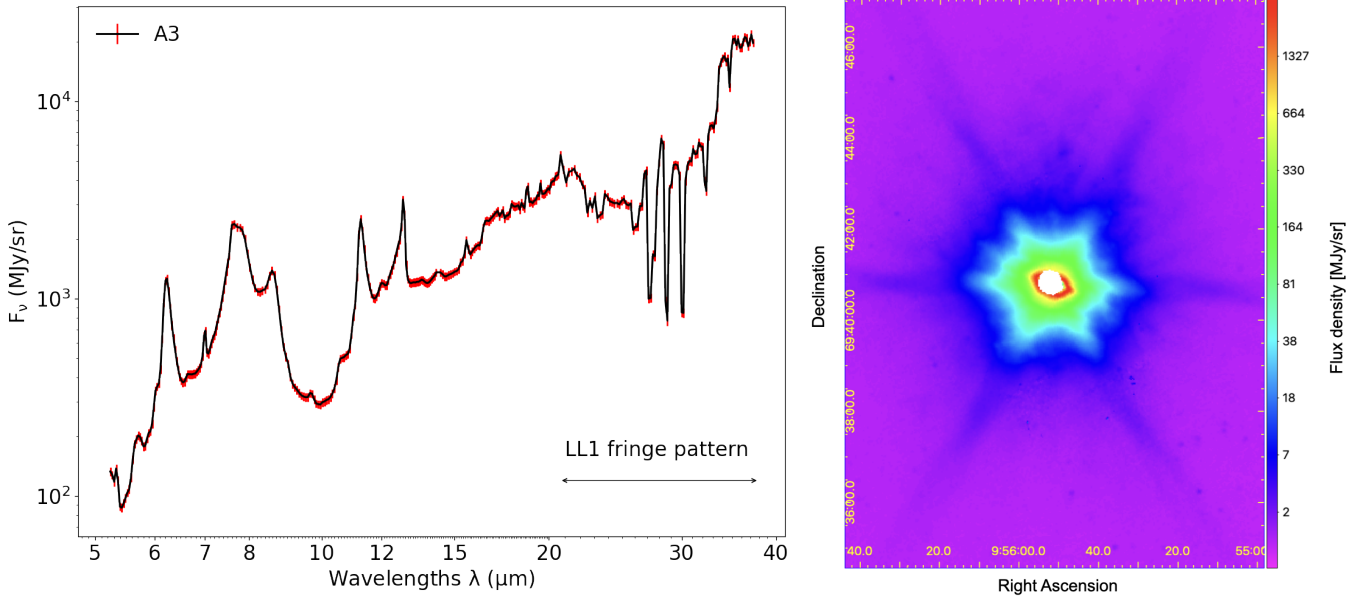


Figure 2.20 – Saturation effect in *Spitzer* observations.

Panel (a) shows the *Spitzer*/IRS A3 spectrum located in the M 82 center which presents a fringe pattern artifact in the LL1 regime ($> 20\ \mu\text{m}$). Panel (b) shows the *Spitzer*/MIPS $_{24\mu\text{m}}$ map (source: SINGS) of M 82, where the lack of data in the central nucleus is due to the saturation effect.

Then, we have followed the inter-calibration process described in Sect. 2.3 to derive a global correction factor for each IRC individual slit (using the IRAC $_{3.6\mu\text{m}}$ map; linearly fitting the correlation without an offset;) and each IRS-SL map (using the IRAC $_{8\mu\text{m}}$ map; linearly fitting the correlation with an offset; Fig. D.10. 1 – 6). Next, we have corrected the spectra with the inferred scaling factors, ranging from ~ 0.4 to 2.2 for the IRC spectra and from ~ 0.7 to 1.7 with non-negligible offsets for the IRS-SL spectra. As for IRS-LL maps, we have only shown the inter-calibration results in Fig. 2.21. a and Fig. D.10. 7 – 12 (using the MIPS $_{24\mu\text{m}}$ maps) without doing any correction at this step. We have simply stitched the IRS-LL spectra to the IRS-SL spectra because the saturation effect shown in Fig. 2.20 prevents any reliable inter-calibration of the long-wavelength module.

Given that IRS observations fully cover almost all IRC slits except the E1-4 and N1-2 (Fig. 2.19), we have reprojected all IRS maps on the grid of IRC slits with the same pixel size (Sect. 2.2.3.1). After the image reprojection and spectrum stitching, we have applied a second inter-calibration to the combined spectra of 41 rebinned IRC sub-slits (A1-7, B1-7, C1-7, D1-4, F1-2, G1-2, H1-2, I1-2, J1-2, K1-2, L1-2 and M1-2; Fig. 2.21. b – d) to inspect residual discrepancies. Overall, the synthetic

photometry of the final spectra fits well the IRAC images with scaling factors of 1.026 for the IRC regime and 1.017 for the IRS-SL regime, respectively. As for the IRS-LL regime, the outliers of the fit (*i.e.* synthetic photometry of the A2, A3 and A7 spectra; Fig. 2.21. d) correspond to the pixels partially in the bright zone in the center of M 82. They suffer from the saturation hole of the MIPS_{24μm} map²⁵. On the other hand, the other outliers, in faint regions (*e.g.* synthetic photometry of the L, M and N spectra), originate from the low-surface-brightness-end dispersion at the first inter-calibration stage, as shown in Fig. D.10. 9 & 10 (*i.e.* northern outer wind and cap regions). We have found a scaling factor of 0.97 for the IRS-LL regime after excluding the sub-slits affected by the MIPS saturation hole. Unlike the first inter-calibration, we have not corrected the final IRS spectra with the fitted scaling factor because this will be taken care of in our spectral fitting by treating the calibration error (Sect. 3.2.1.2).

Table 2.9 – Spectrum stitching process for M 82.

First, we have stitched both IRS-SL2 and SL1 spectra to the bonus order SL3 (Sect. 2.2.3.2). *Idem* for the IRS-LL modules. Then, we have inter-calibrated the IRC spectra with IRAC_{3.6μm} and the SL spectra with IRAC_{8μm}, respectively. Both the LL1 spectra and the MIPS_{24μm} image suffer from the saturation in the M 82 central disk region. Consequently, we have not inter-calibrated the LL spectra. After reprojecting IRS maps to the IRC slit grids, we have redone the inter-calibration to anchor the SL spectra. Until this moment, the IRC and SL spectra match well one another, thanks to the consistency of *Spitzer*/IRAC. Finally, we have stitched the LL spectra to the SL spectra.

	IRC - IRS	SL2 - SL1	SL - LL	LL2 - LL1
1st step	-	Stitching to bonus orders (IRS grids)	-	Stitching to bonus orders (IRS grids)
2nd step	Inter-calibrating each IRC slit (IRC grids) with IRAC _{3.6μm} ; Global scaling factor without offset.	-	Inter-calibrating each SL map (IRS grids) with IRAC _{8μm} ; Global scaling factor with offset. Inter-calibrating each LL map (IRS grids) with MIPS _{24μm} ; No correction.	-
3rd step	Inter-calibrating all IRC spectra (IRC grids) with IRAC _{3.6μm} ; No correction.	-	Inter-calibrating all rebinned SL spectra (IRC grids) with IRAC _{8μm} ; No correction. Inter-calibrating all rebinned LL spectra (IRC grids) with MIPS _{24μm} ; No correction.	-
4th step	-	-	Stitching LL to SL (IRC grids)	-

2.4.2.4 Final spectra

As a result, we have obtained 41 spectra of M 82 covering regions from its southern wind to the central disk to the northern wind and up to the northern wind cap. We have presented all these spectra in Figs. 2.22 – 2.24 and Figs. D.11 – D.20. The IRC and IRS-SL spectra, independently inter-calibrated before stitching, match well for all sources. The IRS-LL spectra directly

25. The sub-slits A4, A5 and A6 completely fall into the saturation hole of the MIPS_{24μm} map, so they do not appear in Fig. 2.21. d

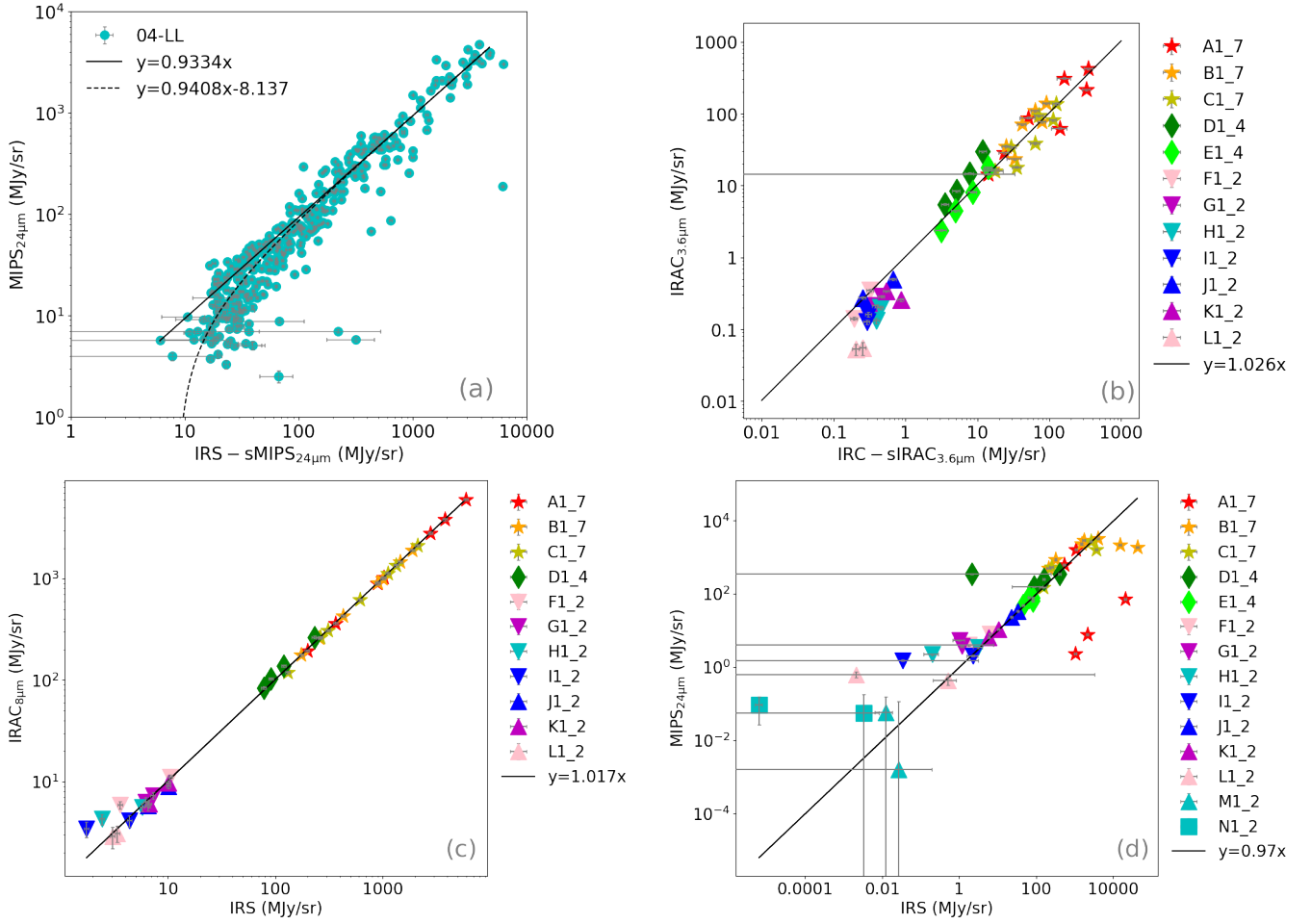


Figure 2.21 – Inter-calibration diagrams.

Panel (a) shows the first inter-calibration of an IRS map. In the case of 04-LL, there is no dedicated sky observation available for the IRS spectra, whereas the MIPS_{24μm} map is background subtracted. This discrepancy explains the fitted offset (dashed line). *Idem* for the second inter-calibrations of the rebinned IRC spectra (panels (b)) and the IRS spectra reprojected to the IRC slit grid (panels (c) and (d)). The absence of the M and N sub-slits (*i.e.* M 82 northern wind cap) is due to the limitation of the IRAC map (source: SINGS) coverage. All linear fits have been performed with the Levenberg-Marquardt algorithm implemented in MINPACK. Uncertainties are estimated with our Monte Carlo *bootstrapping* error propagation, plus the calibration uncertainty: 3% for IRAC, 4% for MIPS, 5% for IRS and 10% for IRC Table 2.3.

stitched to the SL module also agree with the MIPS_{24μm} observations (Fig. 2.21. d). The quality of the LL1 spectra is generally worse. They suffer either the saturation effect in the central disk or the low S/N ratio in the outer wind regions. Therefore, we only present some of the LL1 spectra without obvious artifacts such as A1 and A2 in Fig. 2.22. We will see in the following chapters that there are no UIB features in the spectral range of LL1. Consequently, all the spectra to fit are truncated at the end of the LL2 module and sampled at 419 wavelengths in total.

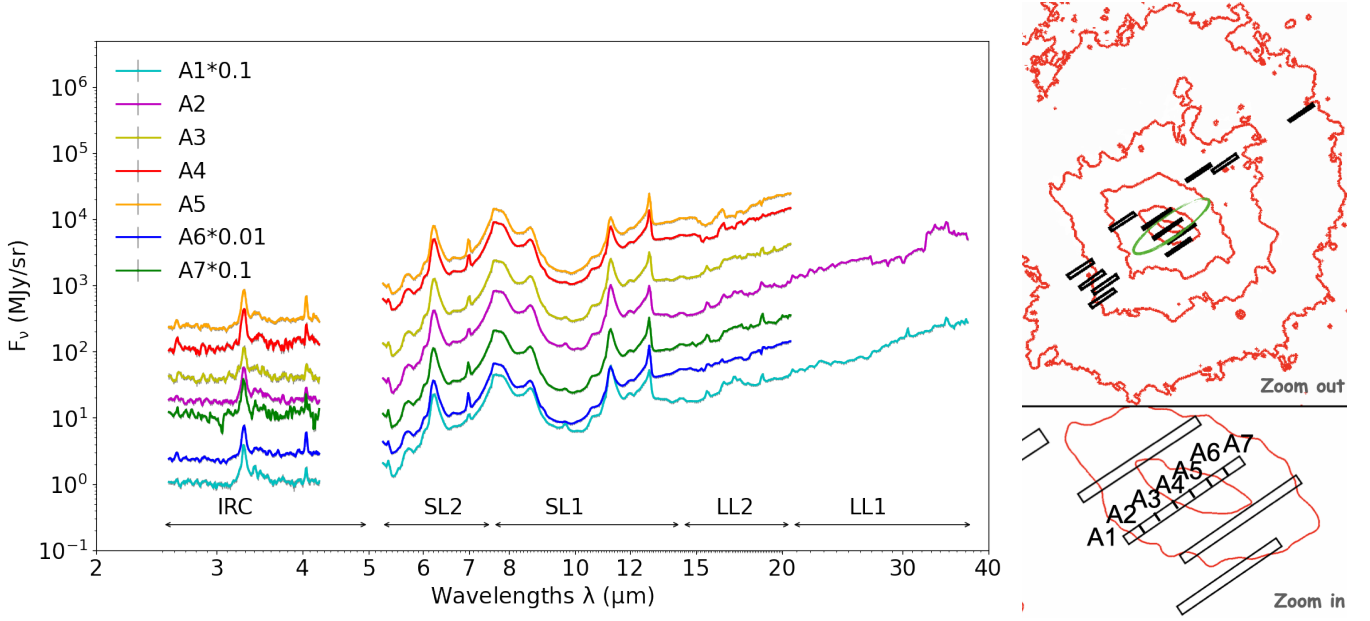


Figure 2.22 – Combined spectra of M 82 (slit A; central disk).

Slit A in the center of M 82 with high S/N ratios. The slit position in the sky (green dashed ellipse) is indicated over the $\text{IRAC}_{8\mu\text{m}}$ map (red contours from inside to outside: 30%, 3%, 0.3%, 0.08% and 0.04%). Note that the A1, A6 and A7 spectra have been scaled by a factor of 0.1, 0.01 and 0.1, respectively, to avoid overlap.

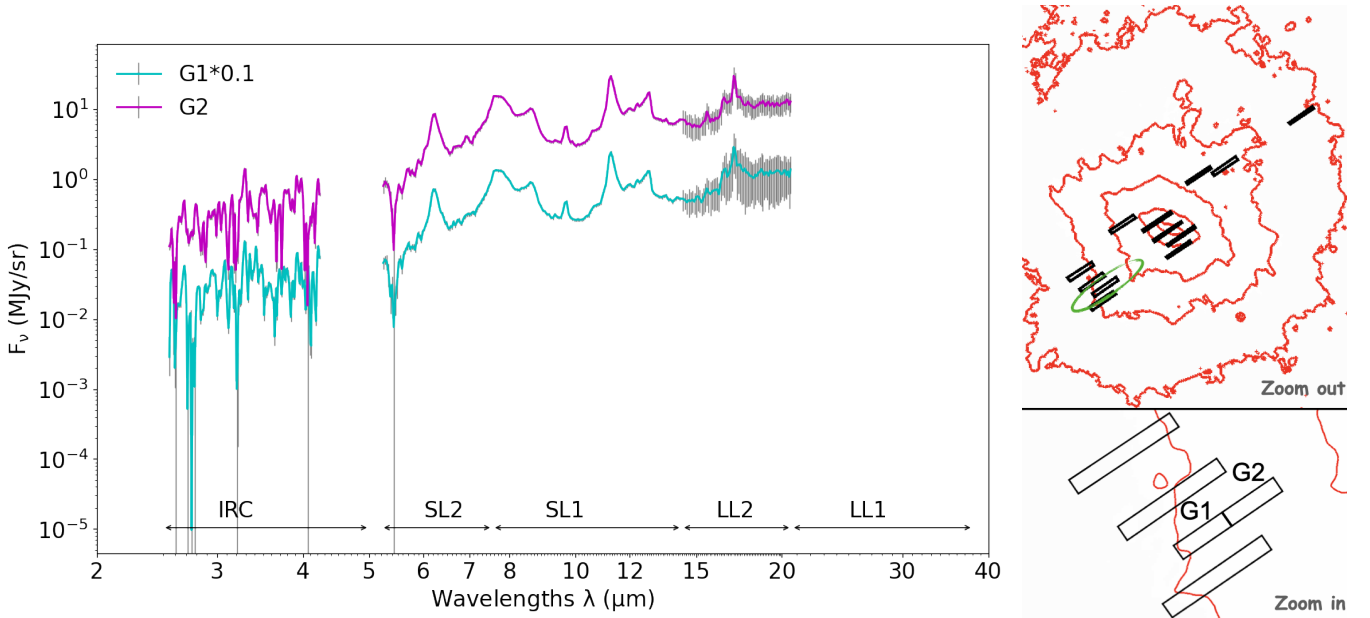


Figure 2.23 – Combined spectra of M 82 (slit G; southern wind).

Slit G in the southern wind of M 82 with relatively lower S/N ratios. The slit position in the sky (green dashed ellipse) is indicated over the $\text{IRAC}_{8\mu\text{m}}$ map (red contours from inside to outside: 30%, 3%, 0.3%, 0.08% and 0.04%). Note that the G1 spectrum has been scaled by a factor of 0.1 to avoid overlap.

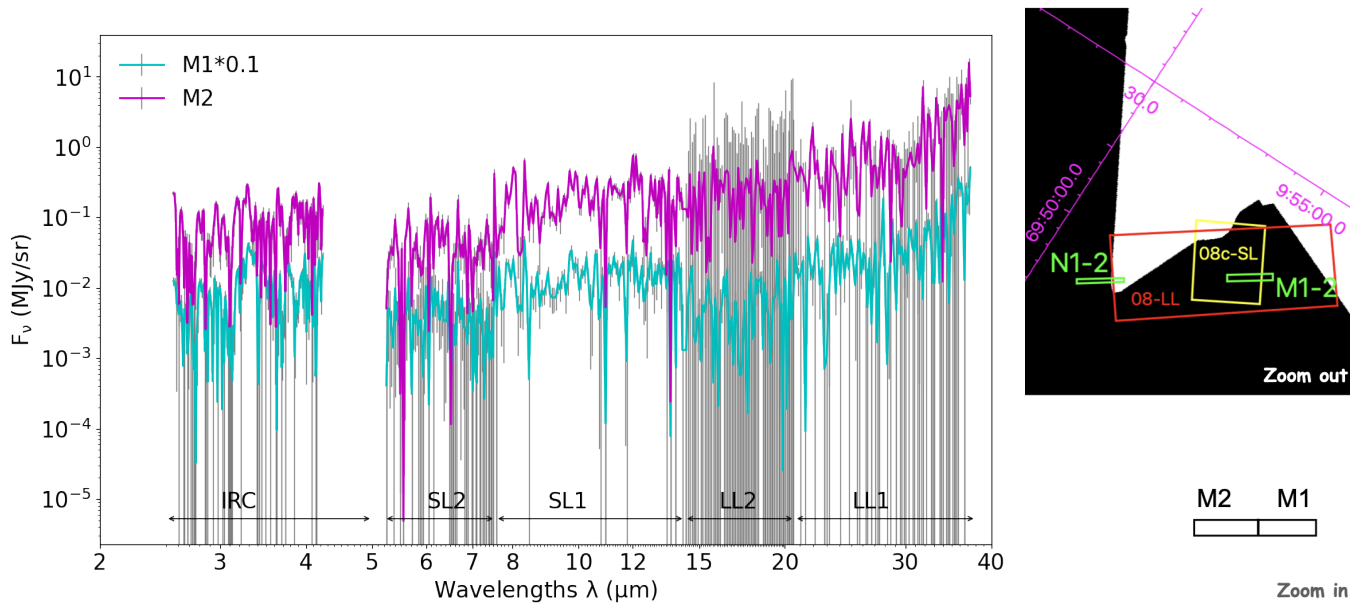


Figure 2.24 – Combined spectra of M 82 (slit M; northern wind cap).

Slit M in the northern wind cap of M 82 with extremely low S/N ratios. This slit is not covered by the SINGS IRAC_{8μm} map, so we put a clip of Fig. 2.19 instead. Note that the M1 spectrum has been scaled by a factor of 0.1 to avoid overlap.

Chapter 3

Modeling MIR emission

What I cannot create, I do not understand.

Richard P. Feynman

This chapter is dedicated to presenting my **MIR** spectral decomposition software, MILES¹, which is one of the main products of this thesis ([Paper I](#)). It is a Fortran code, with a Python interface, that I have developed myself. It uses some of the modules of HerBIE ([Galliano, 2018](#)), especially its Gibbs sampling routine, but MILES and HerBIE are distinct codes, as they are applied to different physical models and have different technical challenges.

First, I describe the different components I use to physically model the **MIR** spectrum. I discuss the calibration of **UIB** profiles using high-resolution, high-signal-to-noise ratio spectra of Galactic regions. The resulting model has a relatively large number of parameters (significantly larger than HerBIE), which makes its optimization challenging. I have implemented the least-squares, standard Bayesian and hierarchical Bayesian methods to statistically fit observed spectra. Finally, after assessing the performances of MILES using a set of simulated galaxy spectra, I fit the combined M 82 spectra produced by MIRAGE and presented in [Sect. 2.4](#).

1. MILES: Mid-Infrared Line Extraction Software (open access on <https://github.com/kxxdhdn/MISSILE/tree/main/MILES>).

3.1 Physical model

Our approach is interpretative. We aim to quantify the complex information contained in **MIR** spectra. For that purpose, our model is designed to extract the intensity, and possibly the central wavelength and width, of all **UIBs** of interest. It needs to also account for all the other processes contributing to the **MIR** spectrum: dust grain continuum emission, gas lines, stellar emission, dust and ice absorption. The model that we are going to use thus needs to be carefully crafted to account for all these components with a minimum number of parameters.

3.1.1 The Technical Challenges

To study variations of the **UIB** properties across environments, we need to adopt a functional band profile. Assuming the band behaves as a damped harmonic oscillator, we can model a **UIB** with a Lorentz profile (Verstraete et al., 1996; Boulanger et al., 1998). From an observational point of view, several **UIBs** appear asymmetric. This could be due to either the intrinsic anharmonicity of the features or the blending of several sub-features (see discussion in Boulanger et al., 1998). Asymmetric features are thus necessary to accurately fit good quality spectra. The difficulty in the **MIR** spectrum modeling lies in the following aspects.

- These features have relatively large intrinsic widths ($\Delta\lambda \approx 1 \mu\text{m}$) compared to gas lines. Their broad wings contribute to the spectral mixture (*i.e.* the band-band, band-line and band-continuum degeneracy) as well. Consequently, deblending adjacent bands and their underlying continuum is uncertain.
- The **UIB** profiles are not precisely constrained and are known to vary. In Sect. 3.1.2, we have used high-spectral-resolution, high-signal-to-noise ratio spectra to identify up to ≈ 40 individual bands, some being very weak. The assumption about the number and spectral properties of these bands, therefore adds another layer of uncertainties.
- A degeneracy between the visual extinction, A_V , and the strength of a few bands is caused by silicate and ice absorption.
- In our case, where spectra from different observation modules are jointly fitted, the calibration error is also a significant source of uncertainties.

There exist several distinct methods to decompose a **MIR** emission spectrum. For example, in Fig. 3.1. a & b, Galliano et al. (2008b) compared the *spline method* (fitting a spline function; *e.g.* Vermeij et al., 2002) and the *Lorentzian method* (using Lorentz profiles to model the bands; *e.g.* Boulanger et al., 1998). They found the two methods gave different band intensities, but the dynamic range and trends between band ratios were consistent. Rapacioli et al. (2005a) and Berné et al. (2007) proposed a different approach (that we call the *Template method*) which consists in fitting phenomenological templates that were derived using a blind-signal separation analysis. These templates are the following: neutral **PAHs** (PAH^0), ionized **PAHs** (PAH^+), large ionized **PAHs** (PAH^x) and evaporating **Very Small Grains** (eVSGs), as presented in Fig. 3.1. c. Compared to the Lorentzian method, this model produces fewer degeneracies because it has a smaller number of free parameters. In addition, the fitting results provide a more straightforward physical interpretation in terms of the mixing of different types of grains. However, it

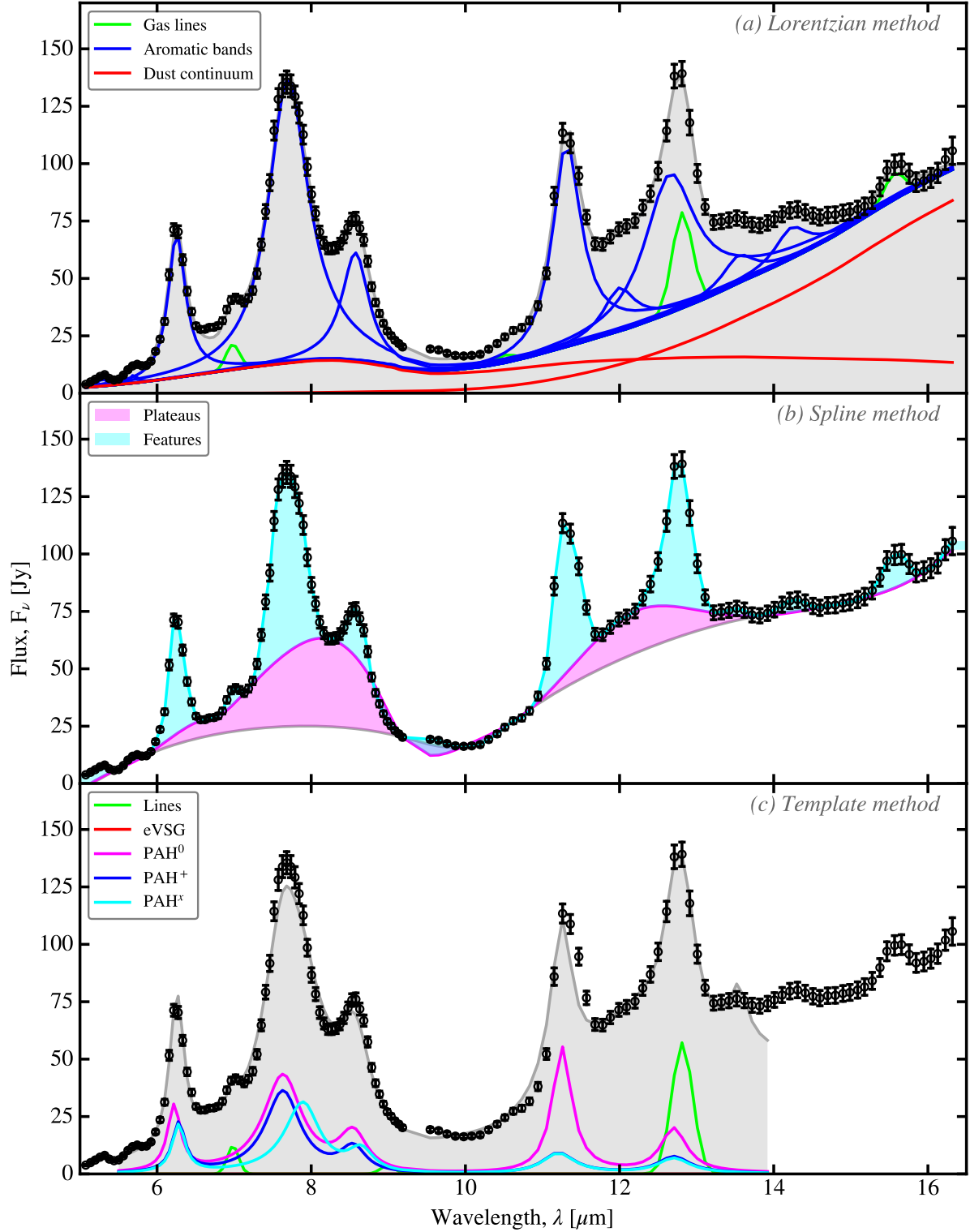


Figure 3.1 – Comparison of three MIR spectral fitting methods.

The observation (black circles with error bars) is the total ISO-CAM spectrum of M 82 presented by [Galliano et al. \(2008b\)](#). The model of panel (a) has been fitted with a least-squares method. Panel (b) is a spline interpolation with arbitrary anchor points to separate bands (cyan), plateaus (magenta), and dust continuum (white). The fit of panel (c) has been performed with PAHtat (least-squares fit; [Pilleri et al., 2012](#)) below 12 μm . Figure taken from [G22](#).

lacks flexibility when looking at high signal-to-noise spectra of peculiar astrophysical environments or at larger scales where different physical conditions blend together. We summarize the characteristics of these three fitting methods in [Table 3.1](#), and we also refer to [Peeters et al. \(2017\)](#) and [G22](#) for similar discussions.

Table 3.1 – Overview of three MIR spectral fitting methods.

Method	Lorentzian	Spline	Template
Profile	Lorentzian (or Drude)	Spline functions	4 classes of components
Feature	Individual bands are identified and calibrated using high-resolution, high-S/N ratio spectra of Galactic regions. Alternatively, laboratory measured or theoretically calculated spectra can be applied.	Extracting the main band complexes by interpolating the spline anchor points relies on arbitrary choices.	Linear combination of a small number of synthetic spectra characterized in different regions with laboratory measured species.
Use case	The Lorentzian method is flexible enough for all use cases given the proper parameterization.	The spline method is impractical to deblend features and lines, such as the 12.7- μm band and $[\text{Ne II}]_{12.81\mu\text{m}}$ at moderate spectral resolution.	In general, the template method is suitable for low- to moderate-S/N ratio spectra. At high S/N ratio, the method will lack free parameters.
Speed	It depends on the number of model parameters and S/N ratio. It is always the slowest method.	Spline fits are analytical functions. This method is virtually instantaneous.	Model parameters are not extremely degenerate, even at low S/N ratio. It is faster than the Lorentzian method, because it has significantly less free parameters. It is however slower than the spline method.
Public Tools	MILES (Paper I), PAHfit (Smith et al., 2007a), <i>etc.</i>		PAHtat (Pilleri et al., 2012), Xie et al. (2018) , <i>etc.</i>

3.1.2 Calibrating the UIB properties

We have seen that we need an asymmetric band profile to fit **UIBs**. The most logical choice is thus to adopt a *split-Lorentz* function. It is similar to the split-normal distribution (Eq. B.2; ν being the radiation frequency), but with a Lorentzian basis instead of Gaussian:

$$F_\nu = I \times \begin{cases} \frac{2}{\pi} \frac{\Delta\nu_s^2}{\Delta\nu_s + \Delta\nu_l} \frac{1}{(\nu - \nu_0)^2 + \Delta\nu_s^2} & \text{for } \nu \geq \nu_0 \\ \frac{2}{\pi} \frac{\Delta\nu_l^2}{\Delta\nu_s + \Delta\nu_l} \frac{1}{(\nu - \nu_0)^2 + \Delta\nu_l^2} & \text{for } \nu < \nu_0, \end{cases} \quad (3.1)$$

The parameters characterizing each individual feature, ν_0 , $\Delta\nu_s$ and $\Delta\nu_l$, can be derived from each fit. However, except for the brightest bands or for high-signal-to-noise ratio spectra, most of these parameters would be poorly-constrained and would drastically slow down the code. For that reason, we have calibrated these parameters (*i.e.* inferred a reference value) using high-resolution, high-signal-to-noise ratio spectra of Galactic regions. Thus, when fitting a spectrum, we can choose to fix some or all of these parameters.

This calibration is demonstrated in Fig. 3.2.

1. We have first fitted the ISO-SWS spectrum of the Red Rectangle nebula, in order to calibrate the narrow bands (*cf.* Fig. 3.2. a). The very wide bands, also called *plateaus*, are not very prominent in this region.
2. We then fix the narrow band parameters and infer the $\lambda \simeq 8 \mu\text{m}$ and $\lambda \simeq 12 \mu\text{m}$ plateau parameters by fitting the ISO-SWS spectrum of the planetary nebula NGC 7027 (*cf.* Fig. 3.2. b). The $\lambda \simeq 17 \mu\text{m}$ complex is too weak to be calibrated using this spectrum.
3. The $\lambda \simeq 17 \mu\text{m}$ complex is calibrated by fitting the *Spitzer*/IRS spectrum of the **PDR M 17** (*cf.* Fig. 3.2. c).
4. The aromatic and aliphatic bands in the $\lambda \simeq 3 \mu\text{m}$ region are calibrated by fitting the $\lambda = 3 - 5 \mu\text{m}$ spectrum of NGC 7027 (*cf.* Fig. 3.2. d). The continuum in this range is indeed clean and there are no other blended bands.

Table 3.2 gives the resulting band parameters. With these parameters fixed, we can fit even low-signal-to-noise ratio spectra varying only the intensity of each band (the parameter I in Eq. 3.1). We can however choose to let some band parameters free to vary in case we are analyzing a high-signal-to-noise ratio spectrum.

For the following model description, we have adopted the convention that each profile in the fitting model is defined as a function of frequencies in Hz because this is more physical. However, we have converted the calibrated parameters as a function of wavelengths in μm because this corresponds to the observations. We have adopted the convention that each profile in the fitting model has the unit of spectral flux density, F_ν (MJy/sr), as a function of frequencies, ν (Hz^{-1}).

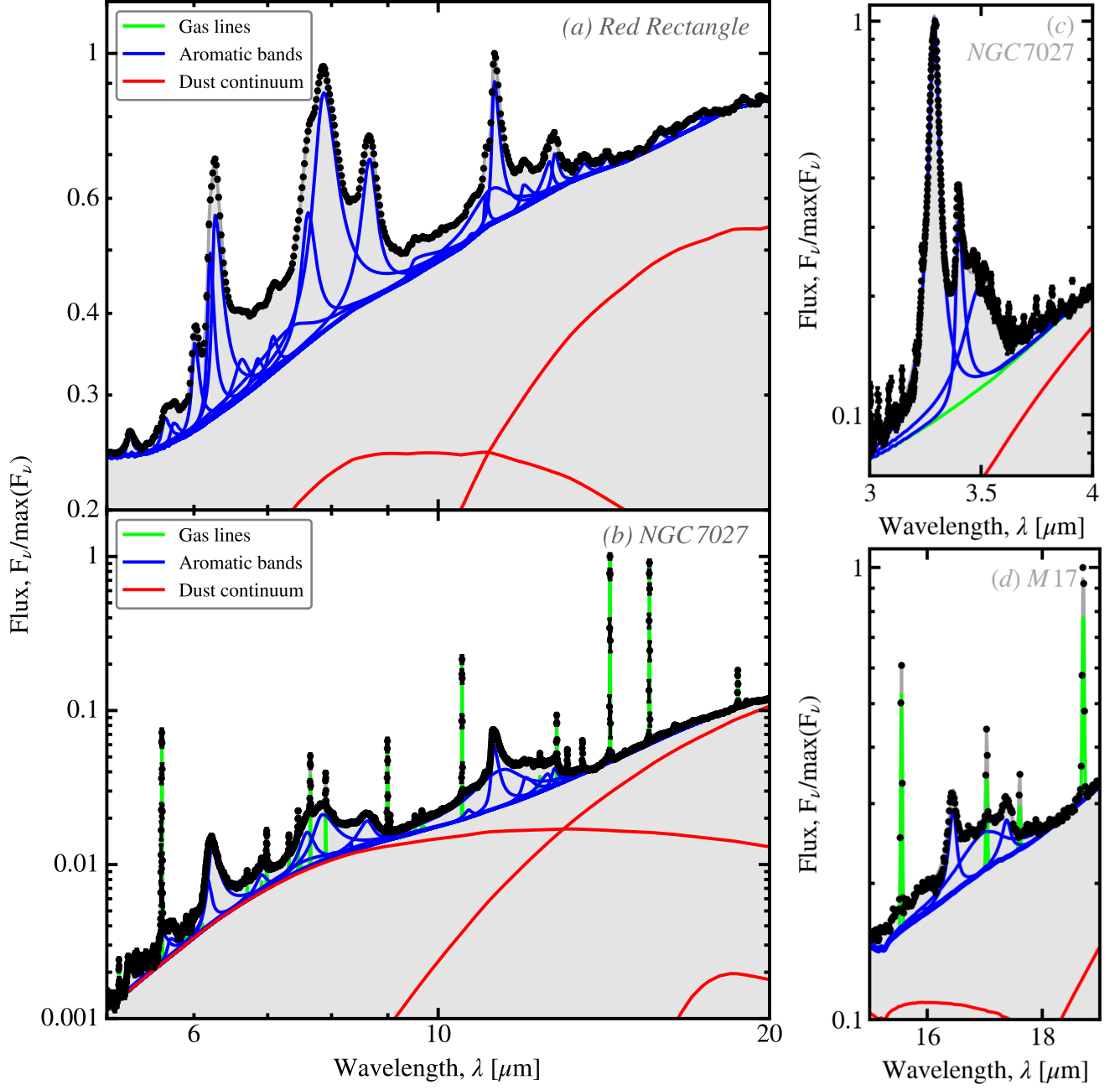


Figure 3.2 – Empirical calibration of UIB profiles.

In each panel, the black dots with error bars represent the observations. These are ISO-SWS spectra except for M 17, which is an *Spitzer*/IRS spectrum. The fitted model is the sum of the different individual components: (i) gray bodies for the dust continuum; (ii) Gaussian profiles for gas lines; and (iii) split-Lorentz profiles (Eq. 3.1) for UIBs.

3.1.3 UIB features

The SwING library², that our code is based on, has the following parameterization for a split-Lorentz distribution:

$$F_v^{\text{band}}(\nu; i) = I^{\text{band}}(i) \times \begin{cases} \frac{\eta(i)\tau(i)^2}{(\nu - \nu_0(i))^2 + \frac{\Lambda(i)^2\tau(i)^2}{4}} & \text{for } \nu \geq \nu_0(i) \\ \frac{\eta(i)}{(\nu - \nu_0(i))^2 + \frac{\Lambda(i)^2}{4}} & \text{for } \nu < \nu_0(i), \end{cases} \quad (3.2)$$

where $\nu_0(i)$ is the central frequency of the i^{th} **UIB** feature, the scale parameter $\Lambda(i)$ which is the equivalent **FWHM** corresponding to the long-wavelength (low-frequency) side; the shape parameter $\tau(i)$ and the pseudo normalization parameter $\eta(i)$. In order to apply Eq. (3.2) to our **UIB** feature calibration (Sect. 3.1.2), we have reparameterized as follows:

1. the scale parameter, $\Lambda(i) = 2\Delta\nu_l(i)$,
2. the shape parameter, $\tau(i) = \Delta\nu_s(i)/\Delta\nu_l(i)$,
3. the pseudo normalization parameter, $\eta(i) = \Lambda(i)/[\pi(1 + \tau(i))]$,

with $\Delta\nu_s(i)$ and $\Delta\nu_l(i)$ feature widths on the short- and long-wavelength sides³. This way, Eq. (3.1) becomes Eq. (3.2) in our effective model.

The free parameters of the **UIB** component are the integrated band intensity $I^{\text{band}}(i)$, the band peak location $\nu_0(i)$ and the **Half Width at Half-Maximum (HWHM)** on each side $\Delta\nu_s(i)$ and $\Delta\nu_l(i)$. Some of the bands given in Table 3.2 have widths limited by the spectral resolution. We have thus degraded $\Delta\nu_s$ and $\Delta\nu_l$ of each band at the spectral resolution of the instruments, σ_{inst} :

$$\Delta\nu_{s, \text{fit}} = \sqrt{\Delta\nu_s^2 + \sigma_{\text{inst}}^2}, \text{ idem for } \Delta\nu_l. \quad (3.3)$$

In addition, instead of inferring the intensities of a band, I^{band} , we are working with the ratio, R^{band} , of this band with a reference band (usually the “Main 11.2” band). This way, we have only one extensive parameter that is, the intensity of the “Main 11.2” band. All the other band parameters are intensive. It thus helps reducing degeneracies. Moreover, we sample the natural logarithm of the band intensities, as their probability distributions are usually more symmetric in the log-space. Finally, it is possible to customize the initial guess and limits for each free parameter in the input file of a specific fit; otherwise, we will automatically set default values, as presented in Table 3.5. The I^{band} or R^{band} can be initiated using the observed spectrum, while ν_0 , $\Delta\nu_s$ and $\Delta\nu_l$ are taken from Table 3.2. By default, ν_0 is limited to $\pm 0.1 \mu\text{m}$ if not fixed. $\Delta\nu_s$ and $\Delta\nu_l$ should be larger than the spectral sampling interval and can vary up to twice their initial values.

2. SwING, standing for *SoftWares for Investigating Nebulae and Galaxies*, is a marvelous Fortran library with IDL/Python wrap-ups developed by Dr. Frédéric GALLIANO.

3. Note that ν_0 is not the mean and that neither $\Delta\nu_s(i)$ nor $\Delta\nu_l(i)$ is the standard deviation because the standard deviation of a Lorentzian is undefined (infinite).

Table 3.2 – UIB profile parameters.

These are the parameters of Eq. (3.1) resulting from our UIB feature calibration described in Sect. 3.1.2. We have converted the frequencies to wavelengths by setting:

- $\nu_0 = c/\lambda_0$,
- $\Delta\nu_s = c/(\lambda_0 - \Delta\lambda_s) - c/\lambda_0$,
- $\Delta\nu_l = c/\lambda_0 - c/(\lambda_0 + \Delta\lambda_l)$.

λ_0	$\Delta\lambda_s$	$\Delta\lambda_l$	MILES input notation
3.291 μm	0.020 μm	0.019 μm	Main 3.3
3.399 μm	0.011 μm	0.024 μm	Main 3.4
3.499 μm	0.077 μm	0.071 μm	Small 3.5
5.239 μm	0.025 μm	0.058 μm	Small 5.2
5.644 μm	0.040 μm	0.080 μm	Small 5.7 (1)
5.749 μm	0.040 μm	0.080 μm	Small 5.7 (2)
6.011 μm	0.040 μm	0.067 μm	Small 6.0
6.203 μm	0.031 μm	0.060 μm	Main 6.2 (1)
6.267 μm	0.037 μm	0.116 μm	Main 6.2 (2)
6.627 μm	0.120 μm	0.120 μm	Small 6.6
6.855 μm	0.080 μm	0.080 μm	Small 6.8
7.079 μm	0.080 μm	0.080 μm	Small 7.1
7.600 μm	0.480 μm	0.502 μm	Plateau 7.7
7.617 μm	0.119 μm	0.145 μm	Main 7.7 (1)
7.870 μm	0.170 μm	0.245 μm	Main 7.7 (2)
8.362 μm	0.016 μm	0.016 μm	Small 8.3
8.620 μm	0.183 μm	0.133 μm	Main 8.6
9.525 μm	0.107 μm	0.600 μm	Small 9.5
10.707 μm	0.100 μm	0.100 μm	Small 10.7
11.038 μm	0.027 μm	0.073 μm	Small 11.0
11.238 μm	0.053 μm	0.153 μm	Main 11.2
11.400 μm	0.720 μm	0.637 μm	Plateau 11.3
11.796 μm	0.021 μm	0.021 μm	Small 11.8
11.950 μm	0.080 μm	0.222 μm	Small 11.9
12.627 μm	0.200 μm	0.095 μm	Main 12.7 (1)
12.761 μm	0.081 μm	0.140 μm	Main 12.7 (2)
13.559 μm	0.160 μm	0.161 μm	Small 13.6
14.257 μm	0.152 μm	0.059 μm	Small 14.2
15.893 μm	0.178 μm	0.200 μm	Small 15.6
16.483 μm	0.100 μm	0.059 μm	Small 16.4
17.083 μm	0.496 μm	0.562 μm	Plateau 17.0
17.428 μm	0.100 μm	0.100 μm	Small 17.4
17.771 μm	0.031 μm	0.075 μm	Small 17.8
18.925 μm	0.037 μm	0.116 μm	Small 18.9

3.1.4 Gas lines

To resolve typical **MIR** gas lines, we would need a spectral resolution $R \equiv \lambda/\Delta\lambda \gtrsim 30\,000$ (i.e. $v \simeq 10$ km/s). Given the spectral resolution of AKARI/IRC ($R \sim 120$ for the *NG* mode; Table 2.1) and *Spitzer*/IRS ($R \sim 150$; Table 2.2), or even JWST (e.g. $R \sim 3\,000$; MIRI-MRS), all the gas lines in our spectra are unresolved. The fitted line widths will be determined by the instrumental resolution. We have fitted each gas line with a Gaussian profile:

$$F_{\nu}^{\text{line}}(\nu; i) = \frac{I^{\text{line}}(i)}{\sqrt{2\pi}\sigma(i)} \times \exp\left[-\frac{(\nu - \nu_c(i))^2}{2\sigma(i)^2}\right], \quad (3.4)$$

where the parameters for the i^{th} line are:

1. The integrated intensity, $I^{\text{line}}(i)$, which is free to vary;
2. The line central frequency, $\nu_c(i)$, which is either fixed or free to vary by $\pm 1/2$ pixel;
3. The line width, $\sigma(i)$, which is either fixed to the spectral resolution of the instrument σ_{inst} or free to vary between $\sigma_{\text{inst}}/2$ and $2\sigma_{\text{inst}}$, because the instrumental resolution as a function of wavelength is not precisely known.

Similarly to the band intensities, we also allow users to normalize all line intensities, I^{line} , to the same reference band intensity (usually the “Main 11.2” band), thus inferring a line-to-reference-band ratio, R^{line} . We also sample the logarithm of the line intensity. Finally, we set the initial guess of $\ln(R^{\text{line}})$ or $\ln(I^{\text{line}})$ the same way as **UIB** features. ν_c is taken from Table 3.3 and σ is defined by the spectral resolution. By default, ν_c is limited to $\pm\sigma$ if not fixed. σ should be larger than the spectral sampling interval and can vary up to twice this value (cf. Table 3.5).

3.1.5 Dust continuum

The dust grain continuum has been fitted with a linear combination of N_{grain} modified blackbodies (Eq. 1.26), where Eq. (1.22) gives the realistic absorption opacities $\kappa_{\text{abs}}(\lambda, a)$, with the mass density ρ , radius a and absorption coefficient Q_{abs} . From Table 3.4, we can select a combination of grain compositions:

$$F_{\nu}^{\text{grain}}(\nu; i) = \frac{3\xi(i)}{4\rho(i)} \left[\frac{Q_{\text{abs}}(\nu; i)}{a(i)} \right] B_{\nu}(T(i); \nu), \quad (3.5)$$

where an extensive parameter, $\xi(i) = M/d^2$, depending on the mass M and on the distance d , and the temperature of the modified blackbody, $T(i)$, are the two free parameters for the i^{th} component. In addition, rather than sampling the parameters ξ , we work with the monochromatic flux density $F_{\nu, \text{ref}}$ at a given wavelength, ν_{ref} . This parameter is equivalent, but it avoids us quoting dust masses, which are physically questionable, as we do not know if these grains are actually at thermal equilibrium. As for T , we generate a temperature grid ranging from 50 to 500 K⁴, by default. In practice, we use the lower temperature and positive temperature increments, dT , for the hotter dust components. As for the other parameters varying over a large dynamic range,

4. According to Wien’s displacement law, the dust emission will peak between $\sim 5.8 - 58 \mu\text{m}$, perfectly covering the **MIR** wavelength regime.

Table 3.3 – Most prominent MIR gas lines.

This table lists the gas excitation lines available in our spectral fitting model. We have indicated the Gaussian center of each species and its corresponding transition.

Central wavelength	Species	Transition ^a	Type
4.052 μm	H I	Brackett α	recombination
5.129 μm	H I	6–10	recombination
5.511 μm	H ₂	0–0 S(7)	ro-vibrational
5.610 μm	Mg v	³ P ₂ – ³ P ₁	forbidden
5.908 μm	H I	Humphreys γ	recombination
5.981 μm	K IV	³ P ₁ – ³ P ₂	forbidden
6.109 μm	H ₂	0–0 S(6)	ro-vibrational
6.709 μm	Cl v	² P ₀ – ² P ₀	forbidden
6.910 μm	H ₂	0–0 S(5)	ro-vibrational
6.948 μm	He II	8–9	recombination
6.985 μm	Ar II	² P _{3/2} – ² P _{1/2}	forbidden
7.318 μm	Na III	² P ₀ – ² P ₀	forbidden
7.460 μm	H I	Pfund α	recombination
7.502 μm	H I	Humphreys β	recombination
7.652 μm	Ne VI	² P ₀ – ² P ₀	forbidden
7.815 μm	Fe VII	³ F ₃ – ³ F ₄	forbidden
7.902 μm	Ar v	³ P ₁ – ³ P ₂	forbidden
8.025 μm	H ₂	0–0 S(4)	ro-vibrational
8.760 μm	H I	7–10	recombination
8.991 μm	Ar III	³ P ₂ – ³ P ₁	forbidden
9.042 μm	Ni VI	⁴ P ₅ – ⁴ F ₅	forbidden
9.527 μm	Fe VII	³ F ₂ – ³ F ₃	forbidden
9.665 μm	H ₂	0–0 S(3)	ro-vibrational
9.713 μm	He II	9–10	recombination
10.339 μm	Si I	¹ P ₁ – ¹ P ₂	forbidden
10.511 μm	S IV	² P _{3/2} – ² P _{1/2}	forbidden
12.279 μm	H ₂	0–0 S(2)	ro-vibrational
12.369 μm	H I	Humphreys α	recombination
12.814 μm	Ne II	² P _{3/2} – ² P _{1/2}	forbidden
13.102 μm	Ar v	³ P ₀ – ³ P ₁	forbidden
13.521 μm	Mg v	³ P ₁ – ³ P ₀	forbidden
14.322 μm	Ne v	³ P ₁ – ³ P ₂	forbidden
15.555 μm	Ne III	³ P ₂ – ³ P ₁	forbidden
17.035 μm	H ₂	0–0 S(1)	ro-vibrational
17.608 μm	H I	11–18	recombination
18.713 μm	S III	³ P ₂ – ³ P ₁	forbidden
19.062 μm	H I	7–8	recombination
21.829 μm	Ar III	³ P ₁ – ³ P ₀	forbidden
24.318 μm	Ne v	³ P ₀ – ³ P ₁	forbidden
25.890 μm	O IV	² P _{3/2} – ² P _{1/2}	forbidden
25.988 μm	Fe II	⁶ D ₇ – ⁶ D ₉	forbidden
28.219 μm	H ₂	0–0 S(0)	ro-vibrational
33.481 μm	S III	³ P ₁ – ³ P ₀	forbidden
34.815 μm	Si II	² P _{3/2} – ² P _{1/2}	forbidden
35.349 μm	Fe II	⁶ D _{5/2} – ⁶ D _{7/2}	forbidden
36.014 μm	Ne III	³ P ₁ – ³ P ₀	forbidden

^a. Following the spectroscopic notations described in Sect. 1.3.2.2 ⁸, we extend the designation to atoms or ions with more than one electron. Considering the LS coupling between electrons, the total orbital angular momentum \vec{L} and total spin \vec{S} give the total angular momentum $\vec{J} = \vec{L} + \vec{S}$. Then, the letters S, P, D, F indicate $L = 0, 1, 2, 3$, respectively. $r = 1, 2, 3, 4$ is the multiplicity (*i.e.* singlet, doublet, triplet, quartet), corresponding to $S = 0, 1/2, 1, 3/2$, *etc.* Finally, an electron configuration with quantum numbers LSJ is designated as $^r(L - symbol)_J$.

we sample the logarithm of $F_{\nu, \text{ref}}$ and T . Then, the initial value of $F_{\nu, \text{ref}}$ can be guessed using the modified blackbody calculated with the initial temperatures (*cf.* Table 3.5) and comparing to the observed spectrum.

Although Eq. (3.5) represents grains at thermal equilibrium with the radiation field, a collection of such functions can approximate the emission of small stochastically-heated grains, as it will result in a broad spectrum. Similarly to UIB features, the physical interpretation of the dust components in our fitting model is limited because of the uncertainty on their heating rate. They are simply designed to provide a realistic parameterization of the continuum.

3.1.6 Stellar contamination

To account for stellar contamination, we include an additional component. This MIR stellar continuum, accounting for the Rayleigh-Jeans emission of stellar populations, $F_{\nu}^*(\nu)$, is modeled with a single star-formation burst at age 5 Gyr, using PÉGASE (Fioc & Rocca-Volmerange, 1997, 2019). In practice, this old stellar population can also account for the tail of young stars as we are sampling only the Rayleigh-Jeans regime (Fig. 1.17). Alternatively, it is also possible to simply model the stellar emission by assuming a blackbody with a high enough temperature so that it emits in the MIR range in the Rayleigh-Jeans regime ($T_{\star} \gg 5000$ K for $\lambda \simeq 3 \mu\text{m}$). Either way, this component is fitted with a single scaling parameter and it only contributes at short wavelengths in our MIR spectra. In the case of modeled stars, the scaling parameter is the monochromatic flux density, $F_{\nu, \text{ref}}^*$, at the reference wavelength, ν_{ref} . As for blackbody stars, the scaling parameter is the total stellar power L^* assuming Stefan–Boltzmann law. Since the extensive parameter L^* (or $F_{\nu, \text{ref}}^*$) has a large dynamic range, we sample its natural logarithm.

3.1.7 Foreground extinction

We account for potential extinction. At the moment, we assume a foreground slab extinction⁵ by two components: dust and ices. The silicate-to-ice optical depth ratio varies from one source to another (*e.g.* Yamagishi et al., 2015). We have thus one free parameter per component: A_V^{dust} for dust, $A_{3.05 \mu\text{m}}^{\text{H}_2\text{O}}$ for H_2O , $A_{4.67 \mu\text{m}}^{\text{CO}}$ for CO and $A_{15.2 \mu\text{m}}^{\text{CO}_2}$ for CO_2 . The wavelength-dependent absorption probability is thus:

$$\mathcal{P}_{\text{abs}}(\nu) = \exp \left[- \left(A_V^{\text{dust}} \tau_{\text{dust}}(\nu) + A_{3.05 \mu\text{m}}^{\text{H}_2\text{O}} \tau_{\text{H}_2\text{O}}(\nu) + A_{4.67 \mu\text{m}}^{\text{CO}} \tau_{\text{CO}}(\nu) + A_{15.2 \mu\text{m}}^{\text{CO}_2} \tau_{\text{CO}_2}(\nu) \right) / 1.086 \right], \quad (3.6)$$

where

- $\tau_{\text{dust}}(\nu)$ is the wavelength-dependent optical depth (Eqs. 1.4 – 1.6, hereafter) of the standard dust composition (*i.e.* silicate and graphite) normalized in V-band (*e.g.* Weingartner & Draine, 2001);
- $\tau_{\text{H}_2\text{O}}(\nu)$ is the wavelength-dependent optical depth of H_2O ice (Öberg et al., 2007) normalized at $3.05 \mu\text{m}$;
- $\tau_{\text{CO}}(\nu)$ is the wavelength-dependent optical depth of CO ice (Bouwman et al., 2007) normalized at $4.67 \mu\text{m}$;

5. We plan, in the near-future, to add more complex geometries.

Table 3.4 – Grain optics.

This table lists the dust grain components available in the spectral fitting model of MILES. For each species, we present the parameters used to calculate dust continuum emission, including the mass density ρ , radius a , and absorption coefficient Q_{abs} (the reference of the latter two are given).

Species	ρ (10^3 kg/m ³)	Reference for Q_{abs} and a	MILES input notation
Big a-C(:H) + 20 nm a-C	1.51	Jones et al. (2017)	a-C man20nm big
a-C(:H) + 20 nm a-C	1.30	Jones et al. (2013)	a-C man20nm J13
Small a-C(:H) + 20 nm a-C	1.60	Jones et al. (2017)	a-C man20nm small
a-Enstatite + 10 % Fe/FeS + 5 nm a-C (13)	1.60	Jones et al. (2013)	a-Enst Fe man5nm J13
a-Enstatite + 10 % Fe/FeS + 5 nm a-C	2.19	Jones et al. (2017)	a-Enst Fe man5nm
a-Forsterite + 10 % Fe/FeS + 5 nm a-C (13)	1.60	Jones et al. (2013)	a-Forst Fe man5nm J13
a-Forsterite + 10 % Fe/FeS + 5 nm a-C	2.19	Jones et al. (2017)	a-Forst Fe man5nm
ACAR amorphous carbon	1.85	Zubko et al. (1996)	ACAR Z96
ACH2 amorphous carbon	1.85	Zubko et al. (1996)	ACH2 Z96
BE amorphous carbon	1.85	Zubko et al. (1996)	BE Z96
Iron Oxide FeO	5.70	Henning et al. (1995)	FeO H95
Graphitic carbon (1/3-2/3)	2.24	Draine (2003b)	Gra D03
Original graphitic carbon (1/3-2/3)	2.24	Laor & Draine (1993)	Gra LD93
Ionized PAHs modified for the DHGL model	2.24	Compiègne et al. (2011)	PAHi DL07 C11
Ionized PAHs modified for the ZDA04 model	2.24	Galliano et al. (2011)	PAHi DL07 G11
Ionized PAHs	2.24	Draine & Li (2007)	PAHi DL07
Original ionized PAHs	2.24	Li & Draine (2001)	PAHi LD01
Neutral PAHs modified for the DHGL model	2.24	Compiègne et al. (2011)	PAHn DL07 C11
Neutral PAHs modified for the ZDA04 model	2.24	Galliano et al. (2011)	PAHn DL07 G11
Neutral PAHs	2.24	Draine & Li (2007)	PAHn DL07
Original neutral PAHs	2.24	Draine & Li (2007)	PAHn LD01
Silicon carbide	3.22	Laor & Draine (1993)	SiC LD93
Astronomical silicate	3.50	Draine (2003b)	Sil D03
Smoothed UV astronomical silicate & submm excess	3.50	Li & Draine (2001)	Sil LD01
Original astronomical silicate	3.30	Laor & Draine (1993)	Sil LD93
Silicate Mg 0.7 Si O 2.7	3.50	Jäger et al. (2003)	Sil Mg07 J03
Smoothed UV astronomical silicate	3.50	Weingartner & Draine (2001)	Sil WD01

— $\tau_{\text{CO}_2}(\nu)$ is the wavelength-dependent optical depth of CO_2 ice (White et al., 2009) normalized at $15.2 \mu\text{m}$.

A_V can vary from 0 up to ~ 100 mag in some highly extinguished regions (*e.g.* the A_V inferred from the $9.7 \mu\text{m}$ silicate absorption attains 90 mag in Arp 220; Smith et al., 1989). Therefore, we sample $\ln(A_V)$ and limit its variations between 0 and 5 (*i.e.* $1 < A_V < 150$; Table 3.5).

3.1.8 Total model

With our simple screen geometry, the total **MIR** spectrum model, which is the combination of all the individual components we have discussed, is:

$$F_{\nu}^{\text{mod}}(\nu) = \left(F_{\nu}^{\star}(\nu) + \sum_{i=1}^{N_{\text{grain}}} F_{\nu}^{\text{grain}}(\nu; i) + \sum_{i=1}^{N_{\text{band}}} F_{\nu}^{\text{band}}(\nu; i) + \sum_{i=1}^{N_{\text{line}}} F_{\nu}^{\text{line}}(\nu; i) \right) \times \mathcal{P}_{\text{abs}}(\nu) \quad (3.7)$$

This model allows us to measure all **UIB** features and gas lines at once, taking into account the degeneracies arising from spectral blending and extinction. This is necessary to obtain consistent band or line intensity ratios.

In practice, we have adopted the following fitting configuration, for M 82 (results presented in Sect. 4.1):

- For **UIB** features, we have varied the intensity ratios R^{band} for all the bands in Table 3.2 (*i.e.* 34 in total).
- For gas lines, we have visually checked for the presence in the spectrum of those listed in Table 3.3. We have found 12 lines: $[\text{Br}\alpha]_{4.05\mu\text{m}}$, $\text{H}_2 \text{ 0-0 S}(7)_{5.5\mu\text{m}}$, $[\text{Hu}\gamma]_{5.91\mu\text{m}}$, $[\text{Ar II}]_{6.98\mu\text{m}}$, $[\text{Ar III}]_{8.99\mu\text{m}}$, $\text{H}_2 \text{ 0-0 S}(3)_{9.7\mu\text{m}}$, $[\text{S IV}]_{10.51\mu\text{m}}$, $\text{H}_2 \text{ 0-0 S}(2)_{12.3\mu\text{m}}$, $[\text{Ne II}]_{12.81\mu\text{m}}$, $[\text{Ne III}]_{15.56\mu\text{m}}$, $\text{H}_2 \text{ 0-0 S}(1)_{17.0\mu\text{m}}$ and $[\text{S III}]_{18.68\mu\text{m}}$. We have fitted these 12 lines by only varying their intensity ratios, R^{line} ;
- For the dust continuum, we have fitted three sets of amorphous carbon (*i.e.* BE Z96 with independent temperatures) and one silicate (*i.e.* Sil D03) components, each with two free parameters, $F_{15 \mu\text{m}}$ and T ;
- For the stellar continuum, we have used a blackbody at temperature $T_{\star} = 50\,000$ K, which results in one free parameter, L^{\star} ;
- For the extinction, we have only varied A_V^{dust} without adding any ice extinction.

In total, we have fitted our model with 56 free parameters⁶. All the free parameters are set to their logarithmic form in the fit.

6. We have also sampled the mean and covariance matrix of all the free parameters as the hyperparameters in our hierarchical model that we will see in Sect. 3.2.4

Table 3.5 – MILES default input settings for model parameters.

We present the default settings of MILES inputs, including the initial guess and parameter range of each group of model parameters that can vary. These values depend on the parameterization and can be configured within the input file of every fit. In particular, we leave an option to use the full set of χ^2 best-fitted parameters as the initial guess for both non-hierarchical and hierarchical Bayesian fits (Sects. 3.2.3 – 3.2.4). This “*chi2init*” option works efficiently to find the region of high probability in parameter space with our random sampling method (Sect. 3.2.5.1).

Parameter	Input label	Initial guess	Lower limit	Upper limit
UIB features				
$\ln(I^{\text{band}})$	$\ln\text{Rband}^a$	$\ln(F_{\nu_0}^{\text{obs}} / f_{\nu_0}^{\text{band}})^b$	$-\infty$	∞
$\ln(R^{\text{band}})$	$\ln\text{Rband}$	$\ln(F_{\nu_0}^{\text{obs}} / f_{\nu_0}^{\text{band}}) - \ln(F_{\nu_b}^{\text{obs}} / f_{\nu_b}^{\text{band}})^c$	$-\infty$	∞
ν_0	Cband	Table 3.2	$\nu_0 - 0.1 \mu\text{m}$	$\nu_0 + 0.1 \mu\text{m}$
$\Delta\nu_s$	WSband	Table 3.2 ^d	Instrumental limit	$2 \times \Delta\nu_s$
$\Delta\nu_l$	WLband	Table 3.2 ^d	Instrumental limit	$2 \times \Delta\nu_l$
Gas lines				
$\ln(I^{\text{line}})$	$\ln\text{Rline}^a$	$\ln(F_{\nu_c}^{\text{obs}} / f_{\nu_c}^{\text{line}})^e$	$-\infty$	∞
$\ln(R^{\text{line}})$	$\ln\text{Rline}$	$\ln(F_{\nu_c}^{\text{obs}} / f_{\nu_c}^{\text{line}}) - \ln(F_{\nu_b}^{\text{obs}} / f_{\nu_b}^{\text{band}})^c$	$-\infty$	∞
ν_c	Cline	Table 3.3	$\nu_c - \sigma$	$\nu_c + \sigma$
σ	Wline	Instrumental limit	Instrumental limit	$2 \times \sigma$
Dust continuum				
$\ln(F_{\nu, \text{ref}})$	$\ln\text{Fcont}$	$\ln(F_{\nu, \text{ref}}^{\text{obs}} / f_{\nu, \text{ref}}^{\text{grain}})^f$	$-\infty$	∞
$\ln(T)$	$\ln\text{T}$	$\ln[T_{\min} + (T_{\max} - T_{\min}) \times i / N_{\text{grain}}]^g$	$\ln(50 \text{ K} / 1 \text{ K})$	$\ln(500 \text{ K} / 1 \text{ K})$
$\ln(dT)$	$\ln\text{T}^a$	$\ln[(T_{\max} - T_{\min}) \times i^{\text{grain}} / N_{\text{grain}}]^g$	$-\infty$	$\ln[T_{\max} - T(i - 1)]$
Stellar continuum				
$\ln(F_{\nu, \text{ref}}^{\star})$	$\ln\text{Lstar}^a$	$\ln(F_{\nu, \text{ref}}^{\text{obs}} / f_{\nu, \text{ref}}^{\text{star}})^h$	$-\infty$	∞
$\ln(L^{\star})$	$\ln\text{Lstar}$	$\ln(F_{\nu, \text{ref}}^{\text{obs}} / f_{\nu, \text{ref}}^{\text{star}} \times \sigma_{\text{S-B}} T_{\star}^4)^i$	$-\infty$	∞
Foreground extinction				
$\ln(A_V)$	$\ln\text{Av}$	0	0	5

a. The reparameterized band intensity ratio R^{band} (cf. Sect. 3.1.3) shares the same input label with the integral band intensity I^{band} . *Idem* for other reparameterization described in Sects. 3.1.4 – 3.1.6: I^{line} to R^{line} , T to dT and L^{\star} to $F_{\nu, \text{ref}}^{\star}$.

b. $f_{\nu_0}^{\text{band}}$ is the value of normalized split-Lorentz function (Eq. 3.1) at ν_0 .

c. ν_b is the center of the reference band selected to reparameterize I^{line} to R^{line} .

d. The fitted band widths are degraded by the instrumental spectral resolution (Eq. 3.3).

e. $f_{\nu_c}^{\text{line}}$ is the value of normalized Gaussian function (Eq. B.1) at ν_0 .

f. $f_{\nu, \text{ref}}^{\text{grain}}$ is the value of normalized modified blackbody (Eq. 3.5) at ν_{ref} .

g. A uniform grid nestled in the temperature range is auto-generated in order to attribute the initial temperature of the i^{th} dust grain component among N_{grain} . In case there exists more than one components of the same kind, T will be reparameterized to its positive increment dT automatically. This operation ensures an ascending temperature sampling and reduces model degeneracies. By default, the limits of any temperature are $(T_{\min}, T_{\max}) = (50, 500) \text{ K}$.

h. $f_{\nu, \text{ref}}^{\text{star}}$ is the value of normalized stellar spectrum modeled via PÉGASE at ν_{ref} .

i. $f_{\nu, \text{ref}}^{\text{star}}$ is the value of normalized blackbody (Eq. 1.25) at ν_{ref} . $\sigma_{\text{S-B}} = 5.67 \text{ W m}^{-2} \text{ K}^{-4}$ is called the *Stefan–Boltzmann constant*.

3.2 Fitting methods

When fitting a model (controlled by a set of parameters) to a set of observations, a *frequentist* is someone who looks for the model through which the observed data is the most probable, whereas a *Bayesian* quantifies the probability of all possible models knowing the observations. A fit is never perfect because the noise leads to a loss of information. For a frequentist, the accuracy of the fitted parameters is assessed by sampling the observational uncertainties around the best-fit. Alternatively, a Bayesian provides the full probability distribution of the model parameters conditional on the data. In practice, models do not exactly fit observations, even when the model corresponds precisely to the studied phenomenon. That is due to the *measurement errors*, namely *noise* and *systematics*.

We have applied (i) the least-squares method (frequentist approach), (ii) the standard Bayesian method, and (iii) the hierarchical Bayesian method, to fit the rather comprehensive **MIR** emission model described in [Sect. 3.1](#) to realistic spectra. The discrepancies between different fitting methods will be demonstrated in the model justification section, in [Sect. 3.3](#), where we have fitted a sample of simulated spectra.

3.2.1 Observation uncertainties

In our case ([Sect. 2.1.2.1](#) and [Sect. 2.2.2.2](#)), there are two sources of uncertainties on the observed flux F_ν^{obs} : (i) the random noise is a statistical uncertainty characterized by its standard deviation, $\sigma_\nu^{\text{noise}}$. It is assumed to be uncorrelated at different frequencies⁷; (ii) the correlated systematic calibration uncertainties, σ_ν^{syst} , depend on the observation modules. The covariance of the noise is a diagonal matrix, $\mathbf{V}_{\text{noise}}$, whereas systematics have a non-diagonal covariance matrix, \mathbf{V}_{syst} . The total covariance matrix is simply

$$\mathbf{V}_{\text{obs}} = \mathbf{V}_{\text{noise}} + \mathbf{V}_{\text{syst}} \quad (3.8)$$

3.2.1.1 Random noise

Let's assume the observed spectrum is the sum of our emission model, $F_\nu^{\text{mod}}(\nu | \vec{x})$, depending on a set of parameters \vec{x} , and a Gaussian noise, ϵ :

$$\begin{aligned} F_\nu^{\text{obs}}(\nu) &= F_\nu^{\text{mod}}(\nu | \vec{x}) + \epsilon(\nu | \vec{x}) \\ &= F_\nu^{\text{mod}}(\nu | \vec{x}) + \delta(\nu | \vec{x}) \times \sigma_\nu^{\text{noise}}(\nu), \end{aligned} \quad (3.9)$$

where

$$\delta(\nu | \vec{x}) = \frac{F_\nu^{\text{obs}}(\nu) - F_\nu^{\text{mod}}(\nu | \vec{x})}{\sigma_\nu^{\text{noise}}(\nu)} \sim \mathcal{N}(0, 1) \quad (3.10)$$

is the reduced **PDF** of the noise.

7. Compared to [Table 2.3](#), the random noise, σ^{noise} , taken into account in the fit is the combination of the pipeline uncertainty, σ_0 , and the uncertainty due to pointing inaccuracy, σ^{pt} .

3.2.1.2 Calibration factor

Astronomical observations are recorded by detectors that perform electronic readout, which are then converted to a received flux (typically, with the units converted from ADU/s to Jy/pixel). Detectors are calibrated by observing a set of bright sources with well-known fluxes, namely calibrators. The uncertainties on these measures translate into calibration errors. Calibration errors are systematic errors. In our case, they can be assumed to be identical for data from the same observing module, because the same uncertain calibration coefficient was applied to all observations from this module. Calibration errors from different modules can also be correlated since instruments are often cross-calibrated using the same set of calibrators.

The treatment of systematic calibration uncertainties in our fit is described as follows. Note that the calibration uncertainties of the different modules of AKARI/IRC and *Spitzer*/IRS have different amplitudes (Table 2.3). We assume that wavelengths from the same module are fully correlated⁸, which gives a single *calibration factor* for each module. However, we have left the calibration factor varying independently for each spectrum combined from different observations. Although our spectra have been processed in a rather consistent way (Sects. 2.1 – 2.2), adopting independent calibration factor allows us to account for all the residual uncertainties (such as slit loss), and obtain well-stitched spectra. By introducing the *calibration offset* of a given module, $\delta^{\text{cal}}(\text{module})$, Eq. (3.10) becomes:

$$\delta(\nu | \vec{x}, \delta^{\text{cal}}(\text{module})) = \frac{F_{\nu}^{\text{obs}}(\nu) - F_{\nu}^{\text{mod}}(\nu | \vec{x}) \times (1 + \delta^{\text{cal}}(\text{module}))}{\sigma_{\nu}^{\text{noise}}(\nu)}. \quad (3.11)$$

In our fit, it concerns four modules including the IRC (*NG/NP*), SL2, SL1 and LL2. The IRS calibration uncertainties are $\Sigma^{\text{cal}}(\text{SL}) \simeq 5\%$ and $\Sigma^{\text{cal}}(\text{LL}) \simeq 5\%$ with Eq. (2.1). As for IRC, the calibration uncertainty was estimated to be 10% for all dispersers around their central wavelengths and it got worse up to 20% at the longest and shortest edges (Ohyama et al., 2007). To be conservative, we have taken $\Sigma^{\text{cal}}(\text{IRC}) \simeq 20\%$ for IRC. Note that the fitted calibration factor of each detector module, $1 + \delta^{\text{cal}}(\text{module})$, is different from the scaling factor that we have derived assessing inter-calibration (Sect. 2.3). Indeed, δ_{cal} is a random variable that we will probabilistically infer in order to account for calibration uncertainties. For convenience, we have kept the term “*calibration (factor/error/offset)*” in the rest of this manuscript.

3.2.2 Least-squares method

The least-squares method belong to the frequentist approach. Systematic effects are very difficult to account in this framework, as their uncertainty does not correspond to the repetition of a measure. Since our least-squares code is only used as a comparison case, we use Eq. (3.10) without accounting for the calibration offset. In the absence of correlations, the *likelihood* function (hereafter likelihood) can be expressed as the following conditional PDF:

$$p(\vec{F}_{\nu}^{\text{obs}} | \vec{x}) = \prod_{j=1}^m p(\epsilon(\nu | \vec{x})), \quad (3.12)$$

8. In practice, we have no information about the correlations between wavelengths within the same module.

where $\overrightarrow{F_v^{\text{obs}}} = \{F_v^{\text{obs}}(v_j)\}_{j=1,\dots,m}$. The best-fit is obtained by taking the parameter values at the maximum likelihood, that is at the maximum probability in Eq. (3.12). In the general case, this is called a maximum likelihood estimate. In the case where the errors (the p) are normal, it becomes the least-squares method. For that purpose, we have developed a χ^2 -minimization fitter based on the MINPACK (Moré et al., 1980, 1984) Levenberg-Marquardt algorithm that has been converted to Fortran 90⁹.

Starting with an initial guess of the parameters, $\overrightarrow{x}^{(0)}$, the *Levenberg-Marquardt method* (Press et al., 2007) iteratively refines the parameters, $\overrightarrow{x}^{(n+1)} = \overrightarrow{x}^{(n)} + \overrightarrow{\delta x}^{(n+1)}$ (n denoting the iteration), until finding the best-fit solutions. The increment, $\overrightarrow{\delta x}^{(n+1)}$, is estimated from the Jacobian matrix, \mathbf{J} , which gives the derivation of the normalized *residual* between the observations and the model, $\overrightarrow{r} = (\overrightarrow{F_v^{\text{obs}}} - \overrightarrow{F_v^{\text{mod}}})/\sigma_v^{\text{obs}}$:

$$\mathbf{J} \overrightarrow{\delta x} = \overrightarrow{r}. \quad (3.13)$$

In the case where the uncertainties are not correlated, we see that $\chi^2 = |\overrightarrow{r}|^2$.

The iteration stops after at least one among a set of conditions is met. These conditions are, for instance: (i) the maximum number of iterations is reached, (ii) the χ^2 does not improve significantly between iterations, *etc.* A fit is considered as a *good fit* if its reduced χ^2 value is around 1. A $\chi^2 \gg 1$ leads to a *poor fit*, whereas $\chi^2 \ll 1$ implies an *overfit* due to the lack of constraints on some of the parameters. Errors on the best-fit parameters are estimated using the covariance matrix, \mathbf{V}_{par} , which is computed by approximating the gradient of the χ^2 around the best-fit solution. As for the uncertainties on a derived quantity, $f(\overrightarrow{x})$, such as a given band ratio, the rigorous way accounting for correlations between parameters is possible through:

$$\sigma_{f(\overrightarrow{x})}^2 = (\overrightarrow{\nabla} f(\overrightarrow{x}))^T \mathbf{V}_{\text{par}} \overrightarrow{\nabla} f(\overrightarrow{x}), \quad (3.14)$$

where $\overrightarrow{\nabla} f(\overrightarrow{x})$ is the gradient of the derived parameter.

Different initial parameter guesses might lead to different best-fits. This is because there might be local minima the fitter could converge to. The Levenberg-Marquardt method is not efficient at sorting complex parameter spaces. To solve this issue, we have run the least-squares fitter 10 times, starting from different random initial conditions. In the end, the fit with the smallest χ^2 is selected as the best-fit, whereas other fits are discarded.

3.2.3 Non-hierarchical Bayesian (non-HB) inference

The story of Bayesian statistics begins with *Bayes' theorem*. Given the conditional probabilities of two events A and B , Bayes' theorem says the probability of A given B is related to the probability of B given A and to their unconditional probabilities $P(A)$ and $P(B)$, respectively:

$$P(A | B) = \frac{P(B | A)}{P(B)} P(A). \quad (3.15)$$

9. It was originally written in Fortran 77.

If we replace the abstract quantities, A and B , by our parameters, \vec{x} , and our observations, \vec{F}_ν^{obs} , Eq. (3.15) becomes:

$$\underbrace{p(\vec{x} | \vec{F}_\nu^{\text{obs}})}_{\text{posterior}} = \frac{\overbrace{p(\vec{F}_\nu^{\text{obs}} | \vec{x})}^{\text{likelihood}}}{\underbrace{p(\vec{F}_\nu^{\text{obs}})}_{\text{evidence}}} \times \underbrace{p(\vec{x})}_{\text{prior}}. \quad (3.16)$$

The left-hand term is a conditional **PDF** of the model parameters knowing the observations, called the *posterior* distribution (hereafter posterior). On the right side, we have the *prior* distribution (hereafter prior), $p(\vec{x})$, which is the absolute distribution of the parameters. This is the most difficult quantity to grasp. In many instances, it can be assumed flat. $p(\vec{F}_\nu^{\text{obs}} | \vec{x})$ is the likelihood of the observations, similar to the one in Eq. (3.12). $p(\vec{F}_\nu^{\text{obs}})$ acts as a normalization factor, called the *evidence* in the Bayesian approach.

3.2.3.1 Posterior probability distribution

Unlike with the least-squares method, we have accounted for calibration uncertainties in our Bayesian models. We take into account the calibration factor described in Sect. 3.2.1.2 as a *nuisance parameter*. Nuisance parameters are parameters instrumental to obtain a good fit but that are of no interest to our analysis. With the Bayesian formalism, it is easy to introduce these nuisance parameters and marginalize the posterior over them.

We have assumed the calibration factors to be identical for all the wavelengths of each module of a given spectrum. They however spatially vary. That is to say, the $m \times m$ covariance matrix (m is the number of wavelengths) of all calibration factors can be divided into s ($s = 4$ is the number of modules in our model) independent fully correlated sub-matrices. As defined in Eq. (3.11), the calibration factor $(1 + \vec{\delta})$ must be positive, so we have reparameterized it as $\vec{\delta}' = \ln(1 + \vec{\delta})$.

Considering n independent identically distributed observations, $\vec{F}_{\nu,i}^{\text{obs}}$, and denoting the elements of at a certain wavelength with the subscript j , Eq. (3.16) becomes:

$$p\left(\left\{\vec{x}_i, \vec{\delta}'_i\right\}_{i=1,\dots,n} \mid \left\{\vec{F}_{\nu,i}^{\text{obs}}\right\}_{i=1,\dots,n}\right) \propto \prod_{i=1}^n p(\vec{F}_{\nu,i}^{\text{obs}} | \vec{x}_i, \vec{\delta}'_i) \times p(\vec{x}_i) \times p(\vec{\delta}'_i). \quad (3.17)$$

Similar to Eq. (3.12), the likelihood of the model is

$$\prod_{i=1}^n p(\vec{F}_{\nu,i}^{\text{obs}} | \vec{x}_i, \vec{\delta}'_i) = \prod_{i=1}^n \prod_{j=1}^m p(F_{\nu,i,j}^{\text{obs}} | x_i, \delta'_{i,j}) \propto \prod_{i=1}^n \prod_{j=1}^m \exp\left[-\frac{1}{2} (\epsilon(\nu_j, x_i, \delta'_{i,j}))^2\right], \quad (3.18)$$

where we have adopted a normal distribution for random noises. It is also possible to assume (i) a *robust noise* with a $f = 3$ degree-of-freedom Student's t -distribution (or Student-t distribution; Sect. B.1.2), in case of outliers; or (ii) an *asymmetric noise* with a split-normal **PDF**, assuming noises are skewed towards high fluxes due to background galaxies or Galactic cirruses.

3.2.3.2 Prior probability distribution

In the non-hierarchical case, we assume a flat prior for the model parameters, simply expressed as:

$$p(\vec{x}) \propto 1. \quad (3.19)$$

For the prior on the calibration offset, we assume that $(1 + \vec{\delta})$ follows a log-normal distribution (Eq. B.6), thus $p(\vec{\delta}') \sim \mathcal{N}(0, 1)$. Moreover, the amplitude of the calibration errors are used to define the allowed range of this parameter. The upper and lower limits of $\delta(\text{module})$ are $\pm 3 \sigma^{\text{cal}}(\text{module})$. Finally, we have fixed $\delta(\text{SL2}) = 1$ as the reference band.

3.2.4 Hierarchical Bayesian (HB) formalism

Our hierarchical model discussed in the current section is inspired by the work of Kelly et al. (2012) and Galliano (2018) on dust SED fitting. Our hierarchical Bayesian (hereafter HB) framework is based on the standard Bayesian method described in Sect. 3.2.3. In non-hierarchical Bayesian (hereafter non-HB) inference, the choice of the prior distribution of the parameters is subjective. We have assumed it flat. On the contrary, the HB prior is inferred from the data. It is thus less subjective. In practice, we assume a functional form for the HB prior. The parameters controlling this prior are called *hyperparameters*. They are inferred from the data, together with the regular model parameters. If the data is very noisy and the parameters are highly degenerated, then the HB solution will collect information from each source through the hyperparameters, whereas a non-HB, uninformative prior will not correct the likelihood. The HB and non-HB methods will provide similar results, if the intrinsic scatter of the parameters is significantly larger than their individual uncertainties. If it is not the case, the HB method will provide better results.

In our HB model, there are three classes of parameters at play:

- *Model parameters* are those physical quantities used to parameterize the model, as described in Sect. 3.1;
- *Hyperparameters* are the parameters that control the distribution of model parameters (the prior), such as their mean and covariance;
- *Nuisance parameters* are not part of the physical model, but they have a non-negligible impact on the fit, therefore must be considered.

Let us start with the non-HB formalism, and add two groups of hyperparameters: (i) the average of the model parameters, $\vec{\mu}$; and (ii) their covariance matrix, Σ . Eq. (3.17) then becomes the full HB posterior:

$$p\left(\left\{\vec{x}_i, \vec{\delta}'_i\right\}_{i=1,\dots,n}, \vec{\mu}, \Sigma, \mid \left\{F_{\nu,i}^{\text{obs}}\right\}_{i=1,\dots,n}\right) \propto \prod_{i=1}^n \underbrace{p(F_{\nu,i}^{\text{obs}} \mid \vec{x}_i, \vec{\delta}'_i)}_{\text{likelihoods}} \times \underbrace{p(\vec{x}_i \mid \vec{\mu}, \Sigma)}_{\text{parameter priors}} \times \underbrace{p(\vec{\mu}) \times p(\Sigma)}_{\text{hyperparameter priors}} \times \underbrace{p(\vec{\delta}'_i)}_{\text{calibration priors}}, \quad (3.20)$$

where the likelihood of the model is still Eq. (3.18). Following Kelly et al. (2012), we have assumed that the prior follows a $g = 8$ degrees of freedom multivariate Student-t distribution, which is asymptotically flatter than a Gaussian (Sect. B.1.1),

well-suited to account for outliers. The prior in Eq. (3.19) now becomes:

$$\prod_{i=1}^n p(\vec{x}_i | \vec{\mu}, \Sigma) = \prod_{i=1}^n \frac{1}{\sqrt{|\Sigma|}} \times \left(1 + \frac{1}{g} (\vec{x}_i - \vec{\mu})^T \Sigma^{-1} (\vec{x}_i - \vec{\mu}) \right)^{-(g+q)/2}, \quad (3.21)$$

where q is the number of parameters, $\vec{\mu}$ is the mean, and Σ is the $q \times q$ covariance matrix. On the other hand, Eq. (3.21) is also the likelihood of the hyperparameters. Notice that the factor $1/\sqrt{|\Sigma|}$ contains elements of Σ that vary, instead of being a normalization constant as in the non-hierarchical case.

3.2.4.1 Prior of the hyperparameters

Since we are now inferring the hyperparameters from the observations, we need to put a prior on them. We assume the means and the covariances are *a priori* independent:

$$p(\vec{\mu}, \Sigma) = p(\vec{\mu}) \times p(\Sigma). \quad (3.22)$$

We assume that $p(\vec{\mu})$ is uniform. To estimate Σ , we use the separation strategy proposed by Barnard et al. (2000):

$$\Sigma = \mathbf{S} \mathbf{R} \mathbf{S}^T. \quad (3.23)$$

For the diagonal matrix of standard deviation, \mathbf{S} , we have chosen independent normal priors. We center these priors on the standard deviations of the least-squares best-fit parameters, $S_{k,k}^{\chi^2}$:

$$p(\mathbf{S}) = \prod_{k=1}^q \frac{1}{S_{k,k}} \frac{1}{\sqrt{2\pi}\sigma(\ln S_{k,k})} \exp \left[-\frac{1}{2} \left(\frac{\ln S_{k,k} - \ln S_{k,k}^{\chi^2}}{\sigma(\ln S_{k,k})} \right)^2 \right], \quad (3.24)$$

where $\sigma(\ln S_{k,k}) = 10$ provides a weakly informative prior.

Concerning the correlation matrix, \mathbf{R} , its elements should be between -1 and 1. Moreover, \mathbf{R} should be positive definite. To enforce these conditions, we follow Barnard et al. (2000) and assign:

$$p(\mathbf{R}) \propto |\mathbf{R}|^{(h-1)(q-1)/2-1} \left(\prod_{k=1}^q |\mathbf{R}_{(kk)}| \right)^{-h/2} \propto |\mathbf{R}|^{q(q-1)/2-1} \left(\prod_{k=1}^q |\mathbf{R}_{(kk)}| \right)^{-(q+1)/2}, \quad (3.25)$$

where $\mathbf{R}_{(kk)}$ is the principal submatrix of order k . This distribution is chosen so that $p(\Sigma | \mathbf{S})$ follows an inverse Wishart distribution in order to ensure that the covariance matrix is positive definite.

Finally, the hyperparameter prior is:

$$p(\vec{\mu}) \times p(\Sigma) \propto p(\mathbf{S}) \times p(\mathbf{R}). \quad (3.26)$$

3.2.5 Numerical implementation

The total parameter space of the posterior, Eq. (3.20), has the dimension

$$N_{\text{dim}} = \underbrace{n \times q}_{\text{parameters}} + \underbrace{2 \times q + q \times (q - 1)/2}_{\text{hyperparameters}} + \underbrace{n \times (s - 1)}_{\text{calibration}}, \quad (3.27)$$

where q is the number of free model parameters, n is the observation sample size and s is the number of observational modules¹⁰. For a typical sample with $n = 40$ spectra, modelled with $q = 65$ free model parameters, the dimension is $N_{\text{dim}} = 5\,005$. To sample such a posterior on a regular cartesian parameter space is a tedious work. A more efficient, alternative sampling method consists in using a **Markov Chain Monte Carlo (MCMC)**.

3.2.5.1 Markov chain Monte Carlo (MCMC)

A **MCMC** is a random sampling method which visits a point, \vec{x} , with a probability proportional to a given distribution function $\pi(\vec{x})$. In Bayesian methods, we simply take $\pi(\vec{x})$ to be the posterior. Each point, $\vec{x}(t_i)$, in a Markov chain, at step t_i , depends only on the preceding point, $\vec{x}(t_{i-1})$. Drawing the next step requires a transition probability function, $p(\vec{x}(t_i) | \vec{x}(t_{i-1}))$. The distribution of the drawn sample, $\vec{x}(t_i)$, converges toward the true posterior when the sample size increases.

Among numerous **MCMC** samplers, we have applied the *Gibbs sampler* within the *Metropolis-Hastings algorithm*. The Metropolis-Hastings algorithm is a rejection method. It finds the transition probability function $p(\vec{x}(t_i) | \vec{x}(t_{i-1}))$ by calculating an *acceptance probability* and accepting or rejecting accordingly the proposed points drawn from a proposal distribution. The Gibbs sampler is a special case of the Metropolis-Hastings algorithm whose proposals are always accepted. It consists in sampling the conditional probability of one parameter at a time, fixing all the other ones to their current values: $\pi(x_j | \vec{x}) = p(x_j(t_i) | x_j(t_{i-1}), \vec{x}^-(t_i))$, where \vec{x}^- represents the values of all the parameters except x_j . The full Gibbs sampler operates as follows:

1. Cycle through each component of \vec{x} in turn¹¹;
2. For each component, hold all the other components fixed and draw a new value x_j from the full conditional distribution $\pi(x_j | \vec{x}^-)$ of all possible values of that component;
3. Set the component to the new value and go on to the next component.

3.2.5.2 Sampling the posterior

In our model, we have sampled the posterior of Eq. (3.20) with *Gibbs sampling* in the following manner. We have initialized the model parameters, $\vec{x}(t_0)$, with the best-fit values of the least-squares fit. As for the hyperparameters, we have set μ and the diagonal elements of **S** to the mean and standard deviation of the least-squares parameters. The correlation coefficients which

10. We assume the calibration factors of a spectral sample in the same module to be fully correlated (Sect. 3.2.3). The number of calibration factors is thus the number of modules, s , instead of the number of wavelengths, m .

11. In principle, the order of components does not matter. We will see that we have modified this order to optimize our model.

compose \mathbf{R} are 0 at the beginning. Calibration parameters, $\vec{\delta}'_i$, are initially $\vec{0}$. Then, we have performed N_{MCMC} iterations of the following steps:

1. Draw calibration parameters for each module and each spectrum from the function below and attribute them to the corresponding wavelengths.

$$p(\delta'_{i,k(j)} | \vec{\delta}'_{i,k' \neq k}, \vec{x}_i, \vec{F}_{v,i}^{\text{obs}}) \propto p(\vec{\delta}'_i) \times \prod_{j=1}^m p(F_{v,i,j}^{\text{obs}} | \vec{x}_i, \delta'_{i,k(j)}) \quad (3.28)$$

2. Draw each model parameter for each spectrum:

$$p(x_{i,k} | \vec{x}_{i,k' \neq k}, \vec{\delta}'_i, \vec{\mu}, \Sigma, \vec{F}_{v,i}^{\text{obs}}) \propto p(\vec{x}_i | \vec{\mu}, \Sigma) \times \prod_{j=1}^m p(F_{v,i,j}^{\text{obs}} | \vec{x}_i, \delta'_{i,k(j)}) \quad (3.29)$$

3. Draw the hyperparameters, μ_k , for each model parameter:

$$p(\mu_k | \mu_{k' \neq k}, \{\vec{x}_i\}_{i=1, \dots, n}, \Sigma) \propto \prod_{i=1}^n p(\vec{x}_i | \vec{\mu}, \Sigma) \quad (3.30)$$

4. Draw the standard deviations, $S_{k,k}$, of each model parameter:

$$p(S_{k,k} | S_{k' \neq k, k' \neq k}, \{\vec{x}_i\}_{i=1, \dots, n}, \mathbf{R}) \propto p(\mathbf{S}) \times \prod_{i=1}^n p(\vec{x}_i | \vec{\mu}, \Sigma) \quad (3.31)$$

5. Draw elements of the correlation matrix, R_{k_1, k_2} , of each model parameter:

$$p(R_{k_1, k_2} | R_{k'_1 \neq k_1, k'_2 \neq k_2}, \{\vec{x}_i\}_{i=1, \dots, n}, \mathbf{S}) \propto p(\mathbf{R}) \times \prod_{i=1}^n p(\vec{x}_i | \vec{\mu}, \Sigma) \quad (3.32)$$

3.2.5.3 Post-processing

An important but difficult question is knowing when to stop the Markov chain, that is, choosing the correct value of N_{MCMC} . It is a matter of ensuring that our distribution has converged towards the stationary posterior. We first need to subtract the *burn-in* of the chain, which is the first steps before the walker reaches the region of high probability. A useful way to determine the burn-in length is to scrutinize the output. In addition to plotting the chains, where every drawn model parameter or calibration factor as a function of **MCMC** step count, and the parameter distribution histograms after burn-in (e.g. **Fig. 3.8**), we have derived several useful quantities to evaluate the convergence of **MCMC**. The **AutoCorrelation Function (ACF)** of a parameter, x , describes the correlation of x with a delayed copy of itself as a function of the delay (or “*lag*”, the interval between two **MCMC** steps), k :

$$\rho_x(k) = \frac{\text{cov}_t(x^{(t)}, x^{(t+k)})}{\text{var}_t(x^{(t)}) \text{var}_t(x^{(t+k)})}, \quad (3.33)$$

where $x^{(t)}$ is the value of parameter x at the step t of **MCMC**. The subscript t indicates that the variance and covariance are taken over the index t . Since autocorrelation is a particular case of convolution (Press et al., 2007), and since it becomes a regular product in the Fourier space, we have used the **Fast Fourier Transform (FFT)** to compute the **ACF** as follows:

- We apply a **FFT** to \vec{x} at the positive lag between $x^{(t)}$ and $x^{(t+k)}$;
- We multiply the resulting transform by its complex conjugate;
- We inverse transform the product.

The *integrated autocorrelation time* is derived from **ACF** (Sokal, 1997) by:

$$\tau_{\text{int}}(x) = 1 + 2 \sum_{k=1}^{N_{\text{MCMC}}} \rho_x(k), \quad (3.34)$$

which quantifies the length between two independent samplings. The *effective sample size* is thus

$$N_{\text{eff}}(x) = \frac{N_{\text{MCMC}}}{\tau_{\text{int}}(x)}. \quad (3.35)$$

It quantifies the number of truly independent draws of a Markov chain of length N_{MCMC} ¹². In practice, we have find a typical burn-in length of $\sim 3\,000$ steps for our fits.

One of the main advantages of the Bayesian approach is that we can estimate precise uncertainties on any parameter. This can be done with standard statistical estimators, such as the mean and standard-deviation, on the posterior of a parameter, marginalizing on the rest. To extract a representative model after burn-in, equivalent to a frequentist “*best-fit model*”, we display the model density and compare the mean (with standard deviation as symmetric uncertainties) and median (with the intervals of second and fourth 6-quantiles as asymmetric uncertainties; approximately equivalent to $1\text{-}\sigma$ intervals) of the distribution. If most parameter distributions are *uni-modal* or just symmetric, the mean value point of the parameter space fits well the observed spectrum. Otherwise, it is possible to display the model at the median parameter values (*cf.* Sect. 3.3.2). This is the solution we have chosen (*e.g.* Fig. 3.8).

3.2.5.4 Optimizing the algorithm

We have roughly estimated the calculation time of our fitting model using a set of simulated data generated in the way described in Sect. 3.3.2. Our test sample has $n = 40$ spectra, each with a spectral sampling size of 417 wavelengths. They are fitted with a model of $q = 65$ free model parameters. In the HB case, the mean and covariance matrix of each free model parameters are hyperparameters, and the dimension of the total parameter space is $N_{\text{dim}} = 5\,005$ (Eq. 3.27). The length of the **MCMC** is 10 000 long, burn-in included, for both non-HB and HB methods. The actual runtime¹³ is shown as follows:

12. There are also a few so-called “*convergence diagnostic*” tools available (*e.g.* Plummer et al., 2006).

13. The fit has been run with a “2.4 GHz Quad-Core Intel Core i5” processor and a “8 GB 2133 MHz LPDDR3” memory.

- The least-squares method costs 37 minutes 18 seconds;
- The non-HB method costs 34 hours 47 minutes;
- The HB method (version 1) costs 1 044 hours 39 minutes;
- The HB method (version 2) costs 783 hours 29 minutes;
- The HB method (version 3) costs 109 hours 10 minutes.

The difference between the version 1 HB fit and the version 2 HB fit is that the latter applies the **Modified Sherman-Morrison (MSM; Sect. B.2.3)** approach to calculate the inverse of the covariance matrix, Σ , when sampling hyperparameters (Eq. 3.32 and Eq. 3.21). The **MSM** method gives the inverse of a matrix, knowing the inverse of another matrix which differs by only two elements with symmetric position (*i.e.* swapping lines and columns). This allows us to avoid inverting a large number of $q \times q$ matrices to sample Eq. (3.32). Note that **MSM** has not been applied to Eqs. (3.29) – (3.31) due to the fact that, in a single iteration (*i.e.* the “*big loop*” of Eqs. 3.28 – 3.32), we need to perform only one inversion. We have saved $\simeq 25\%$ computation time through this optimization.

Another improvement of our code’s performance has been permitted by studying the integrated autocorrelation time, τ_{int} (Eq. 3.34). The longer this autocorrelation time is (in number of **MCMC** steps), the longer the chain will need to be. Gibbs sampling can indeed explore very slowly the parameter space when there are strong correlations between parameters. It happens that the correlation coefficients are quite demanding in terms of computing time, whereas they have a short integrated autocorrelation time. An example is presented in Fig. 3.3, showing the distribution of the integrated autocorrelation times of several (hyper)parameters. We see that the τ_{int} of the correlation coefficients (panel *c*) is generally smaller than that of the means or standard deviations (panels *a* and *b*). We also see that $\tau_{\text{int}} = 18$ for the worst case in panel (*c*), which gives an effective sample size of $N_{\text{eff}} = 388$ after discarding 30% of the total **MCMC** length, $N_{\text{MCMC}} = 10\,000$, to account for burn-in. In our experience, $N_{\text{MCMC}} \simeq 20\tau_{\text{int}}$ is typically more than adequate for a chain to converge. Consequently, we can afford to sample only once every ten **MCMC** iterations the coefficients of the correlation matrix, \mathbf{R} (Eq. 3.32). This way, the effective sample size reduces to one tenth (*i.e.* $N_{\text{eff}} = 38$; example see Fig. D.9), but is still large enough to obtain a good sampling of the correlation matrix. The total sampling runs significantly faster as expected since there are $C_2^q = 2\,080$ non-zero elements of \mathbf{R} , which accounts for more than 40% of the size of the parameter space. The implementation of this acceleration is what defines the version 3 of our HB code. In the end, we have concluded that our code, after these optimizations, runs roughly ten times faster than the original version 1 HB fit¹⁴.

Finally, we have fine-tuned the order of the sampling sequence of parameters, the “*scan order*”. Indeed, the nature of the scan order (random or systematic) can affect the convergence time (*e.g.* He et al., 2016). However, most theoretical results concerning the statistical efficiency of Gibbs sampling are only for random scans, so we have tested different permutations of

14. For the fit of the simulated sample in Sect. 3.3, we have run the version 2 HB. As for the fit of the observed M 82 spectra in Sect. 4.1, we have run the version 3 HB because the parameter space is much larger, given the same sample size.

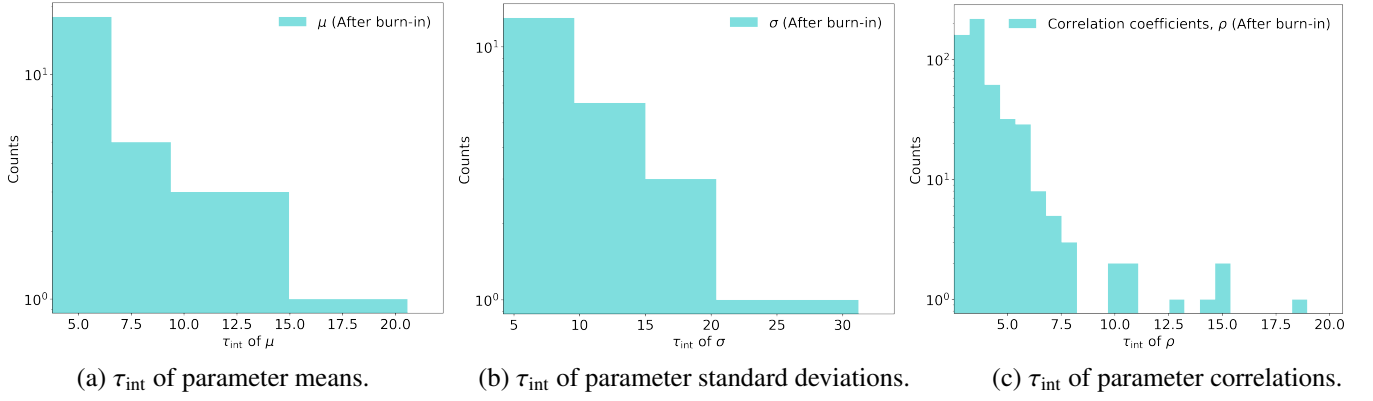


Figure 3.3 – Distributions of hyperparameter integrated autocorrelation times.

Panel (a), (b) and (c) show the distributions of reliable integrated autocorrelation times of the means and standard deviations, and correlation coefficients, in the HB cases.

our parameter set (Table 3.5). We have found that the best systematic scan (*i.e.* sampling order: extinction - dust continua - stellar continuum - **UIBs** - gas lines) is more than 50% faster than the worst case (*i.e.* sampling order: dust continua - gas lines - **UIBs** - stellar continuum - extinction). In principle, we suggest to put parameters that have a global impact on the spectrum (*e.g.* parameters of continuum and extinction) before those controlling only a narrow region of the spectrum (*e.g.* parameters of **UIB** and gas line components).

3.3 Model demonstration

The **MIR** spectral fitting model described in the current chapter is implemented in the software, MILES, that I have developed during this thesis. It has been optimized and tested to fit low- ($R \sim 60$) to moderate-spectral resolution ($R \sim 600$) observations, with a wavelength range between $2.5 \mu\text{m}$ and $40 \mu\text{m}$. This is indeed the typical spectroscopic coverage of AKARI/IRC, *Spitzer*/IRS and the upcoming JWST/MIRI. It includes more than 30 emission bands (split-Lorentzian) and more than 40 unresolved emission lines (Gaussian). Each of them can vary in width, position, and intensity. Optical properties of different dust compounds are available to fit the dust continuum. The stellar continuum is fitted only with a scaling factor. The components above are linearly combined and attenuated by dust and ice, assuming a slab extinction. More complex geometries will be implemented in future versions.

We have designed a series of tests to assess the performances of MILES. In particular, we have simulated and fitted a synthetic sample of galaxy spectra. These simulated spectra have been designed so that the important **UIB** features are known and vary. They can thus be used to compare the performances of different fitting methods. By fitting simulated data, we can assess how accurate our method is to recover parameters, as we know their real values

3.3.1 Generating galaxy spectra

Fitting synthetic spectra is usually the best way to test a model, as we can compare its output to the true values. To simulate realistic galaxy spectra, we have started from a spectrum in our M 82 data cube (*i.e.* A1 in Fig. 2.22). We have fitted it with the non-hierarchical Bayesian method, with the parametrization below Table 3.5:

- 15 UIBs (Table 3.2), Main 3.3, Main 3.4, Small 3.5, Main 6.2 (1), Main 6.2 (2), Small 6.8, Plateau 7.7, Main 7.7 (1), Main 7.7 (2), Main 8.6, Plateau 11.3, Main 12.7 (1), Main 12.7 (2), Plateau 17.0 and the reference Main 11.2, are fitted with intensity ratios $\ln(R^{band})$, except the reference band for which the intensity $\ln(I^{11.2})$ instead of intensity ratio is fitted;
- 10 gas lines (Table 3.3), $[\text{Br}\alpha]_{4.05\mu\text{m}}$, $[\text{Ar II}]_{6.98\mu\text{m}}$, $[\text{Ar III}]_{8.99\mu\text{m}}$, H_2 0-0 S(3) $_{9.7\mu\text{m}}$, $[\text{S IV}]_{10.51\mu\text{m}}$, H_2 0-0 S(2) $_{12.3\mu\text{m}}$, $[\text{Ne II}]_{12.81\mu\text{m}}$, $[\text{Ne III}]_{15.56\mu\text{m}}$, H_2 0-0 S(1) $_{17.0\mu\text{m}}$ and $[\text{S III}]_{18.68\mu\text{m}}$, are fitted with intensity ratios $\ln(R^{line})$;
- 3 dust grain continua (Table 3.4), BE Z96, Gra D03 and Sil D03, with $\ln(F_{15\mu\text{m}})$ and $\ln(T)$;
- 1 stellar continuum, a blackbody at temperature $T_\star = 50\,000$ K, with the total power $\ln(L_{15\mu\text{m}}^\star)$;
- 1 dust extinction, $\ln(A_V^{\text{dust}})$.

In summary, we have fitted 33 model parameters. We also have fitted 3 calibration factors. The fitting result is plotted in Fig. 3.4. a.

In a second time, we have used the fitted parameters, presented in Table 3.6, as the basis to generate a sample of synthetic spectra. Specifically, we have modified three sets of these parameters: (i) the band intensity ratios, (ii) the band-to-continuum ratio and (iii) the signal-to-noise ratio of spectra.

Band intensity ratio. In our simulation, we have generated different correlations between relative intensities of 5 UIBs or *UIB complexes* (*cf.* definition in Table 4.1) at 3.3, 3.4, 6.2, 7.7 and 12.7 μm . These correlations are idealized, but they are meaningful to test our model. Given ten (*i.e.* $C_2^5 = 10$) correlation coefficients, we have generated ten sets of parameters from a multivariate Gaussian, each with fixed means and covariance matrices. The correlation coefficients are:

1. $\text{corr}(R_C^{3.3}, R_C^{3.4}) = -0.9$ (anti-correlated);
2. $\text{corr}(R_C^{3.3}, R_C^{6.2}) = 0.6$ (correlated);
3. $\text{corr}(R_C^{3.3}, R_C^{7.7}) = 0.6$ (correlated);
4. $\text{corr}(R_C^{3.3}, R_C^{12.7}) = 0$ (non-correlated);
5. $\text{corr}(R_C^{3.4}, R_C^{6.2}) = -0.6$ (anti-correlated);
6. $\text{corr}(R_C^{3.4}, R_C^{7.7}) = -0.6$ (anti-correlated);
7. $\text{corr}(R_C^{3.4}, R_C^{12.7}) = 0$ (non-correlated);
8. $\text{corr}(R_C^{6.2}, R_C^{7.7}) = 0.9$ (correlated);
9. $\text{corr}(R_C^{6.2}, R_C^{12.7}) = 0$ (non-correlated);

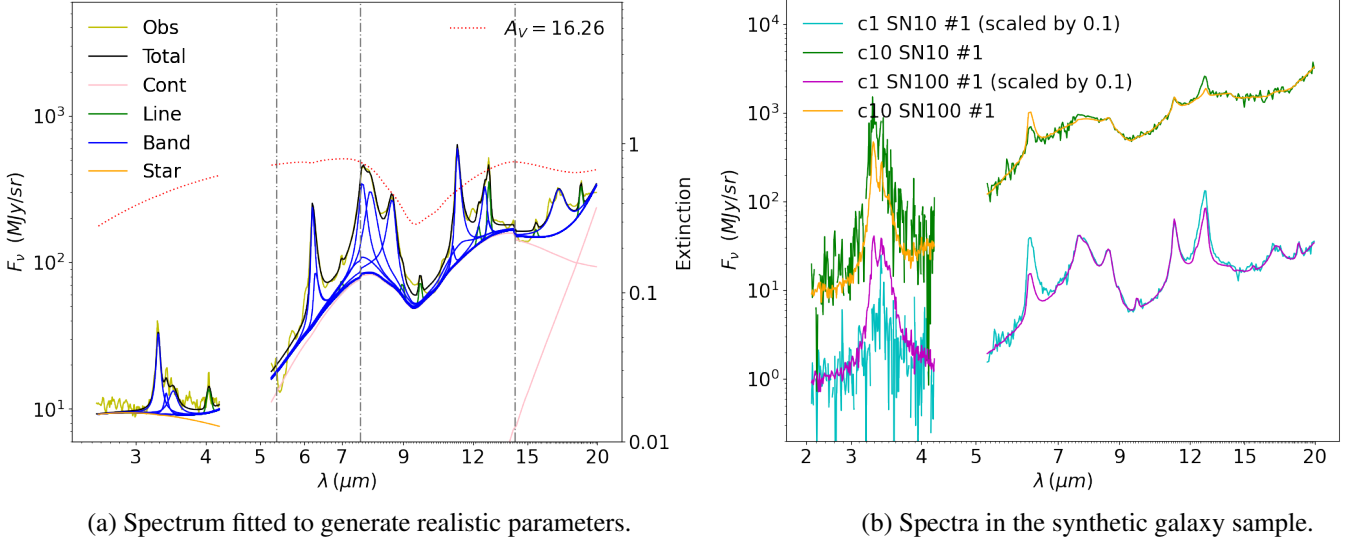


Figure 3.4 – Synthetic galaxy spectra.

Panel (a) shows the non-HB fit of an observed M 82 spectrum (*i.e.* A1 in Fig. 2.22; yellow). The fitted total spectrum (black) (with its components: the gas lines in green, the UIBs in blue, the dust continua in pink and the stellar continuum in orange) is used to generate the parameters of synthetic galaxy spectra. The extinction curve (red dotted) is also overlaid (its fitted amplitude is $A_V = 16.26$). The spectral discontinuities at around 5, 8 and 14 μm are due to the inter-calibration discrepancies and are accounted for with calibration factors. Panel (b) shows a subset of 4 simulated spectra out of 40 with different dust continuum levels and different S/N ratios. “c1” and “c10” mean that the dust continuum is scaled by factors of 1 and 10, respectively. “SN10” and “SN100” mean that the S/N ratio at 15 μm is set to be 10 and 100, respectively, by keeping the normalized S/N ratio profile for the entire spectrum. In addition, two spectra with the same continuum modification (cyan and magenta) are further scaled by a factor of 0.1 to separate from others. There are 9 other subsets with other parameters randomly varied.

$$10. \text{corr}(R_C^{7.7}, R_C^{12.7}) = 0 \text{ (non-correlated } I(7.7)/I(11.3) - I(12.7)/I(11.3);$$

where we have defined the intensity ratios of:

- the 3.3- μm band, $R_C^{3.3} = I^{3.3} / (I^{11.2} + I^{11.3})$, hereafter $I(3.3)/I(11.3)$;
- the 3.4- μm complex, $R_C^{3.4} = (I^{3.4} + I^{3.5}) / (I^{11.2} + I^{11.3})$, hereafter $I(3.4)/I(11.3)$;
- the 6.2- μm complex, $R_C^{6.2} = (I^{6.2(1)} + I^{6.2(2)}) / (I^{11.2} + I^{11.3})$, hereafter $I(6.2)/I(11.3)$;
- the 7.7- μm complex, $R_C^{7.7} = (I^{7.7(p)} + I^{7.7(1)} + I^{7.7(2)}) / (I^{11.2} + I^{11.3})$, hereafter $I(7.7)/I(11.3)$;
- the 12.7- μm complex, $R_C^{12.7} = (I^{12.7(1)} + I^{12.7(2)}) / (I^{11.2} + I^{11.3})$, hereafter $I(12.7)/I(11.3)$.

Once we know the intensity of the complex, we simulate the individual intensities of each of its components, assuming they are uniformly distributed.

Band-to-continuum ratio. The dust continuum can dominate the MIR emission in AGNs or low-metallicity galaxies because aromatic features can not survive extreme physical conditions. In practice, the observed spectra can be much more complex in terms of continuum emission, compared to our model. For instance, we have modeled the dust continuum emission only with 3 modified blackbody components in the Fig. 3.4. a fit. This simple parametrization does not always provide enough flexibility to accurately fit observed spectra (see also the comment in Sect. 3.1.5). When fitting the

synthetic spectrum sample, we have tested the impact of the continuum level on the S/N ratio of bands and lines, given the same spectrum S/N ratio. Given the fixed band and line intensities, we have anchored the dust continuum emission at $15\ \mu\text{m}$, where there are usually no other emission features, and have scaled the extensive physical parameter $F_{15\ \mu\text{m}}$ to simulate a continuum with 1 and 10 times the fitted $F_{15\ \mu\text{m}}$ (noted as “c1” and “c10”, respectively; *e.g.* Fig. 3.4. b). We have thus distinguished 2 groups of spectra in the simulated sample (*e.g.* the magenta and yellow spectra in Fig. 3.4. b).

Total spectrum signal-to-noise ratio. We have also generated another set of synthetic spectrum samples, where we have fixed the continuum level and varied the S/N ratio of the total spectrum. In practice, we have normalized the S/N ratio at each wavelength to the value at $15\ \mu\text{m}$ and assigned a new S/N ratio at $15\ \mu\text{m}$ (here 10 or 100, noted as “SN10” and “SN100”, respectively). Finally, we have distinguished 2 groups of spectra in the simulated sample (*e.g.* the green and yellow spectra in Fig. 3.4. b).

The choice of these sets of parameters is motivated on the fact that we are interested mainly in band and line properties (*i.e.* shape, position and intensity). In total, we have generated 40 spectra divided into two sets: one with 10 subsets dedicated to testing band ratio correlations; the other with 4 subsets for testing the impact of data quality. Examples of the generated sample are shown in Fig. 3.4. b.

Our goal is to assess the performances of the model by comparing the derived and true parameters in different configurations. For that purpose, we have mainly scrutinized the parameter distributions (Sect. 3.3.2.2), analyzed their autocorrelation in the MCMC (Sect. 3.3.2.3) and compared the correlations between UIB relative intensities (Sect. 3.3.3).

Table 3.6: Values of the free parameters used to generate synthetic spectra of galaxy.

Model parameters					
No.	Parameter	Symbol	Value	Unit	Physical quantity
1	lnAv1	$\ln(A_V^{\text{dust}})$	2.789	$\ln(A_V/1\ \text{mag})$	Dust extinction (WD01)
2	lnLstar1	$\ln(L_{15\ \mu\text{m}}^*)$	44.180	$\ln(L^*/1\ \text{MJy Hz})$	Blackbody star at $5\ 10^4\ \text{K}$
3	lnFcont1	$\ln(F_{15\ \mu\text{m}}^{\text{BE Z96}})$	5.264	$\ln(F/1\ \text{MJy sr}^{-1})$	BE Z96 flux density
4	lnT1	$\ln(T^{\text{BE Z96}})$	5.546	$\ln(T/1\ \text{K})$	BE Z96 temperature
5	lnFcont2	$\ln(F_{15\ \mu\text{m}}^{\text{Gra D03}})$	2.886	$\ln(F/1\ \text{MJy sr}^{-1})$	Gra D03 flux density
6	lnT2	$\ln(T^{\text{Gra D03}})$	4.187	$\ln(T/1\ \text{K})$	Gra D03 temperature
7	lnFcont3	$\ln(F_{15\ \mu\text{m}}^{\text{Sil D03}})$	-2.202	$\ln(F/1\ \text{MJy sr}^{-1})$	Sil D03 flux density
8	lnT3	$\ln(T^{\text{Sil D03}})$	3.927	$\ln(T/1\ \text{K})$	Sil D03 temperature
9	lnRline1	$\ln(R^{\text{Bra}})$	-4.414	$\ln(I/I^{11.2})$	[Br α] $_{4.05\ \mu\text{m}}$ intensity ratio
10	lnRline2	$\ln(R^{\text{ArII}})$	-4.506	$\ln(I/I^{11.2})$	[Ar II] $_{6.98\ \mu\text{m}}$ intensity ratio
11	lnRline3	$\ln(R^{\text{ArIII1}})$	-3.793	$\ln(I/I^{11.2})$	[Ar III] $_{8.99\ \mu\text{m}}$ intensity ratio
12	lnRline4	$\ln(R^{\text{H2S3}})$	-3.177	$\ln(I/I^{11.2})$	H ₂ 0-0 S(3) $_{9.7\ \mu\text{m}}$ intensity ratio

Model parameters					
No.	Parameter	Symbol	Value	Unit	Physical quantity
13	lnRline5	$\ln(R^{\text{SiV}})$	-9.086	$\ln(I/I^{11.2})$	[Si IV] _{10.51μm} intensity ratio
14	lnRline6	$\ln(R^{\text{H2S2}})$	-3.476	$\ln(I/I^{11.2})$	H ₂ 0-0 S(2) _{12.3μm} intensity ratio
15	lnRline7	$\ln(R^{\text{NeII}})$	-2.095	$\ln(I/I^{11.2})$	[Ne II] _{12.81μm} intensity ratio
16	lnRline8	$\ln(R^{\text{NeIII1}})$	-4.569	$\ln(I/I^{11.2})$	[Ne III] _{15.56μm} intensity ratio
17	lnRline9	$\ln(R^{\text{H2S1}})$	-9.779	$\ln(I/I^{11.2})$	H ₂ 0-0 S(1) _{17.0μm} intensity ratio
18	lnRline10	$\ln(R^{\text{SIII1}})$	-2.919	$\ln(I/I^{11.2})$	[S III] _{18.68μm} intensity ratio
19	lnRband1	$\ln(R^{3.3})$	-1.963	$\ln(I/I^{11.2})$	Main 3.3 intensity ratio
20	lnRband2	$\ln(R^{3.4})$	-3.913	$\ln(I/I^{11.2})$	Main 3.4 intensity ratio
21	lnRband3	$\ln(R^{3.5})$	-2.987	$\ln(I/I^{11.2})$	Small 3.5 intensity ratio
22	lnRband4	$\ln(R^{6.2 (1)})$	-0.907	$\ln(I/I^{11.2})$	Main 6.2 (1) intensity ratio
23	lnRband5	$\ln(R^{6.2 (2)})$	-1.930	$\ln(I/I^{11.2})$	Main 6.2 (2) intensity ratio
24	lnRband6	$\ln(R^{7.7 (p)})$	-1.118	$\ln(I/I^{11.2})$	Plateau 7.7 intensity ratio
25	lnRband7	$\ln(R^{7.7 (1)})$	-0.048	$\ln(I/I^{11.2})$	Main 7.7 (1) intensity ratio
26	lnRband8	$\ln(R^{7.7 (2)})$	0.209	$\ln(I/I^{11.2})$	Main 7.7 (2) intensity ratio
27	lnRband9	$\ln(R^{8.6})$	0.064	$\ln(I/I^{11.2})$	Main 8.6 intensity ratio
28	lnRband10	$\ln(R^{11.0})$	-2.889	$\ln(I/I^{11.2})$	Small 11.0 intensity ratio
29	lnRband11	$\ln(I^{11.2})$	34.290	$\ln(I/1 \text{ MJy sr}^{-1} \text{ Hz})$	Main 11.2 intensity
30	lnRband12	$\ln(R^{11.3 (p)})$	-1.010	$\ln(I/I^{11.2})$	Plateau 11.3 intensity ratio
31	lnRband13	$\ln(R^{12.7 (1)})$	-1.193	$\ln(I/I^{11.2})$	Main 12.7 (1) intensity ratio
32	lnRband14	$\ln(R^{12.7 (2)})$	-2.889	$\ln(I/I^{11.2})$	Main 12.7 (2) intensity ratio
33	lnRband15	$\ln(R^{17.0 (p)})$	-0.608	$\ln(I/I^{11.2})$	Plateau 17.0 intensity ratio
Nuisance parameters					
No.	Parameter	Symbol	Value	Unit	Physical quantity
i	ln1pd1	$\ln(1 + \delta^{\text{AKARI-NG}})$	0.200	$\ln(1 + \delta^{\text{cal}})$	IRC calibration factor
ii	ln1pd2	$\ln(1 + \delta^{\text{IRS-SL1}})$	0.050	$\ln(1 + \delta^{\text{cal}})$	IRS-SL1 calibration factor
iii	ln1pd3	$\ln(1 + \delta^{\text{IRS-LL2}})$	-0.050	$\ln(1 + \delta^{\text{cal}})$	IRS-LL2 calibration factor

3.3.2 Fit of synthetic spectra

3.3.2.1 Fitted model and median model

In Figs. 3.5 – 3.6, we have presented the fits of two spectra shown in Fig. 3.4. b. To understand the differences between the least-squares and non-HB methods, we have compared the fits of the best quality spectrum, “c1 SN100 #1”, with a relative weak

continuum and high S/N ratios for highlighting **UIB** features. The least-squares and non-HB methods provide quite similar best fits in this case, because the S/N ratio is high. The Bayesian posterior distribution is thus narrow and well-constrained. The most remarkable difference between the two methods is due to the account of the calibration factors correcting the discontinuities at the module edges (AKARI/IRC-*Spitzer*/IRS at $\sim 5 \mu\text{m}$, SL2-SL1 at $\sim 8 \mu\text{m}$ and SL1-LL2 at $\sim 14 \mu\text{m}$; gray dashed line in Fig. 3.5. b). In our simulation, the least-squares method is biased by its inability to account for nuisance variables, such as the calibration factors. The effect of calibration factors can have a more significant role for highly degenerate models and is of great importance for correcting the discontinuity of spectra combined from different observations (*e.g.* Fig. 3.6 in our simulation or Fig. 4.3 for a real galaxy).

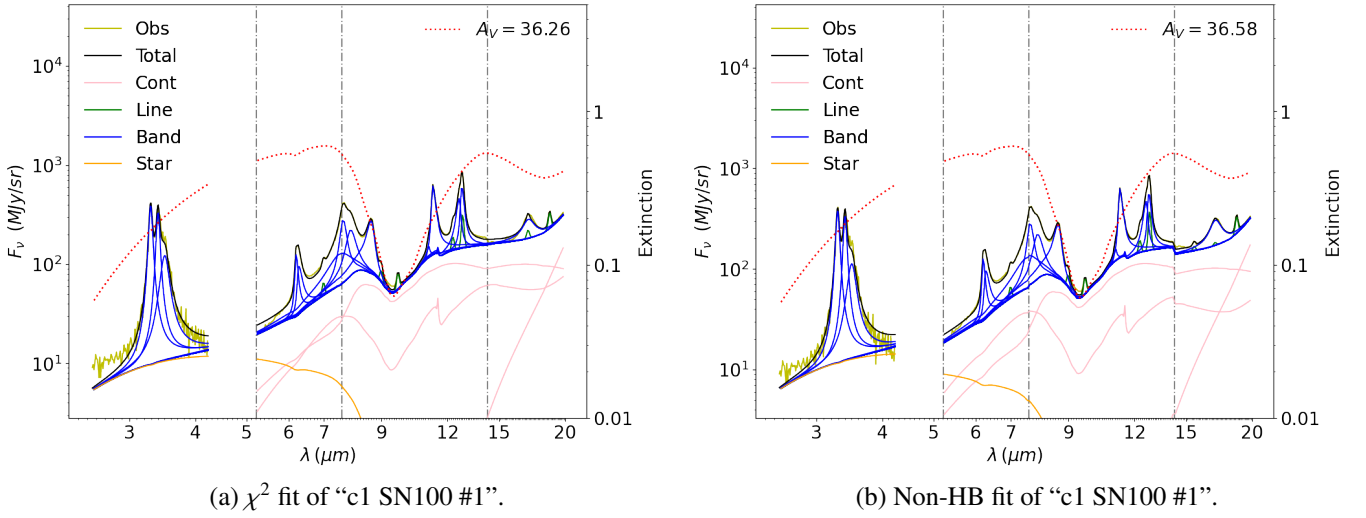


Figure 3.5 – Least-square and non-HB fits of synthetic galaxy spectra.

Panels (a) and (b) show the χ^2 and non-HB fits of the spectrum “c1 SN100 #1”, respectively. The total fitted model (black) along with its components (*i.e.* the gas lines in green, the **UIBs** in blue, the dust continua in pink and the stellar continuum in orange) and the extinction curve (red dotted) is overlaid on the observed spectrum (yellow). In addition, the gray dashed lines divide spectral regimes attributed to different instrument modules, where calibration factors play a role in Bayesian fits. We have used the same plot template to draw all fits in this manuscript.

Unlike the least-squares method, which gives only a set of best-fit parameters, the Bayesian method provides the full probability distribution of each parameter. This distribution can be complex. We thus have to find a way to determine a representative best-fit model. In hierarchical models, hyperparameters help constrain the parameter distribution. In Sect. 3.3.2.2, we will see that it is easier to find a representative value for a narrower parameter distribution, especially in *multi-modal* cases. Fig. 3.6 compares the non-HB and HB fits with the spectrum “c10 SN10 #1”. In this case the **UIB** features are diluted into a ten times stronger continuum emission with ten times more noise than the previous case in Fig. 3.5. In both panels, the model shown corresponds to the mean of the distribution of each parameter. By eye, the two fits differ mainly because the continuum is strongly degenerate with the extinction. It is better looking for the HB fit (panel b), because the distribution is narrower. It shows that one needs to carefully choose the representative model to compare to our observations. It is much more accurate to take the median of the total model calculated at each sampled wavelength in the Markov chain after burn-in (hereafter “*median*”).

model”; Fig. 3.7). We have mimicked the empirical interval estimate rule of normal distribution to define the $1-\sigma$ interval with the 1st and 5th 6-quantiles (*i.e.* sextiles), between which it contains 68% probability. Basically, both Bayesian fits are in better agreement with the “*observed*” spectrum within the $1-\sigma$ interval. This is the correct, probabilistic way to compare a Bayesian fit to the data. In our specific case, the discrepancy at $\sim 10 \mu\text{m}$ is further explored in Sect. D.1.1.

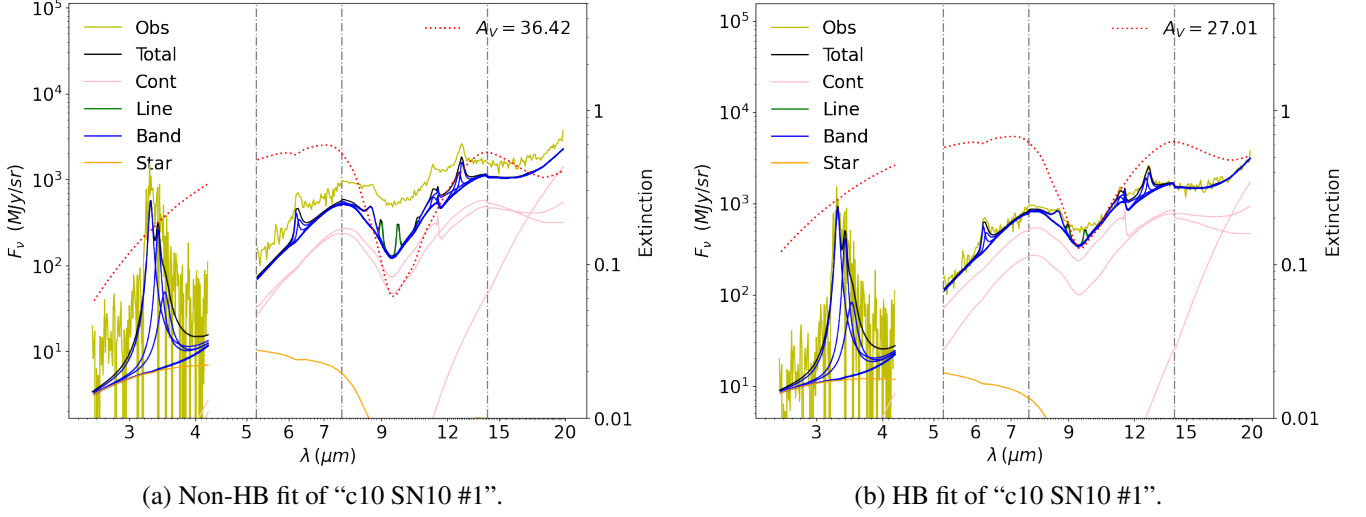


Figure 3.6 – Non-HB and HB fits of synthetic galaxy spectra. Panels (a) and (b) show the non-HB and HB fits of the spectrum “c10 SN10 #1”, respectively.

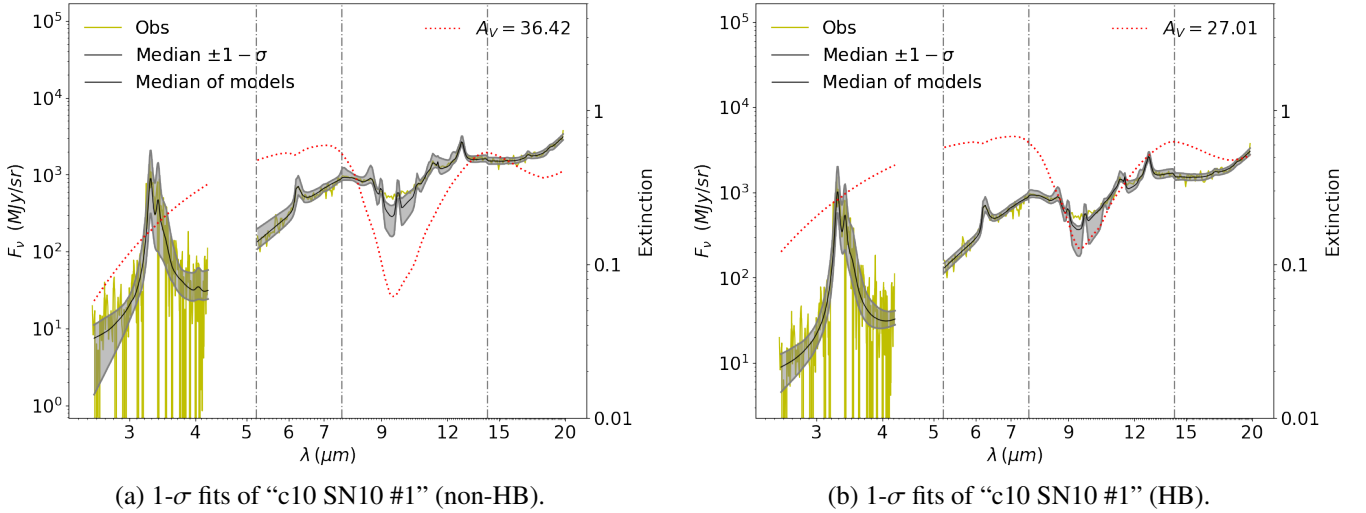


Figure 3.7 – Median models fitted with Bayesian methods. Panels (a) and (b) show the total models calculated at each wavelength in MCMC after burn-in within the $1-\sigma$ interval (gray shadowed; see text) distributed on both sides of the median values (black). The extinction curve (red dotted) is also overlaid.

3.3.2.2 Distributions of fitted parameters

Let us have a close look at the individual distribution of parameters used to draw spectra in Fig. 3.6. Figs. 3.8 – 3.9 represent the MCMC and the distribution of three parameters inferred from the fit of Fig. 3.6, with the non-HB and HB methods. We see that the calibration factors are similarly inferred (panels a). The extinction amplitude, $\ln(A_V)$, is different with the two methods. In both cases it is clearly bi-modal, with two solutions corresponding to the two degenerate solutions high-extinction/high-continuum or low-extinction/low-continuum. The solution around $\ln(A_V) \simeq 3.2$ is however favored by the HB fit, which is closer to the true value. We also see that the HB fit finds a third solution even closer to the true value, with a lower probability, but marginally consistent. It illustrates the power of Bayesian models in solving degeneracies. We see in Fig. 3.8. c that the non-HB fit had trouble constraining the $[\text{Ar II}]_{6.98\mu\text{m}}$ relative intensity, $\ln(R^{\text{ArII}})$, whereas the HB model narrowed it around its true value. This is because the HB approach accounts for the information provided by the whole sample and thus benefits from the law of large numbers.

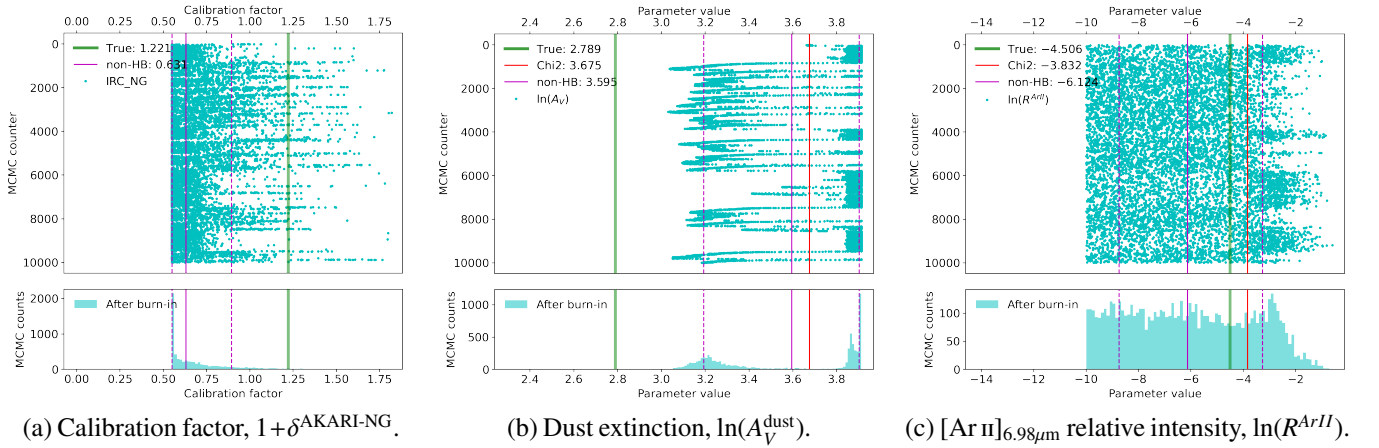


Figure 3.8 – Parameter distributions in the non-HB fit.

Panel (a) shows the Markov chain (top) of a nuisance parameter, the IRC calibration factor, where we have indicated the median (magenta solid) and 1- σ interval (1th and ; magenta dashed) of the distribution after burn-in (bottom), as well as the “true” value (green) used to generate the fitted spectrum, “c10 SN10 #1”. Panels (b) and (c) show in the same way two model parameters, $\ln(A_V^{\text{dust}})$ and $\ln(R^{\text{ArII}})$, respectively. In addition, we have overlaid the χ^2 best-fit values, which is used as the initial guess of Bayesian fits (not available for nuisance parameters).

Bayesian posteriors are complex multivariate distributions that contain all the information on the different parameters. The median model (e.g. Fig. 3.7) is the closest equivalent to the concept of best-fit model, which is frequentist in nature. Bayesian results can reveal degenerate parameters by sampling their multimodal distribution. It however makes it hard to account for correlations between parameters (e.g. Figs. D.3 – D.5). Nonetheless, it is possible to estimate any quantity from the parameters directly at each step of the MCMC and then study its distribution. This is what we will use in Sect. 3.3.3, drawing scatter plots of correlations from the Markov chain to retain all the information in the parameter distributions instead of simply using quantities derived from statistical moments.

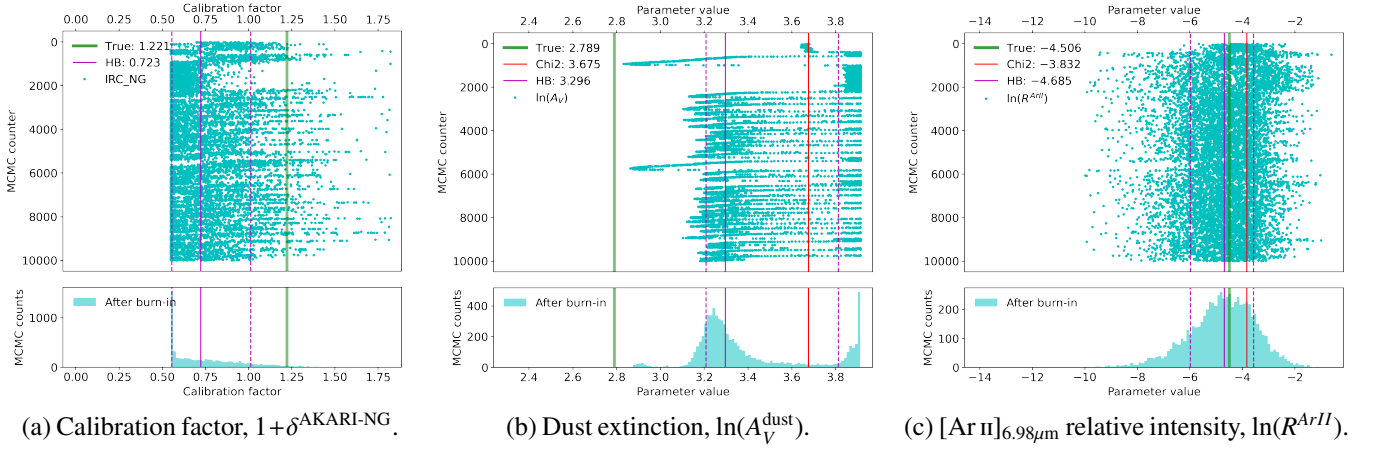


Figure 3.9 – Parameter distributions in the HB fit.

Panels (a) to (c) present the same parameter distributions as Fig. 3.8, but fitted by the HB method.

3.3.2.3 Autocorrelation of parameters

Before entering the final voyage of the MILES test, re-exploring band intensity correlations, we have also studied the parameter ACFs. Another parameter that can be degenerate with A_V is the stellar radiant power, L^* (cf. Fig. D.3). We have calculated the ACFs of the mean and standard deviation of $\ln(A_V)$ as well as the correlation coefficient of $\ln(A_V)$ and $\ln(L^*)$.

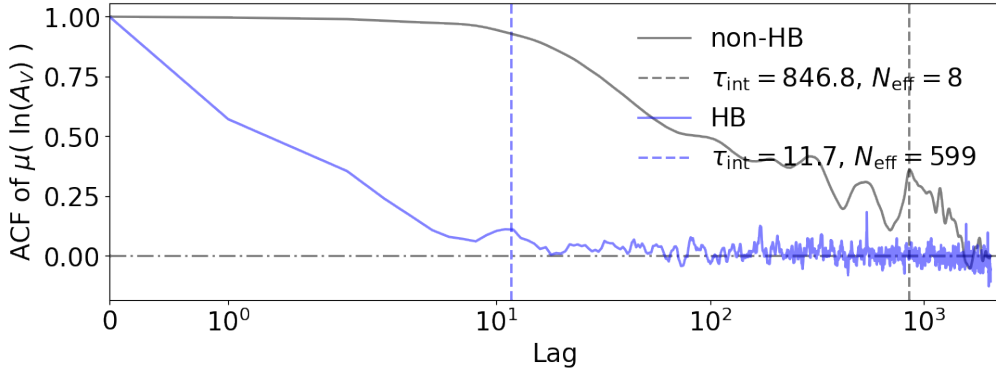


Figure 3.10 – ACFs of the means of a parameter (after burn-in).

We present the ACFs of $\mu(\ln(A_V))$ (black solid: non-HB; blue solid: HB). The non-HB and HB τ_{int} are indicated with black and blue dashed lines, respectively.

In Figs. 3.10 – 3.11, we see the HB ACFs drop to ~ 0 much faster than the non-HB ones for both the mean, $\mu(\ln(A_V))$, and the standard deviation, $\sigma(\ln(A_V))$. A MCMC length $N_{\text{MCMC}} = 10\,000$ is not long enough for non-HB ACFs of both values to converge. This difference in convergence time can be quantified with the integrated autocorrelation time, quoted in each figure. The situation is reversed for the correlation coefficient (Fig. 3.12). The τ_{int} of $\text{corr}(\ln(A_V), \ln(L^*))$ is one of the worst of the HB run Fig. 3.3. c. It is larger than that of the non-HB run, but it is still smaller than that of the other hyperparameters, meaning it will not affect convergence.

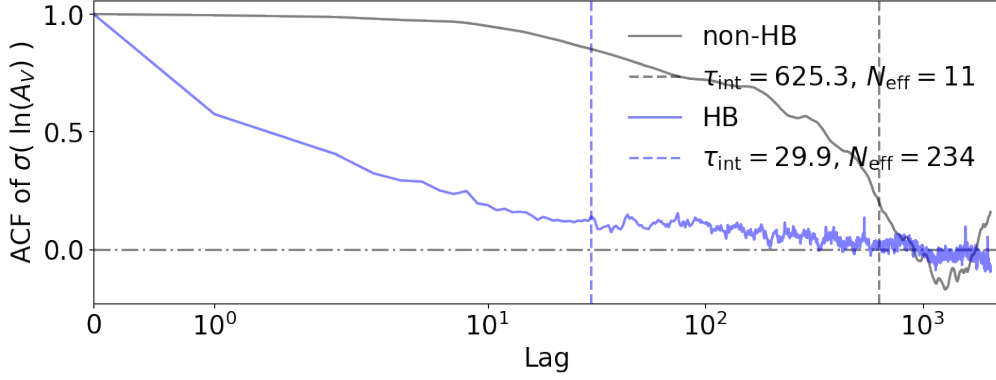


Figure 3.11 – ACFs of the standard deviation of a parameter (after burn-in).

We present the ACFs of $\sigma(\ln(A_V))$ (black solid: non-HB; blue solid: HB). The non-HB and HB τ_{int} are indicated with black and blue dashed lines, respectively.

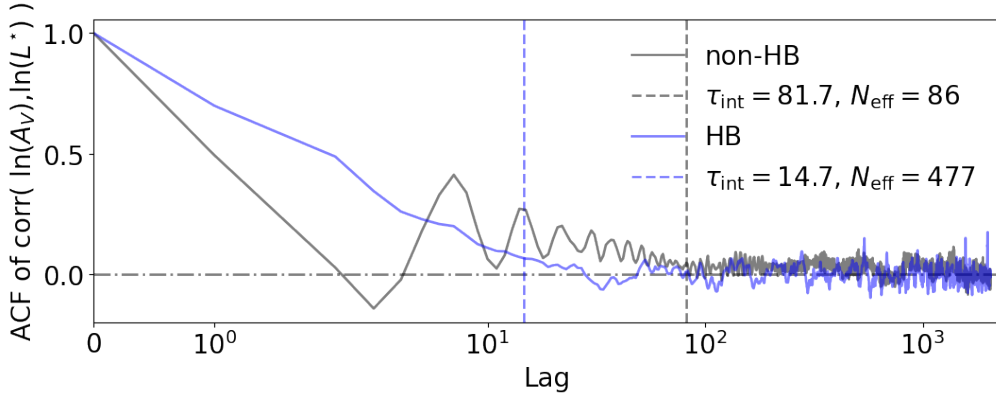


Figure 3.12 – ACFs of the correlation coefficients of two parameters (after burn-in).

We present the ACFs of $\text{corr}(\ln(A_V), \ln(L^*))$ (black solid: non-HB; blue solid: HB). The non-HB and HB τ_{int} are indicated with black and blue dashed lines, respectively.

3.3.3 Correlations of UIBs and UIB complexes

There are large uncertainties on most band ratios because of the degeneracies between adjacent bands (*e.g.* Fig. D.4). The Bayesian methods are designed to account for this type of degeneracy and propagate them through the whole modeling. This is however not the case for the least-squares method, which underestimates the errors and can be biased. By summing adjacent bands that are in competition with each other (*i.e.* UIB complexes), we can obtain lower uncertainties on their intensities. This is because, if we have two adjacent bands, their intensity will be degenerate as the noise will make their individual intensity uncertain, but the sum of the two features will be relatively well constrained.

In Figs. 3.13 – 3.14, we have presented the simulated UIB complex intensity ratios (*i.e.* black points) described on page 111. We have adopted the same colors for the derived intensity ratios at each step of the MCMC when fitting the four groups of spectra, “c1 SN10” (cyan), “c10 SN10” (green), “c1 SN100” (magenta) and “c10 SN100” (yellow), as displayed in Fig. 3.4. b.

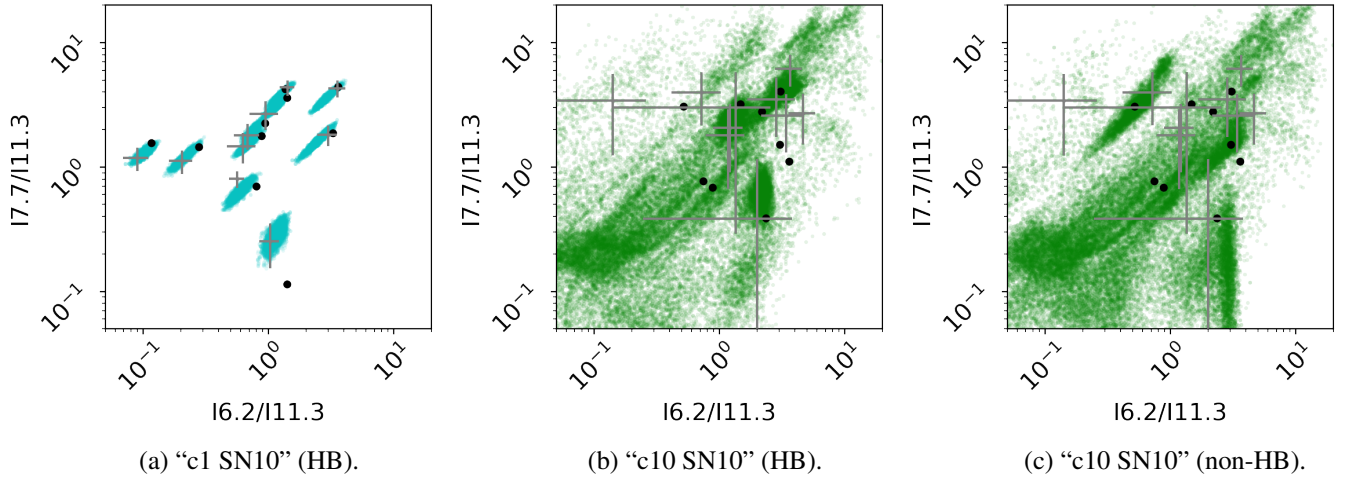


Figure 3.13 – Correlations of intensity ratios fitted by the Bayesian methods.

Panels (a) and (b) show the HB fitted $I(6.2)/I(11.3)$ - $I(7.7)/I(11.2)$ correlations of spectra in the “c1 SN10” (cyan) and “c10 SN10” (green) groups, respectively. The scatter plots are the results calculated from the **MCMC**, which are overlaid with the actual ratios (black) and least-squares best-fit results (grey). Panel (c) is the non-HB counterpart of the panel (b).

The slope and strength of these simulated correlations are not necessarily realistic, but they are aimed at testing the robustness of our model. In our tests, all three methods can reproduce the simulated correlations when the S/N ratio is not too low and the continuum emission is not too strong compared to **UIBs**. Basically, the Bayesian methods (scatter plots) produce fewer outliers than the least-squares method (gray data points with error bars), as shown in **Fig. 3.13**. As for “c10 SN10” (panels b and c), the least-squares method produces many outliers, whereas an evident trend is inferred by the Bayesian methods, with the hierarchical Bayesian method producing a slightly smaller dispersion. Moreover, when comparing the non-HB and HB results, the HB uncertainties are reduced (*e.g.* **Fig. 3.14**).

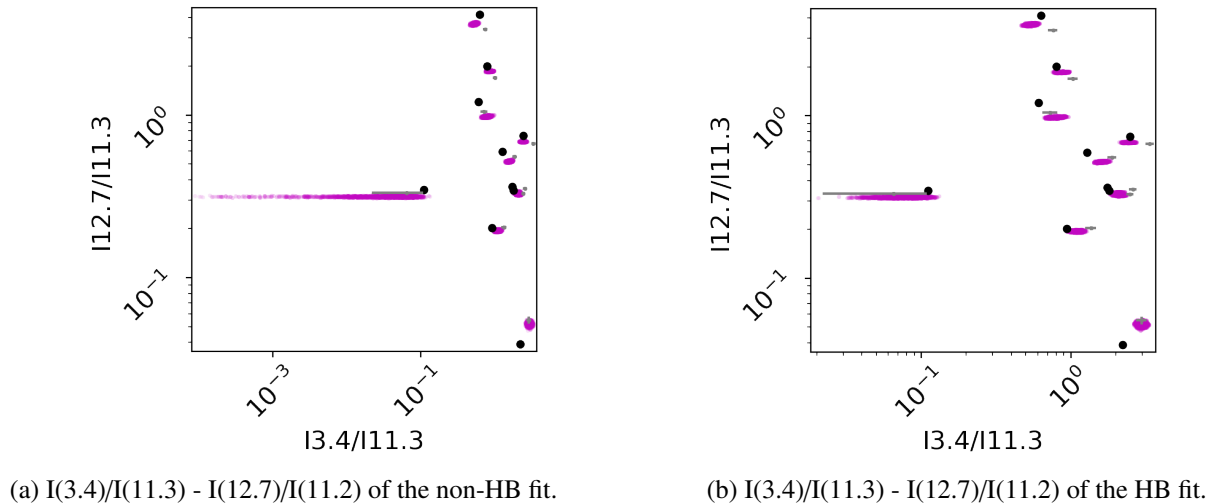


Figure 3.14 – Non-correlated intensity ratios of the non-HB and HB fit.

Panels (a) and (b) present the non-HB and HB fitted non-correlated $I(3.4)/I(11.3)$ and $I(12.7)/I(11.2)$ of spectra in the “c1 SN100” group in our simulated sample. The magenta spots are the results calculated from the **MCMC**. The black points represent the actual ratios, whereas the gray points with error bars are the least-squares best-fit results.

Chapter 4

Exploring the properties of small carbon grains

When Eddington made his famous remark, “Atoms are physics but molecules are chemistry,” he merely expressed, on the one hand, the dream of a physicist of a simple universe, which can be caught in a single equation, and, on the other hand, the dread of a reality where solutions are never clean and simple.

A. G. G. M. Tielens

I now discuss the application of the model demonstrated in [Chap. 3](#) to the observations presented in [Chap. 2](#). My goal is to extract quantitative information from the [MIR](#) spectra of our galaxy sample in order to explore the properties of small carbon grains in these systems. This is the highlight of my thesis, as it consists in applying the modeling tools I have developed to the data I have carefully homogenized. After a brief review of the literature about the small carbon grains that dominate the [MIR](#) emission spectrum, this chapter presents my first results of the empirical constraints on their properties. With the consistently fitted M 82 spectra, I explore the prominent [MIR](#) features by searching correlations between band ratios. I also associate band ratio correlations with physical conditions through theoretical models and study their spatial variations from the galaxy center to the outer regions in its galactic superwind. In the end, I present my ongoing project of a systematic study of small carbon grains in a nearby galaxy sample.

4.1 Fitting results - M 82

Our pilot study focuses on the irregular galaxy M 82 (*cf.* Sect. 2.4.1). We have fitted the 41 spectra across this source, with the least-squares, the non-hierarchical Bayesian (non-HB) and the HB methods within MILES. We have fine-tuned the model settings, in particular, the choice of parameters that are left free and those that are varied, based on the data quality. We have adopted the following configuration. The 56 free model parameters for each spectrum (*i.e.* 2 296 parameters in total) are:

- 8 for the dust continuum: temperature and mass for 3 amorphous carbon (BE Z96) and 1 Astronomical silicate (Sil D03) components (Table 3.4);
- 12 for the gas lines: only varying the intensity, with the line width and position fixed (Table 3.3);
- 34 for the UIBs: only varying the intensity, with the band width and position fixed (Table 3.2);
- 1 for the extinction (A_V^{dust});
- 1 for the stellar continuum (blackbody).

In the HB case, on top of the parameters, we also have 1 540 hyperparameters :

- 56 for the mean of each free model parameter;
- 56 for the standard deviation of each free model parameter;
- $C_2^{56} = 1\,540$ for the correlation coefficients of each combination of free parameters.

Finally, there are also the 3 calibration parameters of the IRC-NG, IRS-SL1 and IRS-LL2 modules, for each spectrum (*i.e.* 123 in total). With Eq. (3.27), we have thus run (i) a least-squares fit with 2 296 parameters, (ii) a non-HB fit with $2\,296 + 123 = 2\,419$ parameters and (iii) a HB fit with $2\,296 + 1\,540 + 123 = 3\,959$ parameters. For the two Bayesian methods, we have run 10 000 iterations with a burn-in length of 3 000 (*i.e.* 30%).

The final fits of the three methods are shown in Figs. 4.1 – 4.3. They are demonstrated on the spectra of three slits having different S/N ratios. All the three methods provide good quality fits in both high (*e.g.* panels *a*) and relatively low S/N ratio regions (*e.g.* panels *b*). However, there are qualitative differences in the fits of the different methods that one can see by eye: (i) the treatment of the calibration factors with the Bayesian methods and (ii) the degeneracy between adjacent bands, such as the relative weight of the different features in the 7.7- μm complex. The superiority of the Bayesian methods is its ability to provide a quantitative account of such degeneracies by giving us access to the full PDF. When we look at individual parameter distributions, many parameters are strongly correlated with multi-modal distributions (*e.g.* Fig. 4.4). In this case, it is hard to find representative values for all parameters. As Sect. 3.3.2.1, we have shown median models of the HB fits (panels *d–f*). For instance, in the panels (*c*) of Figs. 4.2 – 4.3, the fitted models taking the distribution mean of each parameter are not consistent with the M2 spectrum. Instead, (panels *f*). The other HB fitted spectra in our M 82 sample can be found in Fig. D.22.

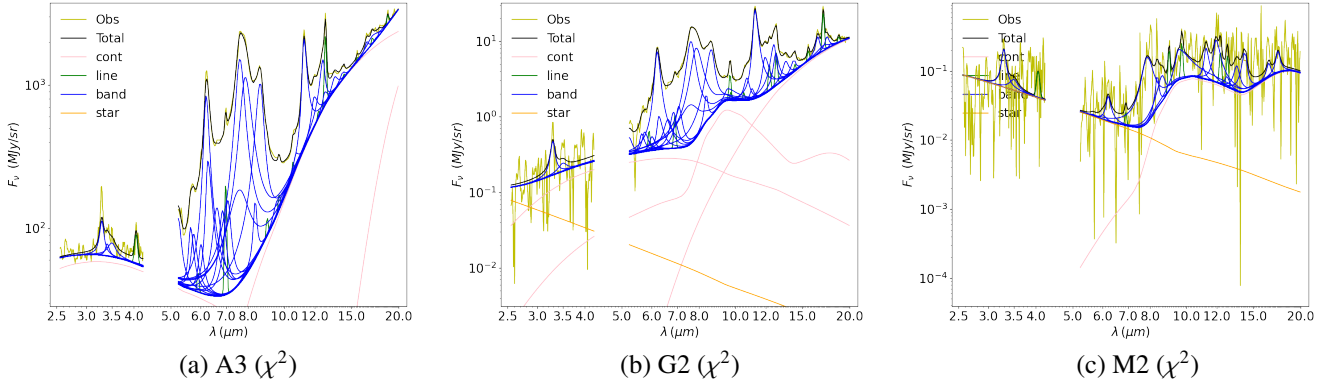


Figure 4.1 – M 82 spectra fitted by least-squares (χ^2).

Panels (a)-(c) show the spectrum of the A3, G2 and M2 slits fitted by the least-squares method, respectively. The observed spectrum (yellow) is fitted by gas lines (green), **UIBs** (blue), dust continua (pink), and stellar continuum (orange). The total fitted model is shown in black.

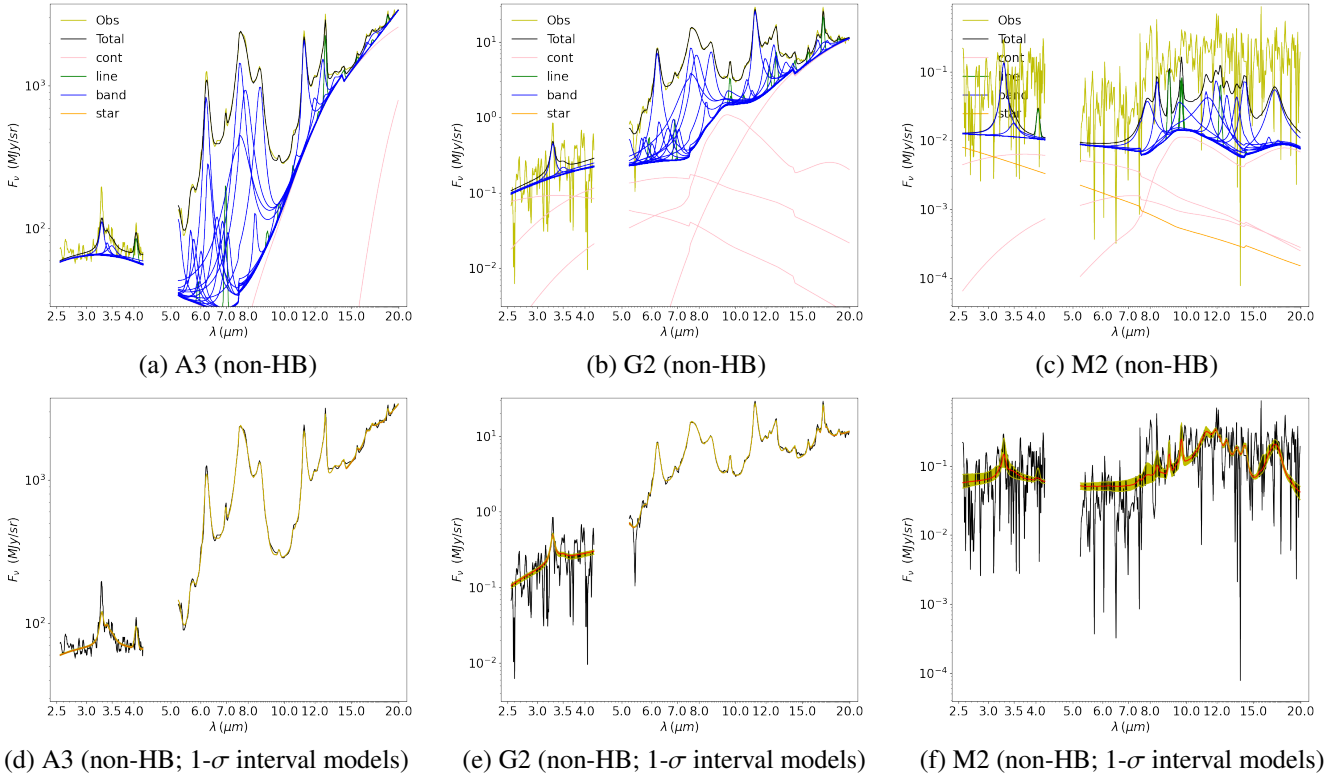


Figure 4.2 – M 82 spectra fitted by non-HB.

Panels (a)-(c) show the spectrum of the A3, G2 and M2 slits fitted by the non-HB method, respectively. The observed spectrum (yellow) is fitted by gas lines (green), **UIBs** (blue), dust continua (pink), and stellar continuum (orange). The total fitted model is shown in black. Panels (d)-(f) show the non-HB fits in panels (a)-(c) with the observed spectra (black), 1- σ interval models of **MCMC** after the burn-in (yellow patch) and median model (red).

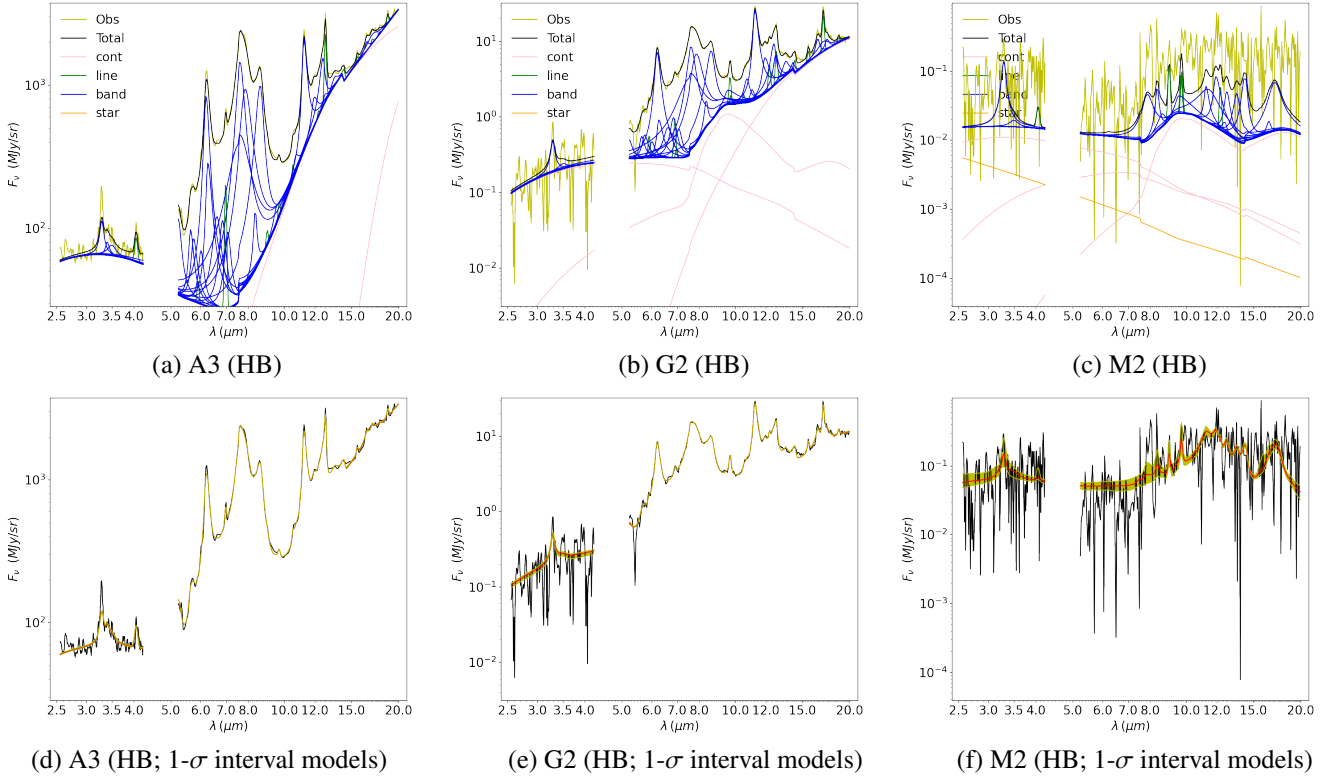


Figure 4.3 – M 82 spectra fitted by HB.

Panels (a)-(c) show the spectrum of the A3, G2 and M2 slits fitted by the HB method, respectively. The observed spectrum (yellow) is fitted by gas lines (green), **UIBs** (blue), dust continua (pink), and stellar continuum (orange). The total fitted model is shown in black. Panels (d)-(f) show the HB fits in panels (a)-(c) with the observed spectra (black), 1- σ interval models of **MCMC** after the burn-in (yellow patch) and median model (red).

4.2 Aromatic features in nearby galaxies

The major interest of our **MIR** spectral decomposition model is to consistently extract **UIB** intensities. Following the discussion in **Sect. 3.3.2**, it is crucial to make sure the other components in the model do not bias the derived **UIB** intensity ratios. To that purpose, in **Sect. 4.2.1**, we first investigate the impact of extinction, which is parametrized by A_V , usually highly degenerate in our model. Then, in **Sect. 4.2.2**, we summarize how the mathematical components of our model can be attributed to **PAH** features (**Table 4.1**). Finally, we present the band ratio correlations, which directly address the questions delineated in **Sect. 4.3**.

4.2.1 Impact of extinction

Considering the very high extinction (up to 90 mag) inferred from the $9.7 \mu\text{m}$ silicate absorption in Arp 220 (**Smith et al., 1989**), we have compared the effect of extinction on the **UIBs** with different $A_V = 1, 10$ and 100 (**Fig. 4.5**). The most affected features are the $8.6 \mu\text{m}$ band and the $11.3 \mu\text{m}$ complex (defined in **Table 4.1**) due to their proximity to the strong silicate absorption feature at $9.8 \mu\text{m}$. Indeed, the entire $\sim 7 - 12 \mu\text{m}$ wavelength interval is affected by silicate absorption. The

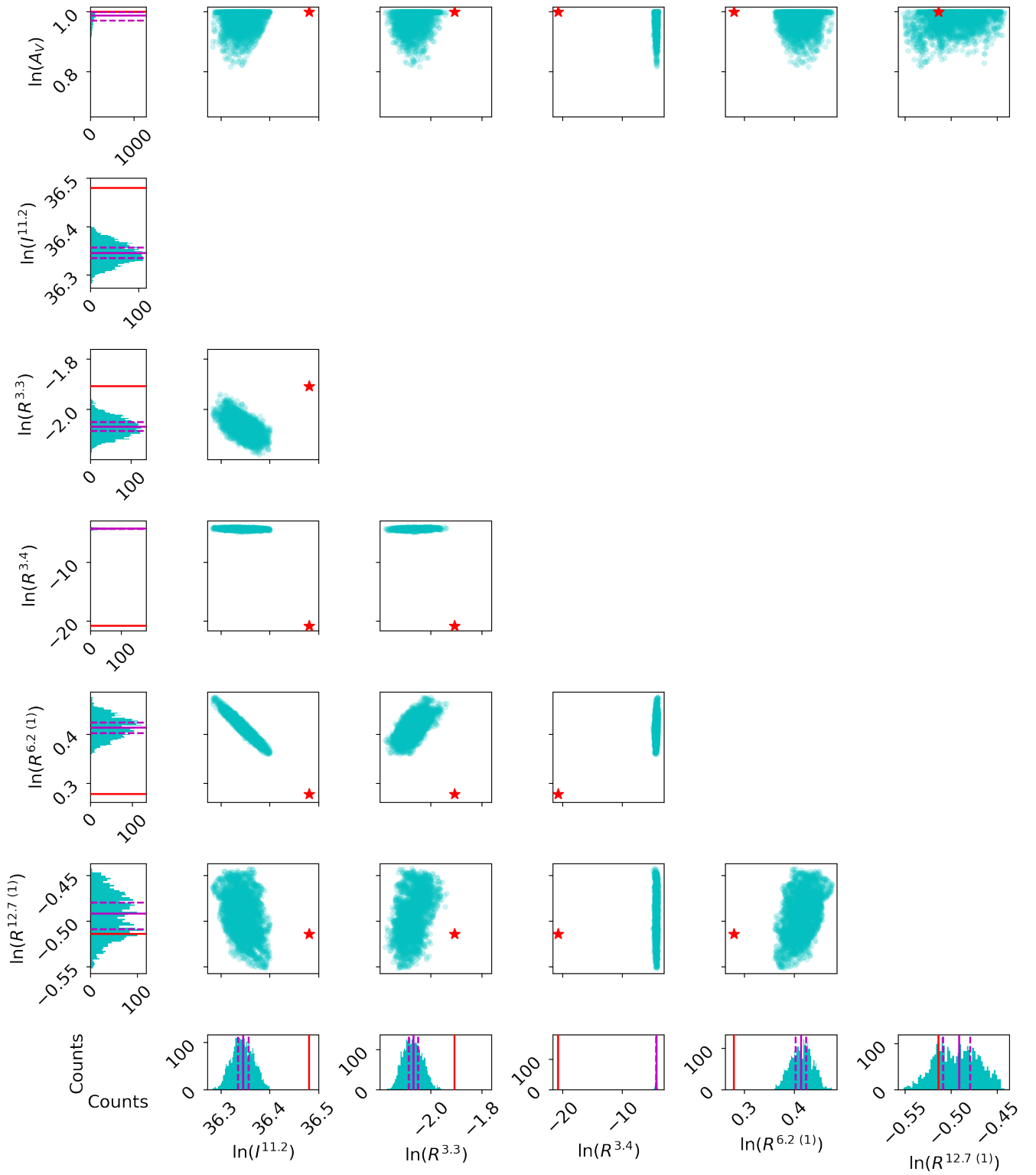


Figure 4.4 – Multivariate distributions between HB fitted parameters.

With the HB fit of the spectrum A4, we present the multivariate distributions between following parameters, $\ln(A_V)$, $\ln(I^{11.2})$, $\ln(R^{3.3})$, $\ln(R^{3.4})$, $\ln(R^{6.2 (1)})$ and $\ln(R^{12.7 (1)})$, along with the distribution histograms of each parameter. The χ^2 best-fit values are marked with red lines and stars. The magenta solid and dashed lines indicate the distribution medians and 1- σ intervals, respectively.

3.3 μm band and the 3.4 μm complex are also affected, especially when we include absorption features such as H_2O or aliphatic absorption features at $\sim 3.4 \mu\text{m}$.

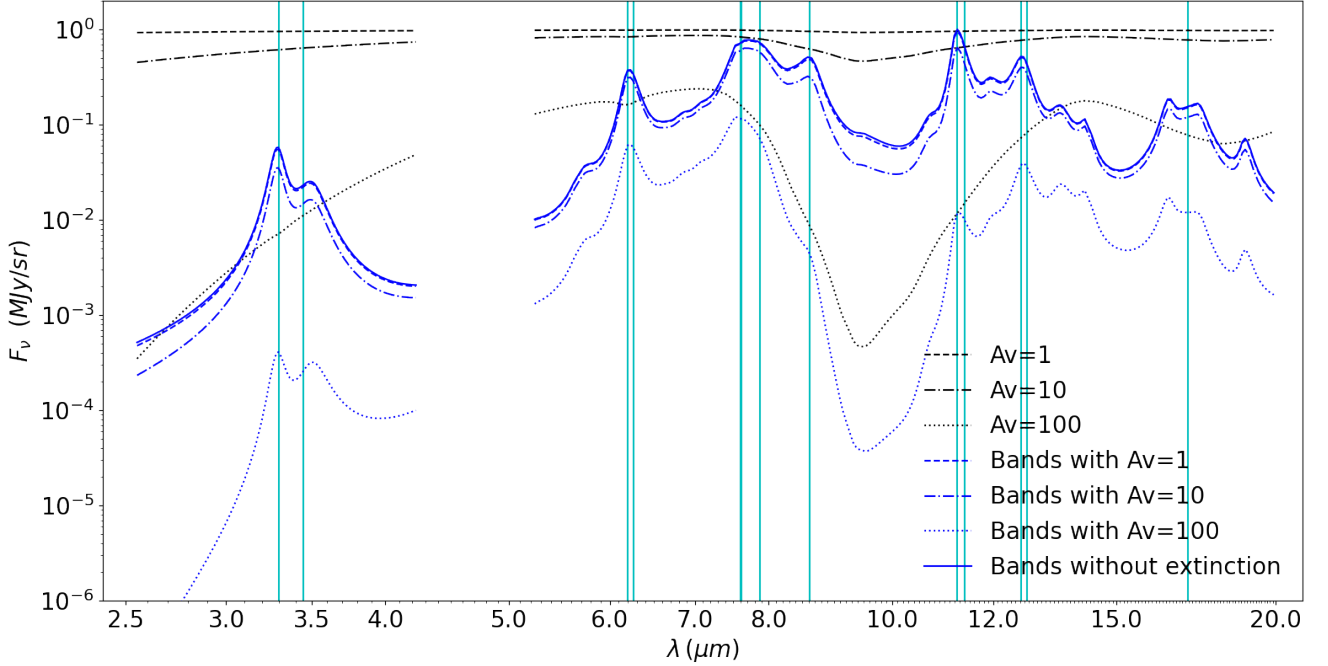


Figure 4.5 – Impact of extinction on fitted UIBs.

The summed **UIB** spectrum from our fit is shown in blue solid line; different A_V are used with the [Weingartner & Draine \(2001\)](#) dust extinction curve. Black dashed, dash-dotted, and dotted lines are the extinction curves with $A_V = 1, 10$ and 100 , respectively. The corresponding escaping spectra are shown in blue dashed, dash-dotted, and dotted lines, respectively. The position of the main **UIB** features are indicated with cyan lines.

The difference between the 11.3 μm complex intensities with and without A_V is not negligible in our fits. However, at first order studying band ratios rather than band intensities will reduce the importance of the extinction, as it will be partly canceled in the ratio. Our normalization choice ¹ can thus reduce the degeneracies between feature intensities and extinction.

For our case study, [Förster Schreiber et al. \(2001\)](#) derived $23 < A_V < 45$ for several regions in M 82 covering an area closer to the infrared peaks. Consequently, we can reasonably assume that $A_V \simeq 50$ will be the maximum extinction in M 82. We have thus limited A_V from 1 to 50 throughout the entire M 82 map in our fit.

4.2.2 Emission band assignments

Our method is purely empirical. We are fitting a series of mathematical functions to our spectra, without knowing *a priori* about the origin of these features. Interpreting these results, however, requires assigning a physical origin to the quantities we are studying. We have thus reviewed the literature to lay out the current, consensual assignment of potential carriers with predominant charge state to the emission features in [Table 3.2](#). Basically, a flurry of studies have assigned molecular modes

¹. In our fitting model, we have normalized the intensity of **UIBs** and gas lines to the intensity of the 11.2 μm band (peaking at 11.238 μm in accordance with [Table 3.2](#)). However, during the post-processing of fitting results, it is the 11.3 μm complex, summing up both the 11.2 μm band and a plateau peaking at 11.400 μm , that we have normalized to.

to the astronomical **UIB** features based on laboratory-measured and/or computational studies of specific species (*e.g.* samples including **PAHs**, **PAH** clusters, hetero-atom-substituted **PAHs**, **PAH** complexes with metal atoms, *etc.*). Our synthesis is listed in **Table 4.1**. We emphasize that there is some uncertainty about the origin of several bands.

Importantly, we stress that these **UIBs** have been assigned to molecular properties by looking at different astrophysical environments (from the circumstellar medium to the **ISM**) and at different spatial scale (from stellar ejecta to galaxy-wide scales). To begin with, [Allamandola et al. \(1989\)](#) discussed the attribution of **PAH** vibrational modes to various interstellar **MIR** features. After comparing the spectra from UKIRT (*e.g.* [Geballe et al., 1985](#)) and KAO (*e.g.* [Russell et al., 1977](#)) to their laboratory database, they concluded that the data generally failed to match the interstellar band positions and relative intensities. However, the spectral similarities still supported the hypothesis that unknown **PAH** mixtures were responsible for **UIBs**. The answer lied in the complexity of the molecular mix to infer in order to reproduce the observations. To assign the 3.40 and 3.51 μm aliphatic features, [Bernstein et al. \(1996\)](#) compared the spectra of the Orion Bar ([Geballe et al., 1989](#); [Sloan et al., 1997](#)) and IRAS 05341+0852 ([Geballe & van der Veen, 1990](#)) observed by UKIRT with the spectra of several **Hydrogenated Polycyclic Aromatic Hydrocarbons (HPAHs)** species. [Hony et al. \(2001\)](#) investigated the 10 – 15 μm spectral range with a sample of H II regions, **YSOs**, reflection nebulae and evolved stars observed by ISO-SWS. [Peeters et al. \(2002b\)](#) and [Bauschlicher et al. \(2008\)](#) used a ISO-SWS sample with object types similar to [Hony et al. \(2001\)](#) by adding several extragalactic galaxies (*e.g.* NGC 253 and M 82). [Peeters et al. \(2004b, 2012, 2017\)](#) further included the more sensitive *Spitzer*/IRS data for weaker bands, in particular, a plethora **PAH** emission bands detected in the 15 – 20 μm range (*e.g.* [Moutou et al., 2000](#); [Van Kerckhoven et al., 2000](#)) and the vibrational transitions of (neutral) C_{60} at 7.0, 8.5, 17.4 and 18.9 μm ([Cami et al., 2010](#); [Sellgren et al., 2010](#)).

These results are not specific to our current study, which mainly concentrates on the **ISM** at the galaxy scale. However, they are compatible with our **UIB** feature calibration (**Sect. 3.1.2**) in terms of astronomical implications, and some of the references even used the same observations as ours (*e.g.* ISO-SWS spectra of NGC 7023). The discrepancies between the spectral feature properties (*i.e.* position and shape) in **Table 3.2** and those of the original assignments are negligible once we let the band position and width parameters slightly vary around the central value during the fit. If there are new spectral features calibrated with future observations such as JWST, we will also be able to include additional bands in the library of MILES. Moreover, we are aware that our approach does not allow us to access the specific composition of the small grains carrying the **UIBs**, but we are focusing on the variations of the spectral properties with the local physical conditions.

Table 4.1 – UIB feature assignments.

The assignments of the vibrational mode, likely carrier and predominant charge state of the **UIBs** listed in **Table 3.2** are compiled from various laboratory and computational studies in comparison with astronomical emission bands. The bands and plateaus that make up the UIB complexes presented in **Chap. 4** are shaded grey.

λ_0 (μm)	Type	Assignment	Carrier	Charge ^a
3.291	Main	C-H aromatic stretching ^b	Small PAH neutrals and anions ^c	0 and \pm ^c
3.399 ^d	Main	C-H aliphatic stretching ^e	PAHs with excess H ^e	
3.499	Small	C-H aliphatic stretching ^e	PAHs with excess H ^e	
5.239	Small	C-H out-of-plane bending (overtone) and C-H in-plane bending ^b		
5.644	Small	C-H out-of-plane bending (overtone), C-C stretching and C=O stretching ^b	PAHs, PAH clusters and PAH-rich VSGs ^f	0 ^f
5.749	Small	C-H out-of-plane bending, C-C stretching and C=O stretching ^b	PAHs, PAH clusters and PAH-rich VSGs ^f	0 ^f
6.011	Small	C=O stretching and C-C stretching ^c	Oxygenated PAHs ^c	
6.203 ^g	Main	C-C stretching ^b	Hetero-atom substituted PAHs or PAH clusters ^c	\pm ^c
6.267	Main	C-C stretching ^b	Pure PAHs ^c	\pm ^c
6.627	Small			
6.855	Small	C-C stretching+C-H in-plane bending or -CH ₃ /-CH ₂ aliphatic deformation ^c	PAHs or Aliphatic side-groups on PAHs ^c	\pm ^c
7.079	Small	C-C stretching and C-H in-plane bending ^c	C ₆₀ ^f	0 ^f
7.600 ^h	Plateau	C-C stretching and C-H in-plane bending ^c		
7.617	Main	C-C stretching and C-H in-plane bending ^c	Small PAHs contributing more ^c	\pm ^c
7.870	Main	C-C stretching and C-H in-plane bending ^c	Large ionized PAHs ^c	\pm ^c
8.362	Small	C-H in-plane bending ^c		
8.620	Main	C-H in-plane bending ^c	Large ionized PAHs ^c or neutral C ₆₀ ^f	\pm ^c
9.525	Small			
10.707	Small	C-H out-of-plane bending ⁱ	PAH cations ⁱ	\pm ⁱ
11.038	Small	C-H out-of-plane bending (solo) ⁱ	PAH cations ⁱ	\pm ⁱ
11.238 ^j	Main	C-H out-of-plane bending (solo) ⁱ	Large PAHs ($N_C \gtrsim 100$) ⁱ	0 ⁱ
11.400	Plateau			
11.796	Small			
11.950	Small	C-H out-of-plane bending (duo) ⁱ	Ionized (trio H) or neutral (duo H) PAHs ^c	0 and \pm ⁱ
12.627 ^k	Main	C-H out-of-plane bending (trio) ⁱ	Ionized (trio H) or neutral (duo H) PAHs ^c	0 and \pm ⁱ
12.761	Main	C-H out-of-plane bending (trio) ⁱ	Ionized (trio H) or neutral (duo H) PAHs ^c	0 and \pm ⁱ
13.559	Small	C-H out-of-plane bending (quartet) ⁱ		0 ⁱ
14.257	Small	C-H out-of-plane bending and ⁱ		
15.893	Small	C-C-C in-plane bending ^l	Large neutral PAHs ($N_C \gtrsim 50$) ^l	0 ^l
16.483	Small	C-C-C in-plane bending ^l	Gas-phase PAHs ^l	0 and \pm ^l
17.083	Plateau	C-C-C out-of-plane bending ^l	PAHs, PAH clusters and a-C(:H), etc. ^l	
17.428	Small	C-C-C out-of-plane bending ^l	Gas-phase PAHs ^l or C ₆₀ ^l	\pm and 0 ^l
17.771	Small	C-C-C out-of-plane bending ^l	Neutral and ionized PAHs ^l	0 and \pm ^l
18.925	Small	C-C-C out-of-plane bending ^l	C ₆₀ ^l	

a. The predominant charge state of the **UIB** carriers are indicated with the following signs: (i) 0, neutral PAHs; (ii) \pm , ionized (cationic/anionic) PAHs.

b. Allamandola et al. (1989).

c. Peeters et al. (2002b) and Bauschlicher et al. (2008).

d. By summing up the flux intensity of the bands at 3.399 μm and 3.499 μm , we refer to the intensity of the 3.4- μm aliphatic complex. Note that the name convention of different complexes within this table is valid specifically for the current chapter.

e. Bernstein et al. (1996).

f. Peeters et al. (2017).

g. The 6.2- μm complex includes the bands at 6.203 μm and 6.267 μm .

h. The 7.7- μm complex includes the bands at 7.617 μm and 7.870 μm and the 7.600 μm plateau.

i. Hony et al. (2001).

j. The 11.3- μm complex includes the band at 11.238 μm and the 11.400 μm plateau.

k. The 12.7- μm complex includes the bands at 12.627 μm and 12.761 μm .

l. Peeters et al. (2004b) and Peeters et al. (2012).

4.2.3 Band ratio correlations

We have applied our **MIR** fitting model to M 82 observations as a case study, and compared our results with past studies on M 82 (Gillett et al., 1975a; Förster Schreiber et al., 2001, 2003a,b; Engelbracht et al., 2006; Galliano et al., 2008b; Beirão et al., 2008, 2015; Yamagishi et al., 2012; Maragkoudakis et al., 2020; Foley et al., 2014). The content in the present section is based on the [Paper I](#).

In the first place, we focus on the predominant bands, denoted as the “*Main*” type in [Table 3.2](#). To derive the ratios between different **UIB** features, we have summed several adjacent bands into complexes (see their definition page 111): (i) the 3.4- μm complex, (ii) the 6.2- μm complex, (iii) the 7.7- μm complex, (iv) the 11.3- μm complex, (v) the 12.7- μm complex and Indeed, each complex consists in bands attributed to the same vibrational modes of similar species of carriers (*cf.* [Table 4.1](#)). As an example, we have seen in [Fig. 1.23](#) that the 8.6- μm band, the 6.2 and 7.7- μm complexes are qualitatively tied together by the ionization effect for relatively small **PAHs**. Therefore, it is natural to study the variations of these three features as a function of **PAH** charge states and thus tracing the ambient radiation field. The correlations of intensity ratios, such as $I(6.2)/I(11.3)$, are presented and interpreted in [Sect. 4.3.1](#).

4.3 Physical interpretation

4.3.1 Band ratios as diagnostic tools

The ionization effect on the intrinsic C-C/C-H strength ratios explains most **UIB** variation in galaxies (*e.g.* [Hony et al., 2001](#); [Berné et al., 2007](#); [Galliano et al., 2008b](#)). It is thus of great interest to quantify this effect with band intensity ratios (hereafter band ratios). To that purpose, we have assumed an *ionization balance* (*cf.* [Sect. 1.6.2.1](#)) for an ensemble of molecules. The ionization balance of **PAHs** is mainly set by the photoionization rate and the electron recombination rate. The photoionization rate is quantified by the variable G_0 , the integral of the **ISRF** in the **FUV** ([Sect. 1.6.2.1](#)), whereas the electron recombination rate is roughly proportional to $n_e/T_{\text{gas}}^{0.5}$, with the electron density, n_e , and gas temperature, T_{gas} . Besides, the rates of other processes involving **PAHs** have also been measured experimentally, including (i) electron attachment to neutral **PAHs**, (ii) mutual neutralization reactions between **PAH** anions and atomic or molecular cations and (iii) charge-exchange reactions of neutral **PAHs** with cations (*e.g.* [Tielens, 2008](#)).

We have followed [Galliano et al. \(2008b\)](#) who derived an empirical relation between the ionization parameter, $\gamma \equiv G_0 T_{\text{gas}}^{0.5}/n_e$, and the $I(6.2)/I(11.3)$ ratio by measuring the $I(6.2)/I(11.3)$ ratio in Galactic regions where G_0 , n_e and T_{gas} had been reliably estimated. In particular, they estimated the electron density, n_e , through the gas density, n_{H} :

$$n_e \simeq (C/H)_{\text{gas}} n_{\text{H}} \simeq 1.6 \times 10^{-4} n_{\text{H}} \quad (4.1)$$

where they assumed that all the gas-phase carbon is photoionized in **PDRs** and adopted the carbon abundance, $(C/H)_{\text{gas}}$ (cf. Eq. 1.9), from Sofia et al. (2004). As a result, they found²:

$$\frac{I(6.2)}{I(11.3)} \simeq \frac{G_0/(n_e/1 \text{ cm}^{-3}) \sqrt{T_{\text{gas}}/10^3 \text{ K}}}{1990} + 0.26 \pm 0.16. \quad (4.2)$$

Note that this correlation was calibrated in an edge-on **PDR** inside the Orion Bar and at the global scale of NGC 2023 and NGC 7027.

Then we have applied this empirical relation to our fitted band ratios. It results in Fig. 4.6, where we can see the clear correlation between these ionized bands between 6–9 μm . We have fitted these correlations with the least-squares (Levenberg-Marquardt) method. The ionization is most prominent in the galaxy center, with a rapid decrease along the asymmetric superwinds.

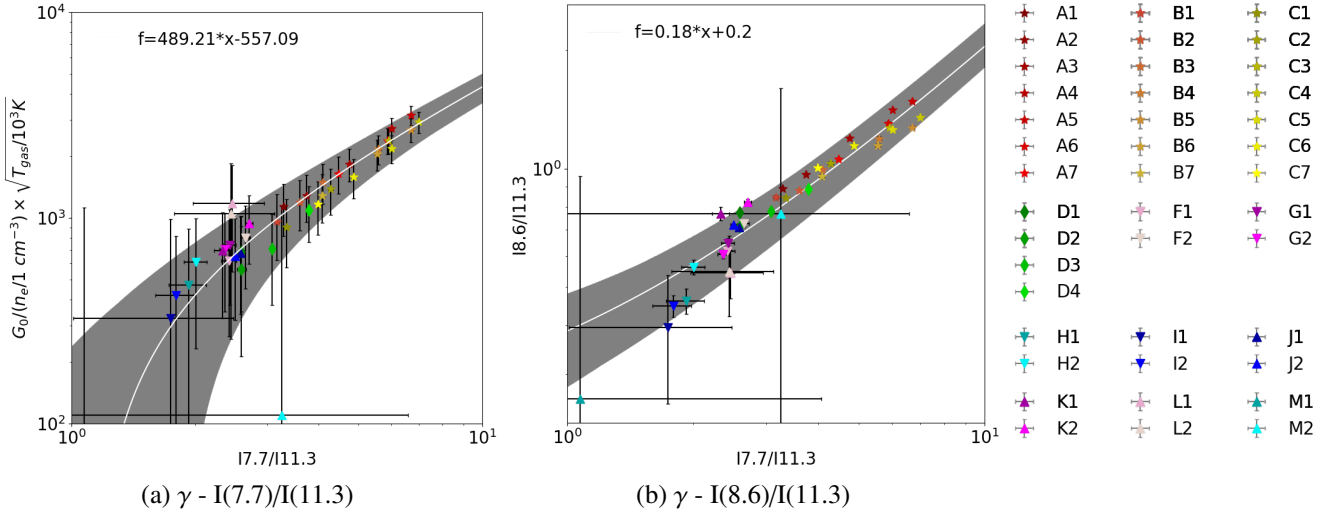


Figure 4.6 – **PAH** band ratio as diagnostics of physical conditions.

Panel (a) shows the correlation between the ionization parameter, $\gamma \equiv G_0 T_{\text{gas}}^{0.5}/n_e$, and the $I(7.7)/I(11.3)$ ratio. Panel (b) shows the correlation between γ and the $I(8.6)/I(11.3)$ ratio. These correlations are the same as in the correlations of $I(6.2)/I(11.3)$, only with this ratio converted to γ using Eq. (4.2).

4.3.2 Decoupling size and charge effects

We have computed theoretical emission spectra of idealized **PAHs**, using the Draine & Li (2007) optical properties. We have solved the stochastic heating (Sect. 1.4.3.2) for each **PAH** mixture characterized by its ionization fraction, f_+ and the number of C atoms of its minimum size cut-off, $N_{\text{C}}^{\text{min}}$, varying the shape and intensity, U of the radiation field. Then, we have fitted the resulting spectra with a linear combination of Lorentz profiles and small graphite for the continuum (cf. Sect. 3.1.3 and Sect. 3.1.5). We obtained the grids in Fig. 4.7, where the black, dark gray and light gray solid lines represent In addition, we

2. Here, we only present the Lorentzian-fitted result which is consistent with the method used in MILES. We do not use the correlation that they derived via spline method.

have indicated the increase trends of **PAH** charge and size via two black solid arrows. The charge is essentially traced by the $I(7.7)/I(11.3)$ ratio whereas the $I(3.3)/I(11.3)$ ratio is rather a size indicator. The $3.3\text{-}\mu\text{m}$ feature is mainly carried by the smallest **PAHs**, whereas the $11.3\text{-}\mu\text{m}$ feature is carried by intermediate sizes. Note that the $I(7.7)/I(11.3)$ ratio is also sensitive to the size. The degeneracy between size and charge for this band ratio can thus be broken using the $I(3.3)/I(11.3)$ ratio.

We have overlaid the results for M 82 in Fig. 4.7. We see an obvious trend of **PAH** size increasing with distance from the galaxy center, along the asymmetric winds. At the same time, **PAHs** in the central disk have a higher ionization fraction.

By comparing the theoretical band ratio grids in panels (a) and (b) of Fig. 4.7, we can also see the impact of the **ISRF**, although not as drastic as that of the charge and size. Note that we have displayed two extreme cases, most astrophysically relevant **ISRFs** will be intermediate between the presented grids. With future observations from JWST, we might need more fine grids calculated for specific cases (different interstellar medium phases, scale, *etc.*) such as those of Maragkoudakis et al. (2018, 2020).

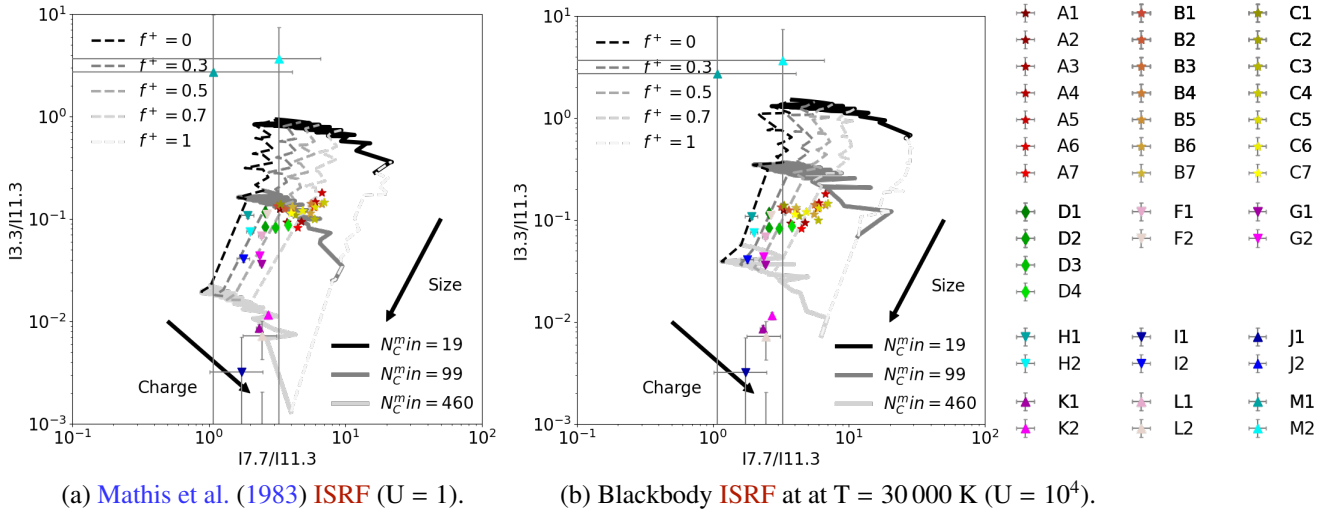


Figure 4.7 – Quantifying band ratio variations with size and charge effects.

These panels show the observed $I(3.3)/I(11.3)$ to $I(7.7)/I(11.3)$ ratios overlaid with the grids calculated via theoretical models. The theoretical band ratios are estimated from the stochastic emission spectra of **PAH** mixtures identified by the ionization fraction, f_+ , and the number of C atoms of the minimum size cut-off, N_C^{\min} . We have adopted the DL07 optical properties and the ZDA04 (BARE-GR-S) model size distribution for these **PAH** mixtures. Two black solid arrows indicate the direction of charge and size increases, respectively. Panel (a) uses the Solar neighborhood **ISRF** with $U = 1$, whereas **PAHs** in panel (b) are assumed to be heated by a blackbody at $T = 30\,000\text{ K}$ ($U = 10^4$).

4.3.3 Dehydrogenation and **ISRF** hardness

In Table 4.1, there are odd **UIBs**, that is, the $3.4\text{-}\mu\text{m}$ complex and the emission band at $6.85\text{ }\mu\text{m}$ (*cf.* the aliphatic hydrocarbon absorption features at 3.4 , 6.85 and $7.25\text{ }\mu\text{m}$ in the diffuse **ISM**; Chiar et al., 2000) which are attributed to C-H aliphatic vibrations. They are carried by **PAHs** with simple aliphatic side-groups.

4.3.3.1 Dehydrogenation

We have detected the $3.4\ \mu\text{m}$ feature in our spectra of M 82 from central disk to superwinds. The $I(3.4)/I(3.3)$ ratios derived from our fits with different fitting methods can be found in Fig. 4.8 where we have compared the ratio of individual sub-slits and the ratio of integrated slits. Basically, at a smaller scale (Fig. 4.8. a), this ratio can vary up to 2 orders of magnitude in regions where these features are both detected. When we integrated each slit which leads to a larger scale (Fig. 4.8. b), this ratio varies by about 1 order of magnitude. This ratio is relatively lower near disk regions (*e.g.* red, orange, yellow and green points) and increases away from the center. This trend is found with all three fitting methods. It is also consistent with former studies (Yamagishi et al., 2012) where it has been interpreted as the production of small a-C(:H) by shattering of large grains in the harsh halo.

4.3.3.2 ISRF hardness

Considering the link between dehydrogenation and the ISRF variations as well as the fact that PAHs are sensitive to a hard radiation field, we have investigated the impact of ISRF hardness. A reliable measure of ISRF hardness is the $[\text{Ne III}]/[\text{Ne II}]$ ratio. It was the parameter that Madden et al. (2006) used to quantify the effect of ISRF hardness on the PAH-to-MIR-continuum ratio, $I(\text{PAH})/I(\text{cont})$. $I(\text{PAH})$ is the sum of all aromatic band intensities and $I(\text{cont})$ is the integrated intensity of the continuum over an arbitrary wavelength range ($10 - 16\ \mu\text{m}$ in the case of Madden et al., 2006). In their study, the $[\text{Ne III}]/[\text{Ne II}]$ ratio is around unity when the interstellar medium is heated by a young star cluster and drops rapidly after a few million years (*i.e.* the age of a massive star). In addition, $[\text{Ar III}]/[\text{Ar II}]$ and $[\text{S IV}]/[\text{S III}]$ are also available in the MIR and can be used to confirm the result of $[\text{Ne III}]/[\text{Ne II}]$. This ratio indeed has a larger dynamics in low-metallicity environments, where line-blanketing effects lead to higher stellar effective temperature (Madden et al., 2006). Still, in Fig. 4.8, we have found a relatively small range of the $[\text{Ne III}]/[\text{Ne II}]$ ratio, varying only by a factor of 4 across the whole galaxy as well as the superwind. In particular, this ratio ranges between 0.1 – 0.2 around the galaxy center, which is consistent with the values reported by former studies (Förster Schreiber et al., 2001; Beirão et al., 2008). We have also noticed that this value increases with distance from the galaxy center. The low $[\text{Ne III}]/[\text{Ne II}]$ ratio in the galaxy disk could be the result of an aged stellar population whose starburst activity ceased more than half a dozen million years ago or due to the edge-on view of the galaxy (Beirão et al., 2008). Away from the galactic plane in the superwind, the increase of $[\text{Ne III}]/[\text{Ne II}]$ ratio may be explained by a lower gas density relative to the number of ionizing photons.

When we look at Fig. 4.8. a–c, we can see a weak negative correlation between the $I(3.4)/I(3.3)$ ratio and the $[\text{Ne III}]/[\text{Ne II}]$ ratio. However, if we integrate sub-slits to enter a large scale, this trend disappears. In addition, it seems that least-squares and non-HB produce a false positive correlation in a global view of the entire M 82. With the HB method, the false correlation is smoothed by regulating a few data points in fainter regions (H, I, J, and K). Note that the three methods have no significant difference in central regions with high S/N ratio (A, B, C, and D). Hence, when combining the dehydrogenation traced by

$I(3.4)/I(3.3)$ and the **ISRF** hardness traced by $[\text{Ne III}]/[\text{Ne II}]$, it is necessary to separate the disk and halo/wind regions. Near the galactic plane, we can see a negative correlation between $I(3.4)/I(3.3)$ and $[\text{Ne III}]/[\text{Ne II}]$, which implies the dehydrogenation of grains by hard **ISRF**s, whereas in galactic outflow we have not observed a large enough variation of the $[\text{Ne III}]/[\text{Ne II}]$ ratio but a significant variation of $I(3.4)/I(3.3)$. It is thus likely that the process is different in the superwind. The dehydrogenation could be caused by the shattering of larger carbon grains (*e.g.* [Rau et al., 2019](#)). Overall, the trend being very weak, this scenario remains hypothetical.

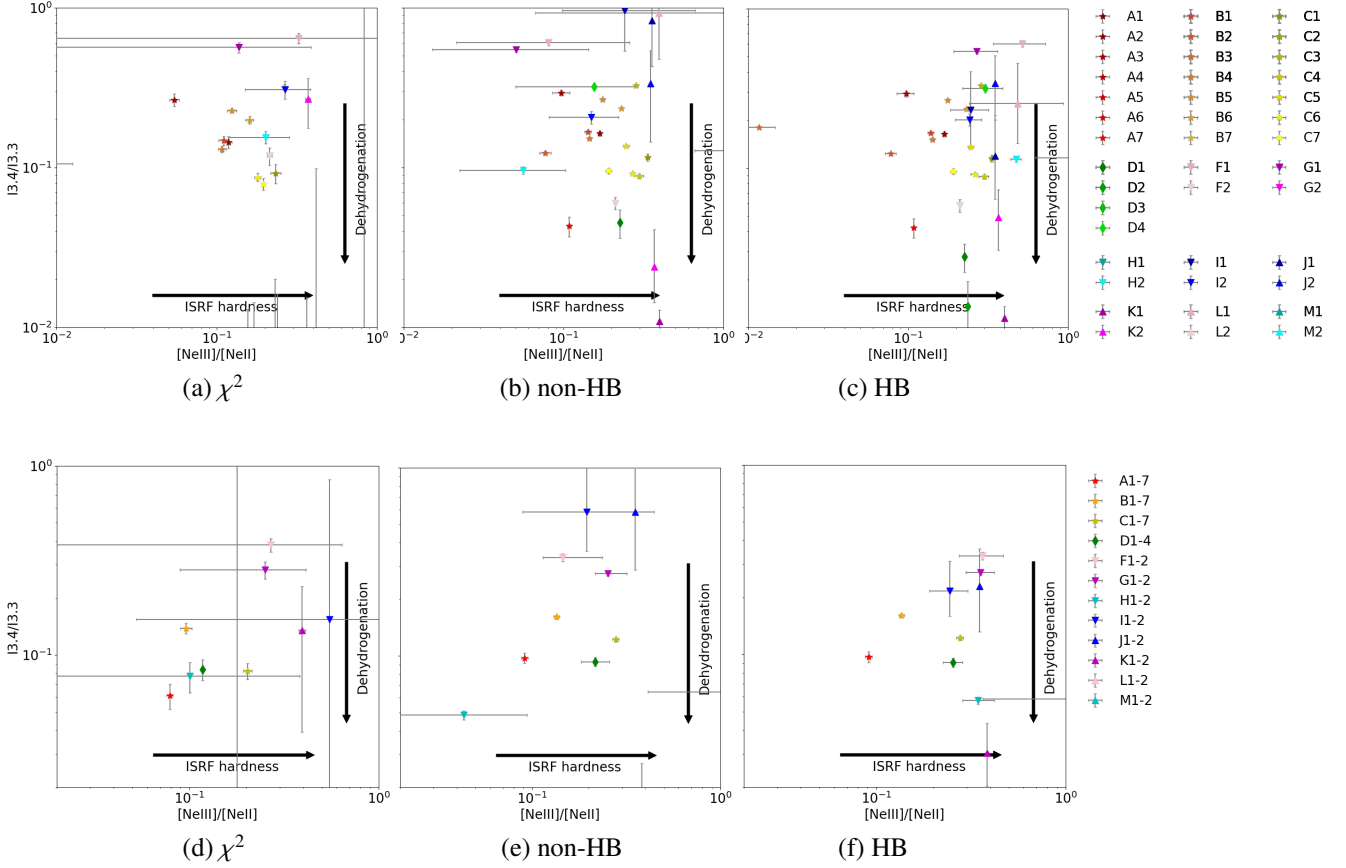


Figure 4.8 – Relation between PAH dehydrogenation and ISRF hardness.

This figure presents the correlation between $I(3.4)/I(3.3)$ and $[\text{Ne III}]/[\text{Ne II}]$. Panels (a)-(c) shows ratios from each spectrum. Panels (d)-(f) shows the same correlation but with ratios of the integrated slit. The variation of the **ISRF** hardness is indicated by $[\text{Ne III}]/[\text{Ne II}]$ whereas $I(3.4)/I(3.3)$ traces the dehydrogenation trend.

Molecular hydrogen (H_2) is the most abundant molecule in the Universe. The formation of molecular hydrogen takes place predominantly on small grains ([Le Bourlot et al., 2012](#)). It is challenging to measure the mass of molecular clouds, because H_2 is a symmetric molecule without dipole moment, thus no rotational transitions. Its first transitions (H_2 0-0 $\text{S}(0)_{28.3\mu\text{m}}$, H_2 0-0 $\text{S}(1)_{17.0\mu\text{m}}$) need temperatures of a few hundred K to be pumped. These transitions fall in the **MIR** so we can use them to probe the warm H_2 , which might link to the low-velocity shocks in the **ISM** (*e.g.* [Beirão et al., 2015](#)).

We have looked at warm H_2 by summing the H_2 0-0 $\text{S}(1)_{17.0\mu\text{m}}$, H_2 0-0 $\text{S}(2)_{12.3\mu\text{m}}$, H_2 0-0 $\text{S}(3)_{9.7\mu\text{m}}$, H_2 0-0 $\text{S}(5)_{6.9\mu\text{m}}$ and H_2 0-0 $\text{S}(7)_{5.5\mu\text{m}}$ lines (other H_2 0-0 lines are not fitted by our current model) and calculating the ratio with the sum of the 7.7 and

8.6 μm C-H modes. The negative correlation here is more evident both in the individual and the integrated slit frames, as shown in Fig. 4.9. With the dehydrogenation inside the outflow away from central disk, there is an increase of warm H_2 . This trend is not counter-intuitive if explained by the fact that warm H_2 in the outflow is excited by low-velocity shocks ($v < 40 \text{ km s}^{-1}$). The shattering of PAHs being driven by the shocks is thus consistently included in this scenario.

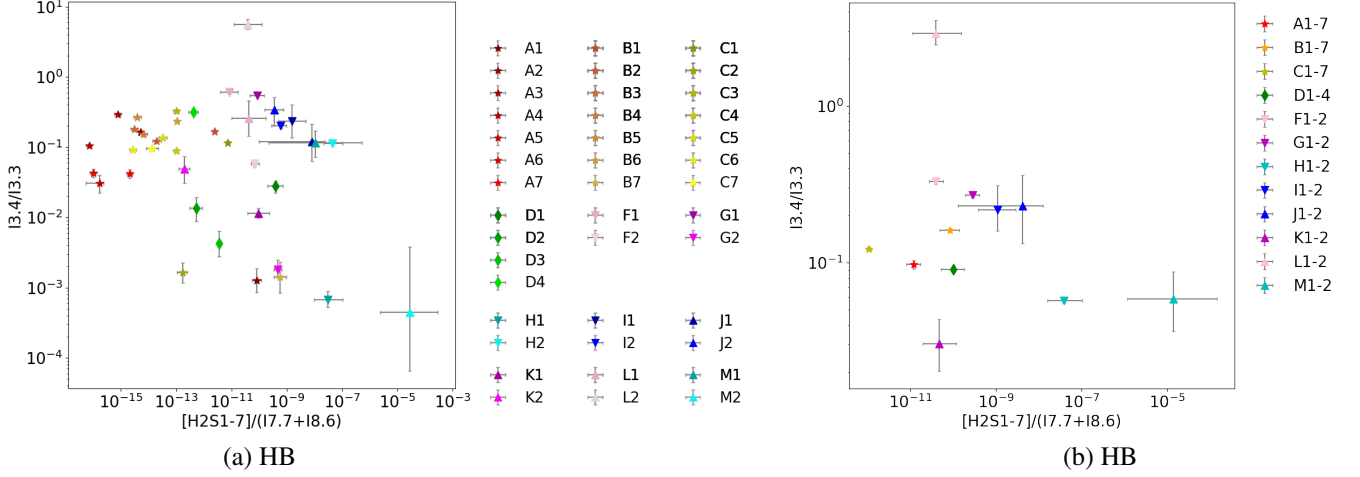


Figure 4.9 – Dehydrogenation probed by warm H_2 .

This figure presents the correlation between $I(3.4)/I(3.3)$ and H_2 0-0/($I(7.7)+I(8.6)$), where H_2 0-0 is the sum of H_2 0-0 S(1) $_{17.0\mu\text{m}}$, H_2 0-0 S(2) $_{12.3\mu\text{m}}$, H_2 0-0 S(3) $_{9.7\mu\text{m}}$, H_2 0-0 S(5) $_{6.9\mu\text{m}}$, and H_2 0-0 S(7) $_{5.5\mu\text{m}}$ lines. Panel (a) shows the ratios from each spectrum identified by the same colors as used in Fig. 4.7. Panel (b) shows the same correlation but with ratios for integrated slits.

4.4 Survey study in nearby Universe

A natural extension of Paper I is applying the method developed during this thesis to analyze a large sample of spatially-resolved galaxies observed by both AKARI/IRC and *Spitzer*/IRS. There are still a lot of questions to explore with abundant *Spitzer* and AKARI archived data, even after the upcoming launch of JWST. Indeed, a systematic study with these observations can prepare the ground for more detailed JWST observations.

One of the realizations of such studies is our ongoing project (Paper II), probing a large sample of spatially resolved sources in nearby galaxies and Galactic regions, which provide wider variations of physical conditions. The sample contains almost 500 pointings of AKARI/IRC slit spectroscopy, all covered by *Spitzer*/IRS maps. They are listed with AKARI AORs in Table D.1. We are using the same workflow from data processing (by MIRAGE) to spectral analysis (by MILES), justified by the case study of M 82. These consistently developed tools along with the powerful HB inference help us extract the most information possible from the observations, as an efficient way to tackle the complexities of MIR spectral features.

4.4.1 Sample selection

Catalog compilation Based on the AKARI archives (Sect. 2.1.1.2), this sample had been pre-selected by Dr. Ronin Wu from a nearby galaxy list compiled by Dr. M. Yamagishi. Then we have further filtered the sample by cross-searching *Spitzer* archives (Sect. 2.2.1.2). The original list includes 158 nearby galaxies and 276 AKARI observations and is referred to as MY-catalog hereafter. The expanded list includes 498 AKARI/IRC slit-spectroscopic observations and is referred to as RW-catalog hereafter.

Data search in the AKARI pool A given AKARI observation is labeled as “xxxxxxx.xxx”, a combination of one 7-digits target-ID and one up-to-3-digits sub-pointing ID. 158 galaxies are included in the original MY-catalog, yet some sub-pointings for several target-IDs are missing. After searching through the “PTM DATA” directory in the AKARI data pool, these missing sub-pointings are added to the catalog. This increases the number of observations from 276 to 388. Most observations in the MY-catalog are observed during the phase-2 and phase-3 of the AKARI mission. An inclusion of observations on these 158 galaxies during the entire AKARI mission increases the total observation number to 498. All these observations are listed in Table D.1.

Cross-search in the *Spitzer* archive We have explored the *Spitzer* archives, SHA, using the coordinates in the RW-catalog, and have included all *Spitzer*/IRS staring and mapping modes spectroscopic observations. At the same time, accounting for the need for inter-calibration during the data processing with MIRAGE, we have collected *Spitzer*/IRAC_{3.6 μ m}, *Spitzer*/IRAC_{8 μ m}, and *Spitzer*/MIPS_{24 μ m} data for each source.

4.4.2 Analysis guideline

Data reduction. Data reduction is our first encountered difficulty. With MIRAGE, we have integrated and automated most steps in the reduction pipeline. The code is flexible enough to adapt to different spectral and spatial resolutions. However, there is still a lot of work that should be done manually and individually, such as the data processing through CUBISM and IRC official pipelines. There is practically no better solution to further automate such processes. Another inconvenience resides in the dependencies of MIRAGE. The current version calls various external softwares, including SWarp, for image reprojection and coaddition, the omnipotent (but bulky, for now) SwING library (Fortran), mainly for synthetic photometry, and an IDL PSF convolution routine, not to mention those actively updating Astropy (Astropy Collaboration et al., 2018) related Python packages. Although MIRAGE’s Python interface is explicit enough for users, the installation and environment ajustement still can take some time.

Chapter 5

Conclusion and perspectives

Data! Data! Data!... I can't make bricks without clay!

Sherlock Holmes via Sir Arthur Conan Doyle

5.1 Concluding remarks

This thesis project mainly focused on the small interstellar carbon grains emitting in the **MIR**, in the nearby Universe. However, I have also expanded my scope beyond the **MIR**, following my interests in **ISM** physics, cosmic dust evolution, and all the open questions about galaxy evolution and star formation that a better knowledge of the dust properties could help us address.

5.1.1 Small carbon grain property

I have explored various correlations between **MIR** band ratios. The originality of my study of the small carbon grain properties primarily concerns the correlations between AKARI/IRC band features (at 3.3 and 3.4 μm) and those in the *Spitzer*/IRS range. I have studied the effects of **HPAH** dehydrogenation, with the variation of the 3.4 μm aliphatic feature. I have analyzed correlations that allowed me to separate the effects of variations of the **PAH** size distribution from the variation of their charge.

I have shown how having a full range **PAH** spectrum can help solve this degeneracy. In addition, I have also tested a scenario where **HPAH** are dehydrogenated by the hard **ISRF** within M 82's galactic plane.

5.2 Perspectives towards the JWST era

5.2.1 In the local Universe

5.2.1.1 Mid-IR spectroscopy

In addition to my large sample study, the modeling of the SAGE-Spec *Spitzer* Legacy program (Kemper et al., 2010) which mapped 12 regions across the Magellanic Clouds with *Spitzer*/IRS could be a natural extension of my work.

On the other hand, the increase in sensitivity of the next generation of instruments, including JWST, will demand more sophisticated spatial and spectral decomposition methods, with a rigorous treatment of the uncertainties. In accordance with the statistical approach I developed, the spectral decomposition of JWST spectra of spatially resolved regions will be the natural extension of my current research. Our state-of-the-art code MILES is pertinent to extract all the emission features (excitation line and aromatic/aliphatic band intensities) in the JWST spectral range and is flexible enough to include more physical components.

5.2.1.2 Diagnostics of the ISM conditions

The JWST offers an angular resolution down to $1''$, which corresponds to spatial scales of ≈ 0.002 pc at a distance of 400 pc (*e.g.* the Horsehead nebula and NGC 7023). Such a scale is much smaller than the mean free path of a visible photon (\mathcal{L}_V for V-band) in local **PDRs**. Applying Eq. (A.7),

$$\mathcal{L}_V = [Y_{\text{dust}} \times m_H \times n_H \times \kappa(V)]^{-1} \simeq \frac{600 \text{ pc cm}^{-3}}{n_H}, \quad (5.1)$$

where Y_{dust} is the dust-to-H mass ratio, m_H is the mass of an H atom, n_H is the gas density and κ is the dust opacity. Therefore with JWST, we will be capable of resolving the dust temperature gradient in dense regions ($\mathcal{L}_V \simeq 0.06$ pc for $n_H \simeq 10^4$). The edge-on cloud as the Horsehead nebula is thus a perfect target for JWST to study dust heating processes.

A promising approach would be to combine dust and gas modeling. First, we would calculate the physical quantities of the atomic and molecular gas using a **PDR** model, such as the Meudon PDR code (Le Petit et al., 2006): the electron density, n_e , the UV radiation field density, G_0 , the gas temperature, T_{gas} , and consequently the ionization/recombination ratio, $G_0/n_e T_{\text{gas}}^{1/2}$. Then, by adopting a dust model, such as THEMIS (Jones et al., 2017), we could model the dust emission, using the DustEM code (Compiègne et al., 2011), together with the radiative transfer code, SOC (Juvela, 2019), in order to calibrate the evolution of dust properties (size, hydrogenation, *etc.*) as a function of the physical conditions derived from the **PDR** model.

5.2.2 Towards distant galaxies

UV-optical bands are redshifted to longer wavelengths when we look back in time. Hence, infrared spectra become essential for studies of stellar populations and ionized lines in the distant universe. In Fig. 5.1, we have shifted the galaxy SED of Fig. 1.4 up to a redshift $z=6$, when the Universe was only a few hundred years past its *Reionization epoch* (Becker et al., 2001). As an example, one of the widely used SFR tracers, the $[\text{H}\alpha]_{656.3\text{nm}}$ line, will emit at $1.3126\text{ }\mu\text{m}$, $2.6252\text{ }\mu\text{m}$, and $4.5941\text{ }\mu\text{m}$ if the source is found at $z=1$ (below which the FUV is only accessible in space; Fig. 1.5), $z=3$ (cosmic noon, or the peak of Star Formation History; Madau & Dickinson, 2014), and $z=6$ (post-Reionization epoch), respectively.

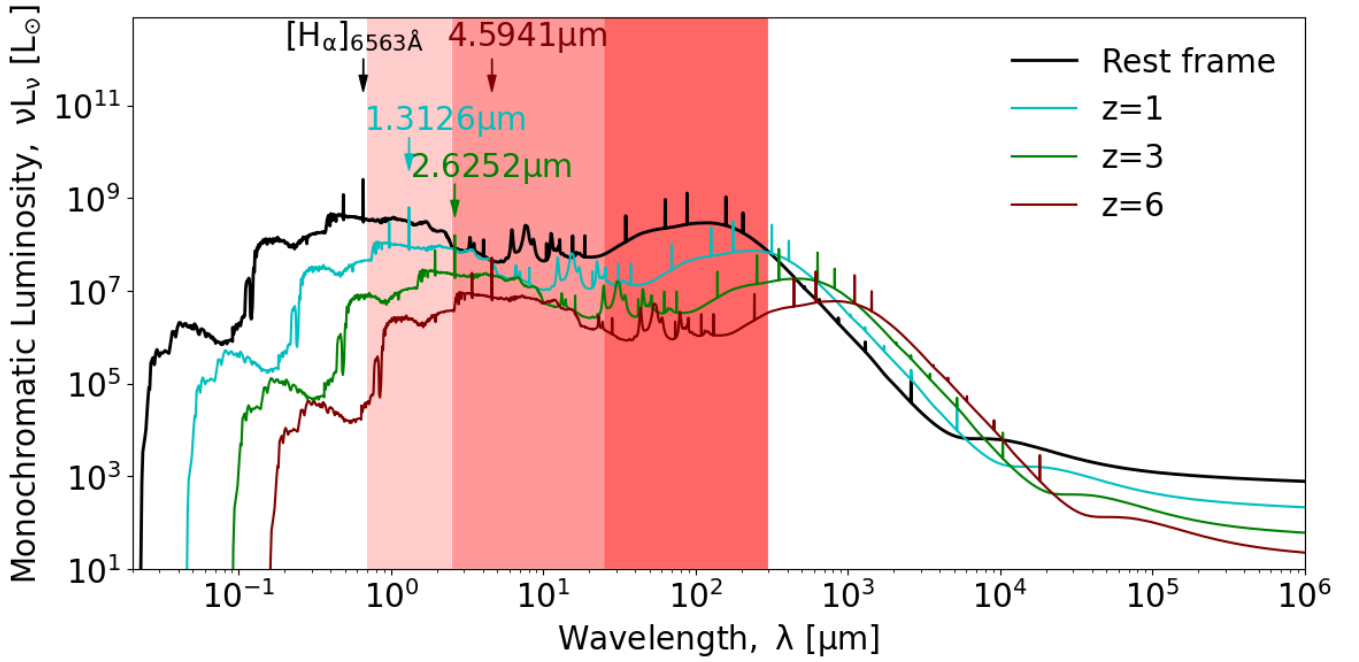


Figure 5.1 – Cosmological redshifting of a galaxy.

Observed galaxy SED if it resides at $z=0$ (rest frame), 1, 3, and 6. The x -axis is the “observed” wavelength. As an example, at $z=6$ the $[\text{H}\alpha]_{656.3\text{nm}}$ is redshifted to $4.6\text{ }\mu\text{m}$. infrared ranges are hatched red.

Based on a large statistical sample of homogenized observations of the local Universe, we will refine our diagnostic of the physical conditions based on UIB features (Sect. 4.3.1). The diagnostic will eventually be applied to high redshift galaxies to characterize warm molecular ISM and investigate its evolution from the present time. Moreover, open questions such as the starburst/AGN discrimination (Genzel et al., 1998), or PAHs as the SFR indicator (Peeters et al., 2004a) could be addressed.

Appendix A

Radiative transfer in a nutshell

Our knowledge of astronomical objects including interstellar dust mainly comes from direct measurements of electromagnetic radiation. However, all photons emitted by our targets have to travel across absorbing and emitting media before reaching us. Therefore, we need a radiative transfer theory to describe the propagation of radiation. Radiative transfer quantities (flux, flux density, intensity, brightness, *etc.*) are not always uniformly defined in the literature. With the microscopic model in [Fig. A.1](#), we have adopted the terminology in [Table A.1](#) for this manuscript.

A.1 Elemental basis and terminology

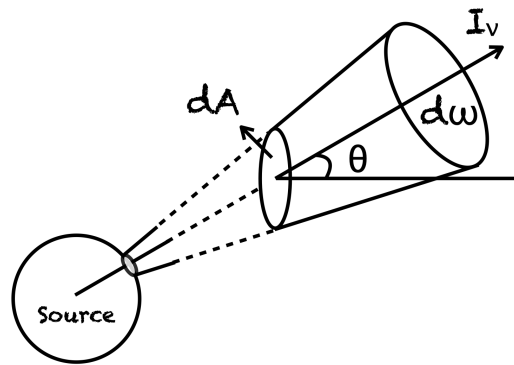


Figure A.1 – Illustration of the specific intensity.

Specific energy intensity, I_ν , passing through a surface area dA into a solid angle $d\Omega$ at an angle θ to the surface.

Suppose a surface unit, dA , on the source (*e.g.* a grain) emits a ray into a solid angle $d\Omega$ at an angle θ with the surface. The emitted energy dE , within a frequency range $[\nu, \nu + d\nu]$ per unit time dt , along the line-of-sight is characterized by the *spectral*

radiance, as known as the *specific intensity*, I_ν , through

$$dE = I_\nu \cos\theta \, dA \, d\nu \, d\Omega \, dt . \quad (\text{A.1})$$

Several other quantities can be derived from this expression, by integration over solid angle, frequency or area. They are listed in [Table A.1](#).

Table A.1 – Physical quantities used to describe the radiation.

Assume an unit energy dE (J) at frequency ν (Hz), leaving a radiative element, with a beam of unit solid angle $d\Omega$ (sr) at an angle θ to the surface, passes through the unit of surface area dA (m^2 ; [Fig. A.1](#)). The amount of energy entering the solid angle with a frequency range $[\nu, \nu + d\nu]$ in the time interval dt will be : $dE = I_\nu \cos\theta \, dA \, d\nu \, d\Omega \, dt$. Spectrum as a function of frequency. Spectral quantities shaded in grey are functions of wavelength.

Physical quantity	Application (Symbol) ^a	Definition	Unit
Energy	E	E	J
Energy density	-	$\frac{dE}{dV}$	J m^{-3}
Energy flux/power	Luminosity (L)	$\frac{dE}{dt}$	W or J s^{-1}
Spectral flux	Monochromatic luminosity (L_ν)	$\frac{dE}{d\nu \, dt}$	W Hz^{-1}
Irradiance	Flux density (F)	$\frac{dE}{dA \, dt}$	W m^{-2}
Spectral irradiance	Monochromatic flux density (F_ν)	$\frac{dE}{dA \, d\nu \, dt}$	$\text{W m}^{-2} \text{Hz}^{-1}$ or Jy^b
Radiance (emitter)	Intensity (I)	$\frac{dE}{d\Omega \, dA \, dt}$	$\text{W sr}^{-1} \text{m}^{-2}$
Spectral radiance (emitter)	Specific intensity (I_ν), or Surface brightness (S_ν) ^c , or <i>Planck's law</i> (B_ν)	$\frac{dE}{d\Omega \, dA \, d\nu \, dt}$	$\text{W sr}^{-1} \text{m}^{-2} \text{Hz}^{-1}$ or Jy sr^{-1}

^a. Different authors define these terms differently, and they are sometimes interchangeable.

^b. $1 \text{ Jy} = 10^{-26} \text{ W m}^{-2} \text{Hz}^{-1}$

^c. In mid-infrared spectroscopy, this quantity frequently appears as Jy pixel^{-1} , given directly by the detector. In the work of this thesis, we have consistently converted to MJy sr^{-1} from the perspective of the observed object (emitter).

A.2 Equation of radiative transfer

Given an incident ray with specific intensity I_ν traveling a distance s in a medium, we can write the equation of radiative transfer (e.g. [Rybicki & Lightman, 1979](#), for a review):

$$\frac{dI_\nu}{ds} = \frac{dI_\nu^{\text{ext}}}{ds} + \frac{dI_\nu^{\text{emit}}}{ds} = -\alpha_\nu I_\nu + j_\nu , \quad (\text{A.2})$$

where the variation of specific intensity dI_ν along the light beam (left side) is determined by extinction and emission (right side).

Emission is characterized by the monochromatic *emission coefficient*, j_ν , which is defined as the energy dE emitted per unit frequency per unit time per unit volume per unit solid angle:

$$\frac{dI_\nu^{\text{emit}}}{ds} = j_\nu \equiv \frac{dE}{d\Omega dA ds dt d\nu} . \quad (\text{A.3})$$

In general, the emission coefficient depends on the direction. For an *isotropic* emitter, we can define the (angle averaged) *emissivity*, ϵ_ν , to describe the energy emitted spontaneously per unit frequency per unit time per unit mass:

$$\epsilon_\nu \equiv \frac{4\pi}{d\Omega} \frac{dE}{\rho dA ds dt d\nu} = \frac{4\pi j_\nu}{\rho} , \quad (\text{A.4})$$

where ρ is the mass density of the emitting medium. As for extinction, we use the *extinction coefficient*, α_ν , to represent the loss of intensity, dI_ν^{ext} , in a beam during its propagation (by convention, α_ν is positive):

$$dI_\nu^{\text{ext}}(\nu, s) = -\alpha_\nu(\nu, s) I_\nu(\nu, s) ds . \quad (\text{A.5})$$

From a microscopic perspective, this phenomenological law can be simply modeled with grains with density n and effective extinction cross-section C_{ext} (Sect. 1.4.2.2):

$$\alpha_\nu(\nu, s) = n(s) C_{\text{ext}}(\nu, s) = \rho(s) \kappa(\nu, s) , \quad (\text{A.6})$$

where we have defined the *mass extinction coefficient* or *opacity*, κ , given the grain mass density ρ . Due to extinction, the *mean free path* of a photon, or the average length that a photon can travel before being absorbed or scattered is:

$$\mathcal{L}_{\text{mean}}(\nu, s) \equiv \frac{1}{\alpha_\nu(\nu, s)} = \frac{1}{\rho(s) \kappa(\nu, s)} . \quad (\text{A.7})$$

The *optical depth*, $d\tau(\nu) = \alpha_\nu(\nu, s) ds$, is a more natural quantity than s , that simplifies the radiative transfer equation. Integrated over the sightline is gives:

$$\tau(\nu, s) = \int_0^s \rho(s') \kappa(\nu, s') ds' . \quad (\text{A.8})$$

Applying this dimensionless quantity to both extinction and emission processes, Eq. (A.2) can be rewritten as:

$$\frac{dI_\nu}{d\tau} = -I_\nu + S_\nu , \quad (\text{A.9})$$

where the *source function*, $S_\nu = j_\nu/\alpha_\nu$, includes all emissive terms such as stellar and dust emission. Noticing that, with Eq. (A.7), $\tau(\mathcal{L}_{\text{mean}}) = 1$, we can define an *optically thin* or *transparent* medium, if $\tau \ll 1$. Oppositely, a medium is *optically thick* or *opaque*, if $\tau \gg 1$.

Appendix B

Recipe for statistics

B.1 Statistical functions

We present the statistical distributions used in [Chap. 3](#), in their univariate form.

B.1.1 Normal (Gaussian) distribution

If a random variable x obeys a *normal distribution* with mean μ and standard deviation σ , then we have

$$x \sim N(\mu, \sigma), \sigma > 0$$
$$p(x) = \frac{1}{\sqrt{2\pi} \sigma} \exp\left[-\frac{1}{2} \left(\frac{x - \mu}{\sigma}\right)^2\right] \quad (\text{B.1})$$

In addition, we can define an asymmetric version of the normal distribution, the *split-normal distribution* ([Villani & Larsson, 2006](#)):

$$p(x) = \sqrt{\frac{2}{\pi}} \frac{1}{\lambda(1 + \tau)} \times \begin{cases} \exp\left[-\frac{1}{2} \left(\frac{x - x_0}{\lambda}\right)^2\right] & \text{if } x \leq x_0 \\ \exp\left[-\frac{1}{2} \left(\frac{x - x_0}{\lambda\tau}\right)^2\right] & \text{if } x > x_0, \end{cases} \quad (\text{B.2})$$

where we have reparameterized with a position parameter x_0 , a scale parameter λ , and a shape parameter τ , as follows:

1. $b = \frac{\pi-2}{\pi}(\tau - 1)^2 + \tau$;
2. $\mu = x_0 + \sqrt{\frac{2}{\pi}}\lambda(\tau - 1)$;
3. $\sigma = \sqrt{b}\lambda^2$.

B.1.2 Student's t-distribution

Another centrally peaked, symmetric distribution is *Student's t-distribution*. The name “*Student*” was the pseudonym of William Sealy Gosset, who used it to publish the discovery of his t-distribution (Student, 1908). By convention, we use a random variable t instead of x . With the mean μ , as well as σ and ν which give the variance $\frac{\nu}{\nu-2}\sigma^2$, the Student's t-distribution can be written:

$$t \sim \text{Student}(\nu, \mu, \sigma), \quad \nu > 0, \quad \sigma > 0 \quad (\text{B.3})$$

$$p(t) = \frac{\Gamma(\frac{1}{2}[\nu + 1])}{\Gamma(\frac{1}{2}\nu) \sqrt{\nu\pi}\sigma} \left[1 + \frac{1}{\nu} \left(\frac{t - \mu}{\sigma} \right)^2 \right]^{-\frac{1}{2}(\nu+1)}$$

The Student's t-distribution has power-law tails at infinity, dropping as $|t|^{-(\nu+1)}$. When $\nu \rightarrow \infty$, we get the normal distribution. When $\nu = 1$, we obtain the *Cauchy distribution*:

$$x \sim \text{Cauchy}(\mu, \sigma), \quad \sigma > 0 \quad (\text{B.4})$$

$$p(x) = \frac{1}{\pi\sigma} \left[1 + \left(\frac{x - \mu}{\sigma} \right)^2 \right]^{-1}$$

B.1.3 Log-normal distribution

For a random variable that resides only on the positive axis, such as the calibration error, $1 + \vec{\delta}$, in Sect. 3.2.3, it is practical to sample them with a normal distribution on the “ $\log(x)$ -axis”. So comes the *log-normal distribution*:

$$x \sim \text{Log-normal}(\mu, \sigma), \text{ if } u \equiv \frac{\log(x) - \mu}{\sigma} \sim \mathcal{N}(0, 1) \quad (\text{B.5})$$

or equivalently

$$x \sim \text{Log-normal}(\mu, \sigma), \quad \sigma > 0 \quad (\text{B.6})$$

$$p(x) = \frac{1}{\sqrt{2\pi} \sigma x} \exp \left[-\frac{1}{2} \left(\frac{\log(x) - \mu}{\sigma} \right)^2 \right], \quad x > 0$$

μ and σ are the mean and standard deviation in the $\log(x)$ space, while in the x space, a log-normal distribution has the mean $\exp(\mu + \frac{1}{2}\sigma^2)$, and the variance $\exp(2\mu) \exp(\sigma^2)(\exp(\sigma^2) - 1)$.

B.2 Numerical matrix inversion

The dependence of two random variables X and Y with their means μ_X, μ_Y and standard deviations σ_X, σ_Y can be measured by the *Pearson correlation coefficient*¹

$$\rho_{X,Y} = \text{corr}(X, Y) = \frac{\text{cov}(X, Y)}{\sigma_X \sigma_Y}, \quad (\text{B.7})$$

where their covariance is expressed in terms of expectation:

$$\text{cov}(X, Y) = \mathbb{E}[(X - \mu_X)(Y - \mu_Y)]. \quad (\text{B.8})$$

Given a set of parameters $\vec{x} = (x_1, x_2, \dots, x_q)$, the $q \times q$ correlation matrix \mathbf{R} can be calculated from the same order covariance matrix $\mathbf{\Sigma}$ and the diagonal matrix of standard deviations \mathbf{S} :

$$\mathbf{R} = \mathbf{S}^{-1} \mathbf{\Sigma} \mathbf{S}^{-1}. \quad (\text{B.9})$$

To sample the prior distribution (Eq. 3.22), we need to calculate the inverse matrix of $\mathbf{\Sigma}$. The computational complexity of this matrix operation increases exponentially with an increase in the order of the matrix. For instance, given a $n \times n$ matrix, it takes approximately $2n^3$ arithmetical operations for the inversion with the Gauss-Jordan elimination (*e.g.* Strassen, 1969). Optimizing the computation of inverse matrix with the properties of covariance matrices benefits significantly the MCMC algorithm since $\mathbf{\Sigma}^{-1}$ is calculated numerous times at each MCMC iteration.

B.2.1 LU decomposition

It is always possible to write a matrix \mathbf{A} as a product of a lower triangular matrix \mathbf{L} and an upper triangular matrix \mathbf{U} . The inverse of \mathbf{A} is thus

$$\mathbf{A}^{-1} = (\mathbf{L} \mathbf{U})^{-1} = \mathbf{U}^{-1} \mathbf{L}^{-1}. \quad (\text{B.10})$$

Note that calculations concerning a triangular matrix are more trivial. The LU decomposition is commonly used for calculations of the inverse and the determinant of a matrix by numerical computation algorithms.

B.2.2 Cholesky decomposition

Given a symmetric and positive-definite square matrix \mathbf{a} , the *Cholesky decomposition* is about a factor of two faster than alternative methods for solving linear equations (Press et al., 2007). Indeed, it is always possible to find a special factorization

1. Also called the Pearson product-moment correlation coefficient, or *Pearson's r*.

of \mathbf{a} with a lower triangular matrix \mathbf{L} such that $\mathbf{a} = \mathbf{L}\mathbf{L}^T$. Thus the inverse of \mathbf{a} becomes

$$\mathbf{A} = \mathbf{a}^{-1} = (\mathbf{L}^{-1})^T \mathbf{L}^{-1}. \quad (\text{B.11})$$

B.2.3 Modified Sherman-Morrison approach

The numerical technique described in this section is an original contribution that I have provided.

The Gibbs sampling we applied to the **MCMC** sampler draws one parameter at a time from its conditional distribution. Thus, at each iteration of the **MCMC**, there is only one unique value changed in the current covariance matrix accounting for its symmetry. Inspired by the *Sherman-Morrison formula* (Sherman & Morrison, 1950), which provides a numerically cheap way to compute one inverse matrix from another inverse matrix that is already known, we came up with a technique to calculate the inverse matrix corresponding to an identical change in two symmetric elements of a symmetric invertible matrix.

Let:

- $a_{ij}, i = 1, 2, \dots, n; j = 1, 2, \dots, n$ denote the elements of an n th order symmetric and positive-definite matrix \mathbf{a} ;
- b_{ij} , denote the elements of \mathbf{b} , the inverse of \mathbf{a} ;
- $A_{ij}^{(0)}$, denote the elements of $\mathbf{A}^{(0)}$ which differs from \mathbf{a} only in one element, say $A_{RS}^{(0)}$;
- $B_{ij}^{(0)}$, denote the elements of $\mathbf{B}^{(0)}$, the inverse of $\mathbf{A}^{(0)}$;
- A_{ij} , denote the elements of \mathbf{A} which differs from $\mathbf{A}^{(0)}$ only in one element A_{SR} , or from \mathbf{a} in two symmetric elements A_{SR} and A_{RS} ;
- B_{ij} , denote the elements of \mathbf{B} , the inverse of \mathbf{A} ;
- $A_{SR} = A_{RS} = A_{RS}^{(0)} = a_{RS} + \Delta a$.

Sherman-Morrison computes $\mathbf{B}^{(0)}$ from Δa and \mathbf{b} by

$$B_{ij}^{(0)} = b_{ij} - \frac{\Delta a}{c_0} b_{iR} b_{Sj}, \quad (\text{B.12})$$

$$(i = 1, 2, \dots, n; j = 1, 2, \dots, n),$$

provided that $c_0 = 1 + b_{SR}\Delta a \neq 0$. Idem we can obtain \mathbf{B} from Δa and $\mathbf{B}^{(0)}$ by

$$B_{ij} = B_{ij}^{(0)} - \frac{\Delta a}{c_1} B_{iS}^{(0)} B_{Rj}^{(0)}, \quad (\text{B.13})$$

$$(i = 1, 2, \dots, n; j = 1, 2, \dots, n),$$

with $c_1 = 1 + B_{RS}^{(0)}\Delta a \neq 0$ in addition to $c_0 \neq 0$. Written as a function of b_{ij} , it becomes:

$$c_0 c_1 = [1 + (b_{SR} - \sqrt{b_{RR}b_{SS}})\Delta a][1 + (b_{SR} + \sqrt{b_{RR}b_{SS}})\Delta a]. \quad (\text{B.14})$$

Note that the inverse matrix of a symmetric matrix is also symmetric. Hence \mathbf{b} and \mathbf{B} are symmetric, but not $\mathbf{B}^{(0)}$. By utilizing Eq. (B.12), the inverse matrix of \mathbf{A} becomes:

$$B_{ij} = b_{ij} - \frac{\Delta a}{c_0} b_{iR} b_{Sj} - \frac{\Delta a}{c_1} \left[b_{iS} - \frac{\Delta a}{c_0} b_{SS} b_{iR} \right] \left[b_{Rj} - \frac{\Delta a}{c_0} b_{RR} b_{Sj} \right], \quad (i = 1, 2, \dots, n; j = 1, 2, \dots, n). \quad (\text{B.15})$$

The validity of Eq. (B.15) may be demonstrated by multiplying through by A_{ki} , ($i = 1, 2, \dots, n$) as follows:

$$\sum_{i=1}^n A_{ki} B_{ij} = \sum_{i=1}^n A_{ki} b_{ij} - \frac{\Delta a}{c_0} b_{Sj} \sum_{i=1}^n A_{ki} b_{iR} - \frac{\Delta a}{c_1} \left[b_{Rj} - \frac{\Delta a}{c_0} b_{RR} b_{Sj} \right] \left[\sum_{i=1}^n A_{ki} b_{iS} - \frac{\Delta a}{c_0} b_{SS} \sum_{i=1}^n A_{ki} b_{iR} \right], \quad (k = 1, 2, \dots, n; j = 1, 2, \dots, n). \quad (\text{B.16})$$

When $k \neq R$ and $k \neq S$, the fact that $A_{ki} = a_{ki}$ cancels the sums in the second and third terms on the right side of Eq. (B.16) because \mathbf{a} and \mathbf{b} are inverse matrices. The cases $k = R$ and $k = S$ give rise to the extra term Δa , which can also be vanished after tedious calculations. Finally we have:

$$\sum_{i=1}^n A_{ki} B_{ij} = \sum_{i=1}^n a_{ki} b_{ij}, \quad (k = 1, 2, \dots, n; j = 1, 2, \dots, n) \quad (\text{B.17})$$

and hence \mathbf{B} is the inverse of \mathbf{A} .

Note that Eq. (B.15) retains a form similar to the original Eq. (B.12), but presents some differences due to the addition of symmetric and positive-definite constraints on the original matrix, as well as to the fact that we changed two symmetric elements instead of one. We call it the **Modified Sherman-Morrison (MSM)** formula.

Appendix C

Recipe for high-redshift universe

The measurement of the Universe, or *cosmography*, is the prerequisite to observing objects at high redshift. As the Euclidian geometry is no longer valid in the expanding Universe, we have to specify the distance between two points with a different metric. Consequently, we need to know cosmology to measure the physical properties of distant galaxies, and, reversely, cosmological parameters are inferred from the known physical properties of distant galaxies.

In the rest of this section, we have adopted the following subscripts:

- “ t ” represents the present time of the observer;
- “ o ” represents the observer;
- “ e ” represents the emitting object.

C.1 Cosmographic parameters

The *Hubble Law* describes the expansion of the Universe (or *Hubble flow*) by regulating recession speed v and *distance* d with the *Hubble constant* H :

$$v = H d \quad (\text{C.1})$$

H has a dimension of inverse time, from which we define the *Hubble time* $t_H \equiv 1/H$. Along with the speed of light c , we get *Hubble distance*, d_H , as:

$$d_H \equiv \frac{c}{H} \quad (\text{C.2})$$

The (baryonic and dark matter) mass density ρ of the Universe and the cosmological constant (or vacuum energy density) Λ are written in their dimensionless forms (Peebles, 1993), Ω_M and Ω_Λ , respectively:

$$\Omega_M \equiv \frac{8\pi G \rho}{3H^2} ; \quad (\text{C.3})$$

$$\Omega_\Lambda \equiv \frac{\Lambda c^2}{3H^2} . \quad (\text{C.4})$$

Note that G is Newton's gravitational constant. In SI units, G has the value $6.67 \times 10^{-11} \text{ m}^3 \text{ kg}^{-1} \text{ s}^{-2}$. To completely determine the geometry of the Universe, we need a third parameter - the present spatial curvature density, Ω_k , defined as follows:

$$\Omega_k = \frac{-k c^2}{a^2} , \quad (\text{C.5})$$

where a is the *scale factor* which represented the size of the Universe¹ and k is the spatial curvature when $a = 1$ (observer's time).

Given the *Friedmann equation*:

$$\Omega_M + \Omega_\Lambda + \Omega_k = 1 , \quad (\text{C.6})$$

we have $H \equiv \dot{a}/a$.

C.2 Cosmological redshift

Given the observed and emitted frequency/wave ν_o , ν_e/λ_o , λ_e of an object, we determine the *redshift*

$$z \equiv \frac{\nu_e}{\nu_o} - 1 = \frac{\lambda_o}{\lambda_e} - 1 \quad (\text{C.7})$$

With special relativity, the redshift can be expressed with the *radial velocity*, v :

$$1 + z = \sqrt{\frac{1 + v/c}{1 - v/c}} . \quad (\text{C.8})$$

This measured redshift consists of two distinct parts: (i) the Doppler shift due to the physical motion of the object with respect to the observer; (ii) the *cosmological redshift* due to the general expansion of the Universe. If the radial velocity of the Doppler motion $v_{\text{Doppler}} \ll c$, the corresponding Doppler shift $z_{\text{Doppler}} \simeq 0$, we assume z to be only cosmological redshift (Hogg, 1999).

Note that redshift is implicitly determined with respect to the observer, it is directly linked to the scale factor by

$$1 + z = \frac{a(t_o)}{a(t_e)} = \frac{1}{a(t_e)} , \quad (\text{C.9})$$

with the scale factor at the time of emitter $a(t_e)$ and of observer $a(t_o) = 1$.

1. More precisely, this is the scale factor of the proper distance at the time t when it was emitted in regard to the measured distance at the reference time t_0 . Therefore $a(t_0) = 1$.

C.3 Distance measures in cosmology

The distance Δd between two nearby objects comoving with the Hubble flow remains constant with epoch. The *total line-of-sight comoving distance* d_C from us to a distant object is the integral of the infinitesimal Δd along the radial direction from $z = 0$ to the object:

$$d_C = \int_0^z \Delta d = d_H \int_0^z \frac{dz'}{E(z')}, \quad (\text{C.10})$$

where $E(z) \equiv \sqrt{\Omega_M (1+z)^3 + \Omega_k (1+z)^2 + \Omega_\Lambda}$.

The comoving distance at the same redshift can be calculated by $d_M \delta\theta$, given the separation angle $\delta\theta$. The *transverse comoving distance* d_M is related to d_C by the product of Hubble distance d_H with trigonometric functions \sinh (for a closed universe) and \sin (for an open universe). For a flat universe $d_M = d_C$.

For a small distance d (small in terms of cosmography, where Euclidean geometry is still valid; large enough for small-angle approximation, compared to the angular separation of objects), given the radius R of an object, its angular size (in radians) is $\delta\theta = R/d$. Similarly in cosmography, the *angular diameter distance* d_A of an object is defined so that its physical transverse size (or proper size) R_e has the following relation with its angular size $\delta\theta$ (constant):

$$\delta\theta = \frac{R_o}{d_M} = \frac{R_e}{a(t_e) d_M} = \frac{R_e}{d_A}, \quad (\text{C.11})$$

where we apply the scale factor to convert the measured size $R_o = R_e/a(t_e)$. Given Eq. (C.9), we have

$$d_A = a(t) d_M = \frac{d_M}{1+z}. \quad (\text{C.12})$$

Indeed, Eq. (C.11) can also be interpreted as d_A being the “*proper distance*” of the object, and R_o being its “*comoving size*”.

In cosmography, the *luminosity distance* d_L is determined in the way that bolometric flux F and bolometric luminosity L follow the Euclidean space flux-luminosity relation $F = L/(4\pi d^2)$. Assuming the absolute luminosity L emitted by a distant object at redshift z , the total flux density F received by the observer is reddened by a factor of $1+z$, given Eq. (C.7). At the same time, cosmological time dilation slows the photons by a factor of $1+z$ (Weinberg, 1972), that is, the flux decreases by $1+z$. It turns out:

$$F = \frac{L}{4\pi d_M^2} \frac{1}{(1+z)^2} = \frac{L}{4\pi d_L^2} \quad (\text{C.13})$$

Given Eq. (C.12), we have:

$$d_L = (1+z) d_M = (1+z)^2 d_A \quad (\text{C.14})$$

We can also write Eq. (C.13) in differential form:

$$\nu_o L_{\nu_o} = \frac{a(t_e)^2}{a(t_o)^2} \nu_e L_{\nu_e} = \frac{\nu_e L_{\nu_e}}{(1+z)^2}, \quad (\text{C.15})$$

where $a(t_0) = 1$ as usual.

C.4 Tolman dimming

Notice the angular diameter distance in Eq. (C.12) has a different behavior from the luminosity distance, whereas the observed surface brightness S_o is a function of flux density per unit angular area. Hence S_o should be redshift dependent. Taking Eq. (C.11) and Eq. (C.13) we have

$$S_o = \frac{F}{\delta\theta^2} = \frac{L}{4\pi d_L^2} \frac{d_A^2}{R_e^2} = \frac{L}{4\pi R_e^2} \frac{1}{(1+z)^4} = \frac{S_e}{(1+z)^4}, \quad (\text{C.16})$$

where the emitted surface brightness is $S_e = L/(4\pi R_e^2)$. Note that the ratio S_o/S_e depends only on redshift and is independent of the cosmological parameters. For this reason, it has been conceived to test cosmological models, known as the *Tolman surface brightness test* (e.g. Hubble & Tolman, 1935).

At redshift z , the surface brightness decreases by a factor of $(1+z)^4$ in the expanding Universe. This effect is called the (*Tolman dimming*). It becomes significant at redshift $z > 3$ with a factor of more than 250. Consequently, it is more difficult to detect more distant galaxies, biasing studies of quantities such as the cosmic **Star Formation History (SFH)**.

C.5 K-correction

When observing the high-redshift universe, there is another critical correction. The *k-correction* is the difference between the observed magnitude of an object at redshift z and the magnitude that would be observed if it were at the rest frame. This difference comes from the different bandpass transmission curves of the filters. Although it is redshift dependent like the surface brightness dimming effect, it has nothing to do with cosmological expansion. Instead, it is a purely instrumental effect.

Appendix D

Complementary figures

D.1 MILES tests

D.1.1 Fits of synthetic spectra

Compared to the HB fitted spectrum “c1 SN10 #1” in Fig. 3.7. b, spectra in Fig. D.1 imply that the fitted models, with either a lower continuum (“c1 SN10 #1”; panel *a*) or higher signal-to-noise ratio (“c10 SN100 #1”; panel *b*), has span a narrower $1-\sigma$ interval.

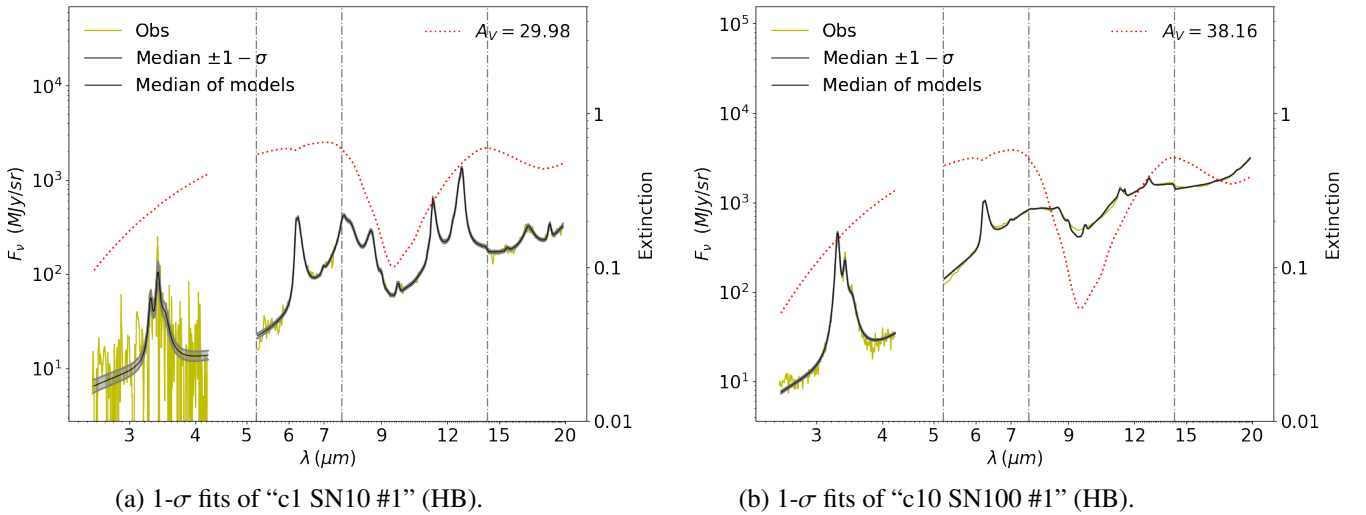


Figure D.1 – Median models fitted with the HB method.

Panels (*a*) and (*b*) show the median models of the HB fitted spectra, “c1 SN10 #1” and “c10 SN100 #1”, respectively.

The extinction amplitude for all the synthetic spectrum sample is $A_V = 16.26$. We have seen in Fig. 3.7. b that A_V can converge to a larger value, $A_V = 36.42$. Spectra generated with the same S/N ratio and continuum settings, but with different UIB intensities, can lead to different A_V distributions. We have presented two extreme cases in our sample in Fig. D.2. The

panel (a) shows the spectrum “c10 SN10 #5”, whose fit has an extinction amplitude, $A_V = 48.98$. The high A_V makes the Bayesian fit so uncertain that even the median model can not reach the actual around $10\ \mu\text{m}$. On the contrary, when this value is initialized to the lowest, $A_V = 17.28$ for the spectrum “c10 SN10 #7”, the fitted models are consistent with the observations (panel b).

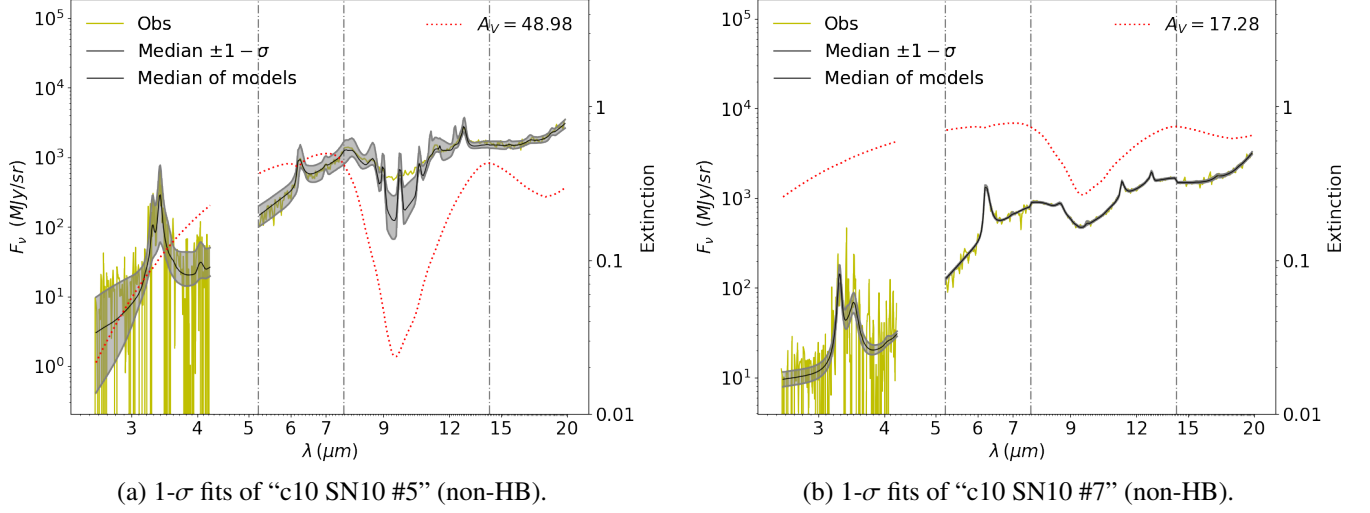
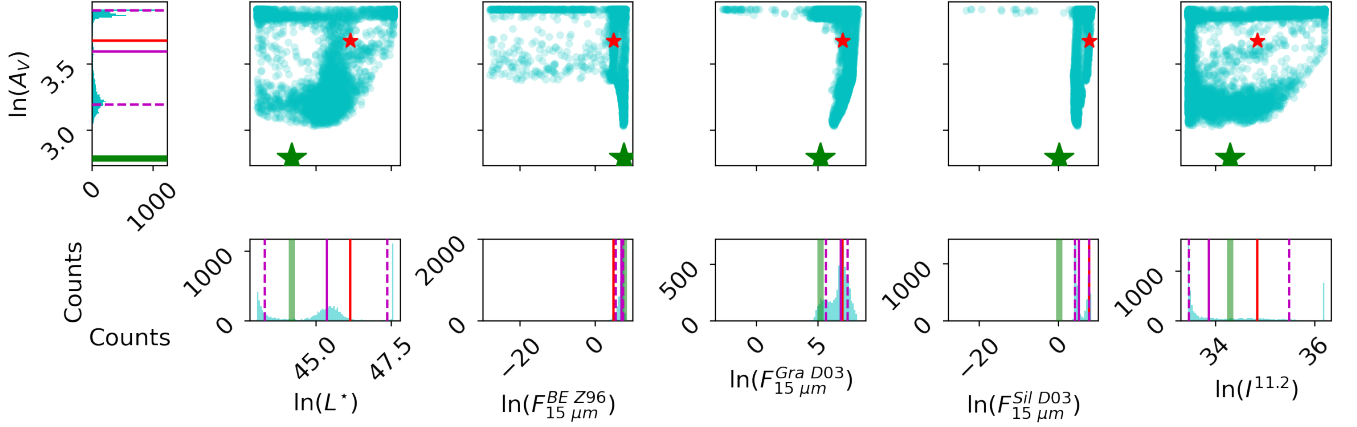


Figure D.2 – Median models fitted with the non-HB method.

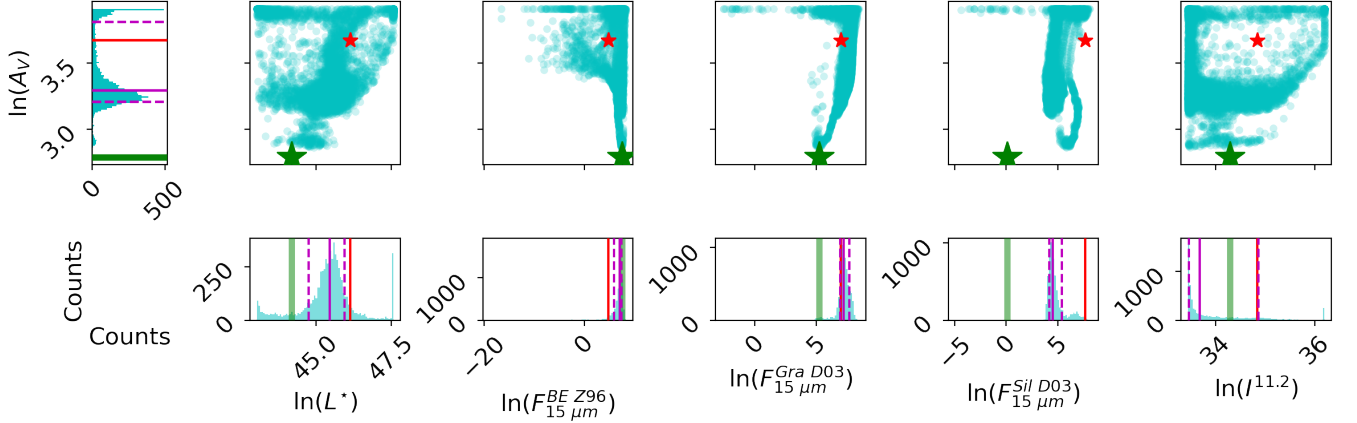
Panels (a) and (b) show the median models of the non-HB fitted spectra, “c10 SN10 #5” and “c10 SN10 #7”, respectively.

D.1.2 Distributions of fitted parameters

In this subsection, we use the scatter plots to better visualize correlations between model parameters. When comparing the non-HB and HB results in Fig. D.3, we see the parameters fitted by the HB method (panel *b*) generally have narrower distributions, whether uni-modal or multi-modal, than the non-HB distributions (panel *a*), for the same MCMC length. In particular, as discussed in Sect. 3.3.2, the degeneracy of $\ln(A_V)$ makes it difficult to interpret the fitting results. In Fig. D.3, we see the impact of the extinction amplitude on extensive physical quantities.



(a) The non-HB fitted parameter distributions.



(b) The HB fitted parameter distributions.

Figure D.3 – Variations of extinction amplitude with extensive quantity parameters.

With the Bayesian fits of the spectrum “c10 SN10 #1”, we present the scatter plots of $\ln(A_V)$ and five extensive quantity parameters in our model, $\ln(L^*)$, $\ln(F_{15 \mu m}^{BE Z96})$, $\ln(F_{15 \mu m}^{Gra D03})$, $\ln(F_{15 \mu m}^{Sil D03})$ and $\ln(I^{11.2})$, along with the distribution histograms of each parameter. The “true” values are marked with green lines and stars. The χ^2 best-fit values are marked with red lines and stars. The magenta solid and dashed lines indicate the distribution medians and $1-\sigma$ intervals, respectively.

Similar plots for the multivariate distributions of $\ln(A_V)$ and the relative intensity of emission lines and bands are also presented in Fig. D.4. We see $\ln(A_V)$ has no effect on line and band relative intensities except at its upper limit (here $\ln(A_V) = 4$). With Fig. D.6, we can roughly discover correlations between individual line and band intensities.

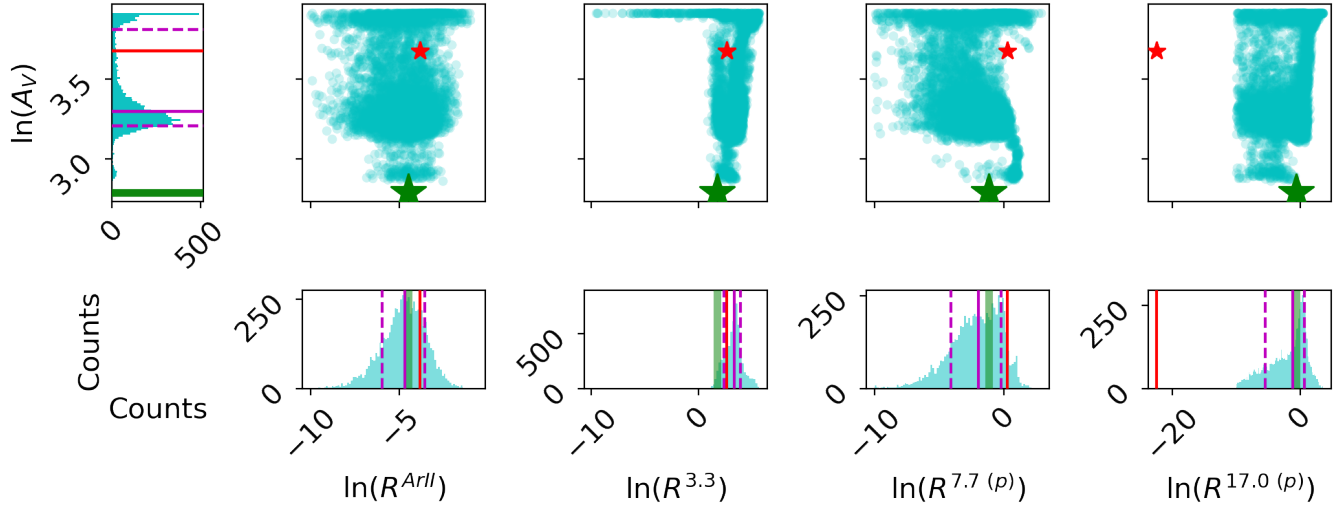


Figure D.4 – Variations of extinction amplitude with emission line and band intensity ratios. With the HB fit of the spectrum “c10 SN10 #1”, we present the multivariate distributions of $\ln(A_V)$ and four line/band relative intensities, $\ln(R^{\text{ArII}})$, $\ln(R^{3.3})$, $\ln(R^{7.7(p)})$ and $\ln(R^{17.0(p)})$, with the same plot template as Fig. D.3.

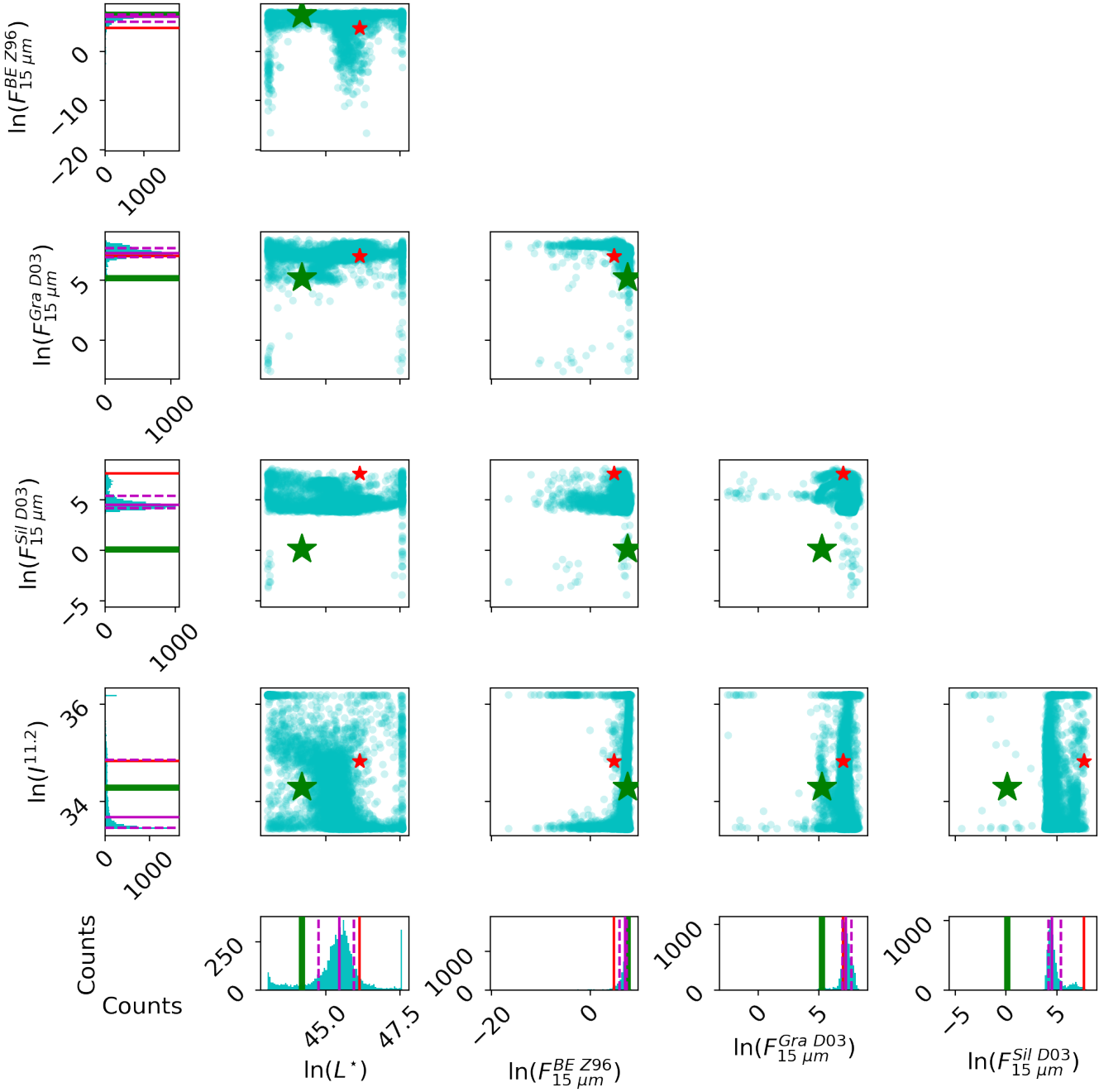


Figure D.5 – Multivariate distributions between extensive physical quantities.

With the HB fit of the spectrum “c10 SN10 #1”, we present the multivariate distributions between five extensive physical quantities, $\ln(L^*)$, $\ln(F_{15\mu\text{m}}^{\text{BE Z96}})$, $\ln(F_{15\mu\text{m}}^{\text{Gra D03}})$, $\ln(F_{15\mu\text{m}}^{\text{Sil D03}})$ and $\ln(I^{11.2})$, with the same plot template as [Fig. D.3](#).

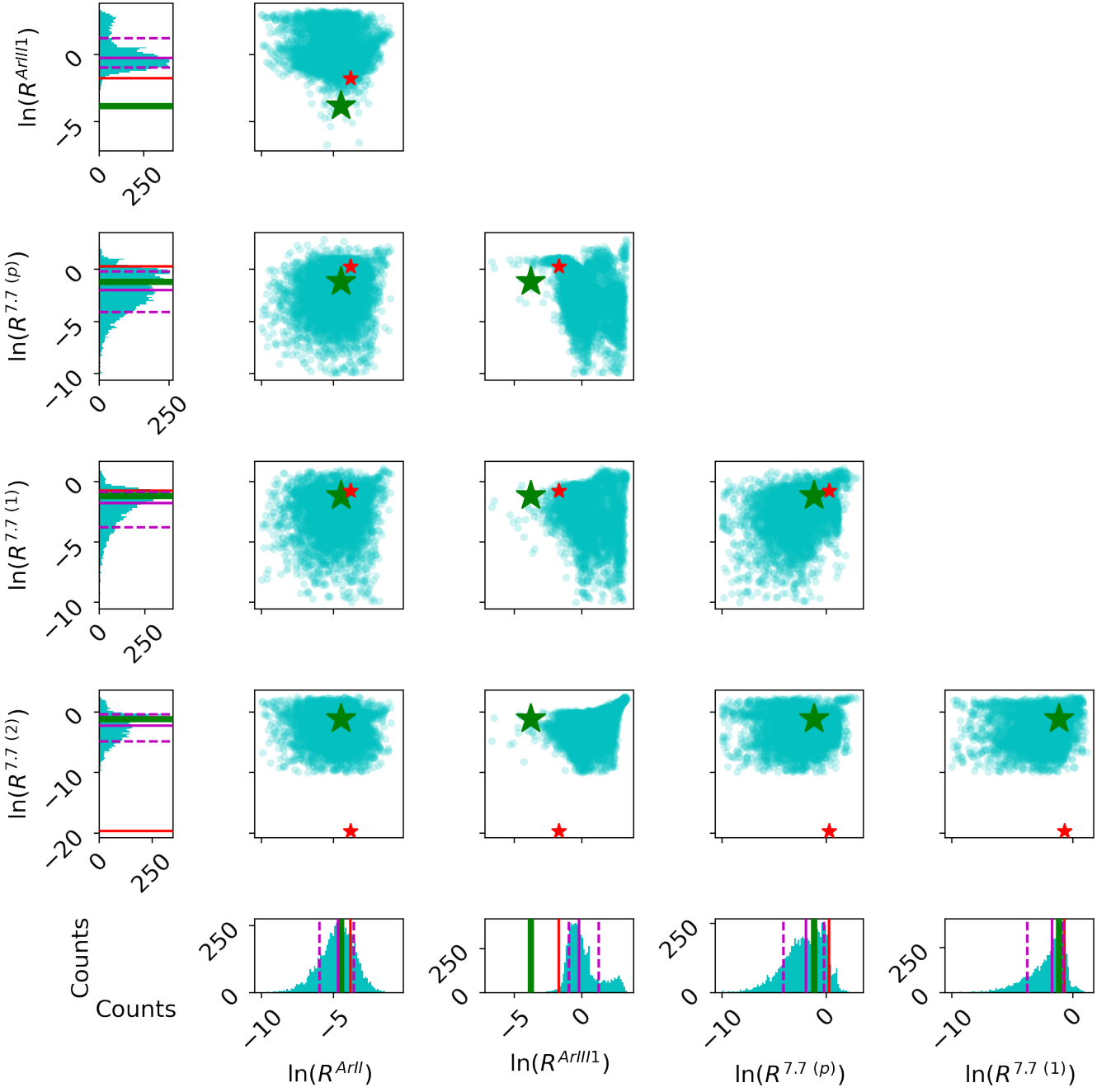


Figure D.6 – Multivariate distributions between emission line and band intensity ratios. With the HB fit of the spectrum “c10 SN10 #1”, we present the multivariate distributions between four line/band relative intensities, $\ln(R^{\text{ArII}})$, $\ln(R^{\text{ArIII}})$, $\ln(R^{7.7(p)})$ and $\ln(R^{7.7(1)})$, with the same plot template as Fig. D.3.

D.1.3 Autocorrelation of parameters

Although we do not sample hyperparameters in the non-HB fit, we can still calculate the means, standard deviations and correlation coefficients of each model parameters. The results (Fig. D.7) permit us to compare the integrated autocorrelation times of these derived quantities with the HB case. It is very evident that τ_{int} in HB fit (Fig. 3.3) is much smaller than in non-HB fit.

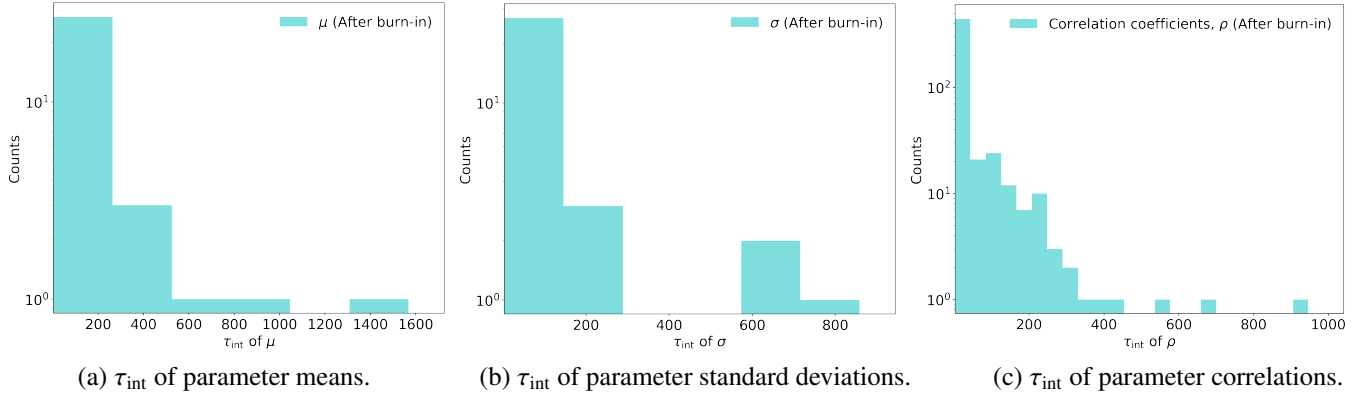


Figure D.7 – Distributions of non-HB integrated autocorrelation times.

Panel (a), (b) and (c) show the distributions of integrated autocorrelation times of the means and standard deviations, and correlation coefficients, in the non-HB cases.

Following Sect. 3.3.2.3, we have checked the ACFs of the correlation coefficient of $\ln(A_V)$ and $\ln(L^*)$ accounting for the entire Markov chain. By comparing Fig. D.8 with Fig. 3.12, we aim to investigate how the burn-in length impacts the autocorrelation. In both chains before and after burn-in, the non-HB fitted $\text{corr}(\ln(A_V), \ln(L^*))$ has not attained our convergence threshold. From Fig. D.8, we can tell $\text{corr}(\ln(A_V), \ln(L^*))$ in the non-HB fit needs a lag of a few hundreds to begin oscillating around 0. In the HB case, τ_{int} is reliably estimated with a value of more than a dex smaller since $\text{corr}(\ln(A_V), \ln(L^*))$ is constrained by a hyperparameter distribution.

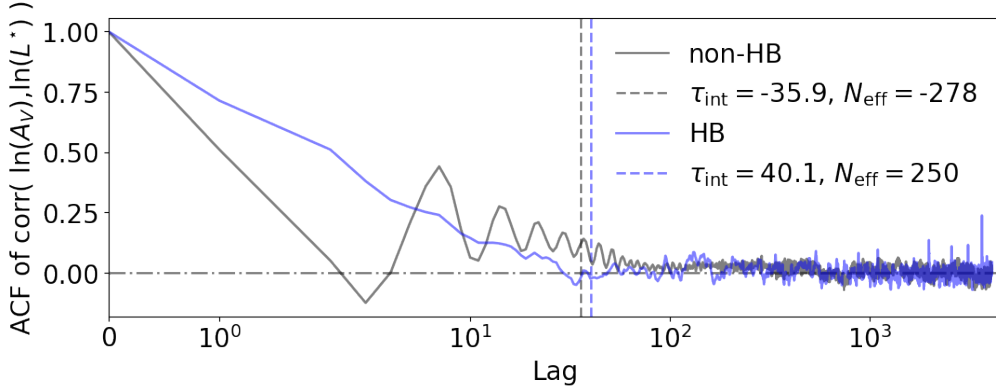


Figure D.8 – ACFs of the correlation coefficients of two parameter (without burn-in). We present the ACFs of $\text{corr}(\ln(A_V), \ln(L^*))$ (black solid: non-HB; blue solid: HB). The non-HB and HB τ_{int} are indicated with black and blue dashed lines, respectively.

In Fig. D.9, we have presented the ACFs of $\text{corr}(\ln(A_V), \ln(L^*))$ with one tenth the steps in the MCMC sampled during a HB fit (*i.e.* the version 3 HB; Sect. 3.2.5.4). Compared to Fig. 3.12, $\tau_{\text{int}} \simeq 100$ is consistent with the value presumed from the version 2 HB result ($\tau_{\text{int}} = 180$).

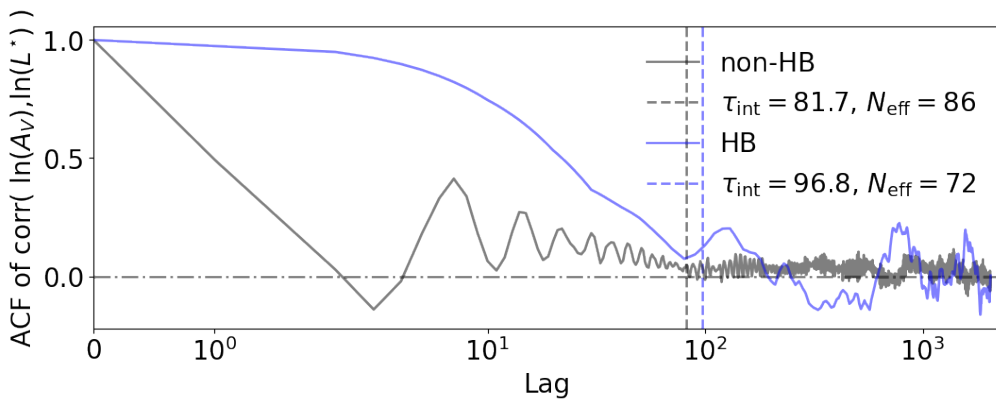
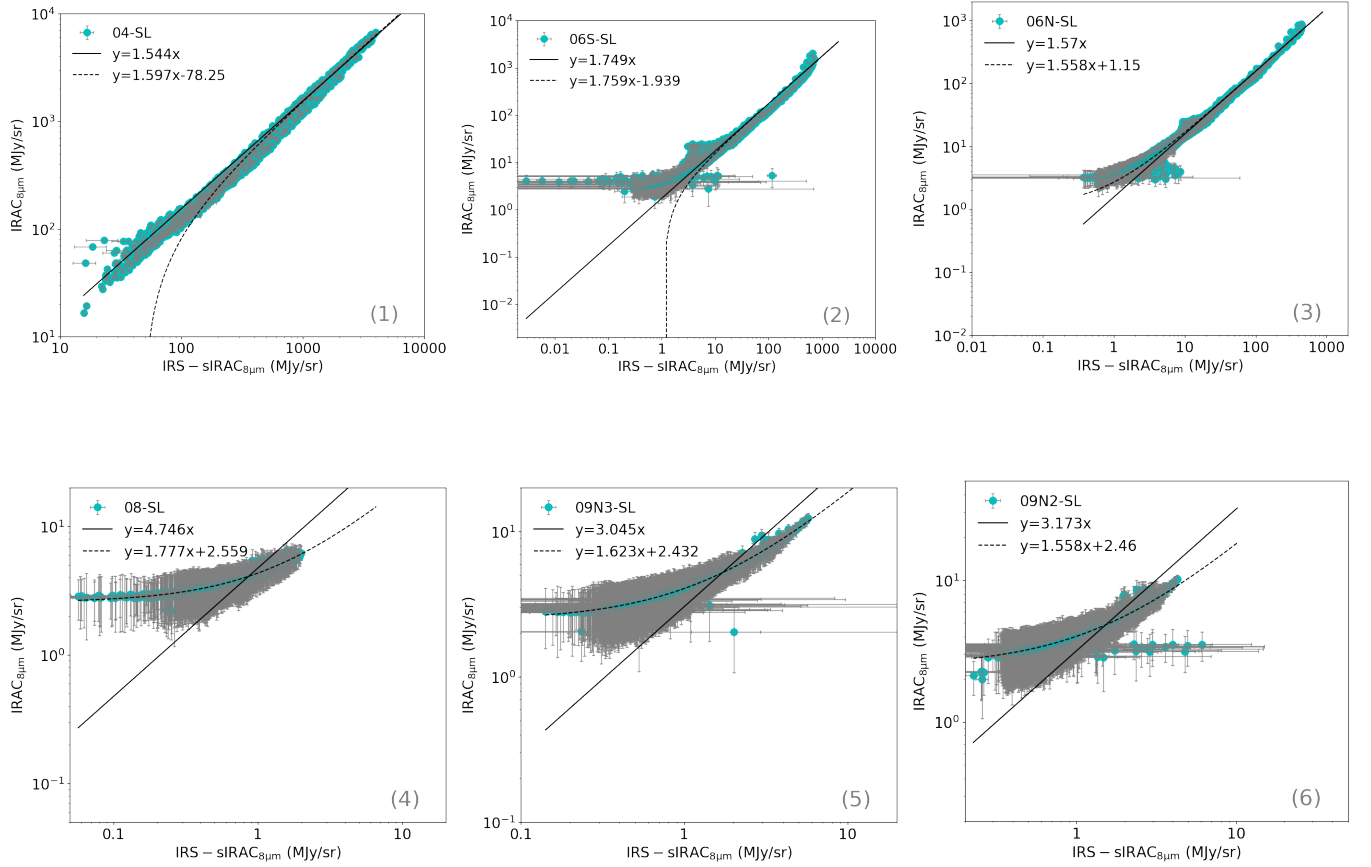


Figure D.9 – ACFs of the correlation coefficients with reduced sampling (after burn-in). We present the ACFs of $\text{corr}(\ln(A_V), \ln(L^*))$ (black solid: non-HB; blue solid: HB). The non-HB and HB τ_{int} are indicated with black and blue dashed lines, respectively.

D.2 M 82 results

D.2.1 Inter-calibration of IRS sub-maps

Following Fig. 2.21. a, we present below the calibration diagrams of the rest of *Spitzer*/IRS sub-maps that are indicated in Fig. 2.19. They are all the “first inter-calibration” results as explained in Sect. 2.4.2.3. Like the 04-LL case in Fig. 2.21. a, the calibration relation of the 05-LL sub-maps (Fig. D.10. 7) presents a small offset of the IRS synthetic photometry caused by the non-subtracted background emission. For the SL sub-maps (Fig. D.10. 1 – 6), on the contrary, it is the $\text{IRAC}_{8\mu\text{m}}$ photometry data that have a residual at the low luminosity end. In general, the LL data are noisier than the SL data, with outliers spreading on both sides of the fitted correlation.



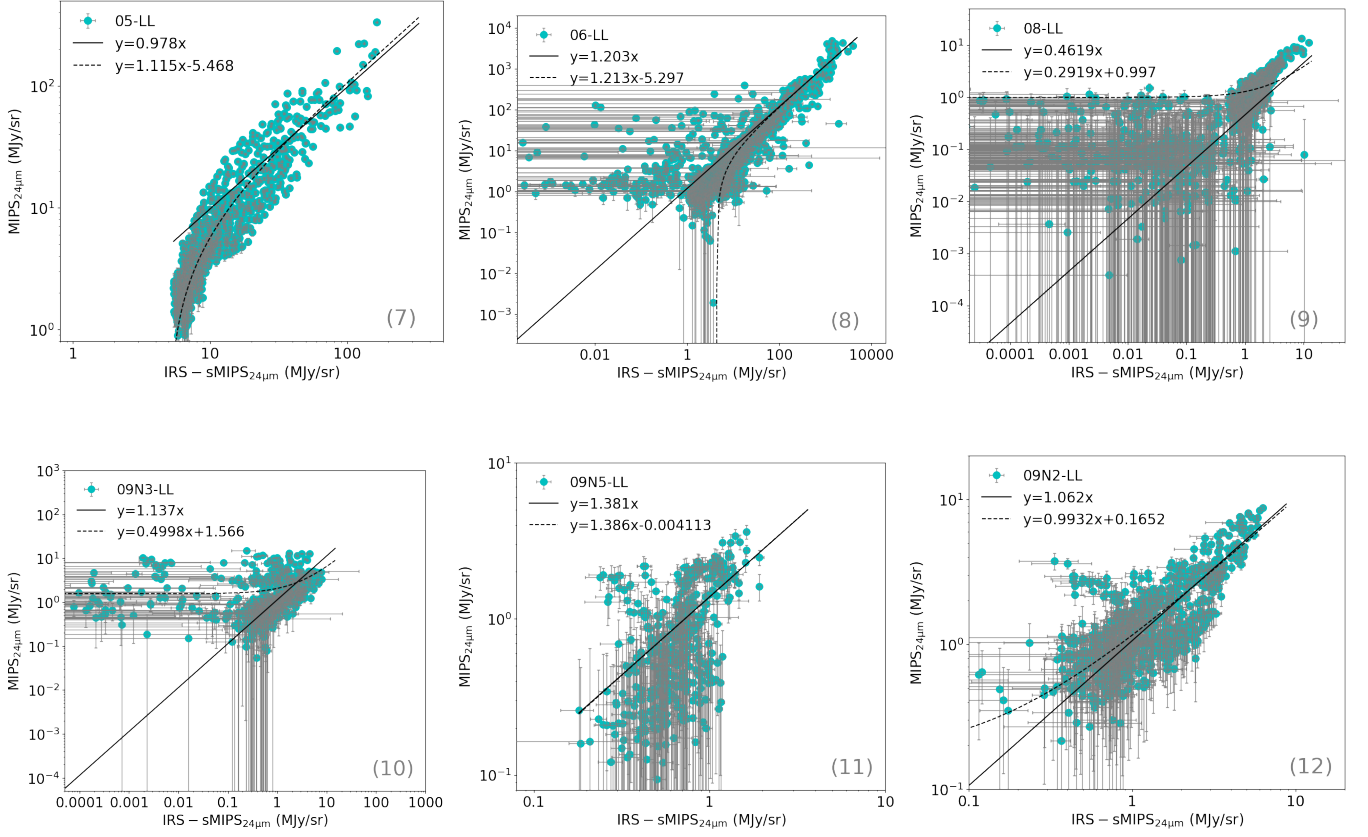


Figure D.10 – Inter-calibration diagrams of *Spitzer*/IRS sub-maps (follow-up of Fig. 2.21).

The synthetic photometry of IRS-SL module is compared with *Spitzer*/IRAC_{8μm} whereas the synthetic photometry of IRS-LL module is compared with *Spitzer*/MIPS_{24μm}. For each panel, we have linearly fitted (with the Levenberg-Marquardt algorithm) the calibration factors both with (dashed) and without (solid) an offset.

D.2.2 Combined spectra

Following Figs. 2.22 – 2.24, we present here the rest of M 82 spectra combined from AKARI/IRC and *Spitzer*/IRS, using our spectroscopy data processing tool, MIRAGE, described in Chap. 2. The LL1 spectra presented in Figs. D.11 – D.13 and Figs. D.15 – D.20 include not only all the spectra ranging from 2.5 to 20 μm that we decomposed with our model, MILES, but also several spectra of LL1 module with relatively good quality. We see that there are no **UIB** features in the LL1 range and the fitting results of MILES are merely affected by including this spectral regime. In addition, we have shown the IRC spectra of the two slits, E and N, not fully covered by the IRS observations. The 3.3 μm feature is clearly detected in slit E, whereas slit N shows no exciting signals. A few IRC spectra (*e.g.* N1-2 in Fig. D.21) are very noisy in the spectral range from ~ 4.3 to 5 μm. We have excluded this regime during the spectral decomposition for the same reason as the treatment of LL1, that is there are neither **UIBs** nor emission lines in the current MILES model (*cf.* Table 3.2 and Table 3.3).

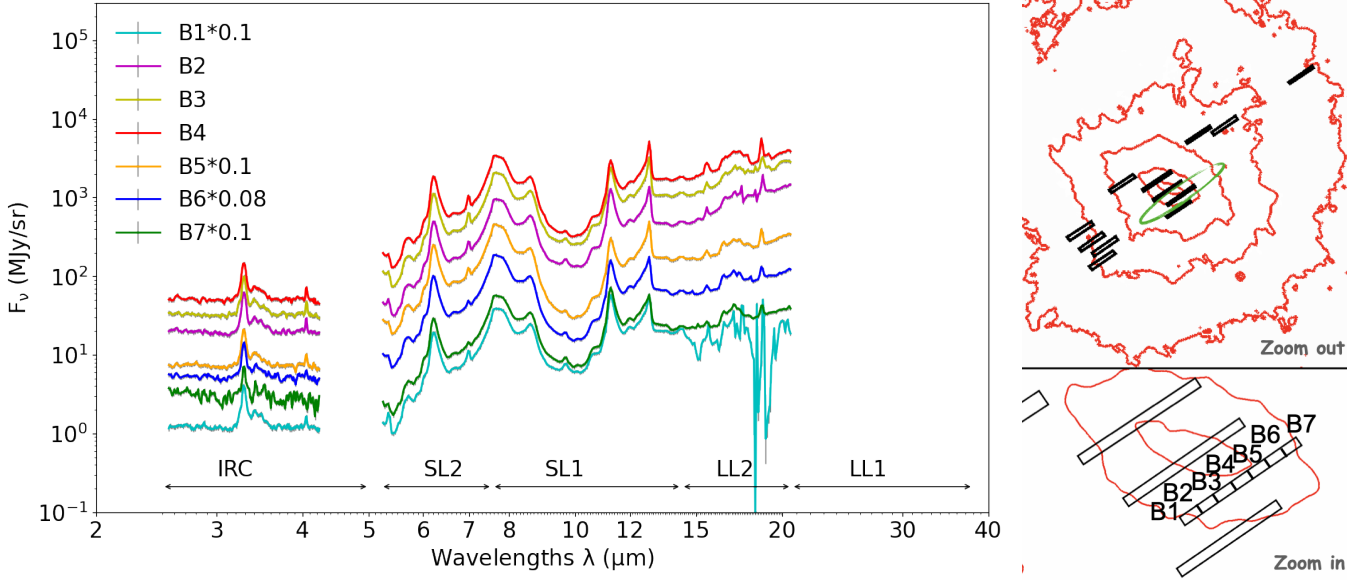


Figure D.11 – Combined spectra of M 82 (slit B; central disk).

The slit position in the sky (green dashed ellipse) is indicated over the $\text{IRAC}_{8\mu\text{m}}$ map (red contours from inside to outside: 30%, 3%, 0.3%, 0.08% and 0.04%). Note that the B1, B5, B6 and B7 spectra have been scaled by a factor of 0.1, 0.1, 0.08 and 0.1, respectively, to avoid overlap.

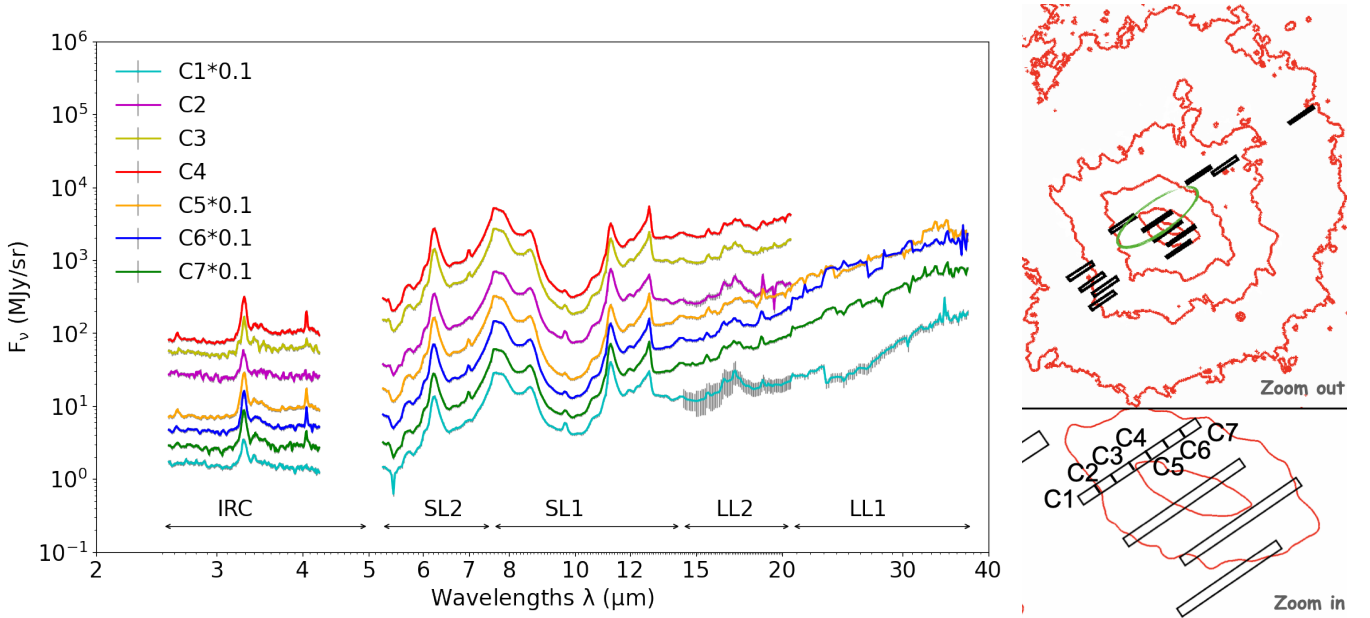


Figure D.12 – Combined spectra of M 82 (slit C; central disk).

The slit position in the sky (green dashed ellipse) is indicated over the $\text{IRAC}_{8\mu\text{m}}$ map (red contours from inside to outside: 30%, 3%, 0.3%, 0.08% and 0.04%). Note that the C1, C5, C6 and C7 spectra have been scaled by a factor of 0.1 to avoid overlap.

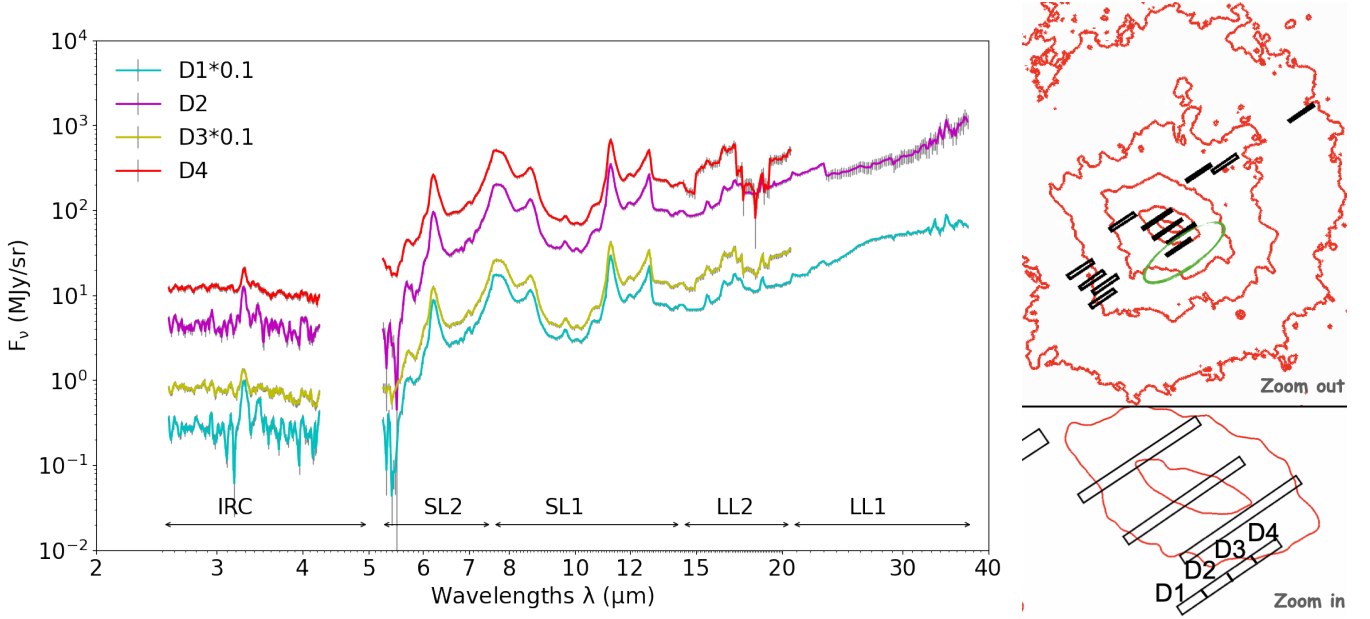


Figure D.13 – Combined spectra of M 82 (slit D; disk edge).

The slit position in the sky (green dashed ellipse) is indicated over the $\text{IRAC}_{8\mu\text{m}}$ map (red contours from inside to outside: 30%, 3%, 0.3%, 0.08% and 0.04%). Note that the D1 and D3 spectra have been scaled by a factor of 0.1 to avoid overlap.

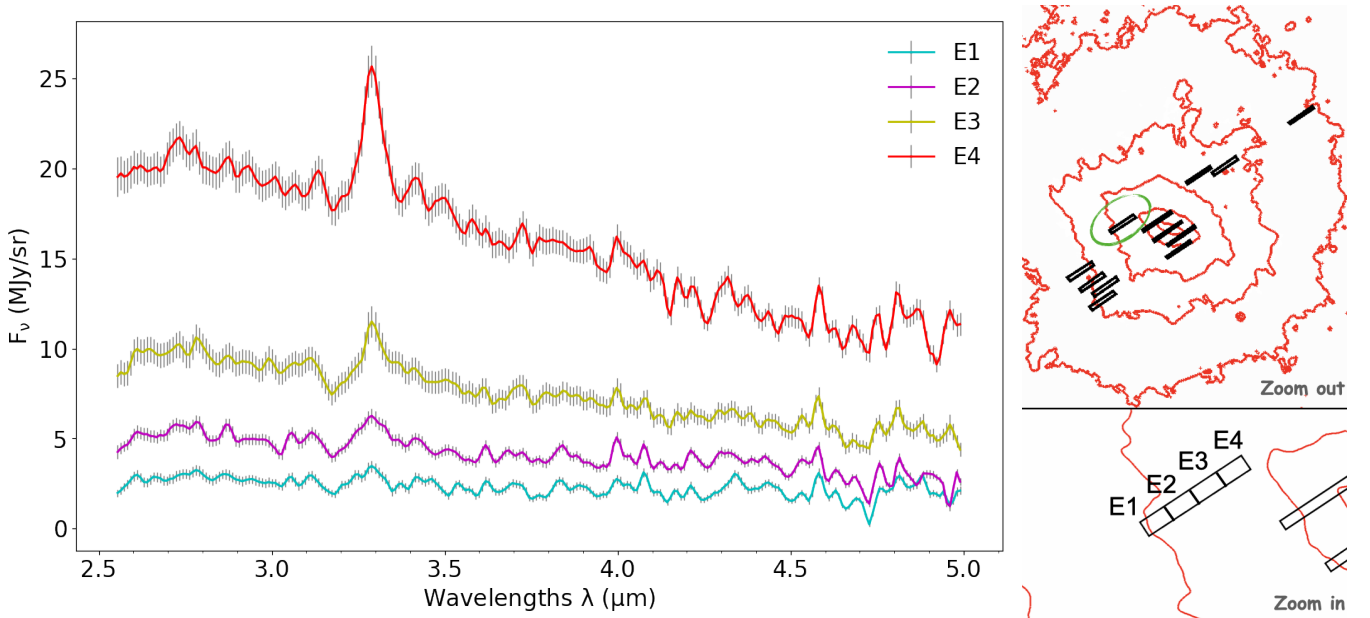


Figure D.14 – IRC spectra of M 82 (slit E; disk edge).

Slit E is not covered by *Spitzer*/IRS, which we only show the AKARI/IRC spectra. The slit position in the sky (green dashed ellipse) is indicated over the $\text{IRAC}_{8\mu\text{m}}$ map (red contours from inside to outside: 30%, 3%, 0.3%, 0.08% and 0.04%).

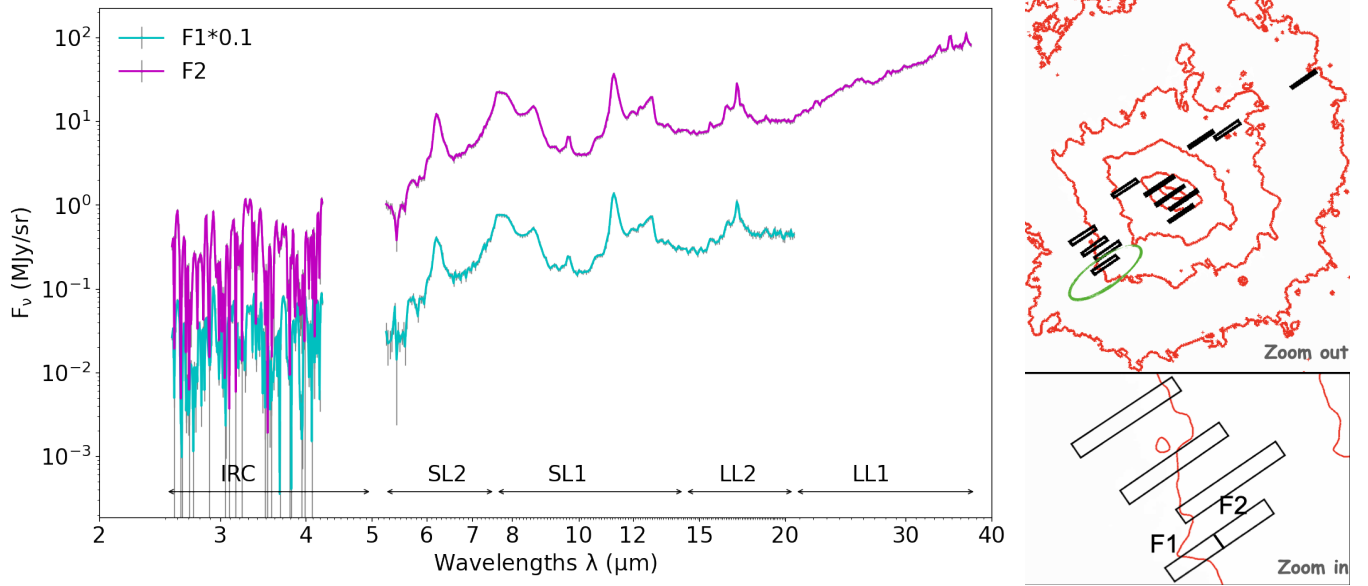


Figure D.15 – Combined spectra of M 82 (slit F; southern wind).

The slit position in the sky (green dashed ellipse) is indicated over the IRAC_{8 μ m} map (red contours from inside to outside: 30%, 3%, 0.3%, 0.08% and 0.04%). Note that the F1 spectrum has been scaled by a factor of 0.1 to avoid overlap.

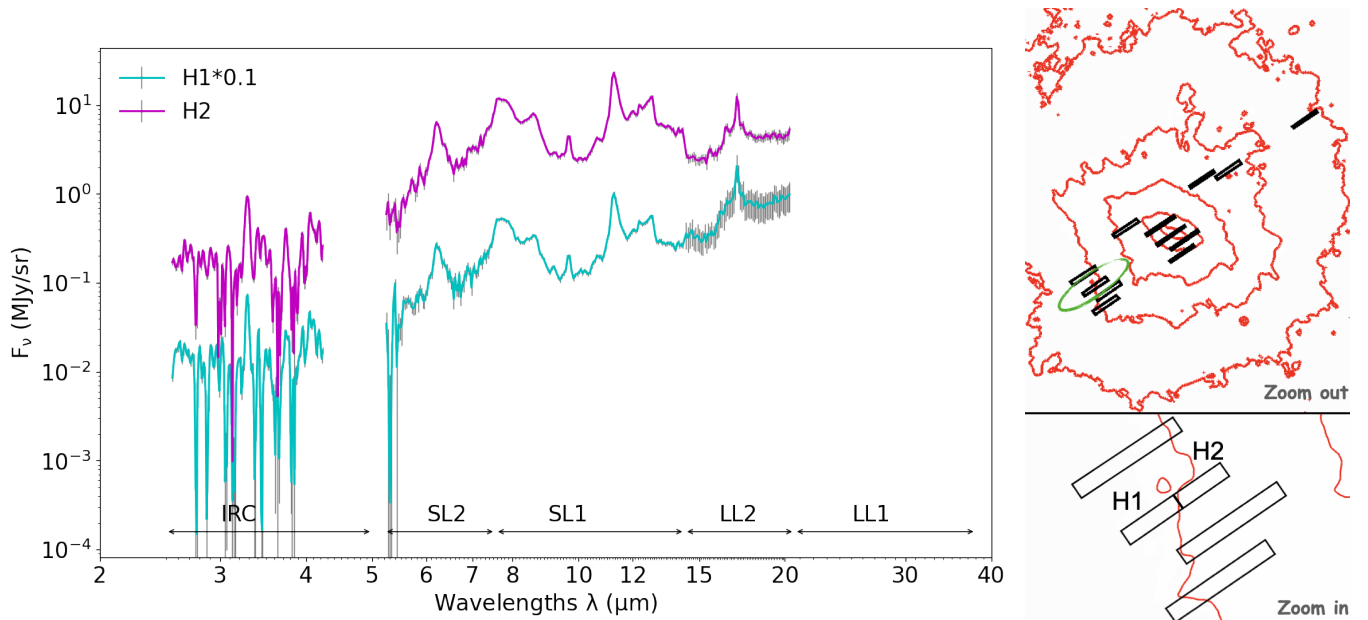


Figure D.16 – Combined spectra of M 82 (slit H; southern wind).

The slit position in the sky (green dashed ellipse) is indicated over the IRAC_{8 μ m} map (red contours from inside to outside: 30%, 3%, 0.3%, 0.08% and 0.04%). Note that the H1 spectrum has been scaled by a factor of 0.1 to avoid overlap.

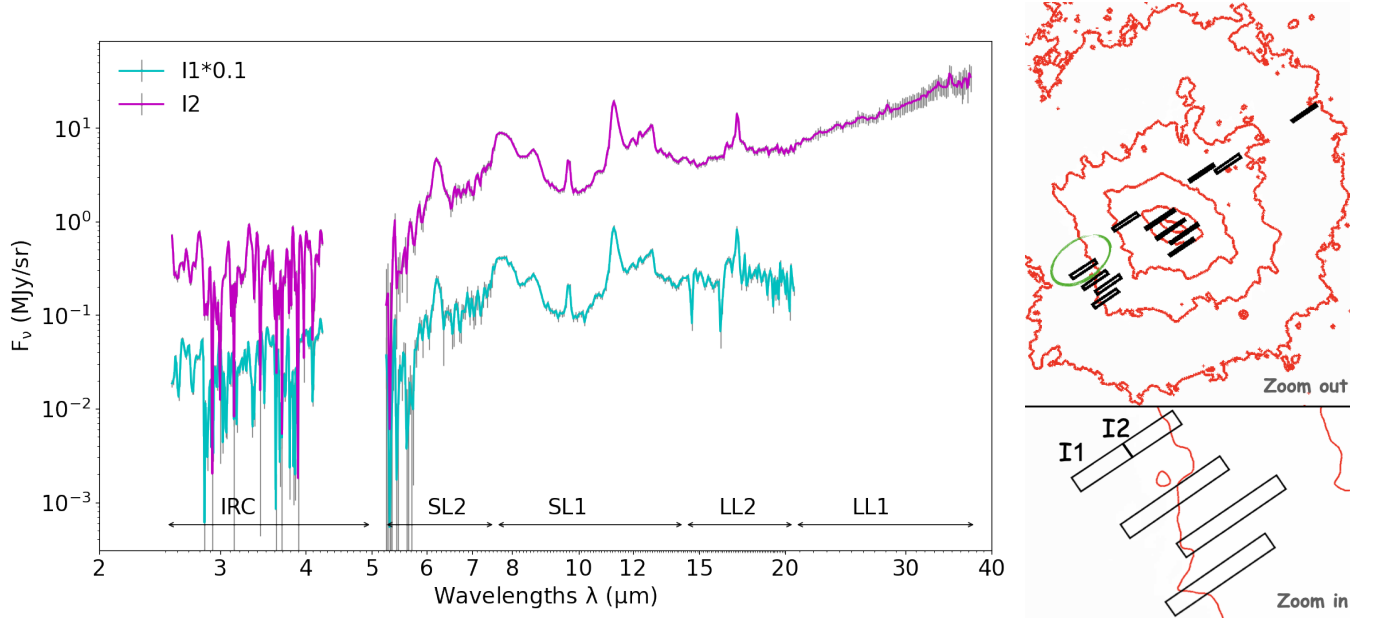


Figure D.17 – Combined spectra of M 82 (slit I; southern wind).

The slit position in the sky (green dashed ellipse) is indicated over the $\text{IRAC}_{8\mu\text{m}}$ map (red contours from inside to outside: 30%, 3%, 0.3%, 0.08% and 0.04%). Note that the I1 spectrum has been scaled by a factor of 0.1 to avoid overlap.

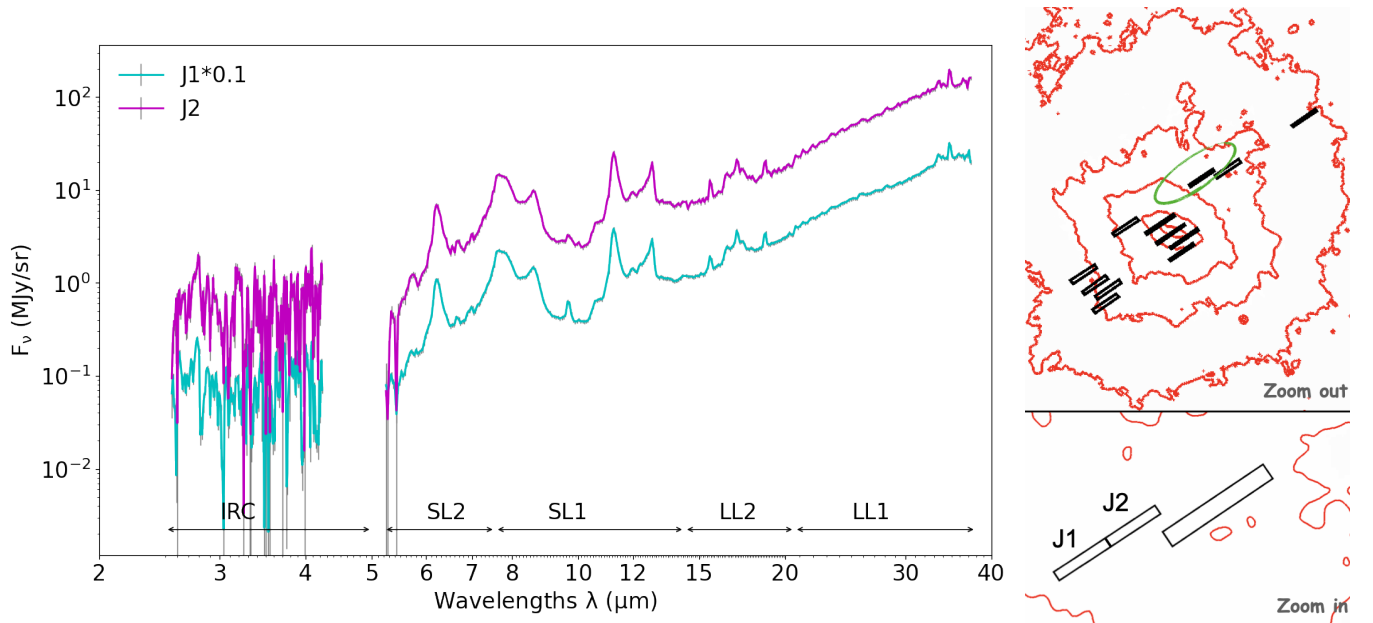


Figure D.18 – Combined spectra of M 82 (slit J; northern wind).

The slit position in the sky (green dashed ellipse) is indicated over the $\text{IRAC}_{8\mu\text{m}}$ map (red contours from inside to outside: 30%, 3%, 0.3%, 0.08% and 0.04%). Note that the J1 spectrum has been scaled by a factor of 0.1 to avoid overlap.

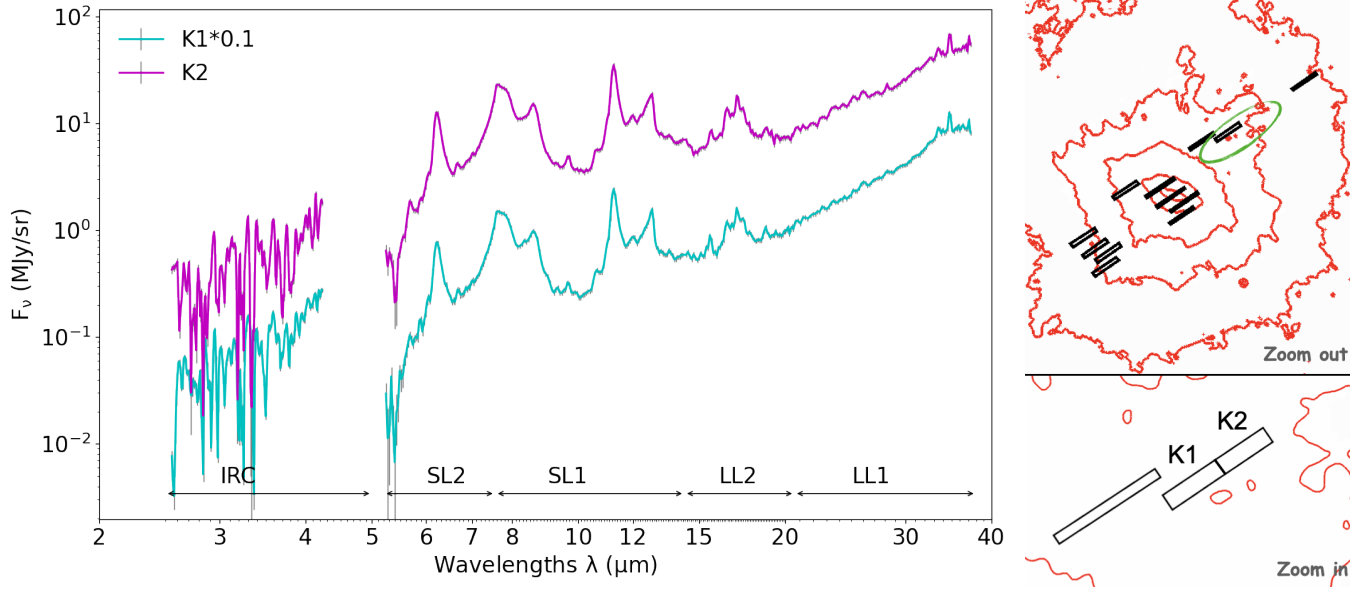


Figure D.19 – Combined spectra of M 82 (slit K; northern wind).

The slit position in the sky (green dashed ellipse) is indicated over the IRAC_{8 μ m} map (red contours from inside to outside: 30%, 3%, 0.3%, 0.08% and 0.04%). Note that the K1 spectrum has been scaled by a factor of 0.1 to avoid overlap.

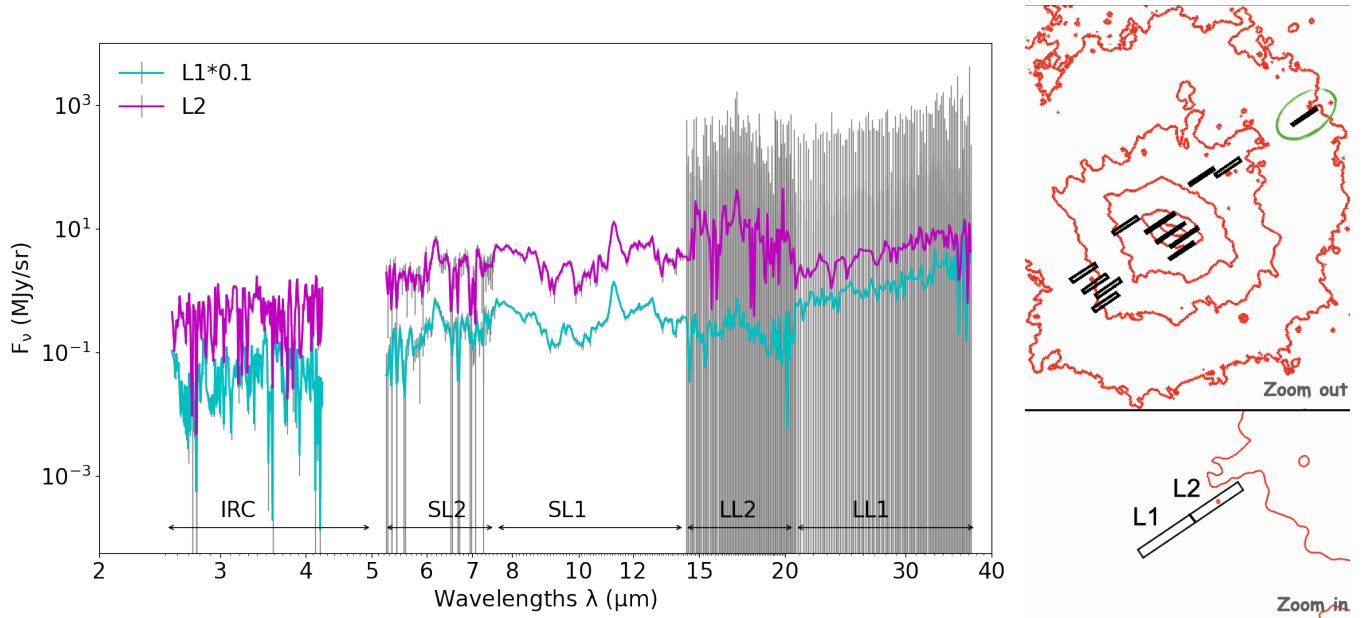


Figure D.20 – Combined spectra of M 82 (slit L; northern outer wind).

The slit position in the sky (green dashed ellipse) is indicated over the IRAC_{8 μ m} map (red contours from inside to outside: 30%, 3%, 0.3%, 0.08% and 0.04%). Note that the L1 spectrum has been scaled by a factor of 0.1 to avoid overlap.

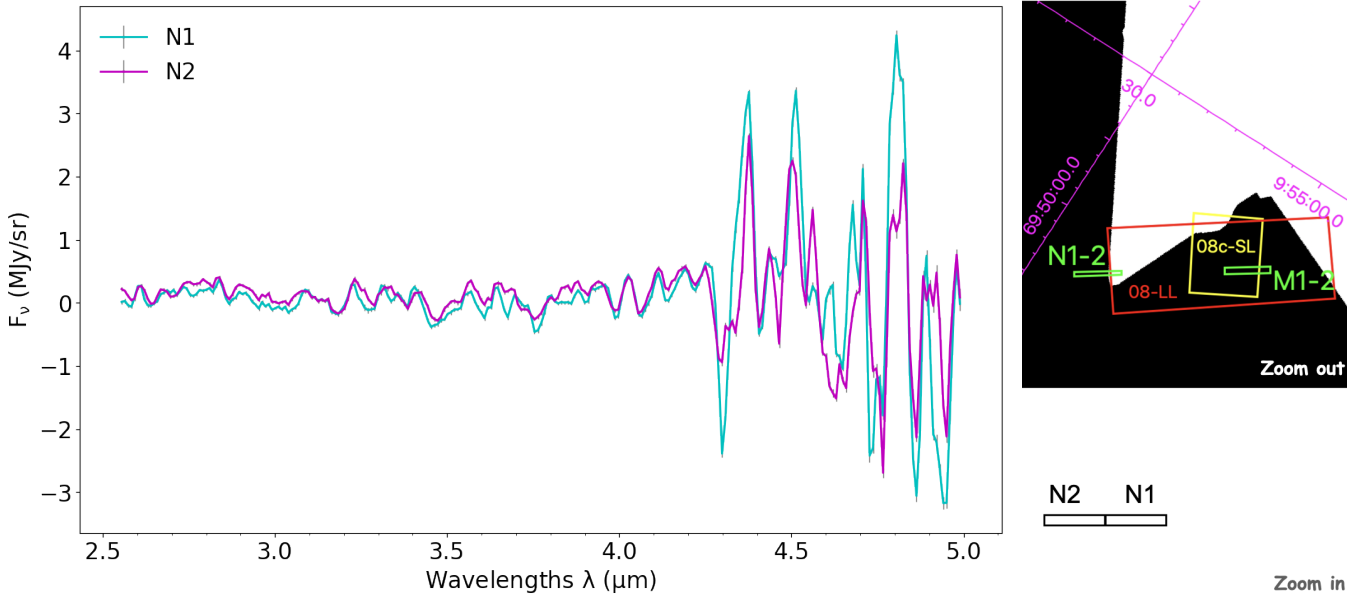


Figure D.21 – IRC spectra of M 82 (slit N; northern wind cap).

Slit N in the northern wind cap of M 82 with extremely low S/N ratios. This slit is not covered by *Spitzer*/IRS, which we only show the AKARI/IRC spectra. It is not covered by the SINGS IRAC_{8μm} map, either, so we put a clip of Fig. 2.19 instead.

D.2.3 Fitted spectra (HB method)

Following Figs. 4.1 – 4.3, we present here the remaining M 82 spectra in Figs. 2.22 – 2.24 and Figs. D.11 – D.20, decomposed by the hierarchical Bayesian (HB) fitter of our MIR spectral fitting software, MILES, described in Chap. 3. We have added a model density diagram (Fig. D.22. 39) for the M1 spectrum, whose fitted components failed to reproduce the original total spectrum (Fig. D.22. 38) due to the multi-modal distribution.

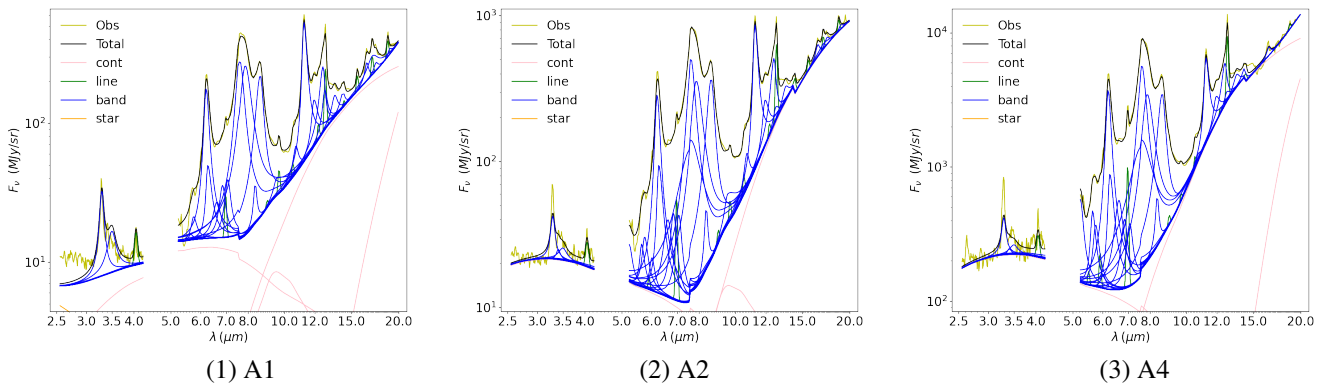
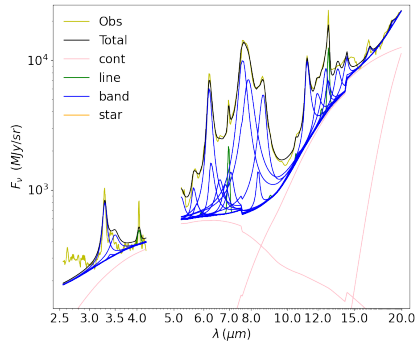
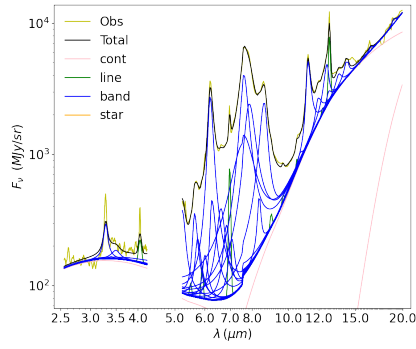


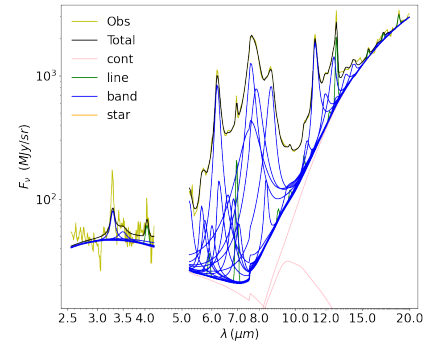
Figure D.22 – HB fits of M 82 spectra.



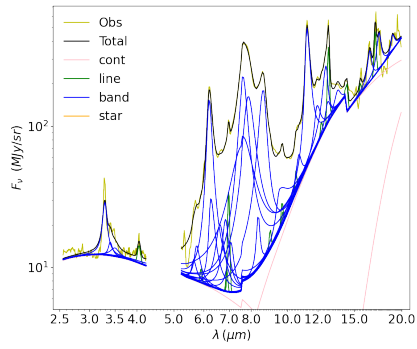
(4) A5



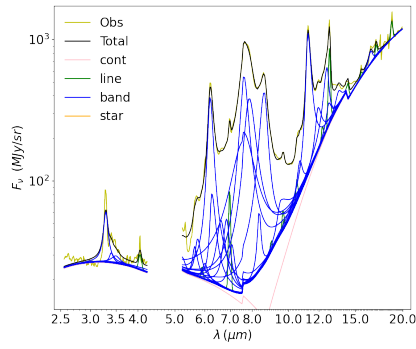
(5) A6



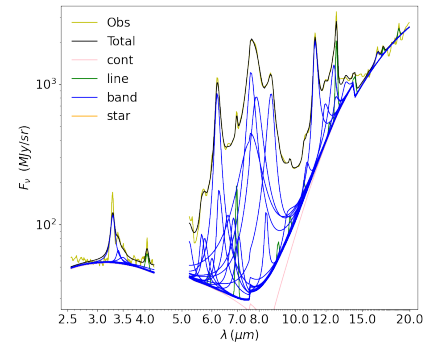
(6) A7



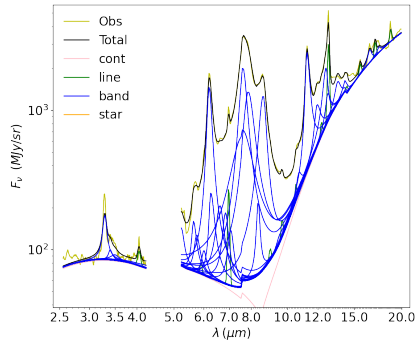
(7) B1



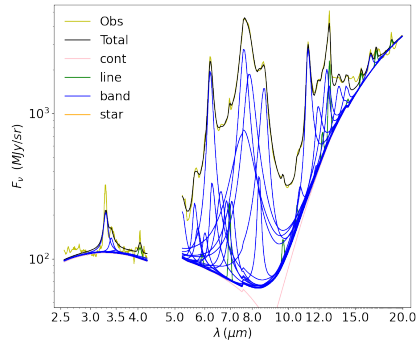
(8) B2



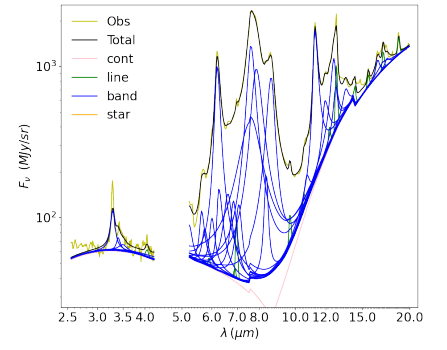
(9) B3



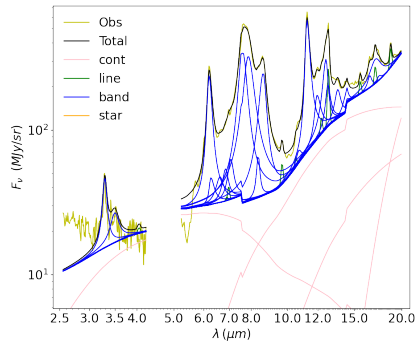
(10) B4



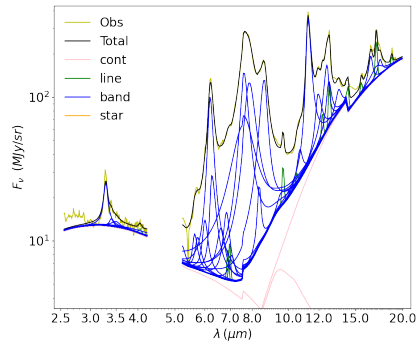
(11) B5



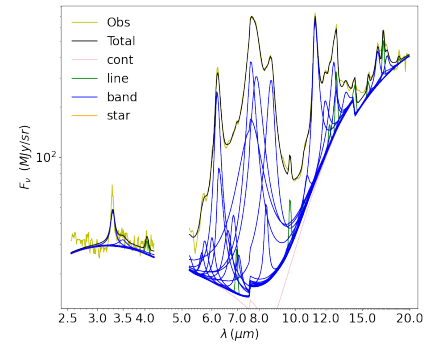
(12) B6



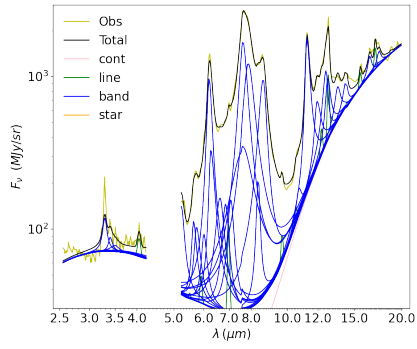
(13) B7



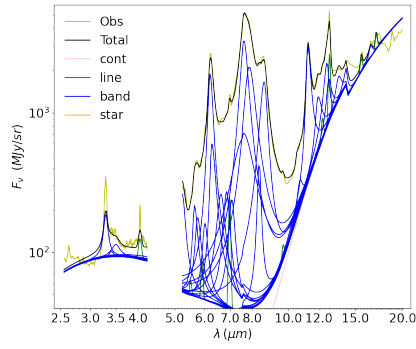
(14) C1



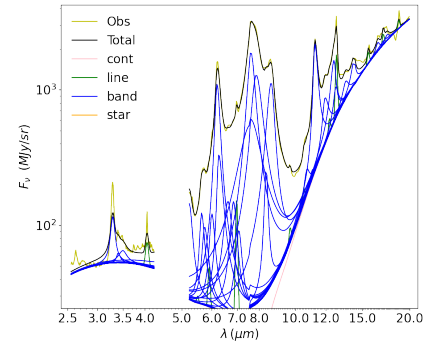
(15) C2



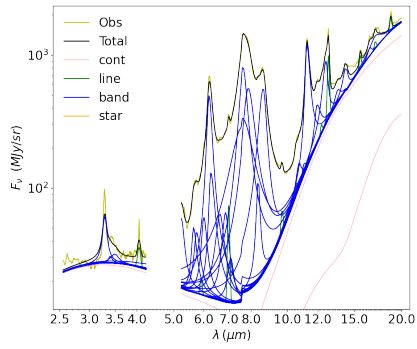
(16) C3



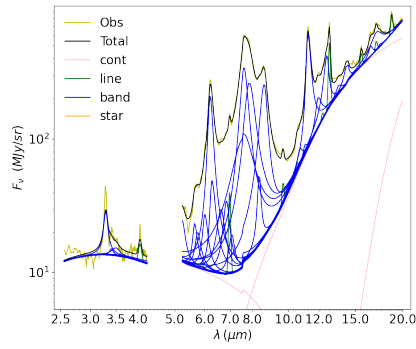
(17) C4



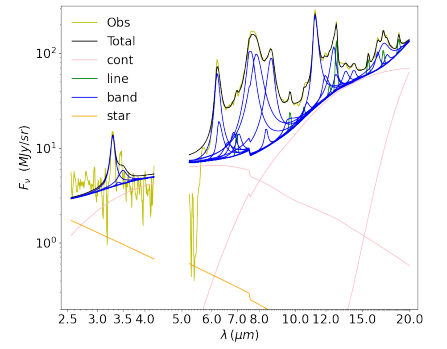
(18) C5



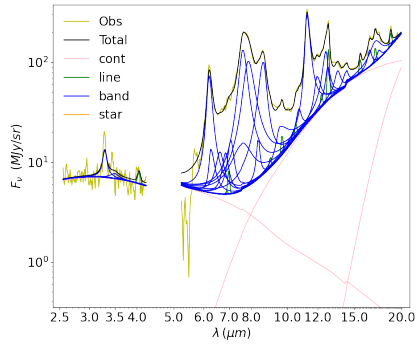
(19) C6



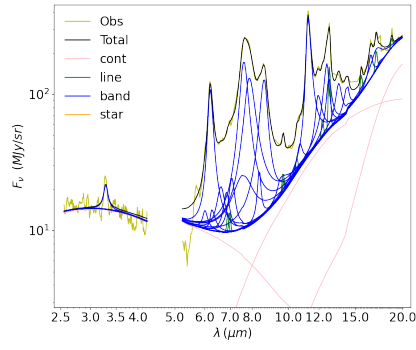
(20) C7



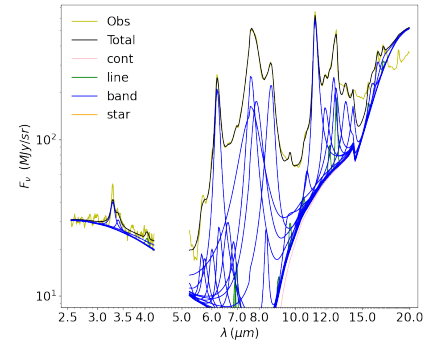
(21) D1



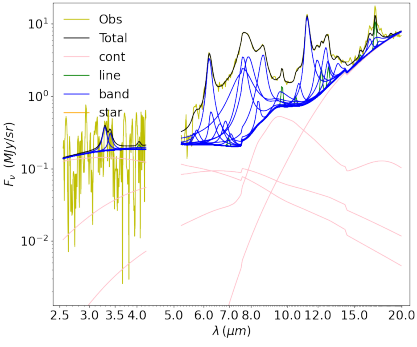
(22) D2



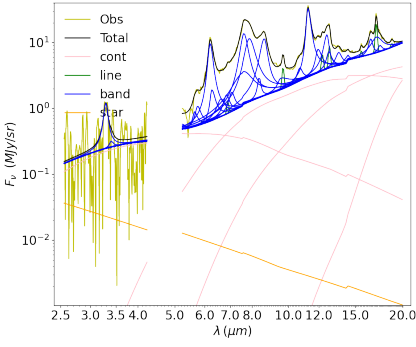
(23) D3



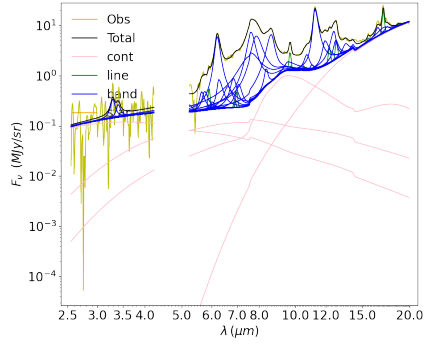
(24) D4



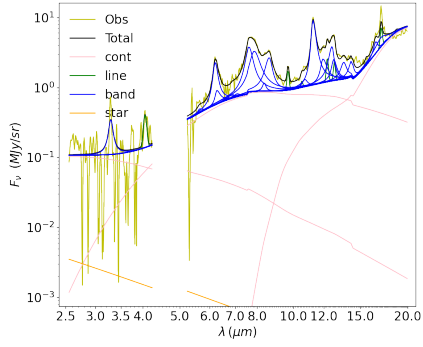
(25) F1



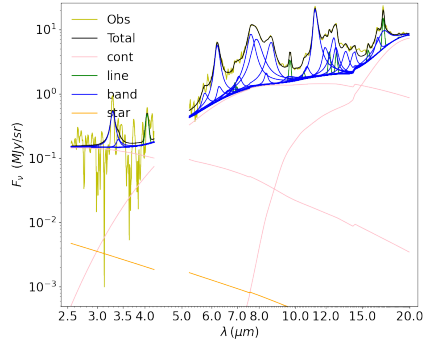
(26) F2



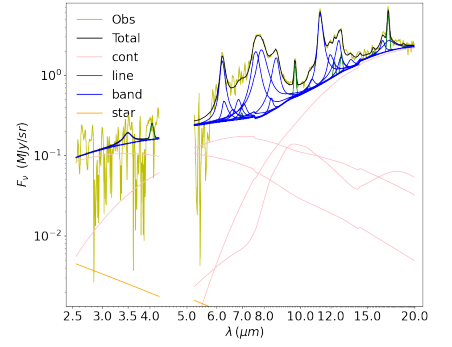
(27) G1



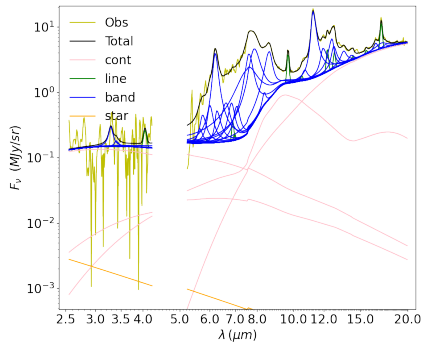
(28) H1



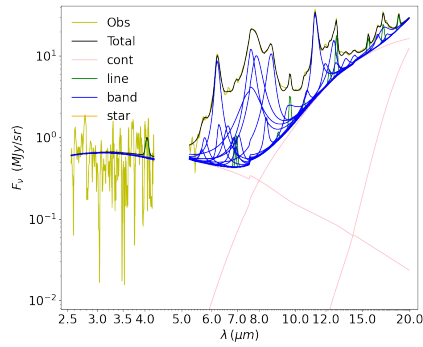
(29) H2



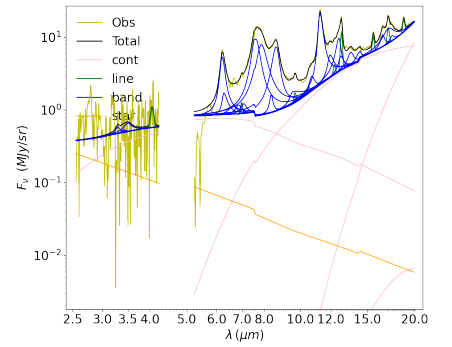
(30) I1



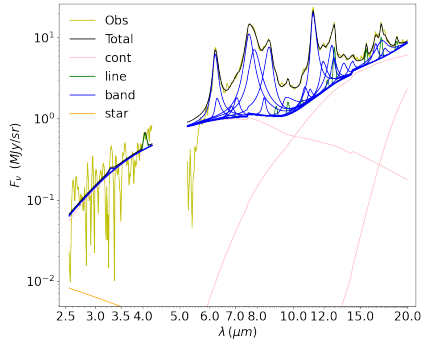
(31) I2



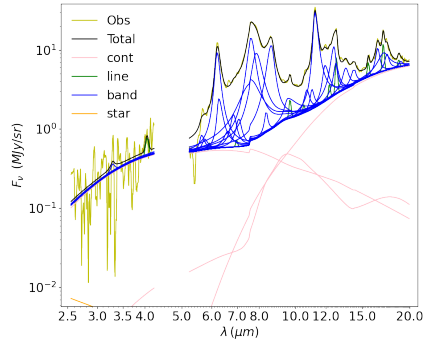
(32) J1



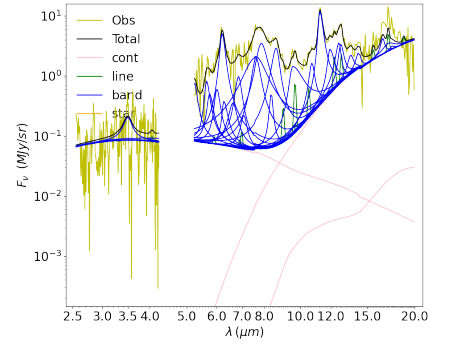
(33) J2



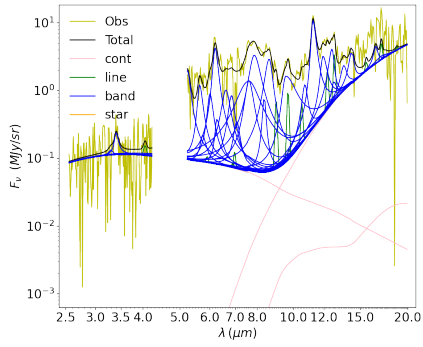
(34) K1



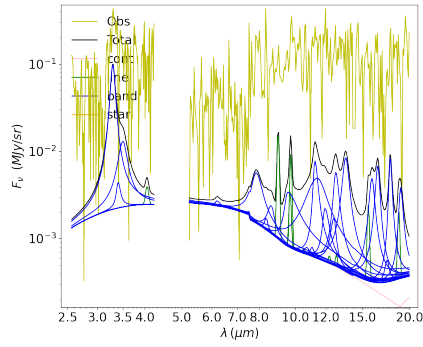
(35) K2



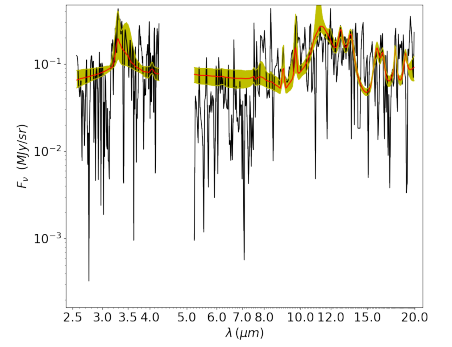
(36) L1



(37) L2



(38) M1



(39) M1 (HB; model density)

D.3 Nearby galaxy sample

Table D.1 – Sample selection with AKARI observations. I.

MAIN TG NAME	REDSHIFT	AKARI ID/SUBID	MAIN OBJ RA	MAIN OBJ DEC	MAIN AOT	MAIN AOTP	DATETIME START	DATETIME END
UGC128	0.015114	5200528.1	3.44625	35.97889	IRCZ4	b ₁ Ns	2009-01-08-14:08:32	2009-01-08-14:38:32
		5200528.2	3.44625	35.97889	IRCZ4	b ₁ Ns	2009-01-08-15:47:24	2009-01-08-16:17:24
		1420351.1	3.67833	-60.32842	IRCZ4	b ₁ Ns	2008-11-18-05:13:59	2008-11-18-05:43:59
		5126752.2	3.67917	-60.32889	IRCZ4	b ₁ Ns	2008-05-18-15:12:47	2008-05-18-15:42:47
NGC53	0.015237	1420334.1	3.72333	-39.19664	IRCZ4	b ₁ Ns	2008-06-04-17:22:29	2008-06-04-17:52:29
		1420334.2	3.72333	-39.19664	IRCZ4	b ₁ Ns	2008-06-05-14:47:34	2008-06-05-15:17:34
		1422151.1	5.07225	59.30378	IRCZ4	b ₁ Ns	2010-01-25-21:34:54	2010-01-25-22:04:54
		1420332.2	5.07225	59.30378	IRCZ4	b ₁ Ns	2008-07-28-22:31:46	2008-07-28-23:01:46
IC10	-0.001161	1422651.2	5.11117	59.29444	IRCZ4	b ₁ Ns	2010-01-26-00:52:37	2010-01-26-01:22:37
		1422651.1	5.11117	59.29444	IRCZ4	b ₁ Ns	2010-01-25-23:13:45	2010-01-25-23:43:45
		1420395.1	9.21962	-33.55531	IRCZ4	b ₁ Ns	2008-06-14-17:54:07	2008-06-14-18:24:07
		1420395.2	9.21962	-33.55531	IRCZ4	b ₁ Ns	2008-06-14-19:32:58	2008-06-14-20:02:58
Haro-1	0.012622	1420056.1	10.092	41.66864	IRCZ4	b ₁ Ns	2009-07-20-02:25:45	2009-07-20-02:55:45
		1420053.1	10.092	41.70197	IRCZ4	b ₁ Ns	2009-07-19-19:50:21	2009-07-19-20:20:21
		1420054.1	10.092	41.68531	IRCZ4	b ₁ Ns	2009-07-19-21:29:12	2009-07-19-21:59:12
		5125002.1	10.24767	41.08585	IRC04	b ₁ Ns	2007-07-20-01:43:03	2007-07-20-02:13:03
NGC205	-0.000804	1420001.1	10.34583	41.18222	IRCZ4	b ₁ Ns	2008-07-18-22:03:55	2008-07-18-22:33:55
		1420002.1	10.3625	41.20667	IRCZ4	b ₁ Ns	2009-01-17-04:07:06	2009-01-17-04:37:06
		1422222.1	10.50417	41.07333	IRCZ4	b ₁ Ns	2010-01-17-00:57:27	2010-01-17-01:27:27
		1422222.2	10.50417	41.07333	IRCZ4	b ₁ Ns	2010-01-17-02:36:18	2010-01-17-03:06:18
M31	-0.001001	1422222.3	10.50417	41.07333	IRCZ4	b ₁ Ns	2010-01-17-04:15:10	2010-01-17-04:45:10
		1420044.1	10.50417	41.07333	IRCZ4	b ₁ Ns	2009-07-20-04:04:46	2009-07-20-04:34:46
		1420028.1	10.60417	41.25833	IRCZ4	b ₁ Ns	2008-07-19-11:14:44	2008-07-19-11:44:44
		1420023.1	10.60417	41.26667	IRCZ4	b ₁ Ns	2009-07-19-23:38:12	2009-07-19-23:38:12
NGC221	-0.000667	1420018.1	10.60417	41.275	IRCZ4	b ₁ Ns	2008-07-19-14:32:26	2008-07-19-15:02:26
		1420042.1	10.64167	40.96583	IRCZ4	b ₁ Ns	2009-01-18-11:25:26	2009-01-18-11:55:26
		1420022.1	10.66667	41.26667	IRCZ4	b ₁ Ns	2008-07-19-16:11:18	2008-07-19-16:41:18
		1420027.1	10.66667	41.25833	IRCZ4	b ₁ Ns	2009-07-20-00:47:03	2009-07-20-01:17:03
M31	-0.001001	1420017.1	10.66667	41.275	IRCZ4	b ₁ Ns	2009-01-18-09:46:39	2009-01-18-10:16:39
		5200824.1	10.67413	40.86561	IRCZ4	b ₁ Nh	2009-07-19-11:36:22	2009-07-19-12:06:22
		5200824.2	10.67413	40.86561	IRCZ4	b ₁ Nh	2009-07-19-14:54:03	2009-07-19-15:24:03
		5124407.1	10.68467	41.26904	IRCZ4	b ₁ Nh	2008-01-18-16:42:51	2008-01-18-17:12:51
NGC221	-0.000667	5124409.2	10.68467	41.26904	IRCZ4	b ₁ Ns	2008-01-19-04:14:56	2008-01-19-04:44:56
		5125003.1	10.68467	41.26904	IRC04	b ₁ Ns	2007-07-21-02:35:13	2007-07-21-03:05:13
		5124406.1	10.68467	41.26904	IRCZ4	b ₁ Ns	2008-01-18-15:03:59	2008-01-18-15:33:59
		5124410.1	10.68467	41.26904	IRCZ4	b ₁ Nh	2008-01-19-14:08:09	2008-01-19-14:38:09
M31	-0.001001	1420047.1	10.6875	41.14222	IRCZ4	b ₁ Ns	2008-07-19-12:53:38	2008-07-19-13:23:38
		1420007.1	10.69583	41.56528	IRCZ4	b ₁ Ns	2008-07-19-19:28:56	2008-07-19-19:58:56
		1420041.1	10.72083	41.0375	IRCZ4	b ₁ Ns	2008-07-19-03:00:32	2008-07-19-03:30:32
		1420016.1	10.72917	41.275	IRCZ4	b ₁ Ns	2008-07-19-22:46:43	2008-07-19-23:16:43
NGC221	-0.000667	1420021.1	10.72917	41.26667	IRCZ4	b ₁ Ns	2009-01-18-08:07:46	2009-01-18-08:37:46
		1420026.1	10.72917	41.25833	IRCZ4	b ₁ Ns	2008-07-19-21:07:52	2008-07-19-21:37:52
		1420008.1	10.75833	41.44194	IRCZ4	b ₁ Ns	2009-01-17-23:53:30	2009-01-18-00:23:30
		1420052.1	10.8	41.42111	IRCZ4	b ₁ Ns	2009-07-21-03:08:35	2009-07-21-03:38:35
NGC221	-0.000667	1422228.1	10.8	41.42111	IRCZ4	b ₁ Ns	2010-01-17-09:11:48	2010-01-17-09:41:48
		1422228.2	10.8	41.42111	IRCZ4	b ₁ Ns	2010-01-17-10:50:39	2010-01-17-11:20:39
		1420048.1	10.80833	41.31139	IRCZ4	b ₁ Ns	2009-01-18-04:50:03	2009-01-18-05:20:03

Table D.2 – Sample selection with AKARI observations. II.

	1420039.1	10.84167	41.11333	IRCZ4	b _i Ns	2009-01-18-06:28:52	2009-01-18-06:58:52
	1420049.1	10.8625	41.38694	IRCZ4	b _i Ns	2009-07-21-01:29:45	2009-07-21-01:59:45
	1420038.1	10.89167	41.16306	IRCZ4	b _i Ns	2008-07-20-15:15:17	2008-07-20-15:45:17
	1420036.1	10.9875	41.24722	IRCZ4	b _i Ns	2009-01-18-03:11:09	2009-01-18-03:41:09
	1420035.1	11.01667	41.28778	IRCZ4	b _i Ns	2008-07-20-13:36:25	2008-07-20-14:06:25
	5125004.1	11.17608	41.70634	IRC04	b _i Ns	2007-07-22-01:47:49	2007-07-22-02:17:49
NGC253	1422187.2	11.88792	-25.28833	IRCZ4	b _i Ns	2009-12-21-11:01:58	2009-12-21-11:31:58
	1422187.1	11.88792	-25.28833	IRCZ4	b _i Ns	2009-12-21-06:05:23	2009-12-21-06:35:23
	1422196.1	11.88792	-25.29028	IRCZ4	b _i Ns	2009-12-21-01:08:48	2009-12-21-01:38:48
	1422196.2	11.88792	-25.29028	IRCZ4	b _i Ns	2009-12-21-02:47:39	2009-12-21-03:17:39
	3390006.1	11.88833	-25.28808	IRCZ4	b _i Nh	2009-06-20-22:32:41	2009-06-20-23:02:41
	1422197.1	11.88875	-25.28556	IRCZ4	b _i Ns	2009-12-21-14:19:41	2009-12-21-14:49:41
	1422190.2	11.88917	-25.25947	IRCZ4	b _i Ns	2009-12-22-13:23:44	2009-12-22-13:53:44
	1422190.1	11.88917	-25.25947	IRCZ4	b _i Ns	2009-12-22-01:51:43	2009-12-22-02:21:43
NGC315	5200826.2	14.45371	30.35278	IRCZ4	b _i Ns	2009-07-18-14:14:18	2009-07-18-14:44:18
	5200826.1	14.45371	30.35278	IRCZ4	b _i Ns	2009-07-18-12:35:27	2009-07-18-13:05:27
	1422229.1	14.45375	30.3525	IRCZ4	b _i Ns	2010-01-15-01:07:32	2010-01-15-01:37:32
	1422229.2	14.45375	30.3525	IRCZ4	b _i Ns	2010-01-15-02:46:23	2010-01-15-03:16:23
IC1623	5200015.1	16.94821	-17.50678	IRCZ4	b _i Nh	2008-06-29-20:18:26	2008-06-29-20:48:26
	5200015.2	16.94821	-17.50678	IRCZ4	b _i Nh	2008-06-30-21:01:13	2008-06-30-21:31:13
NGC404	5200827.1	17.36229	35.718	IRCZ4	b _i Ns	2009-07-22-13:46:25	2009-07-22-14:16:25
	5200827.2	17.36229	35.718	IRCZ4	b _i Ns	2009-07-22-15:25:16	2009-07-22-15:55:16
ESO_244-G012	5200013.1	19.53463	-44.46206	IRCZ4	b _i Nh	2008-06-14-21:15:31	2008-06-14-21:45:31
	5200013.2	19.53463	-44.46206	IRCZ4	b _i Nh	2008-06-14-22:54:22	2008-06-14-23:24:22
NGC514	5200470.1	21.01625	12.91639	IRCZ4	b _i Ns	2009-01-13-12:39:11	2009-01-13-13:09:11
	5200470.2	21.01625	12.91639	IRCZ4	b _i Ns	2009-01-14-13:22:09	2009-01-14-13:52:09
Mink-obj	1422147.3	21.43417	-1.37931	IRCZ4	b _i Ns	2010-01-10-00:42:02	2010-01-10-01:12:02
	1422147.2	21.43417	-1.37931	IRCZ4	b _i Ns	2010-01-09-11:31:10	2010-01-09-12:01:10
	1422147.1	21.43417	-1.37931	IRCZ4	b _i Ns	2010-01-09-01:38:00	2010-01-09-02:08:00
	1420396.1	21.43433	-1.37931	IRCZ4	b _i Ns	2008-07-10-13:15:45	2008-07-10-13:45:45
	1420396.2	21.43433	-1.37931	IRCZ4	b _i Ns	2008-07-10-14:54:36	2008-07-10-15:24:36
NGC584	1420482.2	22.83579	-6.86775	IRCZ4	b _i Ns	2008-07-10-03:24:11	2008-07-10-03:54:11
	1420482.1	22.83579	-6.86775	IRCZ4	b _i Ns	2008-07-10-01:45:20	2008-07-10-02:15:20
NGC612	1420097.1	23.49058	-36.49325	IRCZ4	b _i Ns	2008-12-25-00:28:55	2008-12-25-00:58:55
	1420096.1	23.49058	-36.49325	IRCZ4	b _i Ns	2008-06-26-19:54:20	2008-06-26-20:24:20
	5200014.1	24.09746	-37.32169	IRCZ4	b _i Nh	2008-06-26-21:33:27	2008-06-26-22:03:27
	5200014.2	24.09746	-37.32169	IRCZ4	b _i Nh	2008-06-26-23:12:18	2008-06-26-23:42:18
NGC772	5200830.1	29.83138	19.00797	IRCZ4	b _i Ns	2009-07-26-13:24:59	2009-07-26-13:54:59
	5200830.2	29.83138	19.00797	IRCZ4	b _i Ns	2009-07-27-12:28:52	2009-07-27-12:58:52
	5200471.2	29.83458	19.00611	IRCZ4	b _i Ns	2009-01-23-16:31:44	2009-01-23-17:01:44
	5200472.2	30.06292	31.43111	IRCZ4	b _i Ns	2009-01-28-15:13:03	2009-01-28-15:43:03
NGC777	5200472.1	30.06292	31.43111	IRCZ4	b _i Ns	2009-01-28-13:34:11	2009-01-28-14:04:11
	3221004.1	31.85518	2.11656	IRC04	b _i Ns	2007-07-24-00:25:22	2007-07-24-00:55:22
HCG-15	1420388.1	32.35292	-10.13625	IRCZ4	b _i Ns	2008-07-17-23:15:09	2008-07-17-23:45:09
NGC835	1420132.1	35.61958	42.3166	IRCZ4	b _i Nh	2008-08-10-04:24:18	2008-08-10-04:54:18
NGC891	1420134.1	35.63154	42.33701	IRCZ4	b _i Nh	2009-08-10-00:56:31	2009-08-10-01:26:31
	1420136.1	35.64346	42.35742	IRCZ4	b _i Nh	2009-08-10-02:35:22	2009-08-10-03:05:22
	1420138.1	35.65542	42.37783	IRCZ4	b _i Nh	2009-08-10-04:14:13	2009-08-10-04:44:13
NGC959	5200065.1	38.1	35.49472	IRCZ4	b _i Ns	2008-08-08-15:41:27	2008-08-08-16:11:27
	5200065.2	38.1	35.49472	IRCZ4	b _i Ns	2008-08-09-16:24:16	2008-08-09-16:54:16
NGC1023	5200066.2	40.1	39.06328	IRCZ4	b _i Ns	2008-08-11-17:49:07	2008-08-11-18:19:07

Table D.3 – Sample selection with AKARI observations. III.

NGC1052	0.005037	5200066.1	40.1	39.06328	IRC74	b _i Ns	2008-08-11-16:10:16	2008-08-11-16:40:16
NGC1068	0.003793	1402108.1	40.27	-8.25578	IRC04	b _i Ns	2007-07-27-22:59:26	2007-07-27-23:29:26
NGC1058	0.001728	5125030.1	40.66962	-0.01336	IRC04	b _i Ns	2007-08-01-02:26:37	2007-08-01-02:56:37
NGC1097	0.00424	5200067.1	40.87458	37.34083	IRC74	b _i Ns	2008-08-12-15:14:44	2008-08-12-15:44:44
		1420462.1	41.579	-30.27464	IRC74	b _i Ns	2008-07-18-01:00:01	2008-07-18-01:30:01
NGC1140	0.005007	1420462.2	41.579	-30.27464	IRC74	b _i Ns	2008-07-18-02:38:52	2008-07-18-03:08:52
		1422155.2	43.63975	-10.02783	IRC74	b _i Ns	2010-01-27-04:32:22	2010-01-27-05:02:22
		1422155.3	43.63975	-10.02783	IRC74	b _i Ns	2010-01-27-06:11:13	2010-01-27-06:41:13
		1422155.1	43.63975	-10.02783	IRC74	b _i Ns	2010-01-27-02:53:30	2010-01-27-03:23:30
		5126463.2	43.64	-10.02775	IRC74	b _i Ns	2008-01-28-15:22:39	2008-01-28-15:52:39
		5126463.1	43.64	-10.02775	IRC74	b _i Ns	2008-01-28-13:43:47	2008-01-28-14:13:47
NGC1291	0.002799	1420457.1	49.32787	-41.10825	IRC74	b _i Ns	2008-07-19-00:07:21	2008-07-19-00:37:21
		1420457.2	49.32787	-41.10825	IRC74	b _i Ns	2008-07-19-01:46:12	2008-07-19-02:16:12
NGC1313	0.001568	1420354.2	49.52	-66.50694	IRC74	b _i Ns	2008-06-04-02:43:03	2008-06-04-03:13:03
		1420354.1	49.52	-66.50694	IRC74	b _i Ns	2008-06-01-17:03:12	2008-06-01-17:33:12
		1420353.1	49.56708	-66.49825	IRC74	b _i Ns	2008-12-03-10:56:26	2008-12-03-11:26:26
		1420355.2	49.59833	-66.47722	IRC74	b _i Ns	2008-06-02-16:07:09	2008-06-02-16:37:09
		1420355.1	49.59833	-66.47722	IRC74	b _i Ns	2008-06-02-14:28:18	2008-06-02-14:58:18
NGC1316	0.005871	1422246.2	50.66833	-37.20139	IRC74	b _i Ns	2010-01-22-02:29:17	2010-01-22-02:59:17
		1422246.3	50.66833	-37.20139	IRC74	b _i Ns	2010-01-22-04:08:09	2010-01-22-04:38:09
		1422246.1	50.66833	-37.20139	IRC74	b _i Ns	2010-01-22-00:50:26	2010-01-22-01:20:26
		1400125.1	50.67379	-37.20822	IRC04	b _i Ns	2007-01-23-00:44:48	2007-01-23-01:14:48
		1420439.2	50.67383	-37.20822	IRC74	b _i Ns	2008-07-24-03:40:30	2008-07-24-04:10:30
		1420439.1	50.67383	-37.20822	IRC74	b _i Ns	2008-07-24-02:01:39	2008-07-24-02:31:39
		1422245.2	50.67917	-37.21528	IRC74	b _i Ns	2010-01-22-10:43:33	2010-01-22-11:13:33
		1422245.1	50.67917	-37.21528	IRC74	b _i Ns	2010-01-22-05:47:00	2010-01-22-06:17:00
		1422245.3	50.67917	-37.21528	IRC74	b _i Ns	2010-01-22-12:22:24	2010-01-22-12:52:24
NGC1546	0.004284	1400997.1	63.65225	-56.06081	IRC04	b _i Ns	2007-01-18-08:06:29	2007-01-18-08:36:29
NGC1549	0.00419	1400019.1	63.93804	-55.59225	IRC04	b _i Ns	2007-01-18-14:43:45	2007-01-18-15:13:45
NGC1566	0.005017	1420467.1	65.00233	-54.93789	IRC74	b _i Ns	2008-07-21-19:45:03	2008-07-21-20:15:03
		1420467.2	65.00233	-54.93789	IRC74	b _i Ns	2008-07-21-21:23:54	2008-07-21-21:53:54
NGC1569	-0.000347	5125050.1	67.66637	64.84597	IRC64	b _i Ns	2007-09-10-05:46:52	2007-09-10-06:16:52
		5125051.1	67.69558	64.85017	IRC64	b _i Ns	2007-09-10-04:07:21	2007-09-10-04:37:21
		5126479.1	67.69558	64.85017	IRC74	b _i Nh	2008-03-07-15:36:51	2008-03-07-16:06:51
		1420331.2	67.70458	64.84794	IRC74	b _i Ns	2008-09-09-03:49:53	2008-09-09-04:19:53
		1420331.1	67.70458	64.84794	IRC74	b _i Ns	2008-09-08-21:14:27	2008-09-08-21:44:27
NGC1614	0.015938	5126478.1	67.70458	64.84794	IRC74	b _i Nh	2008-03-07-17:15:43	2008-03-07-17:45:43
		5126478.2	67.70458	64.84794	IRC74	b _i Nh	2008-03-07-18:54:35	2008-03-07-19:24:35
		5200049.2	68.49938	-8.57889	IRC74	b _i Nh	2008-08-27-16:17:56	2008-08-27-16:47:56
		5200049.1	68.49938	-8.57889	IRC74	b _i Nh	2008-08-27-14:39:04	2008-08-27-15:09:04
		1420398.2	68.50075	-8.57894	IRC74	b _i Ns	2008-08-28-00:32:13	2008-08-28-01:02:13
		1420398.1	68.50075	-8.57894	IRC74	b _i Ns	2008-08-27-22:53:21	2008-08-27-23:23:21
Mrk1089	0.013406	1420323.2	75.40733	-4.25789	IRC74	b _i Ns	2008-09-06-11:53:28	2008-09-06-12:23:28
		1420323.1	75.40733	-4.25789	IRC74	b _i Ns	2008-09-05-19:24:54	2008-09-05-19:54:54
NGC1808	0.003319	1420357.1	76.92646	-37.51303	IRC74	b _i Ns	2008-09-01-00:14:03	2008-09-01-00:44:03
		1420357.2	76.92646	-37.51303	IRC74	b _i Ns	2008-09-01-01:52:54	2008-09-01-02:22:54
		1402544.1	76.9325	-37.52314	IRC04	b _i Ns	2007-09-01-18:13:59	2007-09-01-18:43:59
		1402545.1	76.94042	-37.53022	IRC04	b _i Ns	2007-09-01-19:53:30	2007-09-01-20:23:30
NGC1961	0.013122	5200185.2	85.51833	69.37944	IRC74	b _i Ns	2008-09-19-14:15:14	2008-09-19-14:45:14
		5200185.1	85.51833	69.37944	IRC74	b _i Ns	2008-09-19-10:57:31	2008-09-19-11:27:31
IIZw40	0.002632	1420299.1	88.92758	3.39219	IRC74	b _i Ns	2009-03-19-04:39:06	2009-03-19-05:09:06

Table D.4 – Sample selection with AKARI observations. IV.

NGC2146	1420399.1	88.92758	3.39219	IRCZ4	b _i Ns	2009-09-20-22:08:32	2009-09-20-22:38:32
	1420399.2	88.92758	3.39219	IRCZ4	b _i Ns	2009-09-20-23:47:23	2009-09-21-00:17:23
	1420400.1	94.65454	78.3565	IRCZ4	b _i Ns	2008-09-22-21:17:59	2008-09-22-21:47:59
	1420400.2	94.65454	78.3565	IRCZ4	b _i Ns	2008-09-22-22:56:51	2008-09-22-23:26:51
	1420387.2	100.77542	-74.22639	IRCZ4	b _i Ns	2008-08-26-15:53:49	2008-08-26-16:23:49
	1420387.1	100.77542	-74.22639	IRCZ4	b _i Ns	2008-08-26-12:36:06	2008-08-26-13:06:06
	1420436.1	114.203	65.59503	IRCZ4	b _i Ns	2008-10-05-17:27:51	2008-10-05-17:57:51
	1420436.2	114.203	65.59503	IRCZ4	b _i Ns	2008-10-05-19:06:43	2008-10-05-19:36:43
	1420358.2	114.2125	65.60256	IRCZ4	b _i Ns	2008-10-05-15:48:59	2008-10-05-16:18:59
	1420358.1	114.2125	65.60256	IRCZ4	b _i Ns	2008-10-05-05:55:50	2008-10-05-06:25:50
ESO034-IG11	1420360.1	114.22617	65.59656	IRCZ4	b _i Ns	2008-10-05-07:34:41	2008-10-05-08:04:41
	1420360.2	114.22617	65.59656	IRCZ4	b _i Ns	2008-10-05-10:52:25	2008-10-05-11:22:25
	5126731.1	114.22875	65.59842	IRCZ4	b _i Ns	2008-04-03-05:16:21	2008-04-03-05:46:21
	5126731.2	114.22875	65.59842	IRCZ4	b _i Ns	2008-04-03-10:12:56	2008-04-03-10:42:56
	5125425.1	114.22875	65.59842	IRC64	b _i Ns	2007-10-07-06:20:23	2007-10-07-06:50:23
	1420359.1	114.27858	65.61114	IRCZ4	b _i Ns	2008-10-05-12:31:16	2008-10-05-13:01:16
	1420359.2	114.27858	65.61114	IRCZ4	b _i Ns	2008-10-05-14:10:07	2008-10-05-14:40:07
	5126730.2	114.32375	65.56289	IRCZ4	b _i Ns	2008-04-03-03:37:29	2008-04-03-04:07:29
	5125424.1	114.32375	65.56289	IRC64	b _i Ns	2007-10-07-07:59:55	2007-10-07-08:29:55
	5126730.1	114.32375	65.56289	IRCZ4	b _i Ns	2008-04-03-01:58:37	2008-04-03-02:28:37
NGC2500	5200304.2	120.47333	50.73806	IRCZ4	b _i Ns	2008-10-15-01:36:38	2008-10-15-02:06:38
	5200304.1	120.47333	50.73806	IRCZ4	b _i Ns	2008-10-14-23:57:46	2008-10-15-00:27:46
	5126732.2	124.8025	70.71881	IRCZ4	b _i Ns	2008-04-06-14:02:04	2008-04-06-14:32:04
	5126732.1	124.8025	70.71881	IRCZ4	b _i Ns	2008-04-06-07:26:38	2008-04-06-07:56:38
	1420361.1	124.80338	70.71903	IRCZ4	b _i Ns	2008-10-08-22:52:38	2008-10-08-23:22:38
	1420361.2	124.80338	70.71903	IRCZ4	b _i Ns	2008-10-09-05:28:04	2008-10-09-05:58:04
	1420362.1	124.81692	70.71625	IRCZ4	b _i Ns	2008-10-09-10:24:39	2008-10-09-10:54:39
	5126733.1	124.87125	70.71678	IRCZ4	b _i Ns	2008-04-06-09:05:30	2008-04-06-09:35:30
	5126733.2	124.87125	70.71678	IRCZ4	b _i Ns	2008-04-06-10:44:22	2008-04-06-11:14:22
	1422149.1	126.5185	45.96786	IRCZ4	b _i Ns	2009-10-21-11:06:18	2009-10-21-11:36:18
UGC4393 He2-010	1420363.1	129.0625	-26.40944	IRCZ4	b _i Ns	2008-11-11-17:58:05	2008-11-11-18:28:05
	1422158.1	129.0625	-26.40944	IRCZ4	b _i Ns	2009-11-13-19:36:50	2009-11-13-20:06:50
	5126734.1	129.0625	-26.40944	IRCZ4	b _i Ns	2008-05-11-04:00:23	2008-05-11-04:30:23
	5126734.2	129.0625	-26.40944	IRCZ4	b _i Ns	2008-05-11-05:39:15	2008-05-11-06:09:15
	1420424.1	134.61125	6.326	IRCZ4	b _i Ns	2009-05-05-15:09:11	2009-05-05-15:39:11
	1401002.1	137.90625	60.03722	IRC04	b _i Ns	2007-04-19-20:07:28	2007-04-19-20:37:28
	1422243.1	137.90625	60.03722	IRCZ4	b _i Ns	2009-10-22-10:06:02	2009-10-22-10:36:02
	1420364.2	138.52071	40.11361	IRCZ4	b _i Ns	2009-04-28-11:57:53	2009-04-28-12:27:53
	1420364.1	138.52071	40.11361	IRCZ4	b _i Ns	2009-04-28-10:19:02	2009-04-28-10:49:02
	1420124.1	140.5	50.9875	IRCZ4	b _i Ns	2009-04-26-17:10:41	2009-04-26-17:40:41
UGC4703 NGC2768	1420122.1	140.51096	50.97652	IRCZ4	b _i Ns	2008-10-29-18:11:54	2008-10-29-18:41:54
	1420123.1	140.525	50.9625	IRCZ4	b _i Ns	2009-04-26-10:35:16	2009-04-26-11:05:16
	1420128.1	146.79167	67.91639	IRCZ4	b _i Ns	2008-10-21-20:38:13	2008-10-21-21:08:13
	5126741.1	146.81442	67.91639	IRCZ4	b _i Nh	2008-04-19-05:12:11	2008-04-19-05:42:11
	1420126.1	146.81442	67.91639	IRCZ4	b _i Ns	2008-10-23-13:49:46	2008-10-23-14:19:46
	5126741.2	146.81442	67.91639	IRCZ4	b _i Nh	2008-04-19-10:08:45	2008-04-19-10:38:45
	1420127.1	146.83333	67.91639	IRCZ4	b _i Ns	2008-10-23-12:10:54	2008-10-23-12:40:54
	5124077.1	148.77291	69.84111	IRC04	b _i Ns	2007-04-18-17:40:17	2007-04-18-18:10:17
	5125990.1	148.77291	69.84111	IRCZ4	b _i Ns	2008-04-17-18:36:45	2008-04-17-19:06:45
	5125990.2	148.77291	69.84111	IRCZ4	b _i Ns	2008-04-17-23:33:19	2008-04-18-00:03:19
NGC2976	5125996.1	148.84021	69.86977	IRCZ4	b _i Ns	2008-04-18-14:23:02	2008-04-18-14:53:02
M82							

Table D.5 – Sample selection with AKARI observations. V.

5126498.2	148.90417	69.70556	IRCZ4	b;Nh	2008-04-19-23:20:08	2008-04-19-23:50:08
5126498.1	148.90417	69.70556	IRCZ4	b;Nh	2008-04-18-16:01:51	2008-04-18-16:31:51
5125403.1	148.90417	69.70556	IRC64	b;Ns	2007-10-22-21:10:50	2007-10-22-21:40:50
3390003.1	148.95583	69.67797	IRCZ4	b;Nh	2008-10-22-03:13:08	2008-10-22-03:43:08
3390001.1	148.96775	69.68022	IRCZ4	b;Nh	2008-10-21-23:55:25	2008-10-22-00:25:25
3390001.2	148.96775	69.68022	IRCZ4	b;Nh	2008-10-22-01:34:17	2008-10-22-02:04:17
3390002.2	148.97917	69.68247	IRCZ4	b;Nh	2009-04-19-04:02:05	2009-04-19-04:32:05
3390002.1	148.97917	69.68247	IRCZ4	b;Nh	2008-10-23-02:17:12	2008-10-23-02:47:12
5125401.1	149.0165	69.68714	IRC64	b;Ns	2007-10-23-05:28:27	2007-10-23-05:58:27
5126496.1	149.0165	69.68714	IRCZ4	b;Nh	2008-04-18-17:40:42	2008-04-18-18:10:42
5126496.2	149.0165	69.68714	IRCZ4	b;Nh	2008-04-19-01:55:00	2008-04-19-02:25:00
5126499.2	149.025	69.65669	IRCZ4	b;Nh	2008-04-18-20:58:25	2008-04-18-21:28:25
5125405.1	149.025	69.65669	IRC64	b;Ns	2007-10-22-22:50:21	2007-10-22-23:20:21
5126499.1	149.025	69.65669	IRCZ4	b;Nh	2008-04-18-19:19:34	2008-04-18-19:49:34
5126768.1	150.21625	55.62	IRCZ4	b;Ns	2008-04-30-11:21:55	2008-04-30-11:51:55
5126768.2	150.21625	55.62	IRCZ4	b;Ns	2008-04-30-17:57:20	2008-04-30-18:27:20
5200783.2	150.21683	55.61883	IRCZ4	b;Ns	2009-04-30-03:35:03	2009-04-30-04:05:03
5200783.1	150.21683	55.61883	IRCZ4	b;Ns	2009-04-29-17:41:57	2009-04-29-18:11:57
1422185.3	150.48542	55.68944	IRCZ4	b;Ns	2009-11-01-18:53:44	2009-11-01-19:23:44
1422185.2	150.48542	55.68944	IRCZ4	b;Ns	2009-11-01-17:14:52	2009-11-01-17:44:52
1422185.1	150.48542	55.68944	IRCZ4	b;Ns	2009-11-01-15:36:01	2009-11-01-16:06:01
1422184.3	150.49083	55.67972	IRCZ4	b;Ns	2009-11-02-13:01:10	2009-11-02-13:31:10
1422184.1	150.49083	55.67972	IRCZ4	b;Ns	2009-11-01-20:32:35	2009-11-01-21:02:35
1422184.2	150.49083	55.67972	IRCZ4	b;Ns	2009-11-02-11:22:18	2009-11-02-11:52:18
1422186.2	150.495	55.66611	IRCZ4	b;Ns	2009-11-03-12:05:11	2009-11-03-12:35:11
1422186.1	150.495	55.66611	IRCZ4	b;Ns	2009-11-03-05:29:45	2009-11-03-05:59:45
1420405.1	150.82946	68.73375	IRCZ4	b;Ns	2009-04-20-19:34:25	2009-04-20-20:04:25
1420405.2	150.82946	68.73375	IRCZ4	b;Ns	2009-04-20-21:13:16	2009-04-20-21:43:16
1420407.1	151.63896	-29.93519	IRCZ4	b;Ns	2009-06-06-09:48:21	2009-06-06-10:18:21
1420407.2	151.63896	-29.93519	IRCZ4	b;Ns	2009-06-06-11:27:12	2009-06-06-11:57:12
5200785.1	154.22483	73.40089	IRCZ4	b;Ns	2009-04-16-00:15:59	2009-04-16-00:45:59
5200785.2	154.22483	73.40089	IRCZ4	b;Ns	2009-04-16-23:19:55	2009-04-16-23:49:55
5200306.2	154.2325	73.40028	IRCZ4	b;Ns	2008-10-21-00:50:15	2008-10-21-01:20:15
5200306.1	154.2325	73.40028	IRCZ4	b;Ns	2008-10-20-23:11:24	2008-10-20-23:41:24
1422162.1	154.52337	21.83158	IRCZ4	b;Ns	2009-11-21-02:01:08	2009-11-21-02:31:08
1420420.1	156.96275	-43.90397	IRCZ4	b;Ns	2008-06-21-06:51:49	2008-06-21-07:21:49
5200009.2	156.96362	-43.90397	IRCZ4	b;Ns	2008-06-23-06:38:32	2008-06-23-07:08:32
5200009.1	156.96362	-43.90383	IRCZ4	b;Nh	2008-06-23-00:03:07	2008-06-23-00:33:07
1420318.1	158.13208	54.40169	IRCZ4	b;Nh	2008-06-21-10:09:31	2008-06-21-10:39:31
1421318.1	158.13313	54.40114	IRCZ4	b;Ns	2008-11-07-19:39:39	2008-11-07-20:09:39
5126745.2	158.13333	54.40097	IRCZ4	b;Ns	2009-05-05-10:26:50	2009-05-05-10:56:50
5126745.1	158.13333	54.40097	IRCZ4	b;Ns	2008-05-06-10:42:37	2008-05-06-11:12:37
5125434.1	158.13333	54.40097	IRC64	b;Ns	2008-05-06-05:46:03	2008-05-06-06:16:03
5200011.2	160.78129	-46.21225	IRCZ4	b;Ns	2007-11-08-21:17:38	2007-11-08-21:47:38
5200011.1	160.78129	-46.21225	IRCZ4	b;Nh	2008-06-28-06:54:36	2008-06-28-07:24:36
5201209.1	160.88008	24.92189	IRCZ4	b;Nh	2008-06-27-07:50:42	2008-06-27-08:20:42
5201209.2	160.88008	24.92189	IRCZ4	b;Ns	2009-11-24-18:58:09	2009-11-24-19:28:09
5200370.2	160.88375	24.92056	IRCZ4	b;Ns	2009-11-25-19:41:03	2009-11-25-20:11:03
5126772.2	160.88375	24.92056	IRCZ4	b;Ns	2008-11-24-18:46:07	2008-11-24-19:16:07
5126772.1	160.88375	24.92056	IRCZ4	b;Ns	2008-05-24-02:01:04	2008-05-24-02:31:04
					2008-05-23-16:07:56	2008-05-23-16:37:56

Table D.6 – Sample selection with AKARI observations. VI.

NGC3377	0.002218	5200370.1	160.88375	24.92056	IRCZ4	b _i Ns	2008-11-24-00:38:36	2008-11-24-01:08:36
		5200372.2	161.92333	13.98333	IRCZ4	b _i Ns	2008-11-29-20:44:46	2008-11-29-21:14:46
		5200372.1	161.92333	13.98333	IRCZ4	b _i Ns	2008-11-29-19:05:54	2008-11-29-19:35:54
NGC3412	0.002805	5126776.1	162.72125	13.4125	IRCZ4	b _i Ns	2008-05-30-02:57:25	2008-05-30-03:27:25
		5126776.2	162.72125	13.4125	IRCZ4	b _i Ns	2008-05-30-16:08:13	2008-05-30-16:38:13
		5201213.2	162.72187	13.41214	IRCZ4	b _i Ns	2009-12-01-20:43:27	2009-12-01-21:13:27
		5201213.1	162.72187	13.41214	IRCZ4	b _i Ns	2009-12-01-19:04:35	2009-12-01-19:34:35
NGC3486	0.002272	5200375.2	165.09792	28.97583	IRCZ4	b _i Ns	2008-11-26-18:31:46	2008-11-26-19:01:46
		5200375.1	165.09792	28.97583	IRCZ4	b _i Ns	2008-11-25-21:06:31	2008-11-25-21:36:31
MRK162	0.02154	1420330.1	166.28417	44.747	IRCZ4	b _i Ns	2009-05-17-17:19:15	2009-05-17-17:49:15
		1420330.2	166.28417	44.747	IRCZ4	b _i Ns	2009-05-18-13:05:26	2009-05-18-13:35:26
NGC3557	0.0103	1420070.1	167.49021	-37.53917	IRCZ4	b _i Ns	2008-12-28-00:31:50	2008-12-28-01:01:50
		1420069.1	167.49021	-37.53917	IRCZ4	b _i Ns	2008-06-27-06:14:35	2008-06-27-06:44:35
NGC3621	0.002435	1420438.1	169.56867	-32.81414	IRCZ4	b _i Ns	2008-12-26-00:43:24	2008-12-26-01:13:24
		1421438.1	169.56879	-32.81417	IRCZ4	b _i Ns	2009-06-27-00:03:41	2009-06-27-00:33:41
NGC3627	0.002425	1420435.1	170.06238	12.99128	IRCZ4	b _i Ns	2008-06-06-01:22:11	2008-06-06-01:52:11
		1420435.2	170.06238	12.99128	IRCZ4	b _i Ns	2008-06-06-04:39:53	2008-06-06-05:09:53
NGC3628	0.002812	1420410.2	170.07067	13.58847	IRCZ4	b _i Ns	2009-06-05-14:15:05	2009-06-05-14:45:05
		1420410.1	170.07067	13.58847	IRCZ4	b _i Nh	2009-06-05-12:36:14	2009-06-05-13:06:14
		1420145.1	170.0813	13.58611	IRCZ4	b _i Nh	2009-06-06-05:04:43	2009-06-06-05:34:43
NGC3735	0.008993	1420147.1	173.96557	70.54145	IRCZ4	b _i Ns	2008-10-31-14:34:22	2008-10-31-15:04:22
		1420146.1	173.98954	70.53547	IRCZ4	b _i Ns	2008-10-31-16:13:14	2008-10-31-16:43:14
		1420148.1	174.01066	70.53026	IRCZ4	b _i Ns	2008-10-31-17:52:05	2008-10-31-18:22:05
NGC3894	0.010751	1420073.1	177.20983	59.41567	IRCZ4	b _i Ns	2009-05-14-10:18:53	2009-05-14-10:48:53
		1420072.1	177.20983	59.41567	IRCZ4	b _i Ns	2009-05-13-19:29:14	2009-05-13-19:59:14
		5126784.1	177.20983	59.41567	IRCZ4	b _i Ns	2008-05-14-23:03:20	2008-05-14-23:33:20
NGC3904	0.005257	1420075.1	177.30508	-29.27675	IRCZ4	b _i Ns	2009-07-02-13:32:00	2009-07-02-14:02:00
		1420074.1	177.30508	-29.27675	IRCZ4	b _i Ns	2008-07-02-04:54:58	2008-07-02-05:24:58
NGC3921	0.019667	5126754.1	177.77917	55.07872	IRCZ4	b _i Ns	2008-05-19-16:43:22	2008-05-19-17:13:22
		5126754.2	177.77917	55.07872	IRCZ4	b _i Ns	2008-05-19-18:22:13	2008-05-19-18:52:13
		1422160.1	177.77917	55.07872	IRCZ4	b _i Ns	2009-11-21-10:05:07	2009-11-21-10:35:07
NGC3962	0.006064	1400040.1	178.66708	-13.97503	IRC04	b _i Ns	2006-12-26-20:12:21	2006-12-26-20:42:21
NGC3998	0.003496	5126780.1	179.48333	55.45306	IRCZ4	b _i Ns	2008-05-20-17:26:25	2008-05-20-17:56:25
		5126780.2	179.48333	55.45306	IRCZ4	b _i Ns	2008-05-21-13:12:40	2008-05-21-13:42:40
		5200376.1	179.48333	55.45306	IRCZ4	b _i Ns	2008-11-20-19:02:50	2008-11-20-19:32:50
		5200376.2	179.48333	55.45306	IRCZ4	b _i Ns	2008-11-21-19:45:46	2008-11-21-20:15:46
		5201215.1	179.48358	55.45369	IRCZ4	b _i Ns	2009-11-20-19:15:09	2009-11-20-19:45:09
		5201215.2	179.48358	55.45369	IRCZ4	b _i Ns	2009-11-21-19:58:02	2009-11-21-20:28:02
NGC4041	0.004116	1420369.1	180.55	62.13728	IRCZ4	b _i Ns	2009-05-12-18:47:21	2009-05-12-19:17:21
NGC4125	0.004523	1400043.1	182.02508	65.17414	IRC04	b _i Ns	2006-11-13-08:02:36	2006-11-13-08:32:36
NGC4138	0.002962	5201388.1	182.3745	43.68561	IRCZ4	b _i Ns	2009-12-04-11:10:36	2009-12-04-11:40:36
		5200837.1	182.3745	43.68561	IRCZ4	b _i Ns	2009-06-02-04:01:25	2009-06-02-04:31:25
NGC4157	0.002583	5200377.2	182.76875	50.48444	IRCZ4	b _i Ns	2008-11-27-20:46:40	2008-11-27-21:16:40
		5200377.1	182.76875	50.48444	IRCZ4	b _i Ns	2008-11-27-19:07:48	2008-11-27-19:37:48
		5126781.1	182.76875	50.48444	IRCZ4	b _i Ns	2008-05-27-17:28:40	2008-05-27-17:58:40
		5126781.2	182.76875	50.48444	IRCZ4	b _i Ns	2008-05-28-01:42:56	2008-05-28-02:12:56
NGC4194	0.008342	5126915.1	183.53623	54.52779	IRCZ4	b _i Nh	2008-05-24-05:28:07	2008-05-24-05:58:07
		5126915.2	183.53623	54.52779	IRCZ4	b _i Nh	2008-05-24-10:24:40	2008-05-24-10:54:40
		5126915.3	183.53623	54.52779	IRCZ4	b _i Nh	2008-05-24-13:42:23	2008-05-24-14:12:23
		1422150.3	183.54012	54.52647	IRCZ4	b _i Ns	2009-11-25-03:03:07	2009-11-25-03:33:07
		1422150.1	183.54012	54.52647	IRCZ4	b _i Ns	2009-11-24-17:09:57	2009-11-24-17:39:57

Table D.7 – Sample selection with AKARI observations. VII.

NGC4203	1422150.2	183.54012	54.52647	IRCZ4	b _i Ns	2009-11-25-01:24:15	2009-11-25-01:54:15
NGC4258	5200840.1	183.77137	33.19758	IRCZ4	b _i Ns	2009-06-09-02:22:39	2009-06-09-02:52:39
	1422159.1	184.7385	47.30506	IRCZ4	b _i Ns	2009-12-01-12:18:34	2009-12-01-12:48:34
	1420372.1	184.74167	47.30394	IRCZ4	b _i Ns	2008-06-01-04:33:34	2008-06-01-05:03:34
NGC4261	5200844.1	184.84663	5.82453	IRCZ4	b _i Ns	2009-06-22-16:27:39	2009-06-22-16:57:39
	5200844.2	184.84663	5.82453	IRCZ4	b _i Ns	2009-06-23-15:31:31	2009-06-23-16:01:31
	1420110.1	185.02842	29.28075	IRCZ4	b _i Ns	2009-06-13-05:12:38	2009-06-13-05:42:38
NGC4278	5200845.2	185.47883	4.47347	IRCZ4	b _i Ns	2009-06-25-15:17:48	2009-06-25-15:47:48
NGC4303	5200845.1	185.47883	4.47347	IRCZ4	b _i Ns	2009-06-24-16:13:57	2009-06-24-16:43:57
	1422157.1	185.93542	12.47825	IRCZ4	b _i Ns	2009-12-22-12:38:08	2009-12-22-13:08:08
IC3258	1420421.1	186.07129	67.44011	IRCZ4	b _i Ns	2009-05-08-19:15:31	2009-05-08-19:45:31
MRK206	1420421.2	186.07129	67.44011	IRCZ4	b _i Ns	2009-05-11-06:34:07	2009-05-11-07:04:07
	5201399.1	186.54875	12.94619	IRCZ4	b _i Ns	2009-12-22-15:55:41	2009-12-22-16:25:41
NGC4406	5200010.1	186.72783	-0.87825	IRCZ4	b _i Nh	2008-06-28-02:11:58	2008-06-28-02:41:58
NGC4418	5200010.2	186.72783	-0.87825	IRCZ4	b _i Nh	2008-06-28-03:50:49	2008-06-28-04:20:49
	1400056.1	186.90554	-39.33778	IRC04	b _i Ns	2007-01-13-20:11:52	2007-01-13-20:41:52
IC3370	1420430.2	187.04521	44.09239	IRCZ4	b _i Ns	2009-06-04-16:59:22	2009-06-04-17:29:22
NGC4449	1420430.1	187.04521	44.09239	IRCZ4	b _i Ns	2008-06-05-17:17:21	2008-06-05-17:47:21
	1420101.1	187.70592	12.39111	IRCZ4	b _i Ns	2009-06-23-05:40:23	2009-06-23-06:10:23
	1420100.1	187.70592	12.39111	IRCZ4	b _i Ns	2009-06-22-13:11:55	2009-06-22-13:41:55
NGC4496	5200854.1	187.92042	3.92631	IRCZ4	b _i Ns	2009-06-26-16:00:37	2009-06-26-16:30:37
NGC4552	1422169.2	188.91617	12.55608	IRCZ4	b _i Ns	2009-12-24-14:03:37	2009-12-24-14:33:37
	1422169.3	188.91617	12.55608	IRCZ4	b _i Ns	2009-12-24-22:17:55	2009-12-24-22:47:55
	1422169.1	188.91617	12.55608	IRCZ4	b _i Ns	2009-12-24-12:24:45	2009-12-24-12:54:45
NGC4569	1420458.2	189.20754	13.16297	IRCZ4	b _i Ns	2008-06-24-15:53:11	2008-06-24-16:23:11
	1420458.1	189.20754	13.16297	IRCZ4	b _i Ns	2008-06-24-10:56:38	2008-06-24-11:26:38
	1422174.1	189.21204	13.17453	IRCZ4	b _i Ns	2009-12-24-23:56:35	2009-12-25-00:26:35
	1422174.3	189.21204	13.17453	IRCZ4	b _i Ns	2009-12-25-03:14:19	2009-12-25-03:44:19
	1422174.2	189.21204	13.17453	IRCZ4	b _i Ns	2009-12-25-01:35:27	2009-12-25-02:05:27
	1420472.2	189.43087	11.81822	IRCZ4	b _i Nh	2009-06-25-10:23:32	2009-06-25-10:53:32
NGC4579	1420472.1	189.43087	11.81822	IRCZ4	b _i Nh	2009-06-25-05:27:00	2009-06-25-05:57:00
	1422170.3	189.43108	11.81811	IRCZ4	b _i Ns	2009-12-25-14:46:37	2009-12-25-15:16:37
	1422170.1	189.43108	11.81811	IRCZ4	b _i Ns	2009-12-25-11:28:54	2009-12-25-11:58:54
	1422170.2	189.43108	11.81811	IRCZ4	b _i Ns	2009-12-25-13:07:46	2009-12-25-13:37:46
	1422171.1	189.99796	-11.62242	IRCZ4	b _i Ns	2010-01-04-12:08:20	2010-01-04-12:38:20
	1422171.2	189.99796	-11.62242	IRCZ4	b _i Ns	2010-01-04-13:47:12	2010-01-04-14:17:12
	5200858.1	190.38708	41.15092	IRCZ4	b _i Ns	2009-06-09-05:42:57	2009-06-09-06:12:57
NGC4618	5201409.2	190.38708	41.15092	IRCZ4	b _i Ns	2009-06-09-12:18:20	2009-06-09-12:48:20
	5201409.1	190.38708	41.15092	IRCZ4	b _i Ns	2009-12-11-12:52:57	2009-12-11-13:22:57
	1422238.1	190.7075	2.68778	IRCZ4	b _i Ns	2009-12-11-04:38:41	2009-12-11-05:08:41
NGC4636	1422238.2	190.7075	2.68778	IRCZ4	b _i Ns	2009-12-30-00:15:51	2009-12-30-00:45:51
	1422238.3	190.7075	2.68778	IRCZ4	b _i Ns	2009-12-30-01:54:43	2009-12-30-02:24:43
	1420078.1	190.70779	2.68778	IRCZ4	b _i Ns	2009-12-30-03:33:35	2009-12-30-04:03:35
	1420079.1	190.70779	2.68778	IRCZ4	b _i Ns	2008-06-29-09:31:29	2008-06-29-10:01:29
NGC4670	1420079.1	190.70779	2.68778	IRCZ4	b _i Ns	2008-06-29-11:10:20	2008-06-29-11:40:20
	1420307.1	191.32125	27.125	IRCZ4	b _i Ns	2008-06-18-14:57:56	2008-06-18-15:27:56
	1421307.1	191.32142	27.1255	IRCZ4	b _i Ns	2008-12-20-12:36:49	2008-12-20-13:06:49
NGC4689	5200862.1	191.93996	13.76258	IRCZ4	b _i Ns	2009-06-27-01:56:36	2009-06-27-02:26:36
NGC4697	1420098.1	192.14962	-5.80086	IRCZ4	b _i Ns	2008-07-06-01:18:08	2008-07-06-01:48:08
NGC4696	1420080.1	192.20533	-41.31111	IRCZ4	b _i Ns	2008-07-20-12:47:06	2008-07-20-13:17:06
	1420081.1	192.20533	-41.31111	IRCZ4	b _i Ns	2008-07-20-14:25:57	2008-07-20-14:55:57

Table D.8 – Sample selection with AKARI observations. VIII.

NGC4736	0.001027	1420445.2	192.70567	41.12269	IRCZ4	b;Ns	2008-12-12-13:24:54	2008-12-12-13:54:54
		1420445.1	192.70567	41.12269	IRCZ4	b;Ns	2008-12-12-11:46:02	2008-12-12-12:16:02
		1420444.1	192.72012	41.12014	IRCZ4	b;Ns	2008-06-12-12:23:38	2008-06-12-12:53:38
		1420444.2	192.72012	41.12014	IRCZ4	b;Ns	2008-06-12-14:02:29	2008-06-12-14:32:29
NGC4826	0.001361	1422152.1	192.72237	41.12083	IRCZ4	b;Ns	2009-12-12-11:56:46	2009-12-12-12:26:46
		1420446.2	192.73579	41.11703	IRCZ4	b;Ns	2008-12-12-15:03:46	2008-12-12-15:33:46
		1420446.1	192.73579	41.11703	IRCZ4	b;Ns	2008-06-12-15:41:20	2008-06-12-16:11:20
		1422176.1	194.17208	21.68803	IRCZ4	b;Ns	2009-12-26-13:47:41	2009-12-26-14:17:41
MRK59	0.002616	1422173.3	194.18108	21.68233	IRCZ4	b;Ns	2009-12-26-12:08:50	2009-12-26-12:38:50
		1422173.1	194.18108	21.68233	IRCZ4	b;Ns	2009-12-26-00:36:48	2009-12-26-01:06:48
		1422173.2	194.18108	21.68233	IRCZ4	b;Ns	2009-12-26-02:15:40	2009-12-26-02:45:40
		1420319.1	194.75142	34.84586	IRCZ4	b;Ns	2008-06-17-12:38:33	2008-06-17-13:08:33
NGC5018	0.009393	1420319.2	194.75142	34.84586	IRCZ4	b;Ns	2008-06-17-14:17:24	2008-06-17-14:47:24
		1420082.1	198.25413	-19.51808	IRCZ4	b;Ns	2008-07-15-15:54:36	2008-07-15-16:24:36
		1420083.1	198.25417	-19.51808	IRCZ4	b;Ns	2008-07-16-01:47:43	2008-07-16-02:17:43
		1422240.1	198.25417	-19.51806	IRCZ4	b;Ns	2010-01-15-00:15:00	2010-01-15-00:45:00
NGC5044	0.00928	1422240.2	198.25417	-19.51806	IRCZ4	b;Ns	2010-01-15-01:53:51	2010-01-15-02:23:51
		1422240.3	198.25417	-19.51806	IRCZ4	b;Ns	2010-01-15-03:32:43	2010-01-15-04:02:43
		1420086.1	198.85	-16.38553	IRCZ4	b;Ns	2008-07-15-12:37:45	2008-07-15-13:07:45
		1420087.1	198.85	-16.38553	IRCZ4	b;Ns	2008-07-15-14:16:36	2008-07-15-14:46:36
NGC5055 Cen-A	0.001614 0.001825	1422178.1	198.95612	42.02981	IRCZ4	b;Ns	2009-12-19-03:45:20	2009-12-19-04:15:20
		1422195.1	201.36508	-43.01911	IRCZ4	b;Ns	2010-01-26-21:23:06	2010-01-26-21:53:06
		1420102.1	201.36508	-43.01911	IRCZ4	b;Ns	2008-07-29-06:01:51	2008-07-29-06:31:51
		1420103.1	201.36508	-43.01911	IRCZ4	b;Ns	2008-07-29-10:58:25	2008-07-29-11:28:25
NGC5147	0.003629	1422195.2	201.36508	-43.01911	IRCZ4	b;Ns	2010-01-26-23:01:57	2010-01-26-23:31:57
		1422195.3	201.36508	-43.01911	IRCZ4	b;Ns	2010-01-27-00:40:49	2010-01-27-01:10:49
		5200864.2	201.58254	2.10106	IRCZ4	b;Ns	2009-07-10-16:06:23	2009-07-10-16:36:23
		5200864.1	201.58254	2.10106	IRCZ4	b;Ns	2009-07-10-14:27:32	2009-07-10-14:57:32
M51	0.002	1400388.1	202.44734	47.22706	IRC04	b;Ns	2006-12-17-17:30:26	2006-12-17-18:00:26
		1420415.2	204.25383	-29.86542	IRCZ4	b;Ns	2009-07-26-02:39:11	2009-07-26-03:09:11
		1420415.1	204.25383	-29.86542	IRCZ4	b;Ns	2009-07-26-01:00:20	2009-07-26-01:30:20
		5200514.2	204.38333	8.88556	IRCZ4	b;Ns	2009-01-08-16:23:22	2009-01-08-16:53:22
NGC5248	0.003839	5200514.1	204.38333	8.88556	IRCZ4	b;Ns	2009-01-08-14:44:30	2009-01-08-15:14:30
		1420429.2	204.98283	-31.64019	IRCZ4	b;Ns	2008-07-27-06:18:17	2008-07-27-06:48:17
		1420429.1	204.98283	-31.64019	IRCZ4	b;Ns	2008-07-27-04:39:25	2008-07-27-05:09:25
		1422153.1	204.98337	-31.64006	IRCZ4	b;Ns	2010-01-24-11:39:53	2010-01-24-12:09:53
NGC5253	0.001358	1422153.2	204.98337	-31.64006	IRCZ4	b;Ns	2010-01-24-21:33:02	2010-01-24-22:03:02
		1422153.3	204.98337	-31.64006	IRCZ4	b;Ns	2010-01-24-23:11:54	2010-01-24-23:41:54
		5200866.1	205.53504	35.65414	IRCZ4	b;Ns	2009-06-28-15:56:58	2009-06-28-16:26:58
		1420105.1	206.70433	-60.40817	IRCZ4	b;Ns	2008-08-13-00:11:38	2008-08-13-00:41:38
NGC5273 Cen-B	0.003619 0.012916	1420104.1	206.70433	-60.40817	IRCZ4	b;Ns	2008-08-12-11:00:48	2008-08-12-11:30:48
		1420118.1	207.31333	60.19042	IRCZ4	b;Ns	2008-06-03-20:53:51	2008-06-03-21:23:51
		1420119.1	207.31333	60.19042	IRCZ4	b;Ns	2008-06-04-00:11:34	2008-06-04-00:41:34
		5201418.1	208.36104	40.28283	IRCZ4	b;Ns	2009-12-27-01:13:39	2009-12-27-01:43:39
NGC5353	0.007755 0.008533 0.003799	5200869.1	208.91629	40.46144	IRCZ4	b;Ns	2009-06-29-15:02:20	2009-06-29-15:32:20
		5200517.2	209.02917	5.25528	IRCZ4	b;Ns	2009-01-15-13:10:15	2009-01-15-13:40:15
		5200517.1	209.02917	5.25528	IRCZ4	b;Ns	2009-01-14-15:45:01	2009-01-14-16:15:01
		5200868.1	209.03017	5.25486	IRCZ4	b;Ns	2009-07-18-13:35:23	2009-07-18-14:05:23
SDSSJ135950.7+381056	nan	1380065.1	209.9615	38.18228	IRCZ4	b;Ns	2008-07-01-16:04:29	2008-07-01-16:34:29
		1380065.2	209.9615	38.18228	IRCZ4	b;Ns	2009-06-30-04:12:41	2009-06-30-04:42:41
		1380065.3	209.9615	38.18228	IRCZ4	b;Ns	2009-06-30-05:51:32	2009-06-30-06:21:32

Table D.9 – Sample selection with AKARI observations. IX.

NGC5430	0.009877	1380065.4	209.9615	38.18228	IRCZ4	b _i Ns	2009-06-30-10:48:04	2009-06-30-11:18:04
		1420373.2	210.19063	59.32869	IRCZ4	b _i Ns	2008-06-04-19:57:57	2008-06-04-20:27:57
		1420373.1	210.19063	59.32869	IRCZ4	b _i Ns	2008-06-04-18:19:06	2008-06-04-18:49:06
		1420374.2	210.197	59.32426	IRCZ4	b _i Ns	2008-06-05-14:05:19	2008-06-05-14:35:19
NGC5457	0.000804	1420374.1	210.197	59.32426	IRCZ4	b _i Ns	2008-06-05-12:26:28	2008-06-05-12:56:28
		1420389.1	210.80246	54.34908	IRCZ4	b _i Ns	2008-06-13-13:11:16	2008-06-13-13:41:16
		1420389.2	210.80246	54.34908	IRCZ4	b _i Ns	2008-06-13-14:50:07	2008-06-13-15:20:07
		1420390.1	211.1209	54.39691	IRCZ4	b _i Ns	2008-06-15-22:51:09	2008-06-15-23:21:09
Circinus_Galaxy	0.000991	5125033.1	213.29129	-65.33903	IRC04	b _i Ns	2007-08-23-05:40:07	2007-08-23-06:10:07
		5200872.2	218.18458	9.89214	IRCZ4	b _i Ns	2009-07-25-05:25:41	2009-07-25-05:55:41
		5200872.1	218.18458	9.89214	IRCZ4	b _i Ns	2009-07-24-14:36:03	2009-07-24-15:06:03
		5201422.1	218.35158	4.45083	IRCZ4	b _i Ns	2010-01-25-12:12:15	2010-01-25-12:42:15
NGC5668	0.00526	5200871.2	218.35158	4.45083	IRCZ4	b _i Ns	2009-07-26-14:21:15	2009-07-26-14:51:15
		5200871.1	218.35158	4.45083	IRCZ4	b _i Ns	2009-07-26-12:42:24	2009-07-26-13:12:24
		5200873.1	221.23333	1.95528	IRCZ4	b _i Ns	2009-07-31-16:15:37	2009-07-31-16:45:37
		5200069.2	225.29625	1.70222	IRCZ4	b _i Ns	2008-08-03-14:45:59	2008-08-03-15:15:59
NGC5746	0.005751	5200069.1	225.29625	1.70222	IRCZ4	b _i Ns	2008-08-03-13:07:08	2008-08-03-13:37:08
		1420416.1	233.63333	15.19419	IRCZ4	b _i Ns	2008-08-03-03:34:33	2008-08-03-04:04:33
		1420416.2	233.63333	15.19419	IRCZ4	b _i Ns	2009-02-05-23:10:43	2009-02-05-23:40:43
		1402684.1	241.30375	20.54222	IRC04	b _i Ns	2007-08-17-04:07:25	2007-08-17-04:37:25
NGC6052	0.015808	5200307.1	257.60667	72.30583	IRCZ4	b _i Ns	2008-10-23-00:29:54	2008-10-23-00:59:54
		5200307.2	257.60667	72.30583	IRCZ4	b _i Ns	2008-10-25-00:16:53	2008-10-25-00:46:53
		5126484.1	266.7675	-64.62344	IRCZ4	b _i Nh	2008-03-17-13:42:08	2008-03-17-14:12:08
		5126484.2	266.7675	-64.62344	IRCZ4	b _i Nh	2008-03-18-01:14:10	2008-03-18-01:44:10
NGC6340	0.003996	1420375.1	266.7675	-64.62344	IRCZ4	b _i Nh	2008-09-20-07:34:34	2008-09-20-08:04:34
		1402643.1	266.7675	-64.62344	IRC64	b _i Ns	2007-09-22-00:35:51	2007-09-22-01:05:51
		5126485.1	266.77417	-64.64375	IRCZ4	b _i Nh	2008-03-19-15:07:59	2008-03-19-15:37:59
		5126485.2	266.77417	-64.64375	IRCZ4	b _i Nh	2008-03-19-16:46:51	2008-03-19-17:16:51
IC4662	0.001007	5126483.2	266.775	-64.64031	IRCZ4	b _i Nh	2008-03-19-13:29:07	2008-03-19-13:59:07
		5126483.1	266.775	-64.64031	IRCZ4	b _i Nh	2008-03-19-02:27:05	2008-03-19-02:57:05
		5126486.1	266.78125	-64.65436	IRCZ4	b _i Nh	2008-03-18-22:39:22	2008-03-18-23:09:22
		1420376.2	266.788	-64.638	IRCZ4	b _i Ns	2008-09-20-10:52:17	2008-09-20-11:22:17
NGC6482	0.013129	1420376.1	266.788	-64.638	IRCZ4	b _i Ns	2008-09-20-09:13:25	2008-09-20-09:43:25
		5200686.2	267.95375	23.07194	IRCZ4	b _i Ns	2009-03-17-12:09:51	2009-03-17-12:39:51
		5200686.1	267.95375	23.07194	IRCZ4	b _i Ns	2009-03-16-16:23:34	2009-03-16-16:53:34
		1420377.2	269.0	18.33824	IRCZ4	b _i Ns	2009-03-19-16:54:33	2009-03-19-17:24:33
NGC6500	0.010017	1420377.1	269.0	18.33824	IRCZ4	b _i Ns	2009-03-19-15:15:42	2009-03-19-15:45:42
		1402645.1	269.0	18.33824	IRC64	b _i Ns	2007-09-22-02:38:19	2007-09-22-03:08:19
		5200047.3	273.23079	68.36339	IRCZ4	b _i Nh	2008-07-30-18:50:31	2008-07-30-19:20:31
		5200047.2	273.23079	68.36339	IRCZ4	b _i Nh	2008-07-30-17:11:40	2008-07-30-17:41:40
NGC6621	0.020652	5200047.1	273.23079	68.36339	IRCZ4	b _i Nh	2008-07-29-16:28:51	2008-07-29-16:58:51
		5200687.1	278.70875	70.52417	IRCZ4	b _i Nh	2009-02-04-10:38:49	2009-02-04-11:08:49
		5200687.2	278.70875	70.52417	IRCZ4	b _i Ns	2009-02-04-13:56:33	2009-02-04-14:26:33
		5200256.1	281.82833	45.55056	IRCZ4	b _i Ns	2008-10-13-14:37:56	2008-10-13-15:07:56
NGC6689	0.001558	5200256.2	281.82833	45.55056	IRCZ4	b _i Ns	2008-10-14-10:24:16	2008-10-14-10:54:16
		5200308.1	281.82833	45.55056	IRCZ4	b _i Ns	2008-10-14-07:06:33	2008-10-14-07:36:33
		5200308.2	281.82833	45.55056	IRCZ4	b _i Ns	2008-10-14-16:59:42	2008-10-14-17:29:42
		5126738.2	287.05125	50.93036	IRCZ4	b _i Ns	2008-04-28-02:00:31	2008-04-28-02:30:31
NGC6703	0.007915	5126738.1	287.05125	50.93036	IRCZ4	b _i Ns	2008-04-27-21:03:57	2008-04-27-21:33:57
		5126737.2	287.06667	50.93322	IRCZ4	b _i Ns	2008-04-27-19:25:05	2008-04-27-19:55:05
		5126737.1	287.06667	50.93322	IRCZ4	b _i Ns	2008-04-27-17:46:14	2008-04-27-18:16:14
NGC6764	0.008059							

Table D.10 – Sample selection with AKARI observations. X.

IC4870	0.002919	5125432.1	287.06667	50.93322	IRC64	b _i Ns	2007-10-31-02:19:10	2007-10-31-02:49:10
		1420378.1	287.06838	50.93325	IRCZ4	b _i Ns	2009-04-24-21:32:04	2009-04-24-21:32:04
		5126736.2	294.40417	-65.81139	IRCZ4	b _i Ns	2008-04-03-17:37:52	2008-04-03-18:07:52
		5126736.1	294.40417	-65.81139	IRCZ4	b _i Ns	2008-04-03-02:48:07	2008-04-03-03:18:07
NGC6946	0.000133	1420380.1	294.40667	-65.81183	IRCZ4	b _i Ns	2008-10-05-06:45:12	2008-10-05-07:15:12
		1420443.2	308.71354	60.16083	IRCZ4	b _i Ns	2009-06-18-02:32:37	2009-06-18-03:02:37
		1420443.1	308.71354	60.16083	IRCZ4	b _i Ns	2009-06-18-00:53:46	2009-06-18-01:23:46
		1420440.1	308.718	60.15411	IRCZ4	b _i Nh	2009-06-17-13:21:50	2009-06-17-13:51:50
NGC6951	0.00475	1420440.2	308.718	60.15411	IRCZ4	b _i Nh	2009-06-17-15:00:41	2009-06-17-15:30:41
		1400371.1	309.32429	66.10319	IRC04	b _i Ns	2007-01-06-05:31:27	2007-01-06-06:01:27
		1422242.1	319.6375	26.44694	IRCZ4	b _i Ns	2009-11-24-10:09:37	2009-11-24-10:39:37
		5126750.2	319.63771	26.44692	IRCZ4	b _i Ns	2008-05-23-15:03:20	2008-05-23-15:33:20
NGC7052	0.015584	5126750.1	319.63771	26.44692	IRCZ4	b _i Ns	2008-05-23-11:45:37	2008-05-23-12:15:37
		1420092.1	319.63771	26.44692	IRCZ4	b _i Ns	2009-05-23-12:11:20	2009-05-23-12:41:20
		1420093.1	319.63771	26.44692	IRCZ4	b _i Ns	2009-05-23-13:50:10	2009-05-23-14:20:10
		5125440.1	319.63771	26.44692	IRC64	b _i Ns	2007-11-25-05:58:42	2007-11-25-06:28:42
NGC7080	0.016141	5200795.2	322.50792	26.71797	IRCZ4	b _i Ns	2009-05-25-20:12:23	2009-05-25-20:42:23
		5200795.1	322.50792	26.71797	IRCZ4	b _i Ns	2009-05-25-21:51:14	2009-05-25-22:21:14
		3221001.1	339.01362	33.94786	IRC04	b _i Ns	2007-06-18-03:51:01	2007-06-18-04:21:01
		5126788.1	344.29417	-36.46222	IRCZ4	b _i Ns	2008-05-21-15:35:00	2008-05-21-16:05:00
HCG 92 IC1459	0.006011	1420094.1	344.29417	-36.46222	IRCZ4	b _i Ns	2008-11-22-06:34:19	2008-11-22-07:04:19
		5125441.1	344.29417	-36.46222	IRC64	b _i Ns	2007-11-23-11:02:23	2007-11-23-11:02:23
		1420095.1	344.29417	-36.46222	IRCZ4	b _i Ns	2009-05-20-16:56:58	2009-05-20-17:26:58
		5126748.2	349.58875	-42.35378	IRCZ4	b _i Ns	2008-05-23-18:41:24	2008-05-23-19:11:24
NGC7582	0.005254	5126748.1	349.58875	-42.35378	IRCZ4	b _i Ns	2008-05-23-17:02:32	2008-05-23-17:32:32
		1420383.2	349.58875	-42.35378	IRCZ4	b _i Ns	2009-05-23-17:28:14	2009-05-23-17:58:14
		1420383.1	349.58875	-42.35378	IRCZ4	b _i Ns	2009-05-23-02:38:35	2009-05-23-03:08:35
		5125437.1	349.6	-42.37056	IRC64	b _i Ns	2007-11-25-02:19:08	2007-11-25-02:49:08
NGC7714	0.009333	5126747.2	349.6	-42.37056	IRCZ4	b _i Ns	2008-05-23-13:44:50	2008-05-23-14:14:50
		5126747.1	349.6	-42.37056	IRCZ4	b _i Ns	2008-05-22-22:55:11	2008-05-22-23:25:11
		5126749.1	349.60708	-42.38353	IRCZ4	b _i Ns	2008-05-22-19:37:29	2008-05-22-20:07:29
		5126749.2	349.60708	-42.38353	IRCZ4	b _i Ns	2008-05-22-21:16:20	2008-05-22-21:46:20
NGC7727	0.006231	1420418.1	354.05833	2.15514	IRCZ4	b _i Nh	2008-06-16-14:12:35	2008-06-16-14:42:35
		1421418.1	354.05833	2.15514	IRCZ4	b _i Nh	2008-12-16-10:43:32	2008-12-16-11:13:32
		1420386.1	354.97446	-12.293	IRCZ4	b _i Ns	2008-12-11-10:22:38	2008-12-11-10:52:38
		5200874.1	355.97358	26.07583	IRCZ4	b _i Ns	2009-06-29-18:49:20	2009-06-29-19:19:20
NGC7741	0.002502	5200874.1	355.97358	26.07583	IRCZ4	b _i Ns	2009-06-29-18:49:20	2009-06-29-19:19:20
		5200875.1	356.06571	10.76731	IRCZ4	b _i Ns	2009-06-22-17:11:56	2009-06-22-17:41:56
		1420419.1	357.86129	20.58664	IRCZ4	b _i Ns	2008-06-29-00:20:33	2008-06-29-00:50:33
		1421419.1	357.86167	20.58608	IRCZ4	b _i Ns	2008-12-28-04:33:44	2008-12-28-05:03:44
MRK331	0.018483	5200527.1	359.85625	20.74972	IRCZ4	b _i Ns	2008-12-29-00:19:57	2008-12-29-00:49:57
		5200527.2	359.85625	20.74972	IRCZ4	b _i Ns	2008-12-29-01:58:48	2008-12-29-02:28:48
		5200876.1	359.8565	20.75006	IRCZ4	b _i Ns	2009-06-30-16:16:05	2009-06-30-16:46:05
		5200876.2	359.8565	20.75006	IRCZ4	b _i Ns	2009-06-30-17:54:56	2009-06-30-18:24:56

Appendix E

Summary of my scientific life

E.1 Observational and modeling techniques

I have mastered the data treatment of AKARI/IRC and *Spitzer*/IRS from their instrument design to official pipelines. During the three and a half years of this thesis, I have also spent a lot of time developing diverse skills, especially programming techniques. I have mastered Python and Fortran almost from zero. They have resulted in two major software of observational data processing (MIRAGE) and data analyzing MILES, respectively, as well as a python package `rapyuta`¹ that I update actively for general astrophysics research use. Besides, the time that I have devoted to adapting myself to Emacs proved to be worthy, considering the work efficiency it brought.

E.2 Publications and proposals

Publications

- “*MILES: Modeling mid-infrared emission with hierarchical Bayesian inference. II. Properties of aromatic feature carriers in nearby Universe*”

Hu, D.; Galliano, F.; Hony, S.; Lebouteiller, V.; Onaka, T.; Wu, R.; Sakon, I., *in prep.*

- “*MILES: Modeling mid-infrared emission with hierarchical Bayesian inference. I. A case study of M82*”

Hu, D.; Galliano, F.; Hony, S.; Lebouteiller, V.; Onaka, T.; Wu, R.; Sakon, I., *in prep.*

- “*Study of the photoelectric effect heating proxies in the Magellanic Clouds*”

Lambert-Huyghe, A.; Madden, S.; Lebouteiller, V.; Galliano, F.; **Hu, D.**; Galametz, M.; Ramambason, L.; Polles, F., *in prep.*

- “*Disentangling star-forming regions emission in the Magellanic Clouds: PDR origin of the H ii region tracers*”

Lambert-Huyghe, A.; Madden, S.; Lebouteiller, V.; Galliano, F.; Abel, N.; Galametz, M.; **Hu, D.**; Ramambason, L.;

1. `rapyuta`: libraRy of Astronomical PYthon UTilities for Astrophysics nerds (open access on <https://github.com/kxxdhdn/RAPYUTA>).

Polles, F., *submitted*

- “Tracing the total molecular gas in galaxies: [CII] and the CO-dark gas”

Madden, S. C.; Cormier, D.; Hony, S.; Lebouteiller, V.; Abel, N.; Galametz, M.; De Looze, I.; Chevance, M.; Polles, F. L.; Lee, M. -Y.; Galliano, F.; Lambert-Huyghe, A.; **Hu, D.**; Ramambason, L., 2020, *Astronomy & Astrophysics*, **643**, A141

Observing time allocated

- Co-I of a *SOFIA* Cycle 9 proposal (Time allocated: 49.93 hours)

“*SOFIA Joint Legacy Survey of [CII] in the LMC: LMC+*” (PI: Suzanne Madden)

Other proposals

- Co-I of a JWST Cycle 1 GO proposal (Not accepted)

“*PAHSPECS: A Comprehensive Study of PAHs at Cosmic Noon*” (PI: Irene Shivaiei)

E.3 Scientific communications

Contributed talks

- 24/10/2022, PCMI biennial conference, Paris, France

“*Physical and Statistical modeling of Interstellar Grains*”

- 17/10/2022, Lunch Talk, SWIFAR, YNU, Yunnan, China (Online)

“*Decoding Interstellar Dust and Polycyclic Aromatic Hydrocarbons (PAHs) in the JWST Era*”

- 06/09/2022, The life cycle of cosmic PAHs, Aarhus, Denmark

“*Spectral Modeling of Interstellar PAHs with Hierarchical Bayesian Inference*”

- 22/07/2022, With Two Eyes, Interstellar Institute (I2), Orsay, France

“*Modeling the Mid-infrared Spectra of Interstellar Dust Grains (PAHs)*”

- 28/08/2021, 2021 CSC-Seminar for scholars in Germany and France (Online)

“*Studying Small Carbon Grain Properties in Nearby Galaxies*”

- 28/07/2021, The Grand Cascade, Interstellar Institute (I2), Orsay, France

“*Studying Small Carbon Grain Properties in Nearby Galaxies*”

- 30/06/2021, European Astronomical Society Annual Meeting (EAS 2021), SS14a, Leiden, Netherlands (Online)

“*Studying Small Carbon Grain Properties with Spitzer and AKARI Archived Observations*”

- 07/05/2021, Star Formation Lunch, DAp, CEA, Saclay, France (Online)

“*Studying Small Carbon Grain Properties with Spitzer and AKARI Archived Observations*”

- 22/02/2019, Elbereth conference 2019, Paris, France
“Properties of Aromatic Feature Carriers in Nearby Galaxies”

Organization committee

- 29/11/2019², Member of the organization committee of the Rencontres des Jeunes Physicien-ne-s (RJP; Young Physicists’ Day) conference, Paris, France

Other conferences

- 14/02/2022, IR 2022: An Infrared Bright Future for Ground-based IR Observatories in the Era of JWST (Online)
- 14/06/2021, SAZERAC 2.0: Summer All Zoom Epoch of Reionization Astronomy Conference (Online)
- 14/06/2021, Celebrating Catherine Cesarsky: 50 years of astronomy, Saclay, France (Online)
- 07/06/2021, SF2A virtual conference 2021 (Online)
- 11/05/2021, ISM 2021: Structure, Characteristic Scales, and Star Formation, Beirut, Lebanon (Online)
- 26/10/2020, The Rise of Metals and Dust in Galaxies through Cosmic Time, Marseille, France (Poster; Online)
- 06/07/2020, PCMI Biennial conference 2020, Le Havre, France (Online)
- 26/02/2020, Elbereth conference 2020, Paris, France
- 11/02/2020, Celebrating the Legacy of the Spitzer Space Telescope, Pasadena, US (Poster)
- 20/05/2019, Exploring the Infrared Universe: The Promise of SPICA, Crete, Greece (Poster)

Schools, workshops, and visits

- 24/06/2022, CSST summer school (Online)
- 25/02/2022, JWebbinar 15 - PDRs4all: Simulate NIRCcam Observations of an Extended Source (Online)
- 25/02/2022, JWebbinar 13 - CEERS NIRCcam and MIRI Imaging (Online)
- 19/01/2022, The next generation mid/far-IR space missions – formulating a European perspective, European Mid/Far-IR community workshop, Paris, France (Online)
- 15/12/2021, Workshop on cosmic dust held by ‘The origin and fate of dust in the Universe’ project, Gothenburg, Sweden (Online)
- 12/07/2021, The Interstellar Medium of Galaxies: from the Epoch of Reionization to the Milky Way, International summer school, Banyuls-Sur-Mer, France (Online)
- 31/05/2021, Distant Galaxies: Observations and Models from $z>3$ up to Dark Ages, ED 127 course, Paris, France (Online)

2. Time corresponds to the starting date if the duration was more than one day, *idem* for the rest of events in this section.

- 30/11/2020, Observational Studies of Galaxy Formation and Evolution, University of Padova course, Italy (Online)
- 05/10/2020, Dark and Quiet Skies for Science and Society online workshop (Online)
- 14/09/2020, SPICA Science collaboration meeting (Online)
- 18/05/2020, SPICA Galaxy Evolution Working Group virtual meeting (Online)
- 24/02/2020, JWST France: Preparing for Cycle 1 Observations, workshop, Paris, France
- 13/11/2019, Collaborating visit to University of Tokyo for data reduction with the AKARI team, Tokyo, Japan
- 28/10/2019, SPICA Science collaboration meeting, Saclay, France
- 24/06/2019, PAHs in Extreme Environments, EUROPAH summer school, Toulouse, France
- 12/02/2019, Science Writing, EDP Science workshop, Saclay, France
- 05/11/2018, Bayesian Statistics, ED 127 course, Paris, France
- 10/10/2018, Fortran Base, IDRIS training, Orsay, France
- 04/10/2018, Journée de présentations-discussions autour de la mission spatiale SPICA, Paris, France

Bibliography

- Allamandola, L. J., Hudgins, D. M., & Sandford, S. A. 1999, *ApJ*, 511, L115–L119 P. 39
- Allamandola, L. J., Tielens, A. G. G. M., & Barker, J. R. 1985, *ApJ*, 290, L25–L28 P. 6, 19, 20, 34
- Allamandola, L. J., Tielens, A. G. G. M., & Barker, J. R. 1989, *ApJS*, 71, 733 P. 41, 127, 128
- Alton, P. B., Davies, J. I., & Bianchi, S. 1999, *A&A*, 343, 51–63 P. 76
- Alves, J. F., Lada, C. J., & Lada, E. A. 2001, *Nature*, 409, 159–161 P. 4
- Amelio, G. F., Tompsett, M. F., & Smith, G. E. 1970, *Bell System Technical Journal*, 49, 593–600 P. 13
- Andrews, H., Boersma, C., Werner, M. W., et al. 2015, *ApJ*, 807, 99 P. 42
- Andrews, H., Candian, A., & Tielens, A. G. G. M. 2016, *A&A*, 595, A23 P. 42
- Aniano, G., Draine, B. T., Gordon, K. D., & Sandstrom, K. 2011, *PASP*, 123, 1218 P. 68
- Aoyama, S., Hou, K.-C., Shimizu, I., et al. 2017, *MNRAS*, 466, 105–121 P. 33
- Arimatsu, K., Onaka, T., Sakon, I., et al. 2011, *PASP*, 123, 981 P. 53
- Asplund, M., Grevesse, N., Sauval, A. J., & Scott, P. 2009, *ARA&A*, 47, 481–522 P. 21
- Astropy Collaboration, Price-Whelan, A. M., Sipőcz, B. M., et al. 2018, *AJ*, 156, 123 P. 135
- Baba, S., Nakagawa, T., Usui, F., Yamagishi, M., & Onaka, T. 2019, *PASJ*, 71, 2 P. 49
- Bader, M. & Wagoner, C. B. 1970, *Appl. Opt.*, 9, 265–270 P. 11
- Bakes, E. L. O. & Tielens, A. G. G. M. 1994, *ApJ*, 427, 822 P. 40
- Barnard, E. E. 1919, *ApJ*, 49, 1–24 P. 3
- Barnard, J., McCulloch, R., & Meng, X.-L. 2000, *Statistica Sinica*, 10, 1281–1311 P. 104
- Bauschlicher, C. W., J., Boersma, C., Ricca, A., et al. 2010, *ApJS*, 189, 341–351 P. 38
- Bauschlicher, Charles W., J., Peeters, E., & Allamandola, L. J. 2008, *ApJ*, 678, 316–327 P. 37, 40, 127, 128
- Bauschlicher, Charles W., J., Ricca, A., Boersma, C., & Allamandola, L. J. 2018, *ApJS*, 234, 32 P. 38
- Becker, R. H., Fan, X., White, R. L., et al. 2001, *AJ*, 122, 2850–2857 P. 139
- Becquerel, E. 1842, *Mémoire sur le rayonnement chimique qui accompagne la lumière solaire et la lumière électrique* (Impr. royale) P. 13
- Beintema, D. A., van den Ancker, M. E., Molster, F. J., et al. 1996, *A&A*, 315, L369–L372 P. 6
- Beirão, P., Armus, L., Lehnert, M. D., et al. 2015, *MNRAS*, 451, 2640–2655 P. iii, 76, 129, 133
- Beirão, P., Brandl, B. R., Appleton, P. N., et al. 2008, *ApJ*, 676, 304–316 P. iii, 76, 129, 132

- Berlind, A. A., Quillen, A. C., Pogge, R. W., & Sellgren, K. 1997, *AJ*, **114**, 107–114 P. 7
- Berné, O., Habart, É., Peeters, E., et al. 2022, *PASP*, **134**, 054301 P. 42
- Berné, O., Joblin, C., Deville, Y., et al. 2007, *A&A*, **469**, 575–586 P. 39, 42, 86, 129
- Bernstein, M. P., Sandford, S. A., & Allamandola, L. J. 1996, *ApJ*, **472**, L127 P. 127, 128
- Bernstein, R. A., Freedman, W. L., & Madore, B. F. 2002, *ApJ*, **571**, 107–128 P. 4
- Bianchi, L., Clayton, G. C., Bohlin, R. C., Hutchings, J. B., & Massey, P. 1996, *ApJ*, **471**, 203 P. 7
- Biermann, P. & Harwit, M. 1980, *ApJ*, **241**, L105–L107 P. 34
- Bisschop, S. E., Fuchs, G. W., van Dishoeck, E. F., & Linnartz, H. 2007, *A&A*, **474**, 1061–1071 P. 19
- Bocchio, M., Jones, A. P., & Slavin, J. D. 2014, *A&A*, **570**, A32 P. 42
- Boersma, C., Bregman, J., & Allamandola, L. J. 2016, *ApJ*, **832**, 51 P. 39, 40
- Boggess, N. W., Mather, J. C., Weiss, R., et al. 1992, *ApJ*, **397**, 420 P. 11
- Bohren, C. F. & Huffman, D. R. 1998, *Absorption and Scattering by a Sphere*, in *Absorption and Scattering of Light by Small Particles*, Ch. 4 (John Wiley & Sons, Ltd), 82–129 P. 29
- Bok, B. J. & Reilly, E. F. 1947, *ApJ*, **105**, 255 P. 4
- Bonnamy, A., Jusko, P., Ji, M. C., et al. 2018, *PIRENEA 2: A new setup to study cosmic dust in the laboratory*, in 22nd International Mass Spectrometry Conference 2018 (IMSC 2018), Florence (Italy) P. 37
- Boogert, A. C. A., Gerakines, P. A., & Whittet, D. C. B. 2015, *ARA&A*, **53**, 541–581 P. 17
- Boulanger, F., Boissel, P., Cesarsky, D., & Ryter, C. 1998, *A&A*, **339**, 194–200 P. 86
- Bouwman, J., Ludwig, W., Awad, Z., et al. 2007, *A&A*, **476**, 995–1003 P. 19, 95
- Boyle, W. S. & Smith, G. E. 1970, *Bell System Technical Journal*, **49**, 587–593 P. 13
- Bron, E., Le Bourlot, J., & Le Petit, F. 2014, *A&A*, **569**, A100 P. 5
- Buragohain, M., Pathak, A., Sakon, I., & Onaka, T. 2020, *ApJ*, **892**, 11 P. 37
- Calzetti, D., Kennicutt, R. C., Engelbracht, C. W., et al. 2007, *ApJ*, **666**, 870–895 P. 5, 43
- Cami, J., Bernard-Salas, J., Peeters, E., & Malek, S. E. 2010, *Science*, **329**, 1180 P. 40, 127
- Cardelli, J. A., Clayton, G. C., & Mathis, J. S. 1989, *ApJ*, **345**, 245 P. 16
- Carey, S. J. 2010, *Some Thoughts on Cross-calibration in the Mid-Infrared*, in *Hubble after SM4. Preparing JWST*, 37 P. 66
- Carlos, M. 2020, *Dissociation induite par collisions d’hydrocarbures aromatiques polycycliques dans un piège à ions quadripolaire. Séparation des structures isomériques des composantes de la poussière cosmique*, PhD thesis, Université Toulouse 3 Paul Sabatier (UT3 Paul Sabatier), France P. 38
- Cayrel, R. & Schatzman, E. 1954, *Annales d’Astrophysique*, **17**, 555 P. 34

- Cesarsky, D., Lequeux, J., Abergel, A., et al. 1996, *A&A*, **315**, L309–L312 P. 42
- Chan, K. W., Roellig, T. L., Onaka, T., et al. 2000, *Characterization of the Unidentified Infrared Emission Bands in the Diffuse Interstellar Medium*, in ESA Special Publication, Vol. 456, ISO Beyond the Peaks: The 2nd ISO Workshop on Analytical Spectroscopy, ed. A. Salama, M. F. Kessler, K. Leech, & B. Schulz, 59 P. 6
- Chiar, J. E., Tielens, A. G. G. M., Whittet, D. C. B., et al. 2000, *ApJ*, **537**, 749–762 P. 131
- Clemens, D. P. & Barvainis, R. 1988, *ApJS*, **68**, 257 P. 4
- Clements, D. L., Sutherland, W. J., McMahon, R. G., & Saunders, W. 1996, *MNRAS*, **279**, 477–497 P. 4
- Code, A. D., Houck, T. E., McNall, J. F., Bless, R. C., & Lillie, C. F. 1970, *ApJ*, **161**, 377 P. 9
- Compiègne, M., Verstraete, L., Jones, A., et al. 2011, *A&A*, **525**, A103 P. 11, 24, 35, 36, 37, 96, 138
- Croiset, B. A., Candian, A., Berné, O., & Tielens, A. G. G. M. 2016, *A&A*, **590**, A26 P. 39
- Dale, D. A., Cohen, S. A., Johnson, L. C., et al. 2009, *ApJ*, **703**, 517–556 P. 72
- Danielson, R. E. 1961, *ApJ*, **134**, 275 P. 11
- Dartois, E., Marco, O., Muñoz-Caro, G. M., et al. 2004a, *A&A*, **423**, 549–558 P. 25
- Dartois, E., Muñoz Caro, G. M., Deboffle, D., & d’Hendecourt, L. 2004b, *A&A*, **423**, L33–L36 P. 25
- Daulton, T. L., Eisenhour, D. D., Bernatowicz, T. J., Lewis, R. S., & Buseck, P. R. 1996, *Geochim. Cosmochim. Acta*, **60**, 4853–4872 P. 25
- Davies, J. I., Baes, M., Bianchi, S., et al. 2017, *PASP*, **129**, 044102 P. 72
- Davis, Leverett, J. & Greenstein, J. L. 1951, *ApJ*, **114**, 206 P. 16
- Debye, P. 1909, *Annalen der Physik*, **335**, 57–136 P. 29
- Desert, F. X., Boulanger, F., & Puget, J. L. 1990, *A&A*, **237**, 215, (DBP90) P. 10, 35
- Desert, F. X., Boulanger, F., & Shore, S. N. 1986, *A&A*, **160**, 295–300 P. 32
- Devost, D., Brandl, B. R., Armus, L., et al. 2004, *ApJS*, **154**, 242–247 P. 71
- Dole, H., Lagache, G., Puget, J. L., et al. 2006, *A&A*, **451**, 417–429 P. 18
- Draine, B. T. 1978, *ApJS*, **36**, 595–619 P. 6
- Draine, B. T. 1985, *ApJS*, **57**, 587 P. 27
- Draine, B. T. 2009, *Interstellar Dust Models and Evolutionary Implications*, in Astronomical Society of the Pacific Conference Series, Vol. 414, Cosmic Dust - Near and Far, ed. T. Henning, E. Grün, & J. Steinacker, 453 P. 36, 37
- Draine, B. T. 2011, *Physics of the Interstellar and Intergalactic Medium* (Princeton University Press) P. 2, 30, 31
- Draine, B. T. & Anderson, N. 1985, *ApJ*, **292**, 494–499 P. 32
- Draine, B. T. & Hensley, B. S. 2021, *ApJ*, **909**, 94 P. 27, 28, 29
- Draine, B. T. & Lee, H. M. 1984, *ApJ*, **285**, 89, (DL84) P. 27, 34, 35
- Draine, B. T. & Li, A. 2001, *ApJ*, **551**, 807–824 P. 25
- Draine, B. T. & Li, A. 2007, *ApJ*, **657**, 810–837, dL07 P. iii, 24, 25, 35, 39, 40, 41, 96, 130, 131

- Draine, B. T. o. 2003a, *ARA&A*, **41**, 241–289 P. 3, 16, 24
- Draine, B. T. o. 2003b, *ApJ*, **598**, 1017–1025 P. 29, 96
- Duley, W. W. & Williams, D. A. 1981, *MNRAS*, **196**, 269–274 P. 20, 34
- Dwek, E., Arendt, R. G., Fixsen, D. J., et al. 1997, *ApJ*, **475**, 565–579 P. 11, 35
- Dwek, E. & Scalo, J. M. 1980, *ApJ*, **239**, 193–211 P. 36
- Ebizuka, N., Oka, K., Yamada, A., et al. 2004, *Grism and immersion grating for space telescope*, in ESA Special Publication, Vol. 554, 5th International Conference on Space Optics, ed. B. Warmbein, 743–749 P. 49
- Eddington, A. S. 1926, *The Internal Constitution of the Stars* (Cambridge University Press) P. 34
- Egusa, F. & AKARI/IRC Team. 2017, *Publication of Korean Astronomical Society*, **32**, 33–35 P. 53
- Egusa, F., Usui, F., Murata, K., et al. 2016, *PASJ*, **68**, 19 P. 53, 68
- Engelbracht, C. W., Gordon, K. D., Rieke, G. H., et al. 2005, *ApJ*, **628**, L29–L32 P. 44
- Engelbracht, C. W., Kundurthy, P., Gordon, K. D., et al. 2006, *ApJ*, **642**, L127–L132 P. 76, 129
- Erickson, E. & Meyer, A. 2013, *NASA’s Kuiper Airborne Observatory, 1971–1995: An Operations Retrospective with a View to SOFIA*, Tech. rep., NASA/SP-2013-216025 P. 12
- Falco, E. E., Kurtz, M. J., Geller, M. J., et al. 1999, *PASP*, **111**, 438–452 P. 7
- Fan, H., Hobbs, L. M., Dahlstrom, J. A., et al. 2019, *ApJ*, **878**, 151 P. 8
- Fazio, G. G., Hora, J. L., Allen, L. E., et al. 2004, *ApJS*, **154**, 10–17 P. 55
- Fioc, M. & Rocca-Volmerange, B. 1997, *A&A*, **326**, 950–962 P. 95
- Fioc, M. & Rocca-Volmerange, B. 2019, *A&A*, **623**, A143 P. 95
- Fitzpatrick, E. L., Massa, D., Gordon, K. D., Bohlin, R., & Clayton, G. C. 2019, *ApJ*, **886**, 108 P. 17
- Foley, R. J., Fox, O. D., McCully, C., et al. 2014, *MNRAS*, **443**, 2887–2906 P. 75, 129
- Förster Schreiber, N. M., Genzel, R., Lutz, D., Kunze, D., & Sternberg, A. 2001, *ApJ*, **552**, 544–571 P. 76, 126, 129, 132
- Förster Schreiber, N. M., Sauvage, M., Charmandaris, V., et al. 2003a, *A&A*, **399**, 833–855 P. 76, 129
- Förster Schreiber, N. M., Genzel, R., Lutz, D., & Sternberg, A. 2003b, *ApJ*, **599**, 193–217 P. 76, 129
- Förster Schreiber, N. M., Roussel, H., Sauvage, M., & Charmandaris, V. 2004, *A&A*, **419**, 501–516 P. 43
- Fraunhofer, J. 1817, *Annalen der Physik*, **56**, 264–313 P. 13
- Freedman, W. L., Hughes, S. M., Madore, B. F., et al. 1994, *ApJ*, **427**, 628 P. 73, 75
- Freedman, W. L., Madore, B. F., Gibson, B. K., et al. 2001, *ApJ*, **553**, 47–72 P. 73, 75
- Galametz, M., Hony, S., Albrecht, M., et al. 2016, *MNRAS*, **456**, 1767–1790 P. 42
- Galametz, M., Kennicutt, R. C., Calzetti, D., et al. 2013, *MNRAS*, **431**, 1956–1986 P. 5, 43
- Galliano, F. 2018, *MNRAS*, **476**, 1445–1469 P. 41, 85, 103

- Galliano, F. 2022, *Habilitation Thesis*, 1, (G22) P. 10, 17, 23, 25, 33, 36, 39, 87, 88
- Galliano, F., Galametz, M., & Jones, A. P. 2018, *ARA&A*, 56, 673–713 P. 8, 44
- Galliano, F., Hony, S., Bernard, J. P., et al. 2011, *A&A*, 536, A88 P. 96
- Galliano, F., Madden, S. C., Jones, A. P., Wilson, C. D., & Bernard, J. P. 2005, *A&A*, 434, 867–885 P. 44
- Galliano, F., Madden, S. C., Jones, A. P., et al. 2003, *A&A*, 407, 159–176 P. 44
- Galliano, F., Nersesian, A., Bianchi, S., et al. 2021, *A&A*, 649, A18 P. 36, 41, 44
- Galliano, F., Dwek, E., & Chanial, P. 2008a, *ApJ*, 672, 214–243 P. 44
- Galliano, F., Madden, S. C., Tielens, A. G. G. M., Peeters, E., & Jones, A. P. 2008b, *ApJ*, 679, 310–345 P. iii, 39, 40, 76, 86, 87, 129
- Gardner, J. P., Mather, J. C., Clampin, M., et al. 2006, *Space Sci. Rev.*, 123, 485–606 P. 11
- Geballe, T. R., Lacy, J. H., Persson, S. E., McGregor, P. J., & Soifer, B. T. 1985, *ApJ*, 292, 500–505 P. 127
- Geballe, T. R., Tielens, A. G. G. M., Allamandola, L. J., Moorhouse, A., & Brand, P. W. J. L. 1989, *ApJ*, 341, 278 P. 41, 127
- Geballe, T. R. & van der Veen, W. E. C. J. 1990, *A&A*, 235, L9 P. 127
- Genzel, R. & Cesarsky, C. J. 2000, *ARA&A*, 38, 761–814 P. 10
- Genzel, R., Lutz, D., Sturm, E., et al. 1998, *ApJ*, 498, 579–605 P. 42, 139
- Gibb, E. L., Whittet, D. C. B., Boogert, A. C. A., & Tielens, A. G. G. M. 2004, *ApJS*, 151, 35–73 P. 17
- Gillesen, S., Eisenhauer, F., Perrin, G., et al. 2010, *GRAVITY: a four-telescope beam combiner instrument for the VLTI*, in Society of Photo-Optical Instrumentation Engineers (SPIE) Conference Series, Vol. 7734, Optical and Infrared Interferometry II, ed. W. C. Danchi, F. Delplancke, & J. K. Rajagopal, 77340Y P. 12
- Gillett, F. C. & Forrest, W. J. 1973, *ApJ*, 179, 483 P. 34
- Gillett, F. C., Forrest, W. J., & Merrill, K. M. 1973, *ApJ*, 183, 87 P. 19, 20, 34
- Gillett, F. C., Kleinmann, D. E., Wright, E. L., & Capps, R. W. 1975a, *ApJ*, 198, L65–L68 P. 75, 129
- Gillett, F. C., Forrest, W. J., Merrill, K. M., Capps, R. W., & Soifer, B. T. 1975b, *ApJ*, 200, 609–620 P. 24
- Gordon, K. D., Engelbracht, C. W., Rieke, G. H., et al. 2008, *ApJ*, 682, 336–354 P. 42
- Gordon, K. D., Meixner, M., Meade, M. R., et al. 2011, *AJ*, 142, 102 P. 72
- Greenberg, J. M., Gillette, J. S., Muñoz Caro, G. M., et al. 2000, *ApJ*, 531, L71–L73 P. 42
- Greenstein, J. L. 1938, *ApJ*, 87, 151 P. 34
- Guhathakurta, P. & Draine, B. T. 1989, *ApJ*, 345, 230 P. 32
- Guillet, V., Fanciullo, L., Verstraete, L., et al. 2018, *A&A*, 610, A16 P. 18, 36
- Guillois, O., Ledoux, G., & Reynaud, C. 1999, *ApJ*, 521, L133–L36 P. 26

- Habart, E., Testi, L., Natta, A., & Carbillet, M. 2004, *ApJ*, 614, L129–L132 P. 26
- Hall, J. S. & Mikesell, A. H. 1949, *AJ*, 54, 187–188 P. 34
- Hanine, M., Meng, Z., Lu, S., et al. 2020, *ApJ*, 900, 188 P. 37
- Harris, A. W., Gry, C., & Bromage, G. E. 1984, *ApJ*, 284, 157–160 P. 23
- He, B. D., De Sa, C. M., Mitliagkas, I., & Ré, C. 2016, *Scan Order in Gibbs Sampling: Models in Which it Matters and Bounds on How Much*, in *Advances in Neural Information Processing Systems*, ed. D. Lee, M. Sugiyama, U. Luxburg, I. Guyon, & R. Garnett, Vol. 29 (Curran Associates, Inc.) P. 108
- Heckman, T. M., Armus, L., & Miley, G. K. 1990, *ApJS*, 74, 833 P. 76
- Heckman, T. M., Lehnert, M. D., Strickland, D. K., & Armus, L. 2000, *ApJS*, 129, 493–516 P. 76
- Henning, T. 2010, *ARA&A*, 48, 21–46 P. 24
- Henning, T., Begemann, B., Mutschke, H., & Dorschner, J. 1995, *A&AS*, 112, 143 P. 96
- Henry, R. B. C. & Worthey, G. 1999, *PASP*, 111, 919–945 P. 7
- Hensley, B. S. & Draine, B. T. 2020, *ApJ*, 895, 38 P. 41
- Hensley, B. S. & Draine, B. T. 2021, *ApJ*, 906, 73 P. 17, 18
- Heney, L. G. & Greenstein, J. L. 1941, *ApJ*, 93, 70–83 P. 28
- Herbig, G. H. 1995, *ARA&A*, 33, 19–74 P. 8
- Herschel, W. 1785, *Philosophical Transactions of the Royal Society of London Series I*, 75, 213–266 P. 3
- Herschel, W. 1800a, *Philosophical Transactions of the Royal Society of London Series I*, 90, 284–292 P. 8
- Herschel, W. 1800b, *Philosophical Transactions of the Royal Society of London Series I*, 90, 255–283 P. 8, 13
- Hertz, H. 1888, *Annalen der Physik*, 270, 155–170 P. 9
- Hickox, R. C., Myers, A. D., Greene, J. E., et al. 2017, *ApJ*, 849, 53 P. 14
- Higdon, S. J. U., Devost, D., Higdon, J. L., et al. 2004, *PASP*, 116, 975–984 P. 58
- Hiltner, W. A. . 1949a, *Science*, 109, 165 P. 34
- Hiltner, W. A. . 1949b, *ApJ*, 109, 471 P. 34
- Hirashita, H. 2012, *MNRAS*, 422, 1263–1271 P. 36
- Hogg, D. W. 1999, *arXiv e-prints*, astro-ph/9905116 P. 150
- Hollenbach, D. J. & Tielens, A. G. G. M. 1997, *ARA&A*, 35, 179–216 P. 3, 40
- Hollenbach, D. J. & Tielens, A. G. G. M. 1999, *Reviews of Modern Physics*, 71, 173–230 P. 6
- Hony, S., Van Kerckhoven, C., Peeters, E., et al. 2001, *A&A*, 370, 1030–1043 P. 6, 25, 39, 40, 41, 127, 128, 129
- Houck, J. R., Roellig, T. L., van Cleve, J., et al. 2004a, *ApJS*, 154, 18–24 P. 55
- Houck, J. R., Charmandaris, V., Brandl, B. R., et al. 2004b, *ApJS*, 154, 211–214 P. 13
- Hu, D., Galliano, F., Lebouteiller, V., et al. 2022a, MILES: Modeling mid-infrared emission with hierarchical Bayesian inference. I. A case study of M82, *in prep.* (Paper I) P. ii, 51, 85, 88, 129, 134
- Hu, D., Galliano, F., Lebouteiller, V., et al. 2022b, MILES: Modeling mid-infrared emission with hierarchical Bayesian inference. II. Properties of aromatic feature carriers in nearby Universe, *in prep.* (Paper II) P. iv, 134

- Hubble, E. & Tolman, R. C. 1935, [ApJ](#), **82**, 302 P. 152
- Hubble, E. P. 1926, [ApJ](#), **64**, 321–369 P. 7
- Hudgins, D. M. & Allamandola, L. J. 1999a, [ApJ](#), **513**, L69–L73 P. 40
- Hudgins, D. M. & Allamandola, L. J. o. 1999b, [ApJ](#), **516**, L41–L44 P. 25, 37, 40
- Hudgins, D. M., Bauschlicher, Charles W., J., & Allamandola, L. J. 2005, [ApJ](#), **632**, 316–332 P. 38
- Indebetouw, R., Mathis, J. S., Babler, B. L., et al. 2005, [ApJ](#), **619**, 931–938 P. 17
- IRS Instrument Team & Science User Support Team. 2011, [IRS Instrument Handbook \(version 5.0\)](#) P. 55, 56, 61, 66
- Izotov, Y. I., Chaffee, F. H., Foltz, C. B., et al. 1999, [ApJ](#), **527**, 757–777 P. 44
- Jäger, C., Dorschner, J., Mutschke, H., Posch, T., & Henning, T. 2003, [A&A](#), **408**, 193–204 P. 96
- Jenkins, E. B. 2009, [ApJ](#), **700**, 1299–1348 P. 22, 36
- Joblin, C., Leger, A., & Martin, P. 1992, [ApJ](#), **393**, L79 P. 24
- Joblin, C., Pech, C., Armengaud, M., Frabel, P., & Boissel, P. 2002, [A piece of interstellar medium in the laboratory: the PIRENEA experiment](#), in EAS Publications Series, Vol. 4, EAS Publications Series, ed. M. Giard, J. P. Bernard, A. Klotz, & I. Ristorcelli, 73–77 P. 37
- Joblin, C., Tielens, A. G. G. M., Allamandola, L. J., & Geballe, T. R. 1996, [ApJ](#), **458**, 610 P. 20, 41
- Jones, A. P. 2012, [A&A](#), **540**, A2 P. 25
- Jones, A. P. 2022, [A&A](#), **657**, A127 P. 26
- Jones, A. P., Fanciullo, L., Köhler, M., et al. 2013, [A&A](#), **558**, A62 P. 35, 96
- Jones, A. P., Köhler, M., Ysard, N., Bocchio, M., & Verstraete, L. 2017, [A&A](#), **602**, A46 P. 35, 96, 138
- Jones, A. P., Tielens, A. G. G. M., & Hollenbach, D. J. 1996, [ApJ](#), **469**, 740 P. 42
- Jones, A. P. & Ysard, N. 2022, [A&A](#), **657**, A128 P. 26
- Juvela, M. 2019, [A&A](#), **622**, A79 P. 138
- Kawada, M., Baba, H., Barthel, P. D., et al. 2007, [PASJ](#), **59**, S389 P. 46
- Kelly, B. C., Shetty, R., Stutz, A. M., et al. 2012, [ApJ](#), **752**, 55 P. 103
- Kemper, F., Vriend, W. J., & Tielens, A. G. G. M. 2004, [ApJ](#), **609**, 826–837 P. 24
- Kemper, F., Woods, P. M., Antoniou, V., et al. 2010, [PASP](#), **122**, 683 P. 138
- Kennicutt, Robert C., J., Armus, L., Bendo, G., et al. 2003, [PASP](#), **115**, 928–952 P. 72
- Kennicutt, R. C. & Evans, N. J. 2012, [ARA&A](#), **50**, 531–608 P. 5
- Kessler, M. F., Steinz, J. A., Anderegg, M. E., et al. 1996, [A&A](#), **315**, L27–L31 P. 10
- Kobayashi, N., Tokunaga, A. T., Terada, H., et al. 2000, [IRCS: infrared camera and spectrograph for the Subaru Telescope](#), in Society of Photo-Optical Instrumentation Engineers (SPIE) Conference Series, Vol. 4008, Optical and IR Telescope Instrumentation and Detectors, ed. M. Iye & A. F. Moorwood, 1056–1066 P. 12
- Krist, J. 2006, [Tiny Tim/Spitzer User’s Guide \(version 2.0\)](#) P. 67
- Krügel, E. 2003, [The physics of interstellar dust](#) (IOP Publishing) P. 26, 27

- Lada, C. J. 1987, *Star formation: from OB associations to protostars.*, in *Star Forming Regions*, ed. M. Peimbert & J. Jugaku, Vol. 115, 1 P. 13, 14
- Lada, C. J. & Wilking, B. A. 1984, *ApJ*, 287, 610–621 P. 13
- Lai, T. S. Y., Smith, J. D. T., Baba, S., Spoon, H. W. W., & Imanishi, M. 2020, *ApJ*, 905, 55 P. 58
- Laor, A. & Draine, B. T. 1993, *ApJ*, 402, 441 P. 96
- Le Bourlot, J., Le Petit, F., Pinto, C., Roueff, E., & Roy, F. 2012, *A&A*, 541, A76 P. 6, 133
- Le Floc’h, E., Mirabel, I. F., Laurent, O., et al. 2001, *A&A*, 367, 487–497 P. 7
- Le Page, V., Snow, T. P., & Bierbaum, V. M. 2003, *ApJ*, 584, 316–330 P. 41, 42
- Le Petit, F., Nehmé, C., Le Bourlot, J., & Roueff, E. 2006, *ApJS*, 164, 506–529 P. 138
- Lebouteiller, V., Barry, D. J., Goes, C., et al. 2015, *ApJS*, 218, 21 P. 67
- Lebouteiller, V., Barry, D. J., Spoon, H. W. W., et al. 2011, *ApJS*, 196, 8 P. 67
- Lebouteiller, V., Bernard-Salas, J., Sloan, G. C., & Barry, D. J. 2010, *PASP*, 122, 231 P. 58, 67
- Leger, A. & Puget, J. L. 1984, *A&A*, 137, L5–L8 P. 34
- Leinert, C., Graser, U., Przygodda, F., et al. 2003, *Ap&SS*, 286, 73–83 P. 12
- Li, A. 2005, *Interstellar grains—the 75th anniversary*, in *Journal of Physics Conference Series*, Vol. 6, Journal of Physics Conference Series, 229–248 P. 36
- Li, A. & Draine, B. T. 2001, *ApJ*, 554, 778–802, (LD01) P. 35, 96
- Lindblad, B. 1935, *Nature*, 135, 133–135 P. 34
- Lopez, B., Antonelli, P., Wolf, S., et al. 2008, *MATISSE: perspective of imaging in the mid-infrared at the VLTI*, in *Society of Photo-Optical Instrumentation Engineers (SPIE) Conference Series*, Vol. 7013, Optical and Infrared Interferometry, ed. M. Schöller, W. C. Danchi, & F. Delplancke, 70132B P. 12
- Lorente, R., Onaka, T., Ita, Y., et al. 2016, *AKARI IRC Data User Manual (version 2.2)* P. 47, 49, 53
- Lutz, D., Feuchtgruber, H., Genzel, R., et al. 1996, *A&A*, 315, L269–L272 P. 17
- Lynds, C. R. & Sandage, A. R. 1963, *ApJ*, 137, 1005 P. 73
- Mackie, C. J., Peeters, E., Bauschlicher, C. W., J., & Cami, J. 2015, *ApJ*, 799, 131 P. 37
- Madau, P. & Dickinson, M. 2014, *ARA&A*, 52, 415–486 P. 139
- Madden, S. C. 2000, *NewAR*, 44, 249–256 P. 42
- Madden, S. C., Cormier, D., Hony, S., et al. 2020, *A&A*, 643, A141 P. 13, 44
- Madden, S. C., Galliano, F., Jones, A. P., & Sauvage, M. 2006, *A&A*, 446, 877–896 P. 13, 42, 44, 132
- Mao, Q., van Duin, A. C., & Luo, K. 2017, *Carbon*, 121, 380–388 P. 37
- Maragkoudakis, A., Ivkovich, N., Peeters, E., et al. 2018, *MNRAS*, 481, 5370–5393 P. 131
- Maragkoudakis, A., Peeters, E., & Ricca, A. 2020, *MNRAS*, 494, 642–664 P. 129, 131
- Maret, S., Bergin, E. A., Neufeld, D. A., et al. 2009, *ApJ*, 698, 1244–1260 P. 71

- Martín-Hernández, N. L., Peeters, E., Morisset, C., et al. 2002, *A&A*, 381, 606–627 P. 44
- Martins, F., Schaerer, D., & Hillier, D. J. 2002, *A&A*, 382, 999–1004 P. 42
- Mather, J. C., Cheng, E. S., Cottingham, D. A., et al. 1994, *ApJ*, 420, 439 P. 18
- Mathis, J. S. 1970, *ApJ*, 159, 263 P. 34
- Mathis, J. S., Mezger, P. G., & Panagia, N. 1983, *A&A*, 128, 212–229 P. 31, 131
- Mathis, J. S., Rimpl, W., & Nordsieck, K. H. 1977, *ApJ*, 217, 425–433 P. 25, 34
- Matsuura, M., Dwek, E., Barlow, M. J., et al. 2015, *ApJ*, 800, 50 P. 36
- Mattila, K. 1970, *A&A*, 9, 53 P. 34
- Mattioda, A. L., Hudgins, D. M., Boersma, C., et al. 2020, *ApJS*, 251, 22 P. 37, 38
- Mattioda, A. L., Rutter, L., Parkhill, J., et al. 2008, *ApJ*, 680, 1243–1255 P. 24
- Mattsson, L. 2020, *MNRAS*, 491, 4334–4344 P. 35
- Maxwell, J. C. 1865, *Philosophical transactions of the Royal Society of London*, 459–512 P. 9
- McGuire, B. A., Loomis, R. A., Burkhardt, A. M., et al. 2021, *Science*, 371, 1265–1269 P. 41
- McKee, C. F. & Ostriker, J. P. 1977, *ApJ*, 218, 148–169 P. 2
- Meixner, M., Galliano, F., Hony, S., et al. 2010, *A&A*, 518, L71 P. 44
- Meixner, M., Gordon, K. D., Indebetouw, R., et al. 2006, *AJ*, 132, 2268–2288 P. 72
- Mezger, P. G., Duschl, W. J., & Zylka, R. 1996, *A&A Rev.*, 7, 289–388 P. 7
- Mie, G. 1908, *Annalen der Physik*, 330, 377–445 P. 29
- Mo, H., van den Bosch, F. C., & White, S. 2010, *Galaxy Formation and Evolution* (Cambridge University Press) P. 15
- Moré, J. J., Garbow, B. S., & Hillstom, K. E. 1980, *User Guide for MINPACK-1*, Tech. Rep. ANL-80-74, pub-ANL, pub-ANL:adr P. 101
- Moré, J. J., Sorensen, D. C., Hillstom, K. E., & Garbow, B. S. 1984, *The MINPACK project*, in Sources and development of mathematical software, ed. W. R. Cowell, Vol. 25, 88–111 P. 101
- Mori, T. I., Sakon, I., Onaka, T., et al. 2012, *ApJ*, 744, 68 P. 39
- Moutou, C., Verstraete, L., Léger, A., Sellgren, K., & Schmidt, W. 2000, *A&A*, 354, L17–L20 P. 127
- Mulas, G., Falvo, C., Cassam-Chenaï, P., & Joblin, C. 2018, *J. Chem. Phys.*, 149, 144102 P. 37
- Murakami, H., Baba, H., Barthel, P., et al. 2007, *PASJ*, 59, S369–S376 P. 10
- Neugebauer, G., Habing, H. J., van Duinen, R., et al. 1984, *ApJ*, 278, L1–L6 P. 10
- Nittler, L. R. & Ciesla, F. 2016, *ARA&A*, 54, 53–93 P. 36
- Öberg, K. I., Fraser, H. J., Boogert, A. C. A., et al. 2007, *A&A*, 462, 1187–1198 P. 19, 95
- O’Halloran, B., Satyapal, S., & Dudik, R. P. 2006, *ApJ*, 641, 795–800 P. 44
- Ohyama, Y., Onaka, T., Matsuhara, H., et al. 2007, *PASJ*, 59, S411 P. 53, 66, 100
- Onaka, T., Matsuhara, H., Wada, T., et al. 2007, *PASJ*, 59, S401 P. 46, 47, 53, 66

- Oort, J. H. & van de Hulst, H. C. 1946, *Bull. Astron. Inst. Netherlands*, 10, 187 P. 34
- Paradis, D., Reach, W. T., Bernard, J.-P., et al. 2009, *AJ*, 138, 196–209 P. 44
- Peebles, P. J. E. 1993, *Principles of Physical Cosmology* (Princeton university press) P. 149
- Peeters, E., Bauschlicher, Charles W., J., Allamandola, L. J., et al. 2017, *ApJ*, 836, 198 P. 42, 43, 88, 127, 128
- Peeters, E., Martín-Hernández, N. L., Damour, F., et al. 2002a, *A&A*, 381, 571–605 P. 44
- Peeters, E., Hony, S., Van Kerckhoven, C., et al. 2002b, *A&A*, 390, 1089–1113 P. 127, 128
- Peeters, E., Spoon, H. W. W., & Tielens, A. G. G. M. 2004a, *ApJ*, 613, 986–1003 P. 5, 43, 139
- Peeters, E., Mattioda, A. L., Hudgins, D. M., & Allamandola, L. J. 2004b, *ApJ*, 617, L65–L68 P. 127, 128
- Peeters, E., Tielens, A. G. G. M., Allamandola, L. J., & Wolfire, M. G. 2012, *ApJ*, 747, 44 P. 127, 128
- Pereira-Santaella, M., Alonso-Herrero, A., Rieke, G. H., et al. 2010, *ApJS*, 188, 447–472 P. 64, 67, 68
- Petrov, R. G., Malbet, F., Weigelt, G., et al. 2007, *A&A*, 464, 1–12 P. 12
- Pety, J., Teyssier, D., Fossé, D., et al. 2005, *A&A*, 435, 885–899 P. 6
- Pilbratt, G. L., Riedinger, J. R., Passvogel, T., et al. 2010, *A&A*, 518, L1 P. 10
- Pilleri, P., Montillaud, J., Berné, O., & Joblin, C. 2012, *A&A*, 542, A69 P. 71, 87, 88
- Planck Collaboration, Adam, R., Ade, P. A. R., et al. 2016a, *A&A*, 596, A103 P. 11, 18
- Planck Collaboration, Ade, P. A. R., Alves, M. I. R., et al. 2015, *A&A*, 576, A107 P. 7
- Planck Collaboration, Aghanim, N., Arnaud, M., et al. 2016b, *A&A*, 594, A11 P. 18
- Plummer, M., Best, N., Cowles, K., & Vines, K. 2006, *R news*, 6, 7–11 P. 107
- Pogson, N. 1856, *MNRAS*, 17, 12–15 P. 15
- Povich, M. S., Stone, J. M., Churchwell, E., et al. 2007, *ApJ*, 660, 346–362 P. 42
- Press, W. H., Teukolsky, S. A., Vetterling, W. T., & Flannery, B. P. 2007, *Numerical recipes 3rd edition: The art of scientific computing* (Cambridge university press) P. 101, 107, 146
- Rapacioli, M., Joblin, C., & Boissel, P. 2005a, *A&A*, 429, 193–204 P. 86
- Rapacioli, M., Calvo, F., Spiegelman, F., Joblin, C., & Wales, D. J. 2005b, *Journal of Physical Chemistry A*, 109, 2487–2497 P. 37
- Rau, S.-J., Hirashita, H., & Murga, M. 2019, *MNRAS*, 489, 5218–5224 P. 44, 133
- Rémy-Ruyer, A., Madden, S. C., Galliano, F., et al. 2014, *A&A*, 563, A31 P. 41
- Rémy-Ruyer, A., Madden, S. C., Galliano, F., et al. 2015, *A&A*, 582, A121 P. 42
- Rieke, G. H., Lebofsky, M. J., Thompson, R. I., Low, F. J., & Tokunaga, A. T. 1980, *ApJ*, 238, 24–40 P. 75, 76
- Rieke, G. H., Young, E. T., Engelbracht, C. W., et al. 2004, *ApJS*, 154, 25–29 P. 55

- Riesenfeld, R. F. 1973, *Applications Of B-Spline Approximation To Geometric Problems Of Computer-Aided Design*, PhD thesis, Syracuse University (SU), US P. 70
- Ritter, J. W. 1801, *Annalen der Physik*, 7, 501–528 P. 9
- Robertson, J. 2003, *Semiconductor Science and Technology*, 18, S12–S19 P. 25
- Roche, P. F., Aitken, D. K., Smith, C. H., & Ward, M. J. 1991, *MNRAS*, 248, 606 P. 42
- Roelfsema, P. R., Cox, P., Tielens, A. G. G. M., et al. 1996, *A&A*, 315, L289–L292 P. 6
- Röntgen, W. C. 1895, *Sitzungsber Phys Med Ges Wurtzburg*, 9, 132–141 P. 9
- Russell, R. W., Soifer, B. T., & Forrest, W. J. 1975, *ApJ*, 198, L41–L43 P. 24
- Russell, R. W., Soifer, B. T., & Willner, S. P. 1977, *ApJ*, 217, L149 P. 127
- Rybicki, G. B. & Lightman, A. P. 1979, *Radiative processes in astrophysics* (John Wiley & Sons) P. 142
- Sabbah, H., Bonnamy, A., Papanastasiou, D., et al. 2017, *ApJ*, 843, 34 P. 37
- Salpeter, E. E. 1955, *ApJ*, 121, 161 P. 15
- Sandstrom, K. M., Bolatto, A. D., Bot, C., et al. 2012, *ApJ*, 744, 20 P. 44
- Sandstrom, K. M., Bolatto, A. D., Draine, B. T., Bot, C., & Stanimirović, S. 2010, *ApJ*, 715, 701–723 P. 44
- Sandstrom, K. M., Bolatto, A. D., Stanimirović, S., van Loon, J. T., & Smith, J. D. T. 2009, *ApJ*, 696, 2138–2154 P. 67
- Saslaw, W. C. & Gaustad, J. E. 1969, *Nature*, 221, 160–162 P. 26
- Savage, B. D. & Bohlin, R. C. 1979, *ApJ*, 229, 136–146 P. 22
- Savage, B. D. & Sembach, K. R. 1996, *ARA&A*, 34, 279–330 P. 21, 22
- Schalén, C. 1929, *Astronomische Nachrichten*, 236, 249 P. 34
- Schoenberg, E. & Jung, B. 1937, *Astronomische Mitteilungen der Koeniglichen Universitaets-Sternwarte zu Breslau*, 4, 61–78 P. 34
- Sellgren, K., Werner, M. W., Ingalls, J. G., et al. 2010, *ApJ*, 722, L54–L57 P. 40, 127
- Seok, J. Y., Hirashita, H., & Asano, R. S. 2014, *MNRAS*, 439, 2186–2196 P. 44
- Sherman, J. & Morrison, W. J. 1950, *The Annals of Mathematical Statistics*, 21, 124–127 P. 147
- Shopbell, P. L. & Bland-Hawthorn, J. 1998, *ApJ*, 493, 129–153 P. 76
- Sidhu, A. K. 2021, *Revisiting polycyclic aromatic hydrocarbon emission in Photodissociation regions*, PhD thesis, University of Western Ontario (UWO), Canada P. 24, 40
- Slavin, J. D., Dwek, E., & Jones, A. P. 2015, *ApJ*, 803, 7 P. 37
- Sloan, G. C., Bregman, J. D., Geballe, T. R., Allamandola, L. J., & Woodward, E. 1997, *ApJ*, 474, 735–740 P. 127
- Sloan, G. C., Herter, T. L., Charmandaris, V., et al. 2015, *AJ*, 149, 11 P. 64, 66, 69
- Smith, C. H., Aitken, D. K., & Roche, P. F. 1989, *MNRAS*, 241, 425–431 P. 97, 124
- Smith, J. D. T., Draine, B. T., Dale, D. A., et al. 2007a, *ApJ*, 656, 770–791 P. 39, 58, 88
- Smith, J. D. T., Armus, L., Dale, D. A., et al. 2007b, *PASP*, 119, 1133–1144 P. 58, 68

- Sofia, U. J., Lauroesch, J. T., Meyer, D. M., & Cartledge, S. I. B. 2004, *ApJ*, 605, 272–277 P. 130
- Sofia, U. J. & Meyer, D. M. 2001, *ApJ*, 554, L221–L224 P. 7
- Soifer, B. T. & Neugebauer, G. 1991, *AJ*, 101, 354 P. 4
- Soifer, B. T., Neugebauer, G., & Houck, J. R. 1987, *ARA&A*, 25, 187–230 P. 10
- Sokal, A. 1997, *Monte Carlo Methods in Statistical Mechanics: Foundations and New Algorithms*, in *Functional Integration: Basics and Applications*, ed. C. DeWitt-Morette, P. Cartier, & A. Folacci (Springer US), 131–192 P. 107
- Spitzer, Lyman, J. 1946, *Astronomical advantages of an extra-terrestrial observatory*, (unpublished RAND report) reprinted *Astr.* P. 9
- Spitzer Science Center (SSC). 2007, *Spitzer Space Telescope Observer’s Manual (version 8.0)* P. 66, 69, 70
- SSC Science User Support Team, Instrument Support Teams, & IRSA Science User Support Team. 2017, *Spitzer Data Analysis Cookbook (version 6.0)* P. 58
- Stecher, T. P. 1965, *ApJ*, 142, 1683 P. 34
- Strassen, V. 1969, *Numerische mathematik*, 13, 354–356 P. 146
- Strickland, D. K., Heckman, T. M., Colbert, E. J. M., Hoopes, C. G., & Weaver, K. A. 2004, *ApJS*, 151, 193–236 P. 76
- Student. 1908, *Biometrika*, 6, 1–25 P. 145
- Sutherland, W., Emerson, J., Dalton, G., et al. 2015, *A&A*, 575, A25 P. 12
- Tauber, J. A., Mandolesi, N., Puget, J. L., et al. 2010, *A&A*, 520, A1 P. 11
- Taylor, C. L., Walter, F., & Yun, M. S. 2001, *ApJ*, 562, L43–L46 P. 76
- Thornley, M. D., Förster Schreiber, N. M., Lutz, D., et al. 2000, *ApJ*, 539, 641–657 P. 13
- Thuan, T. X., Sauvage, M., & Madden, S. 1999, *ApJ*, 516, 783–787 P. 13
- Tielens, A. G. G. M. 2005, *The Physics and Chemistry of the Interstellar Medium* (Cambridge University Press) P. 2, 18
- Tielens, A. G. G. M. 2008, *ARA&A*, 46, 289–337 P. 24, 37, 40, 41, 129
- Trumpler, R. J. 1930, *PASP*, 42, 214 P. 34
- Trčka, A., Baes, M., Camps, P., et al. 2020, *MNRAS*, 494, 2823–2838 P. 33
- van Dishoeck, E. F. 2004, *ARA&A*, 42, 119–167 P. 10
- Van Kerckhoven, C., Hony, S., Peeters, E., et al. 2000, *A&A*, 357, 1013–1019 P. 127
- Venghaus, H. 1977, *Physica Status Solidi B Basic Research*, 81, 221–225 P. 25
- Verma, A., Charmandaris, V., Klaas, U., Lutz, D., & Haas, M. 2005, *Space Sci. Rev.*, 119, 355–407 P. 42
- Vermeij, R., Peeters, E., Tielens, A. G. G. M., & van der Hulst, J. M. 2002, *A&A*, 382, 1042–1051 P. 86
- Verstraete, L., Puget, J. L., Falgarone, E., et al. 1996, *A&A*, 315, L337–L340 P. 6, 86
- Villani, M. & Larsson, R. 2006, *Communications in Statistics - Theory and Methods*, 35, 1123–1140 P. 144
- Villard, P. 1900, *C. R. Acad. Sci. Paris*, 130, 1010–1011 P. 9
- Wakelam, V. & Herbst, E. 2008, *ApJ*, 680, 371–383 P. 6

- Walter, F., Weiss, A., & Scoville, N. 2002, *ApJ*, **580**, L21–L25 P. 76
- Weedman, D. W., Hao, L., Higdon, S. J. U., et al. 2005, *ApJ*, **633**, 706–716 P. 42
- Weinberg, S. 1972, *Gravitation and Cosmology: Principles and Applications of the General Theory of Relativity* (John Wiley & Sons) P. 151
- Weingartner, J. C. & Draine, B. T. 2001, *ApJ*, **548**, 296–309, (WD01) P. 7, 19, 95, 96, 112, 126
- Werner, M. W., Roellig, T. L., Low, F. J., et al. 2004, *ApJS*, **154**, 1–9 P. 10
- White, D. W., Gerakines, P. A., Cook, A. M., & Whittet, D. C. B. 2009, *ApJS*, **180**, 182–191 P. 97
- Wollaston, W. H. 1802, *Philosophical Transactions of the Royal Society of London*, 365–380 P. 13
- Wolf, N. J. & Ney, E. P. 1969, *ApJ*, **155**, L181 P. 34
- Wooten, F. 1972, *Optical properties of solids* (Academic Press), 1–14 P. 26
- Wright, E. L., Eisenhardt, P. R. M., Mainzer, A. K., et al. 2010, *AJ*, **140**, 1868–1881 P. 10
- Wu, R., Galliano, F., & Onaka, T. 2018, *Evolution of the Unidentified Infrared Bands in the Nucleus of the Starburst Galaxy NGC 1097*, in *The Cosmic Wheel and the Legacy of the AKARI Archive: From Galaxies and Stars to Planets and Life*, ed. T. Ootsubo, I. Yamamura, K. Murata, & T. Onaka, 133–136 P. 19
- Wu, Y., Charmandaris, V., Hao, L., et al. 2006, *ApJ*, **639**, 157–172 P. 13, 44
- Xie, Y., Ho, L. C., Li, A., & Shangguan, J. 2018, *ApJ*, **860**, 154 P. 88
- Xue, M., Jiang, B. W., Gao, J., et al. 2016, *ApJS*, **224**, 23 P. 17
- Yamagishi, M., Kaneda, H., Ishihara, D., et al. 2012, *A&A*, **541**, A10 P. iii, 76, 129, 132
- Yamagishi, M., Kaneda, H., Ishihara, D., et al. 2011, *ApJ*, **731**, L20 P. 76
- Yamagishi, M., Kaneda, H., Ishihara, D., et al. 2015, *ApJ*, **807**, 29 P. 95
- Young, E. T., Becklin, E. E., Marcum, P. M., et al. 2012, *ApJ*, **749**, L17 P. 12
- Yun, M. S., Ho, P. T. P., & Lo, K. Y. 1994, *Nature*, **372**, 530–532 P. 75
- Zhang, L., Ho, L. C., & Xie, Y. 2021, *AJ*, **161**, 29 P. 67
- Zubko, V., Dwek, E., & Arendt, R. G. 2004, *ApJS*, **152**, 211–249, (ZDA04) P. iii, 24, 35, 37, 41, 96, 131
- Zubko, V. G., Mennella, V., Colangeli, L., & Bussoletti, E. 1996, *MNRAS*, **282**, 1321–1329 P. 27, 28, 96

Index

Symbols

MILES

calculation time test	107
HB	103
initial guess	91
non-HB	103
parameter limits	91
plot template	114
reparameterization	91, 102
scan order	108
three classes of parameters	103

A

abundance	7
gas-phase abundance	21, 130
total abundance	21
acceptance probability	105
albedo	28
amorphous carbon/a-C(:H)	23, 25, 27, 28, 33, 35, 36, 128, 132
atomic gas	
H _I	2, 75, 94
autocorrelation	
ACF	107, 117, 118, 160
effective sample size	107, 108
integrated autocorrelation time	107–109, 117, 159
lag	106

B

B-spline	70
Bayes' theorem	101
Bayesian inference	
evidence	102
likelihood	102–104
posterior	102, 103, 105
prior	103
prior distribution	102
Bayesian modeling	
burn-in	106
hyperparameter	103
MCMC	ii, 105–108, 112, 115–119, 123, 124, 146, 147, 155, 160
median model	115
model parameter	99, 103
nuisance parameter	102, 103
blackbody radiation	
blackbody	30, 95, 97, 98, 110, 112, 122
modified blackbody	9, 93, 95, 98, 111
Rayleigh-Jeans regime	95
Stefan–Boltzmann law	95
Wien's displacement law	93
Boltzmann constant	30
boot-strapping method	49, 51, 65, 74, 82

C

calibration factor	100, 102, 105, 106, 110, 111, 114, 122
--------------------	--

calibration offset	100, 103	Doppler shift	150
cosmic ray	61	dwarf galaxy	19, 42
cross-section		E	
absorption cross-section	28	electric permittivity	26
differential scattering cross-section	28	enthalpy	32
extinction cross-section	26, 28, 143	error analysis	
scattering cross-section	28	calibration error/uncertainty	50, 62, 65, 67, 81, 82, 86, 100, 103
D		pointing error/uncertainty	50, 53, 64, 65, 73
Data processing		statistical error/uncertainty	49, 51, 61, 64, 99
IRC sub-slit	76	systematic error/uncertainty	50, 61, 65, 99, 100
IRS sub-slit/order	56	error vs. uncertainty	49
database		extinction	3, 9, 15
PAHdb	37, 38	dichroic extinction	16
SHA	57–59, 78, 135	extinction curve	7
depletion	21	extinction efficiency	28
depletion factor	21	extinction law	7
depletion strength factor	22	visual extinction	3, 86
desorption	5	visual-to-selective extinction	16
dielectric function	18, 26, 27, 29	extinction curve	26
distribution		F	
bi-modal distribution	116	field-of-view	47, 66, 75
multi-modal distribution	114	free-free emission	2, 8
uni-modal distribution	107	fullerene	
distribution laws		C ₆₀	40, 42, 127, 128
Cauchy distribution	145	C ₇₀	42
Gaussian/normal distribution	49, 90, 93, 98, 99, 102, 103, 109, 110, 115	G	
inverse Wishart distribution	104	Gibbs sampler	105
log-normal distribution	35, 103, 145	Gibbs sampling	85, 105, 108
normal distribution	144	grism	48
split-Lorentz distribution	89–91, 98, 109	H	
split-normal distribution	51, 89, 144	Habing field	40
Student's t-distribution	102, 103, 145		

I

infrared

far-infrared (FIR) 9–13, 18, 34
mid-infrared (MIR) ... i–iv, ix, 8–14, 17–19, 24, 37, 39,
41, 43–45, 49, 55, 69, 74–76, 85, 86, 93, 95, 97, 99, 109, 111,
121, 124, 127, 129, 132–134, 137, 142, 168

near-infrared (NIR) 9–14, 17, 18, 29, 75, 76

total infrared (TIR) 5, 43, 76

initial mass function (IMF) 15

instruments

Spitzer/IRAC ii, 68, 72, 81, 135, 162

Spitzer/IRS ii–iv, ix, 19, 45, 47, 49, 50, 56, 67–70,
74, 76–80, 89, 90, 93, 100, 109, 114, 127, 134, 135, 137, 138,
161, 162, 164, 168, 182

Spitzer/MIPS ii, 68, 72, 80, 135, 162

AKARI/IRC ii–iv, ix, 19, 45, 47, 49, 56, 64, 68,
69, 74, 76, 77, 79, 93, 100, 109, 114, 134, 135, 137, 162, 164,
168, 182

ISO-CAM 43, 76, 87

ISO-SWS ii, 76, 89, 90, 127

JWST/MIRI 109

intensity

specific intensity 142

inter-calibration 68, 71, 77

interstellar dust ... ix, 1, 3, 4, 9, 10, 15, 23, 24, 28, 29, 33, 34,
36, 141

interstellar medium 131, 132

ionization balance 40, 129

ionization parameter 40, 129

ionized gas

H II iv, 2, 42

H II region 2, 3, 6, 8, 42, 44, 127

K

Kramers-Kronig relation 27

L

Levenberg-Marquardt algorithm 82, 101, 130, 162

line-of-sight/sightline 3, 7, 16, 17, 21, 22, 141

low-metallicity 13, 19, 44, 111, 132

M

mean free path 138, 143

metallicity 2, 7, 13, 21

Metropolis-Hastings algorithm 105

Mie scattering 29

Milky Way 3, 6, 7, 16, 21, 24, 34, 36

Galactic 2, 7, 11, 17, 18, 23, 33–35, 41, 129, 134

Galaxy 2, 7

model

DHGL 35, 37, 41, 96

MRN 34, 35

THEMIS 33, 35, 36, 138

models

DBP90 35

DL07 35, 39, 41

DL84 34, 35

LD01 35

ZDA04 35, 37, 41, 96, 131

molecular gas

CH₄ 9

CO 13, 17, 95

CO₂ 9, 17, 19, 95, 97

H₂ iv, 2, 3, 5, 6, 13, 94, 97, 110, 112, 113, 133, 134

H₂O 9, 13, 17, 19, 34, 95, 126

N₂O 9

O₂ 13

O₃ 9

Monte Carlo 34, 37, 50, 51, 82

N

nano-diamond 25

O

observatories

Herschel 10, 11, 35

Planck 18, 35, 36

SOFIA 12, 183

Spitzer .. iii, 7, 10, 11, 35, 42, 43, 45, 51, 55, 57, 58, 66,
67, 80, 134, 135, 138, 183

AKARI ii, iii, 11, 45, 46, 48, 49, 51, 53, 59, 64, 77, 134,
135, 172–181, 183, 185

COBE 11

IRAS 10, 34, 55

IRTF 12

ISO i, 10, 17, 42, 55

JWST iv, ix, 11, 42, 45, 93, 127, 131, 134, 138, 183

KAO 12, 127

UKIRT 12, 127

WISE 10, 53

optical depth 16, 95, 143

optically thick/opaque 143

optically thin/transparent 143

Orion

Orion Bar 20, 41, 127, 130

Orion Nebula 2

oscillator

damping constant 26

Lorentz oscillator 26

natural frequency 26

plasma frequency 26

resonant frequency 26, 27

P

PAH .. i, iii, iv, 6, 19, 20, 23–25, 34, 35, 37–44, 86, 124, 127,
129–132, 134, 137–139

hetero-atom-substituted PAH 127

hydrogenated PAH (HPAH) iii, iv, 137, 138

PAH cluster 127

PAH complex 127

parsec (pc) 2

PDR i, iv, 3, 6, 13, 41–43, 89, 130, 138

phonon 32

photoelectric 2, 3, 6

photoelectron 2, 6

photoelectric efficiency 6

Planck constant 30

Planck's law 30

planetary nebula 19, 20, 34, 89

polarization 7

polarization/polarized 16, 18

prism 13, 48

R

radial velocity 73, 150

radiation hardness 13

radiative transfer 16, 141, 142

emissivity 31, 143

extinction coefficient 143

opacity 30, 143

source function 143

Rayleigh scattering 29

Red Rectangle 89

reddening 4, 5

redshift 139, 150

cosmological redshift 150

high redshift 7, 149

reflection nebula 127

S

sample

MY-catalog 135

RW-catalog 135

scattering phase function 28

signal-to-noise ratio (S/N ratio) 55, 61, 62, 64, 65, 76, 82–86,
88, 89, 110–112, 114, 119, 122, 132, 153, 168

software

Aladin 53

CUBISM 57–64, 66, 67, 70, 71, 77, 135

Emacs 182

HerBIE 85

IRSCLEAN 58

MILES . ii, iii, ix, 85, 88, 92, 96, 98, 109, 117, 122, 127,
130, 134, 138, 153, 162, 168, 182

MINPACK 82, 101

MIRAGE ii, 51, 67, 69, 74, 85, 134, 135, 162, 182

Meudon PDR 138

PAHfit 58, 88

PAHtat 87, 88

PÉGASE 95, 98

SAOImageDS9 53

SMART 58

SOC 138

SWarp 135

SwING 91, 135

rapyuta 182

speed of light 30, 149

standard deviation .. 49–51, 59, 62, 63, 91, 99, 104–109, 117,
118, 122, 144–146, 159

star formation

SFH 139 129

SFR 5, 7, 33, 43, 44, 76, 139

sSFR 7

statistical inference

likelihood 100

maximum likelihood estimate 101

Subaru 12

survey

2MASS 53

DustPedia 72, 79

LVL 72

SAGE-LMC 72

SAGE-SMC 72

SDSS 14

SINGS 58, 72, 80, 82, 84, 168

UKIDSS 14

WISE 14

synchrotron emission 2, 5, 8

synthetic photometry 69, 72, 81

T

thermal equilibrium 30

U

UIB complexes 110, 128

11.3- μm aromatic complex 124, 129

12.7- μm aromatic complex 111, 129

3.4- μm aliphatic complex 111, 126, 129, 131

6.2- μm aromatic complex 111, 129

7.7- μm aromatic complex 111, 122, 129

ultraviolet

far-ultraviolet (FUV) 3, 6, 16, 40, 129, 139

UV field intensity (G_0) 40, 129

V

vibrational modes . 9, 17, 18, 20, 24, 26, 34, 37, 40, 126, 127,

List of Acronyms

ACF AutoCorrelation Function. 106, 107, 117, 118, 160	HIM Hot Ionized Medium. 2, 8
AGB Asymptotic Giant Branch. 36, 44	HPAH Hydrogenated Polycyclic Aromatic Hydrocarbon. iii, iv, 127, 137, 138
AGN Active Galactic Nucleus. iii, 7, 14, 17, 19, 42, 57, 111, 139	HWHM Half Width at Half-Maximum. 91
AOR Astronomical Observation Request. 57–59, 62, 77, 78, 134, 211	IMF Initial Mass Function. 15
AOT Astronomical Observation Template. 48, 49, 56, 77	IP Ionization Potential. 6, 42
BCD Basic Calibrated Data. 57–64	ISM InterStellar Medium. ix, 2, 3, 6, 7, 11–14, 17–19, 21–24, 26, 33–36, 40–42, 127, 131, 133, 137, 139
CCD Charge-Coupled Device. 13	ISRF InterStellar Radiation Field. iii, iv, 30, 31, 39, 43, 44, 129, 131–133, 138, 207
CCSN Core-Collapse SuperNova. 36	LIRG Luminous InfraRed Galaxy. 10
CIB Cosmic Infrared Background. 18	LMC Large Magellanic Cloud. 7, 44, 55
CMB Cosmic Microwave Background. 18	LTG Late-Type Galaxy. 7, 18, 19
CNM Cool Neutral Medium. 2, 36	MCMC Markov Chain Monte Carlo. ii, 105–108, 112, 115–119, 123, 124, 146, 147, 155, 160
DCE Data Collection Event. 57, 58	MIR Mid-InfraRed. i–iv, ix, 1, 9–14, 17–19, 24, 37, 39, 41, 43–45, 55, 69, 74–76, 85, 86, 93, 95, 97, 99, 109, 111, 121, 124, 127, 129, 132–134, 137, 168
DFT Density Functional Theory. 37	MSM Modified Sherman-Morrison. 108, 148
DIB Diffuse Interstellar Band. 8	NIR Near-InfraRed. 9–14, 17, 18, 29, 75, 76
ETG Early-Type Galaxy. 7, 18, 19	NUV Near-UltraViolet. 3
FFT Fast Fourier Transform. 107	PAH Polycyclic Aromatic Hydrocarbon. i, iii, iv, ix, 1, 6, 19,
FIR Far-InfraRed. 9–13, 18, 34	
FUV Far-UltraViolet. 2, 3, 6, 16, 40, 129, 139	
FWHM Full Width at Half-Maximum. 51–53, 67, 68, 71, 91	
HB Hierarchical Bayesian. ii, iv	

20, 23–25, 34, 35, 37–44, 86, 124, 127, 129–132, 134, 137–139, 209

PBCD Post-Basic Calibrated Data. 57

PDF Probability Distribution Function. 99, 100, 102, 122

PDR PhotoDissociation Region. i, iv, 3, 6, 13, 41–43, 89, 130, 138

PSF Point Spread Function. 51–53, 64, 66–69, 71, 73, 135

QSO Quasi-Stellar Object. 7, 14

SED Spectral Energy Distribution. ix, 7, 8, 10, 13–15, 17, 33, 34, 41, 103, 139, 207

SFH Star Formation History. 139, 152

SFR Star Formation Rate. 5, 7, 33, 43, 44, 76, 139

SMC Small Magellanic Cloud. 7, 44, 60

SN SuperNova. 2, 37, 44, 75

SSC Spitzer Science Center. 11, 57, 58, 61

sSFR specific Star Formation Rate. 7

TIR Total InfraRed. 5, 43, 76

UIB Unidentified Infrared Band. i, ii, 1, 9, 18–20, 24, 34, 36, 39, 42, 43, 57, 76, 80, 82, 85, 86, 89–93, 95, 97, 109–112, 114, 118, 119, 122–124, 126–129, 131, 139, 153, 162

ULIRG UltraLuminous InfraRed Galaxy. 4, 10

VSG Very Small Grain. 35, 42, 43, 86

WCS World Coordinate System. 53

WIM Warm Ionized Medium. 2, 8

WNM Warm Neutral Medium. 2

YSO Young Stellar Object. 13, 14, 127

List of Figures

1.1	Optical (BVI) and infrared (JHK) images of the globule Barnard 68 obtained with ESO's VLT and NTT. . . .	4
1.2	Mechanism of H ₂ formation on grain surfaces.	5
1.3	Schematic of the photoelectric heating mechanism.	6
1.4	Panchromatic spectral energy distribution (SED) of a synthetic typical late-type galaxy.	8
1.5	Atmosphere absorbance and multi-wavelength astronomy.	10
1.6	Infrared space telescopes.	11
1.7	Airborne and ground-based infrared observatories.	12
1.8	Infrared SEDs of accretion disks, on stellar and galaxy scales.	14
1.9	Synthetic stellar spectra.	15
1.10	Extinction by dust and ices.	17
1.11	Galaxy spectra observed in the mid-infrared.	19
1.12	Spectral identification of UIBs.	20
1.13	Depletions in cool diffuse clouds towards ζ Oph.	22
1.14	Solid-state structure of interstellar dust candidates.	23
1.15	Vibrational modes and structures of PAHs.	25
1.16	Dielectric functions of different materials.	27
1.17	Absorption, scattering and extinction efficiencies of an astro dust grain.	29
1.18	A day in the life of five carbonaceous grains heated by the local ISRF.	31
1.19	Effect of the ISRF intensity U on the infrared spectrum.	33
1.20	Grain size distributions of different dust models.	35
1.21	Annotated AROMA experimental setup (IRAP, France).	38
1.22	Representation of the NASA Ames PAH experiment.	38
1.23	Laboratory and modeled PAH spectra.	39
1.24	Schematic representation of the evolution of interstellar PAH populations across a PDR.	43
2.1	Bird's-eye view of the IRC.	46

2.2	Relative field-of-view location and size of the three channels of AKARI/IRC.	47
2.3	Demonstration of the <i>bootstrapping</i> method to propagate the uncertainties.	50
2.4	Demonstration of the functions of the IRC pipeline parameters on IRC spectra.	52
2.5	Artifacts around $3.3\ \mu\text{m}$ in the IRC spectra.	54
2.6	The IRS cold assembly.	55
2.7	IRS basic calibrated data (BCDs).	57
2.8	Backtracking bad pixels surviving the Auto-gen tool within CUBISM.	60
2.9	Possible causes for overlooking bad pixels.	61
2.10	Linearity assessment of the CUBISM-processed uncertainty.	62
2.11	Comparison of the uncertainties derived from the sky and from CUBISM.	63
2.12	Effect of pointing uncertainty on S/N ratio.	65
2.13	IRS PSF size variation as a function of wavelength.	67
2.14	Example of a sparse 7×2 spectral map with <i>Spitzer</i> /IRS.	70
2.15	Reconstruction of a sparsely sampled map.	71
2.16	Example of inter-calibration.	72
2.17	An overview of data-processing workflow.	74
2.18	M 82 in the M 81 group.	75
2.19	Illustration of M 82 observations.	79
2.20	Saturation effect in <i>Spitzer</i> observations.	80
2.21	Inter-calibration diagrams.	82
2.22	Combined spectra of M 82 (slit A; central disk).	83
2.23	Combined spectra of M 82 (slit G; southern wind).	83
2.24	Combined spectra of M 82 (slit M; northern wind cap).	84
3.1	Comparison of three MIR spectral fitting methods.	87
3.2	Empirical calibration of UIB profiles.	90
3.3	Distributions of hyperparameter integrated autocorrelation times.	109
3.4	Synthetic galaxy spectra.	111
3.5	Least-square and non-HB fits of synthetic galaxy spectra.	114
3.6	Non-HB and HB fits of synthetic galaxy spectra.	115
3.7	Median models fitted with Bayesian methods.	115
3.8	Parameter distributions in the non-HB fit.	116
3.9	Parameter distributions in the HB fit.	117
3.10	ACFs of the means of a parameter (after burn-in).	117

3.11	ACFs of the standard deviation of a parameter (after burn-in).	118
3.12	ACFs of the correlation coefficients of two parameters (after burn-in).	118
3.13	Correlations of intensity ratios fitted by the Bayesian methods.	119
3.14	Non-correlated intensity ratios of the non-HB and HB fit.	119
4.1	M 82 spectra fitted by least-squares (χ^2).	123
4.2	M 82 spectra fitted by non-HB.	123
4.3	M 82 spectra fitted by HB.	124
4.4	Multivariate distributions between HB fitted parameters.	125
4.5	Impact of extinction on fitted UIBs.	126
4.6	PAH band ratio as diagnostics of physical conditions.	130
4.7	Quantifying band ratio variations with size and charge effects.	131
4.8	Relation between PAH dehydrogenation and ISRF hardness.	133
4.9	Dehydrogenation probed by warm H ₂ .	134
5.1	Cosmological redshifting of a galaxy.	139
A.1	Illustration of the specific intensity.	141
D.1	Median models fitted with the HB method.	153
D.2	Median models fitted with the non-HB method.	154
D.3	Variations of extinction amplitude with extensive quantity parameters.	155
D.4	Variations of extinction amplitude with emission line and band intensity ratios.	156
D.5	Multivariate distributions between extensive physical quantities.	157
D.6	Multivariate distributions between emission line and band intensity ratios.	158
D.7	Distributions of non-HB integrated autocorrelation times.	159
D.8	ACFs of the correlation coefficients of two parameter (without burn-in).	160
D.9	ACFs of the correlation coefficients with reduced sampling (after burn-in).	160
D.10	Inter-calibration diagrams of <i>Spitzer</i> /IRS sub-maps (follow-up of Fig. 2.21).	162
D.11	Combined spectra of M 82 (slit B; central disk).	163
D.12	Combined spectra of M 82 (slit C; central disk).	163
D.13	Combined spectra of M 82 (slit D; disk edge).	164
D.14	IRC spectra of M 82 (slit E; disk edge).	164
D.15	Combined spectra of M 82 (slit F; southern wind).	165
D.16	Combined spectra of M 82 (slit H; southern wind).	165
D.17	Combined spectra of M 82 (slit I; southern wind).	166

D.18 Combined spectra of M 82 (slit J; northern wind).	166
D.19 Combined spectra of M 82 (slit K; northern wind).	167
D.20 Combined spectra of M 82 (slit L; northern outer wind).	167
D.21 IRC spectra of M 82 (slit N; northern wind cap).	168
D.22 HB fits of M 82 spectra.	168

List of Tables

1.1	Abundances of the carriers of infrared (IR) emission components.	41
2.1	IRC module characteristics.	47
2.2	IRS module characteristics.	56
2.3	Uncertainty sources.	66
2.4	Full Width at Half-Maximum (FWHM) of spectral mapping PSF.	68
2.5	MIR spectroscopy and broadband photometry wavelength ranges (μm).	71
2.6	Observational parameter values for the galaxy M 82.	73
2.7	AKARI/IRC AORs of M 82.	77
2.8	<i>Spitzer</i> /IRS AORs of M 82.	78
2.9	Spectrum stitching process for M 82.	81
3.1	Overview of three MIR spectral fitting methods.	88
3.2	UIB profile parameters.	92
3.3	Most prominent MIR gas lines.	94
3.4	Grain optics.	96
3.5	MILES default input settings for model parameters.	98
3.6	Values of the free parameters used to generate synthetic spectra of galaxy.	112
4.1	UIB feature assignments.	128
A.1	Physical quantities used to describe the radiation.	142
D.1	Sample selection with AKARI observations. I.	172
D.2	Sample selection with AKARI observations. II.	173
D.3	Sample selection with AKARI observations. III.	174
D.4	Sample selection with AKARI observations. IV.	175
D.5	Sample selection with AKARI observations. V.	176

D.6 Sample selection with AKARI observations. VI.	177
D.7 Sample selection with AKARI observations. VII.	178
D.8 Sample selection with AKARI observations. VIII.	179
D.9 Sample selection with AKARI observations. IX.	180
D.10 Sample selection with AKARI observations. X.	181

